Bridging Three-Dimensional Numerical Modelling and Experiments to Underpin Extrudate Swelling of Polymer Melts

Verbinden van driedimensionale numerieke modellering en experimenten voor inzicht in het zwelgedrag van geëxtrudeerde polymeersmelten

Dahang Tang

Promotoren: prof. dr. ing. L. Cardon, prof. dr. ir. D. R. D'hooge
Proefschrift ingediend tot het behalen van de graad van
Doctor in de ingenieurswetenschappen: materiaalkunde

UNIVERSITEIT
GENT

Vakgroep Materialen, Textiel en Chemische Proceskunde
Voorzitter: prof. dr. P. Kiekens
Faculteit Ingenieurswetenschappen en Architectuur
Academiejaar 2019 - 2020

ISBN 978-94-6355-407-7
NUR 971
Wettelijk depot: D/2020/10.500/84

PROMOTORS

Prof. L. Cardon
Ghent University Faculty of Engineering and Architecture
Department of Materials, Textiles and Chemical Engineering

Prof. D.R. D'hooge
Ghent University Faculty of Engineering and Architecture
Department of Materials, Textiles and Chemical Engineering

EXAMINATION COMMITTEE

Prof. P. De Baets	(Chair)	Ghent University, Belgium
Prof. L. Cardon	(Promotor)	Ghent University, Belgium
Prof. D.R. D'hooge	(Promotor)	Ghent University, Belgium
Prof. M. Eeckhout		Ghent University, Belgium
Prof. P.H.M. Van Steenberge		Ghent University, Belgium
Prof. G. Mompean		University of Lille Nord de, France
dr. F.H. Marchesini		Ghent University, Belgium

RESEARCH INSTITUTE

Ghent University
Department of Materials, Textiles and Chemical Engineering
Centre for Polymer and Material Technologies
Tech Lane Ghent Science Park/Campus A
Technologiepark Zwijnaarde 130
B-9052 Ghent
dahang.tang@ugent.be

LIST OF PUBLICATIONS

Full length research articles

1) T. Wieme, ***D. Tang***, L. Delva, D.R. D'hooge, L. Cardon 'The relevance of material and processing parameters on the thermal conductivity of thermoplastic composites' *Polym. Eng. Sci.* **2018**, 58, 466 (SCI-IF 2016: 1.449; Special Issue)
2) ***D. Tang***, F.H. Marchesini, D.R. D'hooge, L. Cardon 'Isothermal flow of neat polypropylene through a slit die and its die swell: bridging experiments and 3D simulations' *J. Non-Newton. Fluid Mech.* **2019,** 266, 33 (SCI-IF 2017: 2.3)
3) ***D. Tang***, F.H. Marchesini, L. Cardon, D.R. D'hooge 'Three-dimensional flow simulations for polymer extrudate swell out of slit dies from low to high aspect ratios' *Phys. Fluids* **2019**, 31, 093103 (SCI-IF 2018: 2.627)
4) ***D. Tang***, F.H. Marchesini, L. Cardon, D.R. D'hooge 'Evaluating the exit pressure method for measurement of normal stress differences at high shear rates ' *J. Rheol.* **2020,** 64, 3, 739 (SCI-IF 2019: 3.71)
5) ***D. Tang***, F.H. Marchesini, L. Cardon, D.R. D'hooge 'The impact of upstream contraction flow on three-dimensional polymer extrudate swell from slit dies' *J. Non-Newton. Fluid Mech.* **2020,** 282, 104337 (SCI-IF 2018: 2.270)
6) ***D. Tang***, F.H. Marchesini, L. Cardon, D.R. D'hooge 'State-of-the art for extrudate swell of molten polymers: from fundamental understanding at molecular scale toward optimal die design at final product scale' *Macromol. Mat. Eng.* **2020** (SCI-IF 2019: 3.85), Published online. Doi: 10.1002/mame.202000340.

Extended abstract

1) ***D. Tang,*** N. V. Puymbrouck, F.H. Marchesini, D.R. D'hooge, L. Cardon, Die swell of Polypropylene flow through a slit die: experiment and 3D simulation*:* 8th International Conference on Polymers and Moulds Innovations, Guimarães, Portugal, 19-21 September 2018, **Oral presentation**.

Abstracts

1) ***D. Tang***, F. H. Marchesini, L. Cardon, D.R. D'hooge, Study of the extrudate swell behavior of the planar flow of polypropylene: A comparison of 3D and 2D modelling results. XIXth IWNMNNF, Porto, Portugal, 6-8 June 2019, **Oral presentation**.
2) ***D. Tang***, *Flavio H. Marchesini, et al.*, Three-dimensional simulation for the extrudate swell of polymer melts from slit dies and its application on normal stress measurements, ICR 2020 - 18th International Congress on Rheology, Rio, Brazil, 12/2020, **Oral presentation** (envisaged).

EXPRESSION OF GRATITUDE

Looking back to the past four years since I arrived in Ghent, Belgium, a feeling that arises in my mind that time has gone so fast. Now I am in the place where I can almost step towards the final destination to push for the Phd degree which I describe it as a long-distance journey, during which I am not alone and isolated, instead I have obtained a large amount of amazing support, aids and help from plenty of people who deserve my deepest gratitude. First of all, I would like to express my thanks to my promoters, Prof. Ludwig Cardon and Prof. Dagmar R. D'hooge. I really appreciate the opportunity you've given me to study at the incredible fine-tuned CPMT group of Ghent University. Now I still remember 5 years ago when I first met Prof. Ludwig Cardon in my previous university, Sichuan University, where he was giving a presentation to all of us to introduce Ghent University. Indeed, I have to say this presentation changed my mind and an idea came up in my mind "why not study abroad to pursue the Phd degree" which had never been a priority option for myself. Fortunately, Prof. Ludwig Cardon did not reject me at first even though my spoken English was not good at that time. Additionally, I also thank him very much for providing the essential devices for my research work. Special thanks to Prof. Dagmar D'hooge for his extensive aids and support in each vital period of my Phd study to get through the toughness and darkness along the journey to steer me in the right direction. I also appreciate his patience and fast feedback each time to shear his enthusiasm for some of my ideas and teach me to write a more academic scientific paper with his constructive suggestion, which apparently boosts my academic background to a higher level. Without his paramount contributions, I would have much more difficulty for all my publications until now.

Now a great share of my deep gratitude is delivered to the great family of CPMT research group to create a warm and harmony working environment. Many thanks are given to my colleagues, Karen Van Kets, Dr. Laurens Delva, Dr. Lingyan Duan, Maja Kuzmanovic, Kurt Van Houtte, Dr. Nicolas Mys, Mustafa Erkoç, Sara Hubo, Sisi Wang, Dr. Tom Wieme, Dr. Willem Van De Steene, Nicolas Van Damme and Prof. Kim Ragaert who gave me a big warm welcome on the first day I joined this group and also the kindness towards me in next research periods. I am very grateful to our technical colleagues, Kurt Van Houtte, Mustafa Erkoç, Marcel Moerman and Stefaan Van Biervliet for addressing the equipment issues during my research experiments and thankful also to our administrative colleague, Veerle Van Cauwenberghe, for her large quantities of paper and documents work. Special thanks are delivered to Dr. Flávio H. Marchesini who is an expert in the fields of rheology and mathematical equations. When I have some confusions and tough questions in rheology field, he is always standing there to patiently help me figure out all the puzzles regarding my research work. Without his assistance, my Phd life would have been significantly more stressful. Apparently, office culture is also a good additive element for a nice long Phd journey, so I am also very grateful to my colleagues, Sisi Wang, Andrea La Gala, Dr. Flavio H. Marchesini, Dr. Rudinei Fiorio, Daniel Amaral Ceretti, Zhenmin Jiao, Tom Van Waeleghem, Nan Lin, Ruben Vande Ryse, who create a warm atmosphere to work and communicate with fun. In particular, the ‘cake day’ activity on Thursday of each week is a special moment for us to share our own happiness with each other. In addition, it is also important for me to thank my other colleagues to give me the supports and help during my Phd in many aspects although some of them have left the group: Astrid Van Belle, Amir Bashirgonbadi, Dashang Mi, Ellen Fernandez, Ellen De Tandt, Gianni Vyncke, Dr. Martin Spork, Kerstin Kleinhans, Marie Grodent

and Ruben Demets. Also, my heartfelt gratitude goes toward my Chinese friends in Ghent who helped me get rid of the frustrating topic of numerical modelling for a while to enjoy the fantasy of the life. Finally, I want to express my deepest gratitude again to all of you in this group family to often organise various teambuilding activities to let me have the opportunity to learn about different cultures and food here so that my so-called 'boring' personal life could be much more plentiful.

I would like to thank the members of the examination committee: Prof. Patrick De Baets, Prof. Mia Eeckhout, Prof. Paul Van Steenberge Prof. Gilmar Mompean and Dr. Flavio H. Marchesini. Thanks to their close inspection and meaningful suggestions on my thesis to improve it the quality and readability.

Additionally, I would like to thank the granted scholarship from the China Scholarship Council to support me for my Phd study in the past four years. Specially, my deepest gratitude to the special care and looking-after from our Chinese government organizing the delivery of the masks and detailed printed guidance to us studying abroad during the period of the coronavirus crisis. Also, I want to thank my good friend from Sichuan University in China, Dr. Zhongguo Zhao who gave me a big assistance for the rheological measurements.

Furthermore, special honors are given to my girlfriend, Miss Yalin Zhang who gave me incredible supports, encouragements, and even protections, and pointed the right direction at the cross corners of this long journey when I was in depression and anxiety due to the stress stemming from my research work. I believe the near future of us will be filled with happiness and brightness.

Finally, I would like to give my sincerest attitude to my families: my parents, my grandmother and my aunt. They always love me and give me best supports. Here I

would like to make a best wish for my grandmother who now is fighting against a disease. I wish she will stay healthy in the rest of life.

ENGLISH SUMMARY

Extrusion, a polymer processing method under melt conditions, is widely used in industrial applications. Extrudate swell, which is also known as die swell or Barus effect, is a viscoelastic phenomenon taking place after polymer melt emerges the die exit. An excellent understanding of the extrudate swell behavior plays an important role in the polymer production community for a wide range of applications to control and adjust the processing conditions and die design strategy to obtain the optimized product profiles. Despite that many researchers predominantly attribute the extrudate swell of polymers to the recoverable stress and strain applied to the deformed polymer chains, this phenomenon is still not fully understood. Numerical modellings allowing for the insights into the flow behavior inside and outside the flow channel is recommended to investigate the complicated extrudate swell behavior for a fundamental understanding. This PhD research reviews the previous work which lies in the coverage of all the important aspects, including the fundamental mechanistic understanding at the molecular scale, the combined usefulness of experimental and modelling characterization, and the control of the extrudate swell for complex geometries. Focus of this doctoral study is on the comprehensive investigation of the extrudate swell of polymer and composites melts by a combination of experimental validations and three-dimensional (3D) modelling mainly with the viscoelastic constitutive PTT model based on the finite element method with *PolyFlow* solver. Impacts stemming from the die geometry characteristics, the upstream contraction flow and material molecular characteristics on the complicated 3D extrudate swell behavior, thus highlighting the anisotropic swelling behavior in all dimensions of extrudate from slit dies. It indicates that the simplified 2D modelling is not able to

catch the comprehensive extrudate swell behavior of flow through the slit dies even though the aspect ratio of the die is up to 20. Furthermore, a validation of the exit pressure method for measuring the normal stress difference data at high strain rates is conducted by evaluating the 3D extrudate swelling of various polymer melts with material parameters of PTT model obtained by tuning the corresponding rheological data including the N_1 data.

Firstly, to evaluate the ability of the constitutive models in predicting the three-dimensional behavior of polymer melt flowing through the dies, the simulation results regarding the flow behavior of PP melt at 200 °C through a slit die and upon subsequent swelling is investigated with the generalized Newtonian constitutive model with the Cross law viscosity function and the viscoelastic multi-mode PTT model, which are compared to the extrusion experiments. The pressure profiles predicted by both models inside the die corresponds well to the experimental data obtained for all flow rates evaluated. The larger simulated exit pressure of PTT flow compared to that of Cross law flow leads to the corresponding experimental results for extrudate swell through real-time measurements. Compared to the experiments, the opposite varying trends of the swell behavior in both height and width directions along the distance from the die exit as a function of the flow rates indicate the failure of the Cross law model in predicting the viscoelastic flow behavior of PP melts. In addition, the distance from the die exit in which the final extrudate shape is obtained strongly depends on the die width because the swell ratio in the width direction increases in a much lower rate than the swell ratio in the height direction until equilibrium is achieved in both directions.

Secondly, varying the aspect ratio of the slit dies contributes to a large impact on the 3D extrudate swell ratio. High aspect ratio causes a low width swell ratio B_1 and the

edge height swell ratio B_2 and shifts the onset of the axial equilibrium swelling position to a further distance. Contract flow at the edge of the extrudate height is noted while the increasing edge height swell ratio B_2 is observed. The significant deviation of the middle height swell ratio B_3 profiles of the 3D flow from that of the corresponding 2D simulation highlights the necessity of the 3D numerical modelling to capture the practical flow behavior. This phenomenon of a secondary shrinkage is not eliminated even if the aspect ratio increases to the highest value of 20, highlighting the anisotropic swelling behavior caused by varying the aspect ratio of the slit dies. The mechanism for the above phenomenon is illustrated by the flow velocity and stress fields. A significant deviation of the 3D configurations from the corresponding 2D one inside and outside the die is generally noted. Increasing the aspect ratio of the flow cells narrows the discrepancy but cannot vanish the 3D effect. Furthermore, a parametric study reveals that the secondary shrinkage flow becomes large with decreasing parameter ξ but still cannot be observed in the corresponding 2D flow. This implies that the 3D effect on the extrudate swell behavior depends not only on the geometric characteristics of the flow channel but also on the melt material parameters.

Thirdly, contraction flow stemming from the variations of the area size of the cross section of the flow channels is an obvious phenomenon in extrusion processing and its impact on the subsequent extrudate swell behavior is mainly controlled by the downstream die length/height ratio. The 3D numerical modelling by PTT model of the polymer melt at different flow rates exhibits that decreasing the die length leads to an opposite variation trend of the swell ratio in the width and edge height direction (decreases up to 30%) compared to the middle height direction (increases up to 55%). It is interesting to note that the area swell ratio remains limited decreases below 5%,

specifically for lower flow rates. This implies that an identification of possible anisotropy should in general not be based on the area swell ratio. Furthermore, especially for polymer melts that experience large extensional deformations, a method to obtain an extrudate product with a less uneven profile is to elongate the die.

A detailed study of the flow physical variable fields including the stress and velocity is responsible for the effect on the extrudate swell behavior caused by the upstream contraction flow. For example, the similar final extrudate average axial velocity regardless of the die length l_2 value is consistent with the similar area swell ratios and implies a similar axial velocity redistribution behavior. Outside the die exit, a big difference of the stress redistribution behavior caused by the variations of the die length l_2 illustrates the corresponding anisotropic swell behavior mentioned above. The similar final extrudate average axial velocity regardless of the l_2 value corresponds to the similar area swell ratios and implies a similar axial velocity redistribution behavior. Additionally, the evolution of the transversal velocity v_y and lateral velocity v_z components after the die exit directly illustrates the opposite varying trend of the swell behavior in the extrudate middle height and width direction upon increasing die length. The combined effect of the elongational flow through the converging flow region and the material parameters of polymer melt is firstly comprehensively investigated.

Fourthly, the disputed ‘exit pressure’ method used for measuring the normal stress difference of polymer melts at high stain rate range, which mainly leads to the taking-place of the extrudate swell behavior once the flow emerging the dies, is evaluated by the 3D modelling of the extrudate swell behavior of several polymer melts including neat PP, LDPE and HDPE. For neat polymer melts at 200 ^{o}C, we have comprehensively assessed the exit pressure method via the slit rheometer to measure

N_1 values at high shear rates. In this method, the corresponding exit pressure values is yielded via extrapolating the (quasi-)linear axial pressure profiles for the polymers to die exit at various wall shear rates, which in turn are related to the associated shear stresses to deliver N_1 values. The N_1 values at the shear-rate magnitude order of 10 to 100 s^{-1} as measured by the exit pressure method lie additionally in the value range calculated by the Laun rule with an exponent α of 0 and 0.7.

3D numerical simulations with respect to the extrudate swell behavior have been performed with the differential viscoelastic multi-mode PTT model, whose corresponding material parameters are obtained by tuning the rheological functions including the N_1 data calculated by the empirical Laun rule that are consistent with the exit pressure method based N_1 data. A good agreement between the predicted extrudate swell and experimental measurements for the neat polymer melts further confirms that the exit pressure method is appropriate to determine N_1 values. In addition, the pressure contribution from velocity rearrangement near the die exit allows for *ca.* 25-40% at various shear rates, which although does not dismiss the exit pressure method since the actual simulated N_1 values with 3D modelling by PTT model are consistent with those by the exit pressure method based on the simulated pressure profiles. Overall, the exit pressure method can be reliable utilized for the neat polymers studied, but also have potential for more complex materials like polymer composite since the N_1 values obtained with the exit pressure method appear to be in the extrapolation region of those obtained by the rotational rheometer.

Lastly, with the aim of investigating the extrudate swell behavior of polymer composites, the 3D numerical simulations by PTT model are compared to the experimental measurements. The rheological properties of PP/Graphite composites with various volumetric filler contents are firstly compared and discussed. It is found

that the linear rheological properties including the storage G' and loss G'' modulus for all PP composites are perfectly fitted by the original PTT model. However, with the increasing of the filler content, there is an unignored overprediction of the non-linear rheological properties such as the shear viscosity η_s and the first normal stress difference N_1 by PTT model, especially as the volumetric filler content grows up to 21.1% which results in the largest overprediction by PTT model, although they have at least the right order of magnitude values. A modified PTT model is proposed by means of establishing the functions of the material parameters such as η_i, ξ and ε against the volumetric content of graphite filler, respectively. The results show that the simulated extrudate swell behavior in all dimensional directions firstly decreases with adding filler particles as an expectation corresponding to the experiments. However, swell ratios increase with a further addition of filler content unexpectedly, in contrary to the experimental observations. It indicates that the constitutive PTT model fails in predicting the extrudate swell behavior of polymer composite with high volumetric filler content. Reasons are attributed to the deconstruction of the network between filler and matrix as a large strain is applied, which are not taken into consideration by the original PTT model in this preliminary study.

Overall, this doctoral research demonstrates the comprehensive viscoelastic flow behavior including the extrudate swell behavior of several polymer melts and composites filled with rigid fillers through the slit dies with various die geometrical characteristics and the upstream contraction flow regions, which is on the other hand conducted to validate the exit pressure method for measuring the normal stress differences at high strain rates. The 3D effect caused by the side wall effect on the extrudate swell behavior through the slit dies is illustrated as compared to the corresponding ideal 2D modelling configurations which have been mostly reported in

the aspect of literatures. The failure of the constitutive PTT model in predicting the extrudate swell behavior of the polymer composites with high filler content indicates the need to develop a modified PTT model to account for the interplays between the filler and matrix once strains applied to melt, which is an interesting research topic in the field of rheology regarding the modelling of the complicated extrudate swell behavior.

NEDERLANDSE SAMENVATTING

Extrusie, een kunststofverwerkingsmethode onder smeltomstandigheden, wordt veel gebruikt in industriële toepassingen. Het zwelgedrag van geëxtrudeerd polymeer, ook bekend als matrijszwelling of Barus-effect, is een visco-elastisch fenomeen dat plaatsvindt nadat polymeersmelt de matrijs verlaat. Een goede kennis van het zwelgedrag is belangrijk bij extrusiegebaseerde kunststofverwerking met een breed gamma aan toepassingen, dit om de verwerkingsomstandigheden en de ontwerpstrategie voor matrijzen en producten te optimaliseren. Ondanks het feit dat verschillende onderzoekers het zwelgedrag voornamelijk toeschrijven aan de relaxatiespanning evenals spanning die op de vervormde polymeerketens worden uitgeoefend, is dit fenomeen nog steeds niet volledig doorgrond. Numerieke modellen, die inzicht geven in het stromingsgedrag binnen en buiten het stromingskanaal, worden aanbevolen om het complexe zwelgedrag van polymeren fundamenteel te onderzoeken. Dit doctoraatsonderzoek herbekijkt eerder uitgevoerd werk dat alle belangrijke aspecten bundelt, waaronder het fundamentele mechanisme op moleculaire schaal, de gecombineerde bruikbaarheid van experimentele en modelleer karakterisering, evenals de controle van de zwelgedrag voor complexe geometrieën. De focus van deze doctoraatsstudie ligt op het uitgebreid onderzoek naar de extrudaatzwelling van polymeer- en composietsmelten door een combinatie van experimentele validaties en driedimensionale (3D) modellering, voornamelijk met het visco-elastische constitutieve PTT-model op basis van de eindige-elementenmethode met PolyFlow-software. De matrijsgeometrie, stroomopwaartse samendrukking van de polymeerstroom en de moleculaire eigenschappen van het materiaal beïnvloeden het complexe 3D-extrusie-zwelgedrag, waarbij het anisotrope gedrag in alle dimensies

van extrudaat van matrijzen wordt benadrukt. Het onderzoek geeft eveneens aan dat de vereenvoudigde 2D-modellering niet in staat is om het gedrag van stroming door de matrijzen te bepalen, ook al is de aspectverhouding maximaal 20. Bovendien, een validatie van de polymeersmeltdruk in de matrijs door het meten van de normaalspanning verschillen bij hoge spanningswaarden worden uitgevoerd door de 3D-extrudaatzwelling van verschillende polymeersmeltingen te evalueren met materiaalparameters van het PTT-model verkregen door afstemming van de corresponderende reologische gegevens, inclusief de N_1-gegevens.

Ten eerste, om de mogelijkheden van de constitutieve modellen te evalueren bij het voorspellen van het driedimensionale gedrag van polymeersmelt die door de matrijzen stroomt, worden de simulatieresultaten met betrekking tot het stromingsgedrag van PP-smelt bij 200 °C door een plaatmatrijs en daaropvolgende zwelling onderzocht door middel van het gegeneraliseerde Newtoniaanse constitutieve model, de Cross-law viscositeitsfunctie en het visco-elastische multi-mode PTT-model, te vergelijken met de validatie extrusie-experimenten. De door beide modellen in de matrijs voorspelde drukprofielen komen goed overeen met de experimentele gegevens die zijn verkregen voor alle geëvalueerde stroomsnelheden. De grotere gesimuleerde uitgangsdruk van de PTT-stroom in vergelijking met die van de cross law-stroom leidt tot de overeenkomstige experimentele resultaten voor extrudaatzwelling door middel van real-time metingen. Vergeleken met de experimenten wijzen de tegengestelde variërende trends van het zwelgedrag in zowel hoogte- als breedterichtingen langsheen de matrijsuitgang als een functie van de stroomsnelheden op een falen van het Cross law-model bij het voorspellen van het visco-elastische stromingsgedrag van PP-smelt. Bovendien hangt de afstand tot de matrijsuitgang waarin de uiteindelijke extrudaatvorm wordt verkregen sterk af van de matrijsbreedte omdat de

zwelverhouding in de breedterichting met een veel lagere snelheid toeneemt dan de zwelverhouding in de hoogterichting, dit totdat in beide richtingen een evenwicht wordt bereikt.

Ten tweede draagt het variëren van de aspectverhouding van plaatmatrijzen bij tot een grotere impact op de 3D extrudaat zwelverhouding. Een hoge aspectverhouding veroorzaakt zowel een lage zwelverhouding B_1 en zwelverhouding B_2 van de randhoogte, evenals verschuift het begin van de axiale evenwichtstoestand naar een verdere afstand. Samentrekking van de polymeerstroom aan de rand van de extrudaathoogte wordt vastgesteld terwijl het toenemen van de randhoogte zwelverhouding B_2 wordt waargenomen. De significante afwijking van de B_3-profielen met gemiddelde zwelverhouding van de 3D-stroom van die van de overeenkomstige 2D-simulatie benadrukt de noodzaak van 3D-numerieke modellering om het polymeer stromingsgedrag vast te leggen. Dit fenomeen van secundaire krimp wordt niet geëlimineerd, zelfs niet als de aspectverhouding toeneemt tot 20, wat het anisotrope zwelgedrag benadrukt dat wordt veroorzaakt door het variëren van de aspectverhouding van plaatmatrijzen. Het mechanisme voor het bovenstaande fenomeen wordt geïllustreerd door de stroomsnelheid- en spanningsvelden. Over het algemeen wordt een significante afwijking van de 3D-configuraties tegenover de corresponderende 2D binnen en buiten de matrijs opgemerkt. Door de aspect ratio van de 2D elementen te vergroten, wordt de discrepantie verkleind, doch kan het 3D-effect niet oplossen. Bovendien laat een parametrische studie zien dat de secundaire krimpstroom groot wordt met afnemende parameter ξ, maar nog steeds niet kan worden waargenomen in de overeenkomstige 2D-stroom. Dit houdt in dat het 3D-effect op het zwelgedrag niet alleen afhangt van

de geometrische kenmerken van het stromingskanaal, maar ook van de smeltparameters van het extrudaat.

Ten derde is de contractiestroom die het gevolg is van de variaties van de oppervlakte van de dwarsdoorsnede van de stromingskanalen een duidelijk fenomeen bij extrusie polymeerverwerking en wordt de invloed ervan op het daaropvolgende extrudaatzwelgedrag voornamelijk bepaald door de stroomafwaartse matrijslengte/hoogteverhouding. De 3D numerieke modellering door het PTT-model van de polymeersmelt bij verschillende stroomsnelheden laat zien dat het verkleinen van de matrijslengte leidt tot een tegengestelde variatietrend van de zwelverhouding in de breedte-en randhoogterichting (neemt af tot 30%) in vergelijking met de middelste hoogte richting (neemt toe tot 55%). Interessant om op te merken is dat de doorsnede zwelverhouding voor lagere stroomsnelheden beperkt blijft en onder de 5% daalt. Dit houdt in dat een identificatie van mogelijke anisotropie in het algemeen niet mag worden gebaseerd op de oppervlaktezwelverhouding. Bovendien, in het bijzonder voor polymeersmelt die grote extensievervormingen ondergaan, is het verlengen van de matrijs een methode om een extrudaatproduct met een minder ongelijkmatig profiel te verkrijgen.

Een gedetailleerde studie van de stroomfysische variabelen inclusief de spanning en snelheid is verantwoordelijk voor het effect op het extrudaat zwelgedrag, veroorzaakt door de stroomopwaartse contractiestroom. Bijvoorbeeld, de vergelijkbare finale extrudaat gemiddelde axiale snelheid-ongeacht de matrijslengte l_2-waarde is consistent met de zwelverhoudingen van het gebied en impliceert een overeenstemmend herverdelingsgedrag van de axiale snelheid. Buiten de matrijsuitgang illustreert een groot verschil in het spanningsherverdelingsgedrag-

veroorzaakt door de variaties van de matrijslengte l_2 - het overeenkomstige hierboven vernoemd anisotropische zwelgedrag. De uiteindelijke extrudaatgemiddelde axiale snelheid-ongeacht de l_2-waarde-komt overeen met identieke zwelverhoudingen van de doorsnede en impliceert een vergelijkbaar herverdelingsgedrag van de axiale snelheid. Bovendien illustreert de evolutie van de transversale snelheid v_y en laterale snelheid v_z componenten na het verlaten van de matrijs direct de tegenovergestelde variërende trend van het zwelgedrag in de extrudaat middenhoogte en breedterichting bij toenemende matrijslengte. Het gecombineerde effect van de verlengde stroom door het convergerende stroomgebied en de materiaalparameters van polymeersmelt wordt uitvoerig onderzocht.

Ten vierde wordt de gecontesteerde uitstroomdrukmethode die wordt gebruikt voor het meten van het normaalspanningsverschil van polymeersmelt bij een hoog reksnelheidsbereik-wat voornamelijk leidt tot het plaatsvinden van het extrudaat-zwelgedrag zodra de stroom die uit de matrijzen komt-geëvalueerd via 3D modellering van het extrudaat-zwelgedrag van verschillende polymeersmelten, waaronder zuiver PP, LDPE en HDPE. Voor zuivere polymeersmelt bij 200 ^{o}C hebben we de uitstroomdrukmethode uitvoerig geanalyseerd via een capilaire reometer om N_1-waarden bij hoge afschuifsnelheden te meten. Bij deze methode worden de overeenkomstige uitgangsdrukwaarden verkregen door extrapolatie van de (quasi) lineaire axiale drukprofielen van de polymeren naar de matrijsuitgang bij verschillende wand-schuifsnelheden, welke op hun beurt gerelateerd zijn aan de bijbehorende schuifspanningen om N_1-waarden aan te leveren. De N_1-waarden bij de afschuifsnelheidsterkte van 10 tot 100 s^{-1} zoals gemeten met de uitgangsdrukmethode liggen bovendien in het waardebereik berekend door de Laun-regel met een exponent van 0 en 0,7. 3D numerieke simulaties met betrekking tot het extrudaatzwelgedrag

zijn uitgevoerd met het differentiële visco-elastische multi-mode PTT-model, waarvan de overeenkomstige materiaalparameters zijn verkregen door de reologische functies, inclusief de N_1-gegevens, berekend door de empirische Laun-regel die consistent is met de uitgangsdrukmethode gebaseerde N_1-gegevens. Een goede overeenstemming tussen de voorspelde extrudaatzwelling en experimentele metingen voor de zuivere polymeersmelt bevestigt verder dat de uitstroomdrukmethode geschikt is om N_1-waarden te bepalen. Bovendien wordt de drukbijdrage voor ca. 25-40% veroorzaakt door de snelheidsveranderingen bij de uitgang van de matrijs, en dit bij verschillende afschuifsnelheden, wat echter de uitstroomdrukmethode niet ontkend, aangezien de werkelijke gesimuleerde N_1-waarden met 3D-modellering door PTT-model consistent zijn met die van de uitstroomdrukmethode op basis van de gesimuleerde drukprofielen. Over het algemeen kan de uitstroomdrukmethode betrouwbaar worden gebruikt voor de bestudeerde polymeren, maar heeft ook potentieel voor complexere materialen zoals polymeercomposieten aangezien de N_1-waarden die zijn verkregen met de uitstroomdrukmethode in het extrapolatiegebied lijken te liggen; welke verkregen werden door de rotationele reometer.

Ten slotte, met als doel het extrudaat-zwelgedrag van polymeercomposieten te onderzoeken, worden de 3D numerieke simulaties door PTT-model vergeleken met de experimentele metingen. Vooreerst worden de reologische eigenschappen van PP/grafiet composieten met verschillende volumetrische vulstoffen vergeleken en besproken. Het blijkt dat de lineaire reologische eigenschappen inclusief G' en G'' modulus voor alle PP composieten perfect passen bij het originele PTT model. Echter, met de toename van het vulstofgehalte, is er een niet-gefundeerde overschatting van de niet-lineaire reologische eigenschappen zoals de afschuifviscositeit η_s en het eerste normaalspanningsverschil N_1 door PTT-model, vooral omdat het volumetrische

vulstofgehalte stijgt tot 21,1% wat resulteert in de grootste overschatting per PTT-model, hoewel ze op zijn minst de juiste grootte-waarden hebben. Een gemodificeerd PTT-model wordt voorgesteld door de functies van de materiaalparameters zoals η_i, ξ en ε vast te stellen tegen het volumetrische gehalte van grafietvulstof. De resultaten laten zien dat het gesimuleerde extrudaat-zwelgedrag in alle richtingen eerst afneemt met het toevoegen van deeltjes, wat in overeenstemming is met experimenten. De zwelverhoudingen nemen echter onverwacht toe met een verdere toevoeging van vulstof, in tegenstelling tot de experimentele waarnemingen. Het geeft aan dat het constitutieve PTT-model niet slaagt in het voorspellen van het extrudaat-zwelgedrag van polymeercomposieten met een hoog volumetrisch vulstofgehalte. Dit wordt toegeschreven aan de deconstructie van het netwerk tussen vulstof en matrix bij het toepassen van een grote spanning, welke in dit vooronderzoek door het oorspronkelijke PTT-model niet in aanmerking worden genomen.

In het algemeen toont dit doctoraatsonderzoek het uitgebreide visco-elastische stromingsgedrag door plaatmatrijzen aan, inclusief het extrudaat-zwelgedrag van verschillende polymeersmelten en composieten gevuld met grafiet vulstof, rekening houdend met verschillende matrijsgeometrische kenmerken en de stroomopwaartse samentrekkingsstroomgebieden. Anderzijds werd de uitstroommethode voor het meten van de normale spanningsverschillen bij hoge reksnelheden gevalideerd. Het 3D-effect veroorzaakt door het zijwandeffect op het extrudaat-zwelgedrag door de spleetmatrijzen wordt geïllustreerd in vergelijking met de ideale corresponderende 2D-modelleerconfiguraties die meestal in literatuur zijn gerapporteerd. Het falen van het constitutieve PTT-model bij het voorspellen van het extrudaat-zwelgedrag van de polymeercomposieten met een hoog vulstofgehalte geeft de noodzaak aan om een gemodificeerd PTT-model te ontwikkelen dat rekening houdt met de interactie tussen

vulstof en de matrix zodra rek wordt uitgeoefend op de smelt, wat een toekiomstig interessant onderzoeksthema is op vlak van reologie met betrekking tot het modelleren van het complexe extrudaat-zwelgedrag.

TABLE OF CONTENTS

LIST OF PUBLICATIONS i

EXPRESSION OF GRATITUDE iii

ENGLISH SUMMARY vii

NEDERLANDSE SAMENVATTING xv

LIST OF SYMBOLS AND ABBREVIATIONS xxvii

Chapter 1 1

SCOPE AND AIMS 1

Chapter 2 7

State-of-the-art for extrudate swell of molten polymers: from fundamental understanding at molecular scale toward optimal die design at final product scale ... 7

2.1. INTRODUCTION 8
2.2. FUNDAMENTAL INTERPRETATION AT THE MOLECULAR LEVEL 13
2.3. EXPERIMENTAL CHARACTERIZATION TOOLS 15
2.3.1. Offline measurement 17
2.3.2. Online measurement 19
2.4. MAIN EXPERIMENTAL OBSERVATIONS 20
2.4.1. Effect of processing parameters 20
2.4.2. Effect of die geometry parameters 22
2.4.3. Effect of polymer material parameters 23
2.5. MODELING TOOLS 27
2.5.1. Semi-empirical formulas to capture overall die swell 28
2.5.2. Discretization methods and constitutive models for detailed viscoelastic and flow description 30
2.6. REVERSE ENGINEERING: MODEL-BASED DIE DESIGN FOR A CONTROLLED SWELLING FOR COMPLEX GEOMETRIES 53
2.7. CONCLUSIONS 58
REFERENCES 61

Chapter 3 73

Flow of neat polypropylene through a slit die and its die swell: bridging experiments and 3D numerical simulations 73

3.1. INTRODUCTION 74
3.2. 3D MODELLING PRINCIPLES 78
3.2.1. Governing equations 78
3.2.2. Geometry and boundary conditions 80
3.2.3. Details on finite element calculations 81
3.3. 3D MODELLING PRINCIPLES 83

3.3.1. Rheological measurements and parameter tuning for PTT and Cross law model 83
3.4. RESULTS AND DISCUSSION 87
3.4.1. Pressure and profiles 87
3.4.2. Anisotropic extrudate swell 88
3.4.3. Non-uniformity in v_x distributions 93
3.4.4. Non-uniformity in stress distributions 96
3.4.5. Non-uniformity for radial velocity (v_y) and lateral velocity (v_z) 101
3.5. CONCLUSIONS 102
REFERENCE 105
Chapter 4 109
Three-dimensional simulations for polymer extrudate swell out of slit dies from low to high aspect ratios 109
4.1. INTRODUCTION 110
4.2. MODELLING PRINCIPLES 113
4.2.1. Geometric parameters 113
4.2.2. Governing equations 114
4.2.3. General geometry and boundary conditions 117
4.3. RESULTS AND DISCUSSIONS 120
4.3.1. Effect of aspect ratio on the 3D die swell characteristics 120
4.3.2. Relation aspect ratio and velocity fields 127
4.3.3. Relation between aspect ratio and stress field 130
4.3.4. Parametric study regarding non-linear PTT parameters 132
4.4. CONCLUSION 137
REFERENCES 139
Chapter 5 143
The impact of upstream contraction flow on three-dimensional polymer extrudate swell from slit dies 143
5.1. INTRODUCTION 144
5.2. MODELLING PRINCIPLES 147
5.2.1. Geometric parameters 147
5.2.2. Governing equations 148
5.2.3. General geometry and boundary conditions 150
5.2.4. Method of 3D numerical solution 152
5.3. RESULTS AND DISCUSSION 153
5.3.1. Extrudate swell 153
5.3.2. Stress and velocity fields 158
5.3.3. Parametric study of the extrudate swell 165
5.4. CONCLUSIONS 167
REFERENCES 170

Chapter 6 173

Evaluating the exit pressure method for measure- ments of normal stress difference at high shear rates by 3D modelling 173

6.1. INTRODUCTION 174
6.2. MATERIALS AND EXPERIMENTAL CHARACTERIZATION 178
6.2.1. Materials 178
6.2.2. Mass flow rate and pressure measurements 179
6.2.3. Conventional rheological measurements 179
6.2.4. Slit die viscosity measurements 181
6.2.5. Exit pressure method for measurement of first normal stress difference 181
6.2.6. Extrudate swell measurement 182
6.3. MODELLING PRINCIPLE FOR MULTIDIMENSIONAL FLOW CHARACTERISTICS 182
6.3.1. Details on the governing equations and constitutive model 182
6.4. RESULTS AND DISCUSSION 187
6.4.1. Measurement of die pressure profile and shear dependent viscosities 187
6.4.2. Determination of N_1 via the exit pressure method and through conventional rheological analysis 190
6.4.3. Numerical analysis to evaluate the assumptions of the exit pressure method 193
6.5. CONCLUSIONS 201
REFERENCES 204
Chapter 7 209

From die swell for neat polymer melts to composite melts: a preliminary study ... 209

7.2. INTRODUCTION 210
7.2. MODELLING PRINCIPLES 212
7.2.1. Geometric parameters 212
7.2.2. PTT constitutive model 213
7.2.3. Boundary conditions and numerical method 214
7.3. MATERIAL AND CHARACTERIZATIONS 215
7.3.1. Materials 215
7.3.2. Conventional rheological measurements 215
7.4. RESULTS AND DISCUSSION 216
7.4.1 Rheological analysis and tuning of PTT model parameters with increasing filler content 216
7.4.2. Extrudate swell as a function of filler content 223
7.4.3. Theoretical evaluation regarding material parameters 228

7.4.4. From simulations with no slip boundary conditions to simulations doing so 232
7.5. CONCLUSIONS 234
REFERENCES 236
Chapter 8 239
CONCLUSIONS AND OUTLOOK 239
8.1. CONCLUSIONS 239
8.2. OUTLOOK 244
Appendix A 247
Extra details on viscoelastic PTT model 247
A.1. PREDICTIONS OF PTT MODEL IN SIMPLE SHEAR FLOW 247
A.2. PREDICTION OF PTT MODEL IN SHEAR-FREE OR EXTENSIONAL FLOW 250
A.3. CONTRIBUTIONS OF EACH MODE TO FINAL RHEOLOGICAL PROPERTIES 251
A.4. SENSITIVITY OF THE MATERIAL PARAMETERS ON THE RHEOLOGICAL PROPERTIES 254
Appendix B 259
Supplementary information for Chapter 4 259
B.1. MESH PATTERNS FOR 3D AND 2D SIMULATIONS 259
B.2. DETAILS ON EXTRUDATE AREA SWELL 261
B.3. EXTRA INFORMATION ON AXIAL VELOCITY COMPONENT 262
B.4. EXTRA INPUT ON STRESS IN DIE 263
REFERENCES 265
Appendix C 267
Supplementary information for Chapter 5 267
C.1. EXTRA INPUT ON THE REDISTRIBUTION OF STRESS COMPONENTS τ_{xx}, τ_{yy} AND τ_{zz} ALONG FLOW DISTANCE 267
Appendix D 273
Supplementary information for Chapter 6 273
D.1. DETAILED EXPLANATION FOR THE EXIT PRESSURE METHOD THROUGH A SLIT DIE 273
D.2. EXTRA INPUT ON DISCUSSIONS OF CHAPTER 5 277
D.2.1. Extra input on pressure measurements for slit die 277
D.2.2. Geometry and Mesh patterns for 3D modelling 278
D.2.3. Extra information on the rheological properties of PP composites 280
D.2.4. Extra details on the PTT model at 200 °C 281
D.2.5. Extra details on the impact of the flow redistributions 282
D.2.6. Non-isothermal modelling with PTT model 283
REFERENCES 287

LIST OF SYMBOLS AND ABBREVIATIONS

List of symbols

Roman symbols

A	Surface area, mm^2
ABS	Acrylonitrile-butadiene-styrene
ALE	Arbitrary Lagrangian Eulerian
B	Swell ratio
B_*	General swell ratio of Newtonian flow
B_1	Width well ratio
B_2	Edge height swell ratio
B_3	Middle height swell ratio
B_4	Area swell ratio
CCD	Charge coupled camera
CFD	Computational fluid dynamics
$\boldsymbol{C}_t$	Cauchy-Green tensor
$\boldsymbol{C}_t^{-1}$	Finger strain tensor
c_p	Specific heat capacity, J kg^{-1} $^oC^{-1}$
D	Diameter of extrudate, mm
D_0	Diameter of die, mm
D	Strain rate tensor
DCPP	Double-convected pom-pom model
DEVSS	Discrete elastic-viscous split stress
De	Deborah number
tr	Trace of tensor
EEME	Explicitly elliptic momentum equation

EVSS	Elastic-viscous split stress
FDM	Finite difference method
FEM	Finite element method
FVM	Finite volume method
G’	Storage modulus, Pa
G’’	Loss modulus, Pa
GB	Glass bead
GP	Graphite filler
H_E	Height of extrudate, mm
H_D	Height of die, mm
HDPE	High density polyethylene
I_c	First invariants of the Cauchy-Green tensor
$I_{c^{-1}}$	First invariants of the Finger strain tensor
K-BKZ	Kaye-Bernstein-Kearsley-Zapas model
LDPE	Low density polyethylene
LLDPE	Linear low density polyethylene
L/D	Length to diameter ratio
M_m	Mass average molar mass, kg mol^{-1}
M_η	Viscosity average molar mass, kg mol^{-1}
MRP	Micro-encapsulated red phosphorus
MMD	Molar mass distribution
MWCNT	Multi-wall carbon nanotube
N_1	First normal stress difference, Pa
N_2	Second normal stress difference, Pa
Na	Nahme Number: ratio of the viscous dissipation to conduction
PP	Polypropylene

PS	Polystyrene
PSM	Papanatasion-Sxriven-Macosko damping function
PTT	Phan-Thien-Tanner model
PVC	Poly(vinyl chloride)
p	Isotropic pressure, Pa
P_{exit}	Exit pressure, Pa
Rolie-Poly	Rouse linear entangled polymer model
R_g	Universal gas constant
$\boldsymbol{S}$	Orientation tensor
S_r	Stress ratio or recoverable shear modulus
SES	Streamline element scheme
SUPG	Special Streamline-Upwind/Petrov-Galerkin
SU	Streamline-Upwind
T_a	Absolute zero temperature, K
T_r	Room temperature, K
$\boldsymbol{V}$	Velocity vector, mm/s
$\boldsymbol{v_x}$	Axial velocity component, mm/s
$\boldsymbol{v_y}$	Transversal velocity component, mm/s
$\boldsymbol{v_z}$	Lateral velocity component, mm/s
W	Width, mm
Wi	Weissenberg number: shear rate times relaxation time
XPP	Extended pom-pom model
2D	Two dimensional
3D	Three dimensional

Greek symbol

α	Damping function parameter 1
β	Damping function parameter 2
$\dot{\gamma}$	Shear rate, s^{-1}
ΔP_{exit}	Exit pressure drop, Pa
ε	PTT model parameter 1
$\dot{\epsilon}$	Elongational rate (s^{-1})
η	Viscosity, Pa s
η_r	Shear viscosity, Pa s
η_e	Elongational viscosity, Pa s
θ	K-BKZ model parameter
κ	Damping function parameter 3
λ	Relaxation time, s
ξ	PTT model parameter 2
ρ	Density, g/cm^3
∇	Hamilton operator, m^{-1}
$\boldsymbol{\sigma}$	Stress tensor
σ_w	Shear stress at wall, Pa
$\boldsymbol{\tau}$	Extra stress tensor
$\boldsymbol{\tau}_p$	Viscoelastic contribution to extra stress tensor
$\boldsymbol{\tau}_n$	Newtonian contribution to extra stress tensor
$\check{\tau}$	Upper convected derivatives of stress tensor
$\hat{\tau}$	Lower convected derivatives of stress tensor
ω	Angular velocity (rad/s)

Chapter 1

SCOPE AND AIMS

As shown in Figure 1-1, polymer extrudate swell, which is also denoted as die swell or the Barus effect [1,2], is a rheological phenomenon taking place after polymer melt flow emerges the die exit of extrusion equipment. The associated die design is based on the strategy of prohibiting or compensating the swelling behavior downstream the die exit to obtain the final optimized profiles. Here both experimental and modeling tools are relevant.

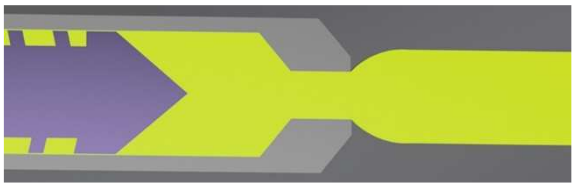


Figure 1-1: Concept of die swell for polymer extrusion.

The key challenge is an understanding of the multidimensional nature of the die swell phenomenon. However, as discussed in Chapter 2 (review submitted to Macromolecular Materials Engineering), most experimental and numerical studies are devoted to a two-dimensional (2D) description. Hence, the current PhD thesis focuses on 3D descriptions, with the gradual degree of complexity highlighted in Table 1-1. Focus is always on so-called rectangular or slit dies.

Table 1-1. Gradual build-up of the PhD thesis to underpin die swell

Chapter	Polymers	Isothermal or Non-isothermal	Rheological Model	Geometric Variables	Flow patterns	Experimental validation
3	Neat PP	Isothermal	Cross law model and PTT model	Slit die with an aspect ratio of 10	Fully developed	This work
4	Neat PP	Isothermal	PTT model	Slit die with aspect ratio ranging from 1 to 20.	Fully developed	This work
5	Neat PP	Isothermal	PTT model	Slit die with an upstream contraction region via varying the slit die length/height ratio.	Developing	This work
6	Neat PP, LDPE, and HDPE	Isothermal and Non-isothermal	PTT model	Slit die with aspect ratio of 10	Fully developed	This work
7	PP/Graphite composites	Isothermal	PTT model	Slit die with aspect ratio of 10	Fully developed	This work and literature data

In Chapter 3, a comprehensive study of the flow behavior of isothermal polypropylene (PP) melt inside and outside a slit die with a fixed aspect ratio of 10 is conducted through a unique combination of multidimensional experimental validation and 3D numerical simulation, considering the viscoelastic constitutive Phan-Thien-Tanner model (PTT) model. The results have been published in the Journal of Non-Newtonian Fluid Mechanics and focus on swelling on the width, middle height and edge height direction. Rheological data are used to tune the PTT parameters.

In Chapter 4, a further investigation is carried on the 3D extrudate swell behavior of polymer melt out of the slit dies with the aspect ratio ranging from 1 to 20. These results have been published in the journal Physics of Fluids. It is highlighted that the

deviation of the 3D extrudate swell from the corresponding ideal 2D modelling decreases with the increasing aspect ratio of the slit dies but does not vanish even though the aspect ratio increases up to 20, stemming from the side wall effect.

In Chapter 5, the obtained insights and research strategy in Chapter 3 and 4 are applied to investigate the impact of the upstream contraction flow on the 3D extrudate swell behavior of still isothermal polypropylene melt. The variable of the die length/height ratio of the downstream flow channel is evaluated thus affecting the distributions of the velocity and stress fields, especially that in vicinity of the converging region. A combined effect stemming from the elongational flow through the converging flow region and the material parameters of polymer melt on the anisotropic extrudate swelling behavior the extrudate is illustrated as well. These results have been provisionally published in Journal of Non-Newtonian Fluid Mechanics.

In Chapter 6, the 3D modelling numerical simulations are utilized to tackle the issues in the field regarding the validity of the exit pressure method, which is used to measure the normal stress difference, a key rheological parameter, at high strain rates. The 3D modeling focuses not only on the evaluation of the predicted anisotropic extrudate swell behavior of various isothermal polymer melts such as High density polyethylene (HDPE), Low density polyethylene (LDPE) and PP by the PTT model with the tuned material parameters based on the measured normal stress difference (N_1) data via the exit pressure method, but also on a comparison between the directly numerically calculated N_1 data and the data calculated by the exit pressure method based on the predicted pressure profiles. Emphasis is also possible non-isothermal effects. These results have been published in Journal of Rheology.

In Chapter 7, focus is on the die swell for composites instead of neat polymers as in the previous chapters. These composites are made based on adding rigid filler particles into the matrix. A modified PTT model is proposed in this preliminary study by establishing functions of the material parameters against the volumetric filler content. It is the goal to publish these results in a later stage in a journal such as AIChE Journal.

Finally, Chapter 8 summarizes the vital findings during the whole doctoral research. Based on these conclusions, recommendations for future research are provided.

REFERENCES

1. Newman, S. and Q.A. Trementozzi, *Barus effect in filled polymer melts.* Journal of Applied Polymer Science, 1965. **9**(9): p. 3071-3089.
2. Robertson, B., *Understanding Extrudate Swell: From Theoretical Rheology to Practical Processing*. 2019, Durham University.

Chapter 2

State-of-the-art for extrudate swell of molten polymers: from fundamental understanding at molecular scale toward optimal die design at final product scale

Polymer extrudate swell, which is also denoted as die swell or the Barus effect, is a rheological phenomenon taking place after polymer melt flow emerges the die exit of extrusion equipment, due to flow redistributions and molecular stress relaxations. The associated die design is based on the strategy of inhibiting or compensating the swelling behavior downstream the die exit. This contribution comprehensively highlights the current knowledge and plethora of experimental and modeling tools to tune extrudate swell of polymer melts. The novelty lies in the combined consideration of the impact and interplay of (i) the processing parameters, (ii) the die geometry, (iii) the macromolecular characteristics (e.g. molar mass distribution and branching level), and (iv) the additive macroscopic properties. Furthermore, the prediction of extrudate swell through various flow geometries by semi-empirical expressions and fundamental viscoelastic constitutive models is compared. Specific focus is on the differential Phan-Thien-Tanner (PTT), the molecular-based double-convected pom-pom model (DCPP), and the integral Kaye-Bernstein-Kearsley-Zapas (K-BKZ) model and their usefulness for 3D swelling descriptions, indicating the optimum model to understand the fundamental relation of molecular parameters and viscoelasticity. The relevance of such detailed analysis is also illustrated by including case studies addressing design at the final product scale.

2.1. Introduction

Polymer extrusion is one of the most important forming operations employed in various industrial applications. In this technique, as shown in Fig. 2-1(a), polymer melts are forced through a (capillarity/slit) die or nozzle to obtain a final polymeric product with a certain three-dimensional (3D) profile [1-6]. In general, the dimensions of the extrudate do not correspond well to the profile of the die or nozzle exit. This phenomenon, which is often denoted as extrudate swell, die swell or the Barus effect, is considered as a flow instability of polymer melts [7, 8]. In practice, swell ratios are considered that vary with distance from the die exit until equilibrium is reached. In most simple cases, one swell ratio is used and defined as the ratio of the height of the extrudate (H_E) to the (fixed) height of the die (H_D), $B = \frac{H_E}{H_D}$, as shown in Fig. 2-1(a). At the molecular level, as depicted in Fig. 1(b), in the die the chains are (more) stretched and once exiting the die recoiling can again take place, explaining the observation of extrudate swell.

The earlier studies on extrudate swell for polymer flows are dated back to the 1960s and focused on general experimental observations and the development of analytical models to grasp these observations [7, 9-11]. For example, Kishi *et al.* [11] experimentally investigated the relation between the swelling and the recoverable shear strain for several polymer melts, highlighting the relevance of the history of shear and thermal treatments. Later in the 1970s, more detailed flow studies have been developed [12-17]. Notably is here the development of the pioneering empirical Tanner expression to predict the swell ratio of polymer melts for a capillary die

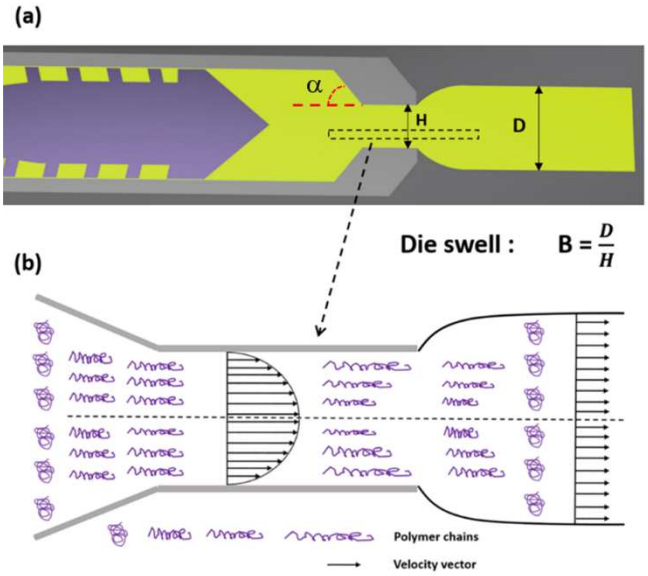


Figure 2-1. (a) Side view of the concept of extrusion processing and the definition of extrudate swell in one direction $B = \frac{H_E}{H_D}$; (b) Velocity profile development and the evolution of the configuration of polymer chains through a die with a converging region before die entry: here for simplicity only extreme cases of coiled and stretched. Focus on slit die as well.

based on regression analysis of experimental results [12, 16]. This expression allows to evaluate the equilibrium extrudate swell ratio assuming an unconstrained elastic recovery and infinite die length:

$$B = \frac{D}{D_0} = B_* + (1 + \frac{{S_r}^2}{2})^{1/6} \quad (2\text{-}1)$$

in which D and D_0 represent the diameter of the extrudate and die exit, B_* is the Newtonian flow limit for the swell ratio, which is equal to 0.13, and S_r is defined as the ratio of the first normal stress difference, N_1, to twice the shear stress at the wall of the die, σ_s.

In any case, one needs to fully acknowledge the typical viscoelastic character of polymer melts, leading to rheological phenomena such as shear-thinning, normal

stress differences depending on shear, strain-hardening and stress memory of historic deformations [18]. For comparison, polymer melts upon emerging the die exit exhibit a significantly larger swelling than typical Newtonian fluids. Despite that many researchers predominantly attribute the extrudate swell of polymers to the recoverable stress and strain applied to the deformed polymer chains, this phenomenon is still not fully understood [19-23]. The earlier studies related to extrudate swell of polymers focused on utilizing the capillary rheometer with a circular or slit die to experimentally study the effect of processing parameters, flow geometry, molecular characteristics, and filler content [24-29]. However, measuring the extrudate swell is a tough task because of its susceptibility to measurement conditions, such as sagging or gravity influences and ambient temperature variations. Therefore, a highly precise measurement method is always an important element regarding the study of the swell behavior of polymer melts [22, 26, 30-34].

It is recommended to also include numerical modeling to investigate the extrudate swell behavior as it possesses the capability to provide insights into the flow behavior inside and outside the die channel, which has been long sought since the 1980s [15, 35-38]. Originally one confronted the difficulty that numerical simulations for extrudate swell were only implemented considering the basic Maxwell constitutive model, due to limitations of numerical solution methods or schemes [35, 39]. In the last decades of the previous century extending the Maxwell-type models for solving extrudate swell problems at high shear rates paved a way of important contributions to the modeling with more realistic constitutive models, such as the nonlinear differential Phan-Thien-Tanner model (PTT model) [15, 33, 40, 41], the molecular-based Double-Convected pom-pom model (DCPP model) [42-45] and the integral Kaye-Bernstein-Kearsley-Zapas model (K-BKZ model) [46-48]. These constitutive

models seem more promising in capturing the extrudate swell at high Weissenberg (Wi) number, thus for a large product of (overall) relaxation time and shear rate, accompanied by a suited die design for industrial applications [49].

On the other hand, as nicely stated by Larson and Desai [18] in their review, a constitutive model that can describe one polymeric liquid might not be adequate for another. An appropriate and dedicated tuning of the constitutive model parameters is required per type polymer considered and thus tuning is non-trivial, keeping in mind

Table 2-1. Overview of experimental and modeling extrudate swell studies for various polymer melts.

Polymer	Measurement Temperature (°C)	Research Type		Reference
		Experiment	Modelling	
HDPE	160-200	Yes		[22, 30]
HDPE	160-200	Yes	Yes	[19, 34, 46, 47, 50-52]
HDPE	180		Yes	[53]
LDPE	150-200	Yes	Yes	[14, 33, 44, 47, 52, 54]
LDPE	150-175		Yes	[54, 55]
LDPE	230	Yes		[56]
LLDPE	180-230	Yes		[57]
LLDPE	160-190	Yes	Yes	[41, 44, 58]
PP	200	Yes	Yes	[45, 59-62]
PP	190-240	Yes		[27, 32, 56, 60, 63]
PS	170-230	Yes		[26, 64, 65]
PS	160-180	Yes	Yes	[8, 66, 67]
PVC	190-230	Yes		[64, 68]
PP/WCNT	190-230	Yes		[69]

PP/Kaolin	180-220	Yes	[60]
PP/MRP	180-205	Yes	[70]
LLDPE/$CaCO_3$	190-230	Yes	[71]
LDPE/GB	150	Yes	[72]

that measurements with respect to normal stress, such as the first and second normal stress difference (N_1 and N_2), and the extensional viscosity (η_e) still encounter great challenges at high strain rates and are mainly conducted for basic commercial polymers. Specific focus has although been on the more general no strain-hardening extensional behavior for linear polymers such as high density polyethylene (HDPE), linear low density polyethylene (LLDPE) and polypropylene (PP) melts [53, 73] with reasonable rheological parameters [45, 58, 59]. In addition, it should be pointed out that currently the numerical calculation divergence for non-Newtonian flow at high Wi numbers still limits the development of numerical modeling [74, 75].

Hence, both experimental and modeling research has been conducted to capture extrudate swell, as also highlighted in Table 2-1, listing important references for both types of research making a distinction between polymer types and ranges of processing temperatures. It follows that most focus has been on standard polymers such as polyolefins, polystyrene (PS) and poly(vinyl chloride) (PVC). To a limited extent one has covered extrudate swell involving less conventional polymers or also blending partners such as calcium carbonate ($CaCO_3$) or glass beads (GBs).

To the best of the authors' knowledge a comprehensive review with respect to the state-of-the-art on the experimental and theoretical understanding of die swell is still lacking. This review therefore aims at the understanding of the complicated extrudate behavior of polymer melts through various flow geometries based on the combination

of experimental and numerical analysis. Numerical efforts for extrudate swell predominantly by means of the development of viscoelastic constitutive models are discussed with their validation based on various measurement methodologies. Specific focus is on the strength of 3D modeling approaches to fully characterize extrudate swell in all relevant directions. We additionally summarize the widely used die design optimization approaches whose crucial objectives are to minimize or compensate the swell behavior after die exit. Open questions on extrudate swell of polymer melts are identified and the corresponding challenging tasks for the numerical modeling of extrudate swell are covered throughout this review.

2.2. Fundamental interpretation at the molecular level

An important fundamental question in the polymer processing field is associated with the origin of the extrudate swelling behavior of viscoelastic melts. Numerous researchers agreed that the mechanism of the extrudate swelling at the die exit is attributed to the reorganization behavior of flow velocity patterns and the inherent elastic retraction or stress relaxation [17, 29, 45, 76-79], which take place to induce the extrudate deformations perpendicularly to the main flow direction. This reorganization is also influenced by the flow history, particularly the impact of the passage at the die entry with a converging region.

At the molecular level, upon die entry, the individual topologies of the polymer chains strongly change with a tending to transform to a state with much less entangled configurations upon flowing through the converging flow region, resulting in (partial) molecular orientation thus stretching, which is also known as straining thinning [8]. The deformation energy builds up and cannot be relaxed immediately so that it is stored in the molecules. In order to re-equilibrate the stored energy, polymer chains

tend to recoil once the flow emerges the die exit in a way that stress relaxation or elastic retraction occurs. This significantly contributes to more robust velocity rearrangements thereby leading to larger extrudate swell deformations as compared to Newtonian liquids or purely viscous flow [45]. Fig. 2-1(b) shows the velocity redistribution behavior for the melt varying from an upstream fully developed flow to a downstream plug flow after the die exit, accompanied by the evolution of the deformed polymer chains relaxing the stress applied on the molecules. In this subfigure, the recoiling of chains in the flow direction causes an expansion in the transversal direction.

This specific complexity of extrudate swell with viscoelastic polymer melts has been illustrated in detail by Yarusso [78], who performed a systematic investigation regarding the variation of velocity profiles of different sorts of flows through a slit die. This author pointed out that elastic fluid with a constant viscosity has a rather similar velocity rearrangement compared to Newtonian flow. In contrast, for viscoelastic flow, the velocity rearrangement occurs more slowly because of the shear-thinning behavior and starts further upstream due to the elastic component. This further indicates the influence of elastic molecular properties on the velocity reorganization behavior thus the extrudate swell. This is specifically consistent with the work of Behzadfar *et al.* [22], who reported that the stress relaxation (elastic recovery) is the main reason for the ultimate extrudate swell of HDPE melt. Based on experimental results these authors found that approximately 76% of the ultimate swelling is caused by the elastic retraction of HDPE molecules.

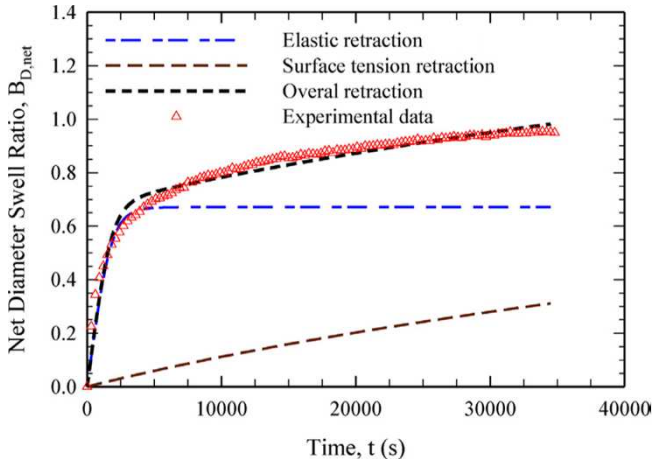


Figure 2-2. Experimental and mathematically analyzed isothermal swell ratio of HDPE at apparent wall shear rate of 64 s^{-1} and 200 ^{o}C through a capillary die with a diameter of 0.79 mm. The extra lines indicate the swell ratio resulting from the elastic, surface tension and overall retraction mechanism, Copyright 2015 [22]. Reproduced with permission from Elsevier Ltd.

In addition, Behzadfar *et al.* [22] also put forward that the surface tension can be another contributor to extrudate swell, with for instance the cylindrical shape of extrudate tending to be deformed into a spherical shape. It is worth mentioning that the relaxation time of surface tension is two or three orders of magnitude higher than that of the elastic retraction, as shown in Fig. 2-2. This indicates that one needs an extremely long time to observe the effect stemming from the surface tension optimization on extrudate swell. This also explains why in most cases the tension force effect is negligible in numerical modeling studies [4, 45].

2.3. Experimental characterization tools

Experimental data of extrudate swell, ideally in several directions, are essential for the general understanding of the relation of viscoelasticity, polymer processing conditions and swelling. Furthermore, with respect to the viscoelastic liquids,

extrudate swell is a benchmark topic for the evaluation of existing and new constitutive mathematic models or numerical schemes from a historical point of view [8, 44, 66, 80], which is discussed in detail later on in this work.

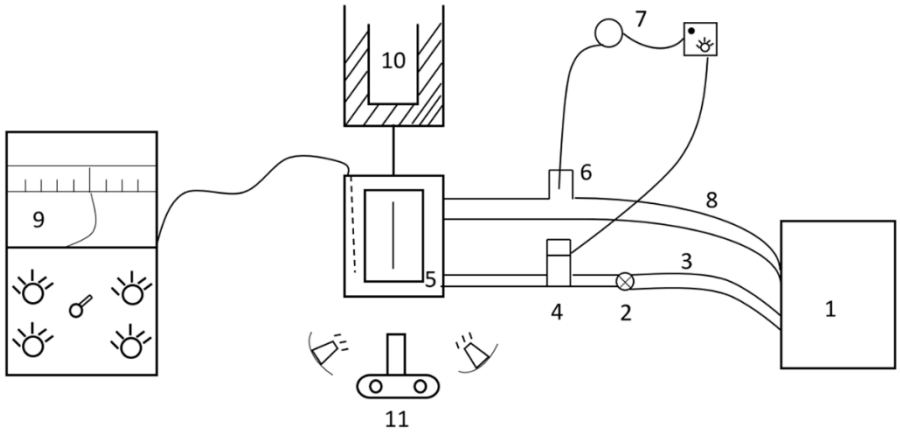


Figure 2-3. Original most promising device as developed by Utrachi *et al.* [68] to measure die swell. Copyright 1975, as reproduced with permission from John Wiley and Sons. Currently more simplified devices are available either focusing on offline or online measurement with key examples covered in Figure 2-4.

A completely accurate measurement of the extrudate swell is still a tough challenge even if following necessary conditions are achieved: (i) steady and isothermal flow; (ii) absence of gravitational sagging and an interfacial tension effect; (iii) a full stress recovery of flow melts [68]. Originally one of the most promising first results was reported by Utrachi *et al.* [68] who designed a complicated device, as shown in Fig. 2-3, to make the polymer extrudate flowing in a liquid with a constant temperature, accompanied by a recording of the changes of the extrudate diameter using a single-

lens reflex camera. At first sights it seems that this operation mode can meet the three requirements mentioned above. However, Yang *et al.* [26] pointed out that the main drawback of the method is the difficulty in finding a suited oil which is not only unable to dissolve the polymer but also has a close density to that of the melt for truly eliminating the sagging effect. In addition, the extrudate diameter measured by photography seemed to be inaccurate to some extent because of the scattering effect, due to the refractive index difference by natural conception.

It can thus be understood why this method in Fig. 2-3 has not been extensively applied by researchers later, although its inception was already in the 1970s. Instead, simpler and more direct measurement methods for extrudate swell are now utilized, which can be classified into two main categories, namely the offline and online measurements as covered in the next two subsections.

2.3.1. Offline measurement

With regard to offline methods, the simplest and conventional way is to quench the extrudate directly in air or a liquid such as water and then cut the solidified extrudate strands for an equilibrium swell measurement, which is named the pinch-off method [26, 81]. This method is thought to underestimate the extrudate swell ratio because it freezes the deformed polymer chains so that it traps the unrelaxed stresses of the extrudate therefore restricting a further swelling.

In contrast, Liang *et al.* [32, 70, 82] measured the swell values of PP composite extrudates after the samples were cooled down naturally in air at room temperature instead of being quenched immediately. With the aim of the stress relaxation at least to a great extent, annealing the extrudate in a liquid bath beyond the glass transition temperature of the polymer was also conducted before the swelling measurements

[27]. As a result, the measured extrudate swell ratios with this method are more reliable in contrast to the method with direct quenching. For example, Anand *et al.* [27] reported that the annealing of PS extruded at a (wall) shear rate of 1500 s^{-1} and a temperature of 200 ^{o}C increases around 6% the final diameter. For PP extrudates, the increase was even up to 30-35% as compared with the results without an annealing processing operation.

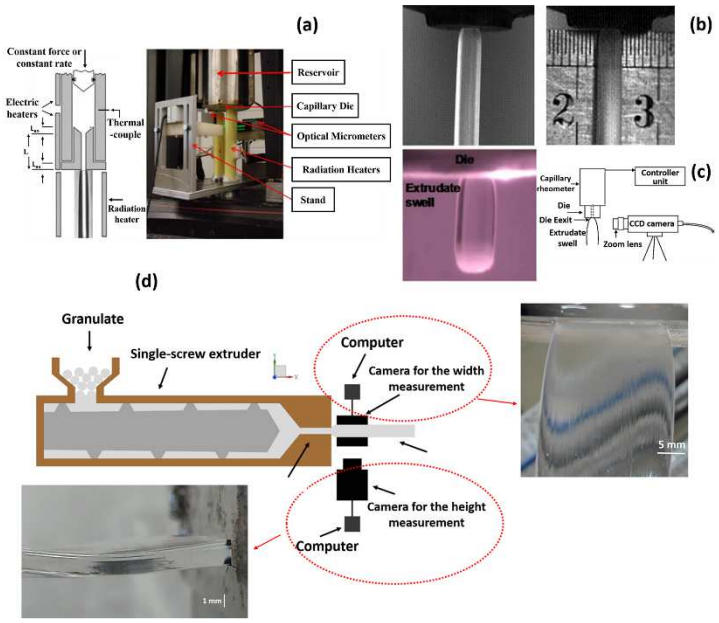


Figure 2-4. Several on-line setups for extrudate swell measurements. (a) HDPE extrudate through capillary die, Copyright 2015 [22]. Reproduced with permission from Elsevier Ltd; (b) LDPE extrudate through circle die, Copyright 2010 [33]. Reproduced with permission from Wiley InterScience; (c) LDPE extrudate through a capillary die, Copyright 2011 [44]. Reproduced with permission from Elsevier Ltd; (d) PP extrudate through a slit die, Copyright 2019 [59]. Reproduced with permission from Elsevier Ltd. In the last case there is a measurement in all relevant directions, including a differentiation according to a difference in the middle and edge height swelling.

2.3.2. Online measurement

Considering the time evolution character of polymer extrudate swell behavior, the offline measurement mentioned above is unable to capture this behavior. Hence, it is not surprising that more recently several online methods for testing extrudate swell have been proposed. Notably Hatzikiriakos and co-workers [22, 34, 51, 83] developed a setup, which is mainly constructed with an optical micrometer using a laser system to record the swelling of polymer melts with a flow direction in the gravity direction. To control the ambient temperature, a pair of radiation heaters on both sides of the extrudate is used to retain the extrudate at a temperature as the same as the extrusion condition or any relevant temperature through adjustments. The details regarding this setup are shown in Fig. 2-4(a). Since all the measurements are performed before a short distance of 20 mm away from the die exit, the gravity effect on the extrudate swell is neglected.

Another widely-used online measurement method employs high-definition camera systems [30, 33, 40, 44, 59-61, 63, 79]. Mu *et al.* [33, 40] reported for instance that for measuring the swelling of LDPE melt, a charge coupled camera (CCD) can be fixed in front of the die lip with a measuring plate placed behind the extrudate, as depicted in Fig. 2-4(b). The advantage of this method is that the extrudate diameter can be directly read from the image with a reference caliper. The difficulty stems from avoiding the contact between the melt and the caliper. Similar work was done by Ganvir *et al.* [44], as described in Fig. 2-4(c), to record the LDPE extrudate swell out of a capillary die.

Very recently Tang *et al.* [59] succeeded to measure the anisotropy swell behavior of PP melt from a slit die by applying two fixed cameras from the bottom and side view, as presented in Fig. 2-4(d). By doing so it was possible to measure the variation in

swelling in both the width and edge height direction with for the latter also through simulation and validation of rheological parameters a differentiation between the edge and middle height swelling. This strategy enables a full 3D picture of swelling data from die exit to actual equilibrium setting. In addition, Intawong *et al.* [65, 84, 85] reported a so-called Parallel Coextrusion Technique (PCT) method to measure the radial extrudate swell and velocity profiles of a polymer flow from a extrusion rheometer. Extruding the colored flow melt into the bulk uncolored melt in the barrel is the crucial principle of this technique. The extrudate swell ratio value is obtained by a comparison of the thickness of the colored melt layers of the extrudate outside the die and that of the layer inside the die.

2.4. Main experimental observations

2.4.1. Effect of processing parameters

Direct processing parameters, such as the temperature and pressure, or lumped processing parameters such as the apparent wall shear rate inducing a certain shear stress, are of great importance to control the final product profile. Generally, as supported by numerous previous reports [22, 26, 32, 63, 82], a higher shear rate results in a larger extrudate swelling ratio due to an increase in the normal stress. For example, Liang *et al.* [32] reported the swelling of PP from a capillary die for various shear rates. Upon increasing the shear rate from 10 to 4×10^2 s^{-1} the swelling values sharply increased from 1.2 to around 1.4. After that a much smaller increase only up to 1.5 was observed as the shear rate increased further to 10^3 s^{-1}.

At one point a critical value for the wall shear stress can be obtained inducing polymer slippage over the die wall solid surface [86-88]. Slippage is expected to lead to a decreasing extrudate swell as the boundary layers under non-slip conditions are

regions of high stress. Notably Hatzikiriakos [86] reviewed the current experimental methods to determine slip. Furthermore, Kraynik *et al.* [89] studied the effect of slippage on the swelling behavior of polyvinyl alcohol solutions through cylindrical tubes with rough and smooth surface to highlight that with the former more slippage is obtained and thus less swelling. Brzoskowski *et al.* [90] on the other hand attempted to deliberately induce slippage through injecting air between the polymer melts and the die wall. A small influence on extrudate swell was although observed.

The deformed polymer molecules require an enough energy to overcome the barriers for the molecular kinematic rotations to relax the energy stored in the polymer chains. Therefore, a higher processing temperature induces a higher stress relaxation rate of polymer chains, resulting in a decrease of the swelling ratio. As a branched polymer melt possesses a higher activation energy for the chain motions than its linear counterpart [91], the temperature effect on extrudate swell is related to the molecular thus material parameters as covered in the next subsection. Indeed, Liang *et al.* [32, 70, 82] found that an increasing processing temperature decreased the extrudate swelling at a given shear stress for polymer melts. Higher apparent shear rates contributed to larger temperature sensitivity on the swelling behavior, highlighting that one should be careful with simply extrapolating results with only one process parameters being varied. Furthermore, Yang *et al.* [26] compared the effect of extrusion processing and die temperature on the extrudate swell of PS melt and reported that the latter has a larger influence. However, a die with a sufficiently large length to diameter ratio seems independent of this temperature effect, implying the achievement of thermal equilibrium for the actual die part of the extrusion equipment.

2.4.2. Effect of die geometry parameters

Polymer melts are forced to enter the die from the (extrusion equipment) reservoir by contraction flow so that complex flow behavior including extensional and shear flow variations is realized. The characteristics or dimensions of the die geometry such as the length to diameter ratio (L/D) [22, 27], the die entrance angle [19, 22], and the ratio between the diameter of reservoir and the die [20, 92], play a significant role in affecting the swelling behavior of viscoelastic flows. Moreover, there can be a difference in the overall geometry with the two important classes being capillary and slit dies.

It should be realized that variations in die geometry induce different distributions of physics variables, such as velocity and stress distributions inside the flow channels. For example, Anand *et al.* [27] reported the extrudate swelling of two types of PP melts through capillary dies with various L/D values. They found that in case the die diameter was set to 5 mm with L/D ratios of 4, 9, 14 and 23 the swelling ratio decreased with the increase of L/D ratio at a given shear rate. This analysis is consistent with many studies also observing this general trend [8, 19, 22, 41, 66]. The most detailed studies have been recently conducted by Tang *et al.* [59, 61], focusing on slit dies with aspect ratios (width to height ratios) ranging from 1 to 20 and PP melts at 200 °C. A variation of the aspect ratio of the die under fully developed flow conditions results in 3D extrudate deformations with absolute variations up to 30% in all Cartesian directions and relative variations up to 10% along a given Cartesian direction [61]. In addition increasing the contraction ratio of the converging flow channels leads to a larger extrudate swell ratio [20, 92]. This has also been confirmed in a recent simulation study of Tang *et al.* [62], who found that the upstream contraction flow region has a significant impact on the extrudate swell behavior of PP

melt from slit dies at 200 °C. The area swell ratio remains however almost unchanged and cannot be used to capture the anisotropic swelling behavior, since there are opposite varying trends of the swell ratios in the extrudate middle height and width direction.

With respect to the inclination angle, increasing this value leads to a larger extrudate swell ratio from a capillary die, which is attributed to a lower and milder elongational deformation, but a larger L/D ratio compromises this growing rate [19]. Hence, the effect stemming from one equipment parameter such as the L/D value of flow channels on extrudate swell can be compromised by varying another geometrical parameter such as the contraction ratio or inclination angle, providing a guidance on the die design to attain a desired extrudate profile.

2.4.3. Effect of polymer material parameters

It is clear that polymer extrudate swell behavior strongly depends on the intrinsic viscoelastic properties of polymer melts, which are determined by molecular parameters such as the overall branching content, average polymer mass and the actual molar mass distribution (MMD). Polymer molecules with a high degree of (long chain) branches or molar mass (also often denoted as molecular weight) possess the ability to entangle strongly with each other, thus resulting in a formation of a physical network and thus a high zero shear rate or Newtonian viscosity [86]. As a rule of thumb under high shear rate more deformations take place at the molecular scale for a branched polymer upon comparison with linear counterparts, as the polymer molecules/segments are typically at larger distance and thus more easily stretched with the applied stress.

It is thus reasonable to expect more elastic recoil behavior for the former (branched) case once the flow emerges the die exit, therefore leading to a larger extrudate swell [41, 44, 56, 64, 93]. Indeed, as reported by Sombatsompop *et al.* [64], highly branched LDPE melt possesses the highest extrudate swell ratios in comparison to other linear polymers such as polystyrene (PS), acrylonitrile-butadiene-styrene polymer (ABS) and poly(vinyl chloride) (PVC), based on capillary rheometer analysis at given apparent wall shear rates.

The most studied polymer parameter has been the molar mass not always with direct overall consistence as one can focus on the average molar mass or the MMD as such with likely differences in shape particularly broadness. For example, in the 1980s, a controversy arised on how the molar mass affects the swelling behavior. Romanini *et al.* [94] found that the extrudate swell ratios decreases with an increase in mass average molecular mass (M_m) of PP melts, highlighting that less elastic recovery after die exit is realized. In contrast, Anand *et al.* [27] reported that PP T30G melt presents larger extrudate swell ratio than PP Q30G, although the latter has a larger viscosity average molar mass (M_η) than the former. They attributed this deviation to a broader MMD for PP T30G with this larger dispersity being more relevant that the lower average molar mass.

More recently Behzadfar *et al.* [22] systemically performed experiments with capillary dies that incorporate an extrudate swell measurement setup with HDPE melts to investigate the effect of the average molar mass and dispersity on the swelling behavior. It is shown in Fig. 2-5a that HDPE-1 and HDPE-6 with very similar relative variation in molar mass (thus similar dispersities) but different average molar mass behave differently. The former has lower average molar mass, showing larger extrudate swell ratio consistent with the discussion above. On the other hand, HDPE-

3 and HDPE-4 present similar swell ratio due to similar dispersities although the former one has a smaller average molar mass putting forward that the dominant molar mass parameter is likely the dispersity. Hence, it is recommended to correlated the swelling within a given family of polymers to dispersity data, as illustrated in Fig. 2-5b [22]. From a fundamental point of view this insight highlights that on a relative basis the shorter chains allow to facilitate stress relaxation of the longer chains inside the die thus decreasing the swelling behavior.

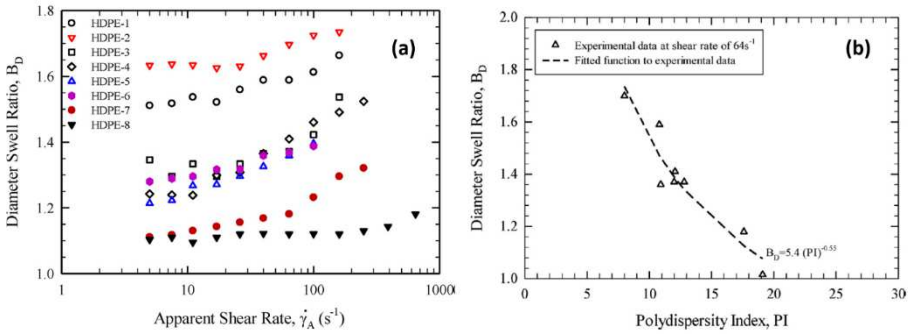


Figure 2-5. (a) Extrudate swell ratio of several HDPE melts as a function of apparent (wall) shear rate through a capillary die with a diameter of 0.79 mm at 200 ºC; (b) The diameter swell ratio as a function of dispersity (also known as polydispersity index, PI) at an apparent (wall) shear rate of 64 s^{-1}, Copyright 2015 [22]. Reproduced with permission from Elsevier Ltd.

It should be mentioned that Robertson *et al.* [8, 66] studied the effect of molar mass on extrudate swell as well selecting three monomodal PS types with various average molar masses and one bimodal PS type with almost the same average molar mass as one of the monomodal counterparts. These authors however found that a higher (average) molar mass contributes to a higher swelling ratio, highlighting that the chemical structure of the polymer could also play a role in the relation of average molar mass and swelling. They although reported a smaller swelling ratio for the

bimodal PS type again confirming the relevance of the shorter chains in compensating die swell phenomena.

Besides molar mass significant focus has also been on the impact of material parameters regarding fillers. For industrial applications, modifications of polymers are essential with often at least the addition of one filler type, which was comprehensively reviewed by Rueda *et al.* [76]. It is currently put forward that fillers can suppress the orientation and stretch deformations of polymer chains in the flow field, and the deformed polymer chains are more restricted to recoil. This explains why it has been observed why swelling is less encouraged upon increasing the filler content [32, 70, 72, 82, 95, 96]. Specifically, Aral *et al.* [96] studied the processing of polydimethylsiloxane (PDMS) filled with up to 60% holly glass spheres and noticed that the swelling of the compounded flow is almost suppressed in the whole range of apparent shear rates, indicating that the swelling problem is less important for an extrusion processing as the filler amount is up to a certain content. As a consequence these increases in filler amount also lower the time needed to reach a stress equilibrium state [97]. Of course, the filler-matrix interaction needs to be sufficiently strong to enable an acceptable degree of dispersion quality [98-100]. It is further recommended to verify the impact on other macroscopic properties [101-104].

It has been additionally indicated that the extrudate swell is influenced by the filler shape as well. It has been for instance reported that a larger swell ratio is obtained for LDPE composites with fillers having a smaller size [72, 95]. Stabik [105] additionally found that larger aspect ratios of fillers lead to smaller extrudate swell, while other factors such as the specific surface and mean diameter contribute less to the swelling of PE and PS melts.

2.5. Modeling tools

Alongside the development of experimental techniques also the theoretical and numerical field has evolved during the last century and initial decades of the current century. Originally focus has been on the development of analytical or semi-empirical formulas to capture the overall swelling trends at equilibrium. More recently numerical algorithms have been developed to map the velocity and stress fields for extrudate swell that can be linked with the appropriate constitutive models to capture viscoelastic properties. Here one can differentiate between molecular or continuum-based differential and/or integral constitutive models, with ultimately the aim of a complete 3D understanding of the relation of viscoelasticity of general melt and extrudate swell. In any case, the validation of material parameters at the level of the constitutive model as the overall model to describe polymer flow in a given geometry is crucial, highlighting the need of the communication between experimental and modeling oriented research.

Table 2-2. Summary of semi-empirical equations for predicting the final thus equilibrated extrudate swell of polymer melts.

Author(s)	**Empirical equation**	**Explanation of parameters**	**Ref.**
Tanner	$B = B_* + (1 + \frac{{S_r}^2}{2})^{1/6}$	B_* is the swell ratio of 0.13 for Newtonian fluid and S_r is the recoverable shear modulus through a capillary die (also Eq. 2-1).	[12]

Minagawa and White	$B = C + (1 + \frac{1}{2}\left(\frac{N_{1W}}{2(\sigma_{12})_w}\right)^2)^{1/6}$	C taken to be 0.1 based on the Newtonian fluid limit and the subscript w indicates evaluation at thewall.	[106]
Menelson, Finger and Bagley	$N_1 = \frac{2\sigma_w}{3}(B^4 + 2B^{-2} - 3)^{1/2}$ $S_R = (B^4 + 2B^{-2} - 3)^{1/2} = \frac{2\sigma_w}{3G}$	σ_w is the shear stress at the wall of the capillary and G is the shear modulus of the polymer melt.	[107]
Tanner	$B = B_* + (1 + \frac{S_r^{\ 2}}{3})^{1/4}$	B_* is the swell ratio of 0.19 for Newtonian fluid through a slit die.	[16]
Liang	$B = (1 + \frac{3\Delta P_{exit}}{\sigma_w})^{1/4}$	ΔP_{exit} is the exit pressure drop through the capillary die and σ_w is shear stress at the wall.	[108]

2.5.1. Semi-empirical formulas to capture overall die swell

Since the 1970s, based on experimental data for extrudate swell from capillary or slit dies, researchers have proposed several semi-empirical mathematical expressions to quantitatively predict the final thus equilibrated extrudate swell [12, 16, 106-109]. The most important expressions have been summarized in Table 2-2. It follows that most empirical expressions focus on the relation between a one-dimensional (height/diameter) extrudate swell ratio and the stress ratio S_r as already introduced in the introduction.

Among the expressions in Table 2-2 the original Tanner equation (entry 1 in Table 2-2; also Equation (1); for slit die: entry 4 in Table 2-2), seems to be most dominantly discussed one [61, 110-112]. Utracki *et al.* reported that there is a good agreement between the predictions of this Tanner equation and the experimental measurements of the extrudate swell for three types of polymers, namely PVC, PS and PE [68], while Meissner *et al.* found a failure of the original Tanner equation for predicting the swell ratio of LDPE melt [25].

Notably Tanner has revised and extended his original equation in 2005 by combining the derivation with constitutive models [16]. Huang *et al.* [112] used this revised Tanner theory combined with three integral constitutive models to predict the extrudate swell ratio of LDPE melt at 160 °C. Fig. 2-6(a) illustrates a clear difference of the S_r values by the three models, but a small deviation of the predicted extrudate swell values is noted in Fig. 2-6(b). A significant underestimation of the experimental measurements in the last subfigure indicates that the Tanner model (even in combinations with these three constitutive models) cannot accurately predict the swell ratio of LDPE, which has strong elastic properties. The failure of the Tanner model can be attributed to two factors. One factor is that a single relaxation time is only allowed for the Tanner equation, which is seemingly not enough to fully describe the stress relaxation behavior as the LDPE flow emerges the die exit. The second factor stems from the ignoring of the die exit effect. Indeed this phenomenon leads to an extensional flow approaching the exit point, thus under-predicting the extrudate swell behavior afterwards if ignored [8, 16, 61, 113].

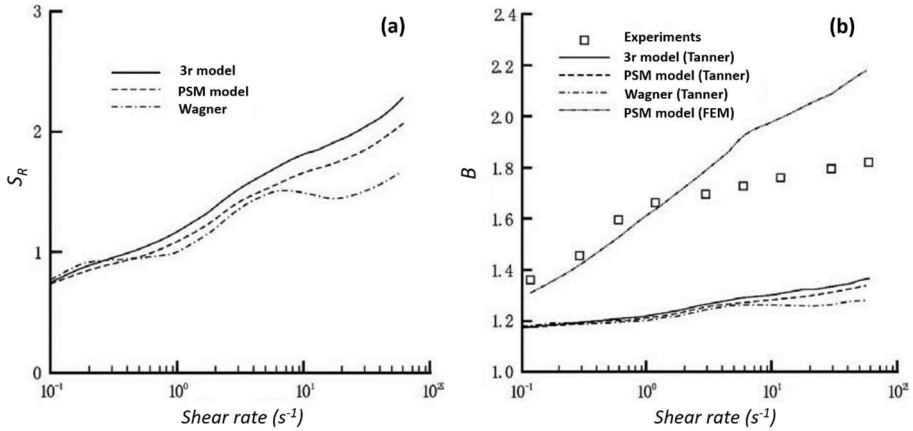


Figure 2-6. (a) The stress ratio S_r of LDPE melt at 160 °C as a function of (apparent wall) shear rate as calculated by the Wagner model [34, 114], the 3r model and the Papanatasion-Sxriven-Macosko (PSM) model [34, 115]; (b) A comparison of the predictions of the extrudate swell ratios of LDPE flow by the Tanner model combined with three constitutive models and the experimental results, together with the simulated results by finite element method (FEM) method with the PSM model (b), Copyright 2010 [112]. Reproduced with a permission from Elsevier Ltd.

2.5.2. Discretization methods and constitutive models for detailed viscoelastic and flow description

The typical character of polymer extrudate swell behavior is its continuous thus spatial and time dependent evolution after emerging the die exit. As explained above, the semi-empirical formulas cannot capture this evolution behavior specifically for more complex melts also bearing in mind that the focus on one or an average swell ratio is only approximate. Numerical modeling is the ideal tool to overcome these limitations and to have an insight on the flow behavior inside and outside the die.

Notably the more early numerical studies concerning creep polymer flow started already in the 1970s [116]. Due to the very limited computational capability at that

point in time these studies were restricted in accounting for larger strains so that it was impossible to implement simulations comparable to most experimental data which are recorded at such larger strains. To tackle this challenge, various numerical solution/discretization methods have been developed in the last decades, including the finite difference method (FDM) [117-119], the finite element method (FEM) [14, 37, 41, 44, 47, 75, 120, 121], and the finite volume method (FVM) [122-125]. Moreover, progresses in numerical algorithms or schemes such as the Streamline-Upwind (SU) or the special Streamline-Upwind/Petrov-Galerkin (SUPG) [14, 40, 51] algorithm, and the explicitly elliptic momentum equation (EEME), the 4×4 subelement method [126], the elastic-viscous split stress (EVSS) method [127, 128], and the discrete elastic-viscous split stress (DEVSS) method [129] contributed to modeling results converged at higher Wi or Deborah (*De*) numbers:

$$\mathrm{Wi} = \lambda\,\dot{\gamma} \qquad (2\text{-}2)$$

$$De = {}^{\lambda}\!/_{t'} \qquad (2\text{-}3)$$

with λ a characteristic (average) relaxation time and $\dot{\gamma}$ is the apparent shear rate for polymer flow and t' is the reciprocal of the wall shear rate in a fully developed flow region.

In any case, the overall core of the numeric modeling is the integrating of the coupled continuity and momentum conservation equations:

$$\frac{\partial \rho}{\partial \mathrm{t}} + \nabla \cdot (\rho \boldsymbol{V}) = 0 \qquad (2\text{-}4)$$

$$\rho \left(\frac{\partial \boldsymbol{V}}{\partial \mathrm{t}} + \mathbf{V} \cdot \nabla \boldsymbol{V} \right) = -\nabla p + \nabla \cdot \boldsymbol{\tau} + \boldsymbol{F} \qquad (2\text{-}5)$$

in which ρ is the density, $\boldsymbol{V}$ is the velocity vector, p is the isotropic pressure, $\boldsymbol{\tau}$ the extra stress tensor, $\boldsymbol{F}$ the external force, and ∇ the Hamiltonian operator. Under non-

isothermal conditions one additionally needs an energy balance [46, 130]. Importantly, the extra-stress tensor $\boldsymbol{\tau}$ is decomposed of a viscoelastic part $\boldsymbol{\tau}_p$ and a purely viscous part $\boldsymbol{\tau}_n$, which is typically written as [45, 131]:

$$\boldsymbol{\tau} = \boldsymbol{\tau}_p + \boldsymbol{\tau}_n \qquad (2\text{-}6)$$

in which τ_p is calculated differently by the basic equations of each type of viscoelastic constitutive model [55] and τ_n is an optional part coming from the Newtonian contribution stress tensor. It should be noted that in Eq. 2-6 τ_n has a positive influence on the mathematical properties of the constitutive equations governing viscoelastic flows. The corresponding viscosity η_n only stemming from the pure Newtonian flow part is presented by considering a ratio r_n of η_n to the total viscosity of η ($\eta = \eta_n + \eta_p$). For example, for the single mode constitutive PTT model, r_n should be larger than 1/9 to improve the modelling convergence when the parameter ε shown in Table 2-3 vanishes [132].

Historically the most crucial input model is the Maxwell model related to the theoretical concept of Maxwell flow [133, 134]. This constitutive model predicts a constant viscosity, a quadratic first normal-stress difference and unbounded elongational viscosity. Chang *et al.* [134] reported the investigation of the extrudate swell problem of simplified 2D flow through a capillary die by numerical simulation based on FEM using the Maxwell model. If the Wi number was 0.2, the simulated extrudate swell ratio of the flow was up to around 1.7, which seemed unreasonable to some extent. After that Caswell *et al.* [35] reported an extended FEM method with the free surface updating scheme using the particle tracking technique to address the extrudate swell problem of Maxwell flow. This method improved the modeling convergent results with a *De* number up to around 0.75. Furthermore, Luo *et al.* [15,

135] proposed a streamline element scheme (SES) to study the swell behavior of Maxwell flow.

Another problem was the difficulty of numerical convergence if the Wi number of the flow increased to 1. It was pointed out that the inherent physical instability of the Maxwell model is responsible for the instability in the calculation of extrusion swell. The original Oldroyd-B model [136] was initially proposed to account for the inclusion of the viscous part $\boldsymbol{\tau}_n$, which was used to reproduce the flow behavior of extrudate swell of viscoelastic melts [36, 113, 125, 137, 138]. It slightly improved the modelling results convergent with higher Wi number but it is still only valid for the behavior in the linear viscoelastic regime [36].

With the aim at advancing in simulating the practical extrudate swell phenomenon of viscoelastic flows the focus should be moved from models, such as the aforementioned Maxwell or Oldroyd-B models to more realistic constitutive models. In the next subsections, focus will be therefore on the practical non-linear viscoelastic models used to simulate the extrudate swell, including the differential, the molecular-based and integral constitutive models.

2.5.2.1 Continuum-based differential constitutive models

In general, multi-mode constitutive models with a relaxation time spectrum are preferable to describe the viscoelastic flow properties compared to single-mode models [139]. The generalized nonlinear practical differential models starting from the Maxwell or Oldroyd-B model is typically written as:

$$\boldsymbol{\tau} = \sum_{i=1}^{N} \boldsymbol{\tau}_{pi} \quad \text{with} \quad F_d(\boldsymbol{\tau}_{pi})\boldsymbol{\tau}_{pi} + \lambda_i\left[\overset{\nabla}{\boldsymbol{\tau}_{pi}} + F_c(\boldsymbol{\tau}_{pi}, \boldsymbol{D})\right] = 2\eta_i \boldsymbol{D} \quad (2\text{-}7)$$

with λ_i, η_i and $\boldsymbol{D}$ the *i*-th relaxation time, the *i*-th viscosity, and the deformation rate.

Table 2-3. Examples of functions $F_d(\tau_{pi})$ and $F_c(\tau_{pi}, D)$ applied in various differential constitutive models; link to Equation (2-7); in many cases the PTT model is used.

Model	$\boldsymbol{F_d(\tau_{pi})}$	$\boldsymbol{F_d(\tau_{pi})}$	Refs
Upper Maxwell ($\boldsymbol{\tau_n}$=0)	1	0	[140, 141]
Oldroyd-B ($\boldsymbol{\tau_n} \neq 0$)	1	0	[113, 136, 142]
White-Metzner ($\lambda(\dot{\gamma})$ and $\boldsymbol{\eta}(\dot{\gamma})$)	1	0	[143]
Exponential PTT	$exp\left[\frac{\varepsilon_i \lambda_i}{\eta_i}\boldsymbol{tr}(\boldsymbol{\tau}_{pi})\right]$	$-\frac{\xi_i}{2}\widetilde{\boldsymbol{\tau}_{pi}} + \frac{\xi_i}{2}\widehat{\boldsymbol{\tau}_{pi}}$	[144, 145]
Linear PTT	$1+\frac{\varepsilon_i \lambda_i}{\eta_i}\boldsymbol{tr}(\boldsymbol{\tau}_{pi})$	$-\frac{\xi_i}{2}\widetilde{\boldsymbol{\tau}_{pi}} + \frac{\xi_i}{2}\widehat{\boldsymbol{\tau}_{pi}}$	[13, 139, 140]
Giesekus Model	$1+\frac{a\lambda_i}{\eta_i}\boldsymbol{\tau}_{pi}$	0	[140, 146]

relaxation time-based function $F_d(\boldsymbol{\tau}_{pi})$ is made of an extra stress tensor $\boldsymbol{\tau}_{pi}$, which actually accelerates the rates at which stress decays at higher stress [140]. The term $F_c(\boldsymbol{\tau}_{pi}, \boldsymbol{D})$ controls the convective time derivative as a function of the extra stress tensor $\boldsymbol{\tau_{pi}}$ and deformation rate $\boldsymbol{D}$. It alters the deformation rate at which the stress tends to build up [140]. If $F_d(\boldsymbol{\tau}_{pi})$ and $F_c(\boldsymbol{\tau}_{pi}, \boldsymbol{D})$ are equal to 1 and 0 separately, Eq. 2-7 is reduced to the Upper Maxwell model. Table 2-3 highlights the most commonly used functions $F_d(\boldsymbol{\tau}_{pi})$ and $F_c(\boldsymbol{\tau}_{pi}, D)$ applied in various differential constitutive models. A literature review shows that the Phann-Thien-Tanner (PTT) model is one of the most extensively used realistic differential viscoelastic models [140, 147]. The two non-linear parameters ε_i and ξ_i for the PTT model mainly control the extensional and shear behavior of polymeric liquids.

The success of the PTT model not only follows from the well-appreciated reflection of the experimental rheological data of benchmark LDPE melts [13] but also from other studies. For instance, Bush *et al.* [36] applied the PTT constitutive model to investigate the extrudate swell using the numerical boundary element method and concluded that the PTT model exhibited a largely promising ability in predicting the significant extrudate swell behavior. Two years later, Luo *et al.* [15] published seminal work on the simulation of extrudate swell of axisymmetric and planar polymer flows by employing the differential PTT model and the FEM numerical method. A rather good agreement was achieved between experiments and simulation results if the Wi number reaches a value of 3.5. This work paved the way for studies of extrudate swell with high Wi with the aid of advanced numerical schemes, such as the DEVSS or EVSS method combining with SUPG or SU schemes, to obtain more accurate and stable computational results as mentioned above. Interesting is here the review of Baaijens focusing on the efforts using differential models such as the PTT model to address the viscoelastic flow problems with the application of the mixed FEM method [75]. Furthermore, Beraudo *et al.* [41] compared the extrudate swell of LLDPE simulated with the multimode PTT model based on a quasi-Newton element method with the corresponding experimental data. It was found that for a contracted long die with a L/D of 19.2, a quantitatively good agreement between simulations and measurements was obtained at an (apparent) wall shear rate of 11 s^{-1}, as shown in Fig. 2-7(a).

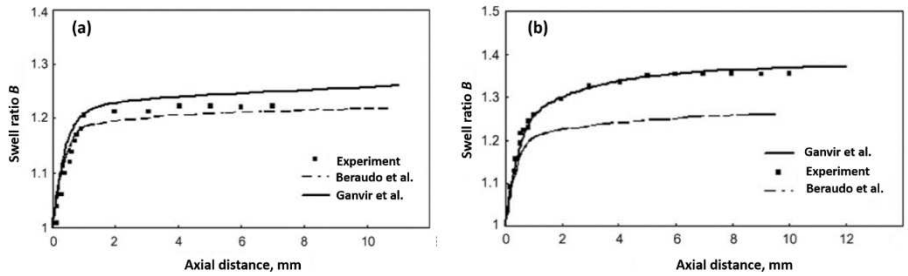


Figure 2-7. Comparison between experiments and simulation for a long capillary die at an (apparent) wall shear rate of (a) 11 s^{-1} and (b) for a short die at 33 s^{-1}. Lines based on the work of Beraudo *et al.* [41] and Ganvir et al. [80]: subfigures as reproduced from Ganvir et al. [80]. Copyright 2009 with permission from Elsevier Ltd.

However, for the case of a short die with a L/D of 4.8, Fig. 2-7(b) shows that the simulation result underestimates the swelling ratio compared to the experimental data at a higher shear rate of 33 s^{-1}. Intrigued by this result, Ganvir *et al.* [80] reproduced the simulated extrudate swell of LLDPE melt later on by adopting the same rheological PTT parameters as Beraudo *et al.* reported based on the FEM but using the Arbitrary Lagrangian Eulerian (ALE) technique they developed. Fig. 2-7(b) reveals a much better agreement with the experimental data for the newly simulated extrudate swell by Ganvir *et al.* These authors put forward that ALE combines advantages of both Lagrangian and Eulerian frameworks, allowing an arbitrary motion of the computational mesh, which was independent of the material motion. They claimed that the challenge of polymer extrudate simulation was the difficulty in accurately predicting the free surfaces, which generally requires special techniques in the widely used Eulerian framework. This indicates that the failure in predicting the extrudate swell of LLDPE melt through a short die in the study of Beraudo *et al.* [41] is not because the PTT model might not be able to account for the memory effect

through a short die with an abrupt contraction flow region at high shear rate, as claimed by some studies [34, 148].

More recently, Konaganti *et al.* [34] reported that the simulated PTT-based swelling ratio of HDPE flow through a capillary die with a L/D of 16 underpredicted the experimental measurements in an apparent wall shear rate range of 5-160 s^{-1}. The deviation seemed although to decrease with a growing shear rate. It should be noted that the PTT parameter ξ_i was fixed at 0 for these simulations, implying the ignoring of the effect of the second normal stress difference (N_2). In fact, how N_2 affects the swelling of polymer melts is still a relatively open question [34, 149]. It should be put forward that a differential constitutive Giesekus model, as also included in Table 3, performed better in predicting the extrudate swell ratio of HDPE melt under the same processing conditions. This observation can be understood by the less extensional thinning behavior of the Giesekus melt at high strain rates [150]. The swell behavior is affected as well by the elongational property because there is an extensional force applied on the flow melt upon the flow approaching the die exit. However, the authors did not exhibit the extensional viscosity functions of both PTT and Giesekus described melts.

Very recently dedicated parameter tuning of the PTT model was therefore performed considering die swell for PP, HDPE and LPDE melt at 200 °C and considering full 3D simulations [52, 61]. A sensitivity analysis highlighted that indeed the appropriate tuning of the PTT model allows to capture many experimentally die swell variations. Moreover, this sensitivity can be translated in several swelling directions as illustrated in Fig. 2-8 focusing on a comparison of the final swelling data of a full 3D model (black full lines) compared to a simplified 2D model (blue dashed dotted lines) for slit

dies with different aspect ratios (red lines; rectangle). Importantly both validation of the PTT model parameters based on rheological testing and of the overall Polyflow solver ultimately allowed to access the middle height, edge height and width swelling trends.

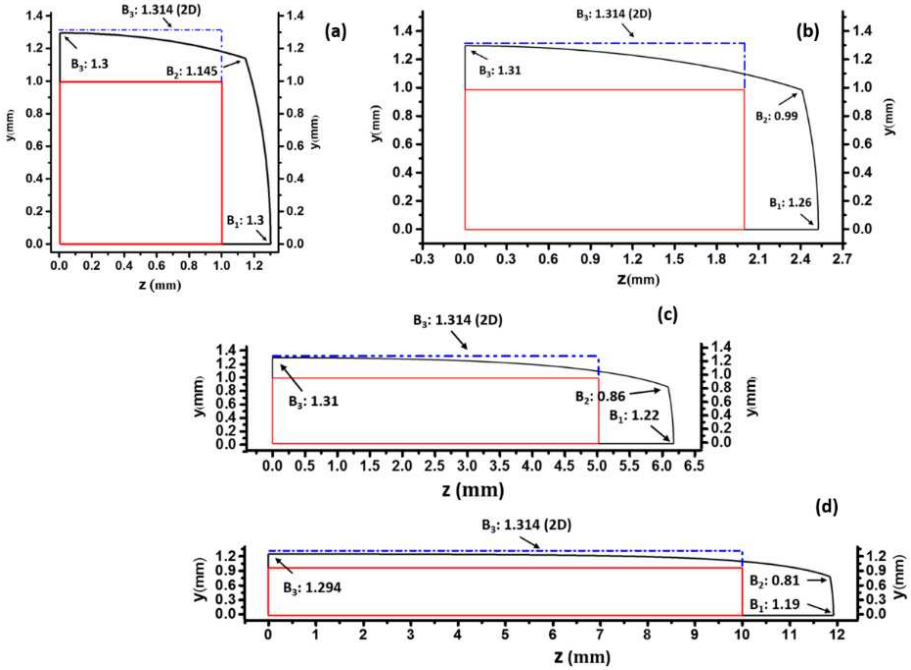


Figure 2-8. Comparison of simulated final die swell simulations (PP melt at 200 °C) between a full 3D model combined with the PTT model (black full lines) and the simplified 2D model (dashed dotted lines) for slit dies with different aspect ratios (red rectangles); one fourth is shown, Copyright 2019 [61]. Reproduced from with permission from AIP.

2.5.2.2. Molecular-based constitutive models

The conventional differential constitutive models, such as the PTT model discussed above, have been derived from the network theory for concentrated polymer solutions and melts [13, 151], as conceptually highlighted Fig. 2-9(a). For the details of their

derivation the reader is referred to the general description of the previous subsection and the specialized literature [13].

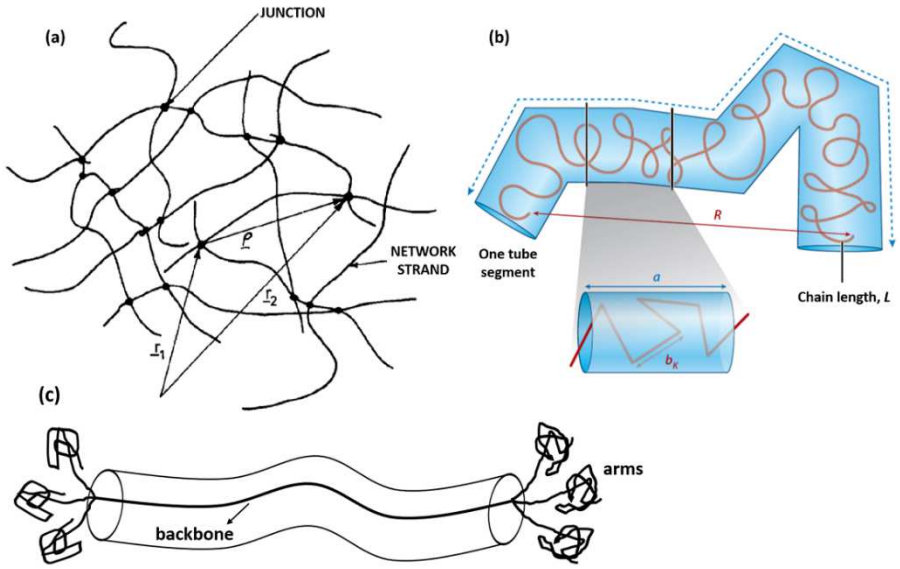


Figure 2-9. (a) Typical network theory of polymer solutions or melts, Copyright 1977 [13]. Reproduced with permission from Elsevier Ltd; (b) Length scales for long polymers with entanglements, constraining a given polymer to tube-like region according to the molecular-based tube theory, Copyright 2015 [18]. Reproduced with permission from Annual Reviews; (c) the tube-based pom-pom molecule model.

To more accurately capture the viscoelastic properties of more complex polymers at the molecular level such as long chain branched polymers, some more new constitutive models that can reproduce more elegantly detailed molecular characteristics have been proposed [42]. In 1998, Larson and Mcleish initially developed a so-called pom-pom model based on the tube theory, as shown in Fig. 2-9(b) starting from the concept that long linear polymer chains are entangled with other chains restricted in a confining tube-like region. For this pom-pom model, as shown in Fig. 2-9(c), so-called arms are connected at the extremities of the tube of the

polymer chains represented by the backbone segment. This mathematically induces a more complicated relaxation process than representative for the movement of linear polymers with a separate relaxation behavior of the orientated backbone and the stretched branches [42]. The ratio of the former relaxation time to the latter one depends on the (average) entanglement degree at the molecular scale. The physical limit is here that both types of relaxation times become identical for a polymer with completely unentangled segments.

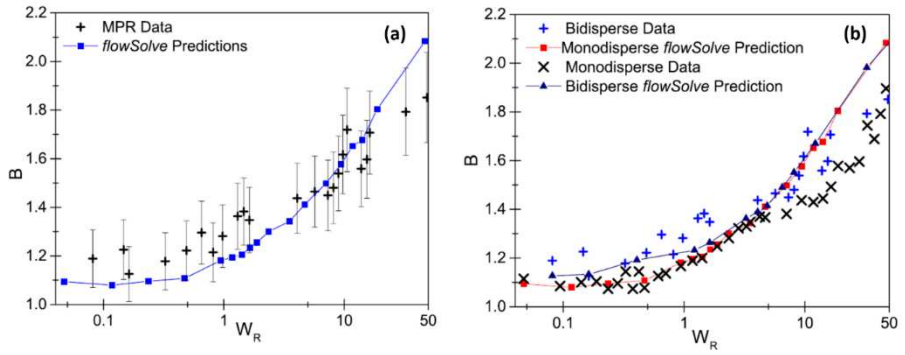


Figure 2-10. (a) Comparison of the predicted extrudate swell from a capillary die for a monodisperse polymer with a mass average molar mass (M_m) of 340 kg mol^{-1} with the experimental measurements for a polymer with a bimodal molar mass distribution (MMD; P627-S) as a function of the W_i (here W_R) number: this bimodal P627-S contains two peaks: one of a high M_m of 340 kg mol^{-1} and another with a low M_m of 160 kg mol^{-1}. The disagreement exhibits the sensitivity of the extrudate swell to the MMD shape; (b) Comparison of the experimental swelling for monodisperse PS281 and bidisperse P627-S melts (similar M_m of 281 and 252 kg mol^{-1}) alongside the *flowSolve* predictions, Copyright 2017 [66]. Reproduced with permission from the Society of Rheology.

The original pom-pom model showed its merit for the application of calculating the non-Newtonian stress in a numerical flow solver, although there were several mathematic drawbacks that needed to be overcome. Therefore, Verbeeten *et al.* [152]

extended the pom-pom model, referred as the XPP model with the ability to predict a non-vanishing N_2. Following the suggestions of these authors, Clemeur *et al.* [43, 153] improved the original model by involving both upper- and lower-convected derivative operators to calculate the orientation tensor $\boldsymbol{S}$, referred as DCPP (Double Convected pom-pom) model. These authors combined the DCPP constitutive model in the commercial Polyflow software with the aim at evaluating the extrudate swell of contracted LDPE flow and revealed that the material parameters strongly influence the swell behavior [43]. Since then, several reports with regard to the use of pom-pom based models to simulate the extrudate swell of viscoelastic melts have been developed [34, 44, 54, 55]. For instance, Ganvir *et al.* [44] incorporated the XPP model into their ALE code to simulate the extrudate swell of LDPE melt through a capillary die, which is in a quantitative agreement with the experimental measurements.

In addition, Graham *et al.* [154, 155] further developed the Doi and Edwards tube model [156] by incorporating constraint release and contour length fluctuations to extend its application in covering the deformation rate range of linear chains for realistic flows. These efforts have resulted in the Rolie-poly (Rouse linear entangled polymer) model. Compared to the pom-pom molecular constitutive model, the Rolie-poly model is a more simple model which is more suited for the description of the entangled linear polymers for instance PS melts, involving the motion terms of chain orientation, chain stretch and convective constraint release [66]. For example, Cao *et al.* [157] employed the Rolie-Poly mode to analyze the extrudate swell of general (theoretical) viscoelastic flows using the interface tracking method with the software OpenFOAM based on the FVM method. They showed that the reptation relaxation time mainly determined the final extrudate swell ratio.

Furthermore, Robertson *et al.* [8, 66, 158] systemically investigated the extrudate swell of PS melts applying the Rolie-poly model with the in-house FEM-based tool *flowSolve*. It is seen in Fig. 10(a) that the predicted swelling assuming a monodisperse polymer with M_m of 340 kg mol^{-1} only agrees with the experimental data for the bimodal polymer P672-S, which contains a peak with high M_m of 340 kg mol^{-1} and another with low M_m of 160 kg mol^{-1}, at higher Wi numbers. Hence, it is worthwhile to improve the Rolie-poly model to capture the impact of dispersity on the viscoelastic properties. This explains why the authors incorporated an additional longer effective stretching time to account for the extrudate swell at low deformation rate range. In this respect, Fig. 2-10(b) compares the experimental swelling of monodisperse PS281 and bimodal PS672-S (similar M_m of 281 and 252 kg mol^{-1}) with the corresponding predictions of swelling by the conventional single stretching-mode Rolie-Poly model and the improved double-mode Rolie-Poly model. A better agreement at low Wi number for the bidisperse PS is observed compared to that in Fig. 2-10(a), which indicates the necessity of additional stretching or non-streching modes for more accurately representing the melts with a broader MMD. These authors also revealed that the polymer stretch relaxation governed by the Rouse motion time played a main role in controlling the extrudate swell [158], which appears to be inconsistent with the report by Cao *et al.* [157]. As stated by Roberson [8] interesting future work would therefore be to include the evaluation of how versatile the Rolie-Poly model is to capture swelling variations for an increasing dispersity value.

Overall it can be concluded that molecular based constitutive models are very useful as they provide a good opportunity to relate the processing phenomenon with detailed molecular characteristics of more complex polymers.

2.5.2.3. Continuum-based integral constitutive models

As in many theoretical derivations in several fields one can opt to describe a certain phenomenon in a differential or integral manner [159, 160]. In the present section we put forward the most important continuum-based integral constitutive models. To predict the viscoelastic deformation behavior at the non-linear strain region, the single integral K-BKZ constitutive model, as firstly proposed 50 years ago [161-163], is often used. The original K-BKZ model was improved by an incorporation of a damping function by Wagner *et al.* [114, 164] and Papanastasiou *et al.* [115]. Compared to the differential constitutive models discussed above, the K-BKZ model explicitly solves the extra stress tensor as a function of time and strain. Its general constitutive equation to compute the viscoelastic stress tensor $\boldsymbol{\tau}_{pi}$ is written as:

$$\boldsymbol{\tau} = \sum_{i=1}^{N} \boldsymbol{\tau}_{pi},\ \boldsymbol{\tau}_{pi} = \frac{1}{1-\theta}\int_{-\infty}^{t} \sum_{n=1}^{N} \frac{g_i}{\lambda_i} e^{(-(t-t')/\lambda_i}\, H(I_{c^{-1}}, I_c) \times [C_t^{-1}(t') + \theta C_t(t')]dt' \qquad (2\text{-}8)$$

in which I_c and $I_{c^{-1}}$ represent the first invariants of the Cauchy-Green tensor, $\boldsymbol{C}_t$, and the Finger strain tensor, $\boldsymbol{C}_t^{-1}$. The material parameter θ controls the second normal stress difference and $H(I_{c^{-1}}, I_c)$ is a damping function on the basis of a strain-dependent memory. For example, the Wagner damping function is written as [114]:

$$H(I_{c^{-1}}, I_c) = \exp(-k(\beta I_{c^{-1}} + (1-\beta I_c) - 3)^{0.5}) \qquad (2\text{-}9)$$

in which k and β are damping parameters, mainly determined from simple shear and extensional flow respectively. Alternatively, the Papanastasiou-Scriven-Macosko (PSM) damping function is written as [115]:

$$H(I_{c^{-1}}, I_c) = \frac{\alpha}{(\alpha-3)+\beta I_{c^{-1}}+(1-\beta)I_c} \qquad (2\text{-}10)$$

in which α and β are material characteristics as determined by fitting the simple shear and extensional flow data respectively.

It should be noted that for the K-BKZ multimode equations, the material characteristics of the damping functions determine the shear and elongational behavior of the simulated flow melt separately in the whole relaxation time spectrum, while for differential PTT multimode equations (see previous subsection), the material characteristics ε_i and ξ_i only control the shear and extensional behavior in the *i*th mode, respectively. This difference in implementation can explain the lower computational cost for K-BKZ equations because of the fewer material characteristics [165].

As for the integral constitutive models one needs to select the correct discretization and flow model. For example, in 1986, Luo *et al.* [135] numerically covered the issue of extrudate swell of complex (e.g. LDPE) viscoelastic melts, using a practical integral K-BKZ constitutive model combined with a PSM damping function considering an SES method. A good agreement between the simulation results and experimental data of swelling was observed in the low and medium Wi number range. The reason for the failure in predicting the swell ratio at the high strain (Wi > 10) was attributed to the over-prediction of the elongation viscosity. After cutting off the elongational viscosity but affecting only to a limited extent the shear viscosity, the simulated swelling corresponded much better to the experimental data. Besides that, they pointed out the stability of the numerical calculations using the SES method at very high Wi numbers, presenting therefore promising prospects in employing the integral constitutive models such as the K-BKZ model for calculating the swell of viscoelastic flows in more complex geometries.

Another example is the work of Goublomme *et al.* [38] who demonstrated the simulated swelling of HDPE flow by means of the K-BKZ model through a long capillary die, while including the converging upstream conical part or not doing so. An acceptable predicted swelling ratio compared to the experimental data in the former case with the conical converging region was obtained at an apparent wall shear rate of 225 and 441 s^{-1}. However, for the latter case, the calculated swelling showed a sharp over-prediction. Goublomme *et al.* [38] found the final swelling ratio strongly dependent on the type of damping function. A significant reduction of the swelling was observed from *B* equal 9.2 to 5.4 with the irreversible PSM damping function instead of its reversible counterpart. In contrast, a satisfactory swelling (B = 2.4) was obtained with the irreversible Wagner damping function, which is in line with the report by Ahmed *et al.* [47] that the reversible damping function leads to a higher extrudate swell ratio than the irreversible one.

It should be mentioned that the lacking experimental elongational viscosity data in a practical deformation range can complicate the determination of the material damping parameters, e.g. k and β. A further study by Goublomme *et al.* [149] pointed additionally out that temperature has little effect on the swelling ratio of HDPE melt but an accurate measurement of N_2 data is required for any realistic modelling of extrudate swell, since a significant decrease in swelling ratio is observed with the increase of the ratio of $|N_2|/|N_1|$. Similar results can be found in other works [48, 61, 166]. It thus appears that the over-predicting of the swelling with the K-BKZ model [41], especially through a flow region with a contraction part, might be attributed to the improper use damping functions.

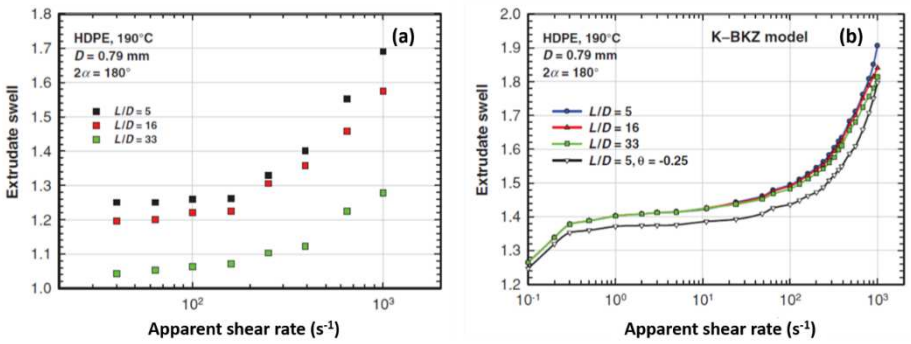


Figure 2-11. The extrudate swell of the HDPE melt at 190 °C as a function of the apparent shear rate for three L/D values by experiments (a) and by simulations with the K-BKZ model (b). In Fig. 11(a), the blue, red and green curves represent the modeling outcomes with the material parameter $\theta = 0$ and the black curve indicates the case with $\theta = -0.25$, Copyright 2012 [46]. Reproduced with permission from Wiley Periodicals.

Recently, Hatzikiriakos, Mitsoulis and coworkers extensively studied the numerical modelling of extrudate swell of HDPE melt within the K-BKZ model [22, 34, 46, 51, 148]. In what follows major results of these studies are summarized. In a first instance, Ansari *et al.* [46] predicted the extrudate swell of HDPE using the K-BKZ model with the PSM damping function. A significant overestimation for swelling from simulation in comparison with experimental data was presented, especially at the low apparent shear rate range, although these authors introduced a slippage condition into the simulation. For example, it is interesting to find in Fig. 2-11(a) that there exists a significant discrepancy between the measured extrudate swell ratios for the flows through capillary dies with various L/D. In contrast, a rather small difference among the three modelling cases is noted in Fig. 2-11(b). These authors attributed this to the non-isothermal condition, crystallization and sagging effects.

In a second instance, Konaganti *et al.* [34] compared the extrudate swell of HDPE flow through a capillary die including the reservoir region, using the K-BKZ model

with two types of damping functions. At a given apparent shear rate, the Wagner damping function resulted in a higher swell ratio than the PSM damping function but they both over-predicted the experimentally measured swell ratios of the flow melts through a contraction channel. However, in case the reservoir part was excluded from the geometry model, the difference between the simulation swell ratios for the two damping functions became much smaller, and both simulation results became comparable to the experimental data. To further exploit the reason for the failure in predicting the extrudate swell behavior through the flow region with a reservoir, Konaganti *et al.* [148] focused on the Wagner damping function and optimized the material parameters of the KBKZ model, k and β, by fitting the measured damping function h against the strain γ. Fig. 2-12 shows that a good agreement between the extrudate swell of the measurement and the simulations for a capillary flow with the reservoir part was obtained using this K-BKZ model with optimized material parameters. This again highlights the relevance of the damping function and the tuning of its parameters in improving the accuracy of the numerical simulation for the prediction of extrudate swell.

In summary, many more detailed descriptions already exist. However, the accuracy of numerical modeling is still hampered by the question which nonlinear constitutive model performs best in describing the rheological properties including both shearing and extensional viscosity of polymer melts [18]. Currently, no constitutive model works perfectly for all polymer melts, such as linear polymers and more complicated long branched polymers.

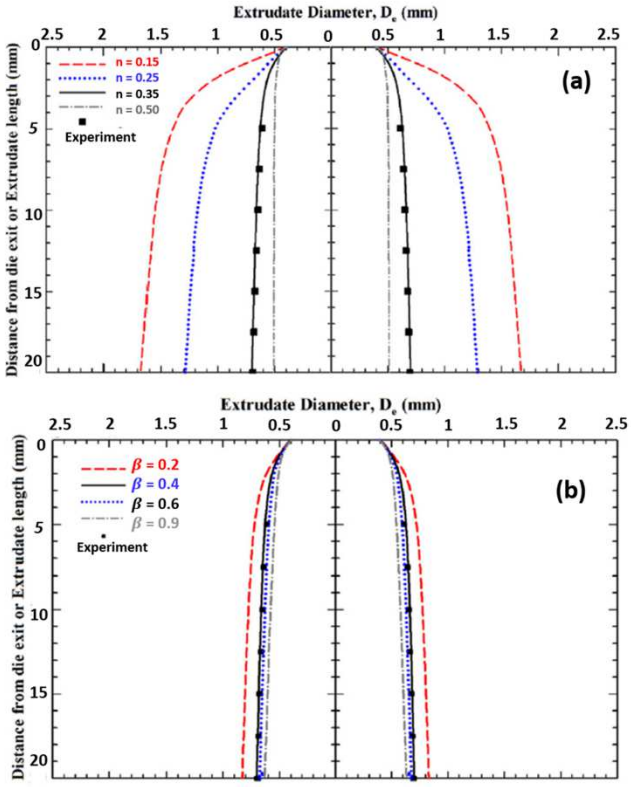


Figure 2-12. (a) Comparison of experimental and simulated swell profiles for the capillary die having L/D = 16 with D = 0.79 mm, an apparent shear rate of 26 s^{-1}, the Wagner exponent *n* ranging from 0.15 to 0.5, and using the optimum value of the Wagner parameter β= 0.4. Solid symbols represent the experimental data; (b) a comparison of simulations results with the Wagner parameter β ranging from 0.2 to 0.9 and using the optimum value of Wagner exponent *n*=0.35, Copyright 2016 [148]. Reproduced with permission from Elsevier Ltd.

2.5.2.4. Strength of 3D flow simulations

At the early stage of addressing the extrudate swell issue, 3D modeling was unachievable due to the limits in computational techniques such as the lack of numerical algorithms or schemes to solve the complete extrudate swell problem.

Significant progress has been made in 3D computational fluid dynamics (CFD) modeling with advances in numerical techniques in the last two decades, although the breakdown of the simulation still occurs as the Wi number reaches a critical value, named as the high Wi problem [110]. From a computational viewpoint it has been demonstrated that the memory-integral constitutive K-BKZ model cannot be elegantly combined with the 3D FEM platform [47] so that in practice one is restricted to the use of the commercial Polyflow package.

It is therefore not surprising that with respect to the flow behavior the realistic full 3D flow behavior has been often simplified into the 2D counterpart for a reduced computational cost. The general complex irregular geometries of flow channels set although the corresponding numerical modeling apart from the simplified 2D configurations [45, 167]. The modeling cases of the extrudate swell through specifically slit dies mentioned above have been mostly implemented based on the 2D configuration while the experimental geometry possesses a third dimension, which can be at least one reason for the discrepancy between experiment and simulation [47].

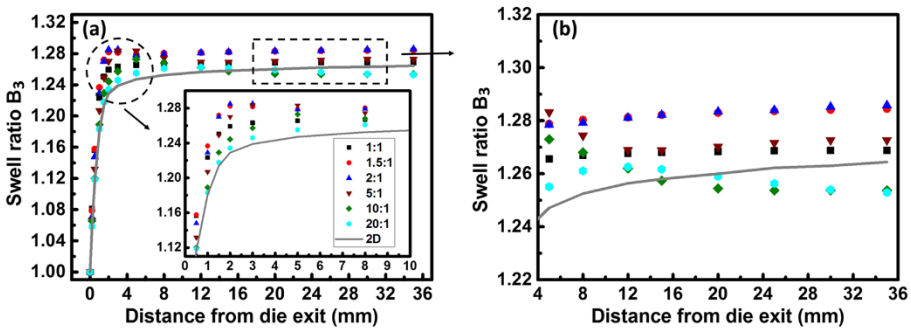


Figure 2-13. (a) Evolution of the predicted middle height swell ratio B_3 of PP extrudate out of a slide die with several aspect ratio at 200 °C at an apparent shear rate of 15 s^{-1}; also shown in the simplified 2D model outcome, Copyright 2019 [61]. Reproduced with permission from AIP; (b) Zoom of (a) in the region away from the die exit. The 3D data are consistent with

experimental data as either validated on the rheological level and/or the explicit measurement of the die swell in several directions.

For fully developed flow, Fig. 2-13 presents the simulated extrudate swell behavior for the middle height for slit dies with an aspect ratio ranging from 1 to 20 according to 3D simulations, as taken from the work of Tang *et al*. considering the PTT constitutive model [61]. In this figure, the simplified 2D simulation results are also included. An evolutionary scheme was conducted for the flow rate to advance the numerical solution from Newtonian to the nonlinear viscoelastic flow, which was applied as well on the term of the relaxation time or non-Newtonian factor generally to converge results at higher Wi numbers. A clear discrepancy between the 3D and 2D modeling results can be observed due to the 3D effect or edge wall effect on the extrudate swell behavior [61]. It follows that the width of the slit die should not be ignored for providing a more accurate prediction of the swelling, even if the aspect ratio increases up to 20. In addition, the impact of the irregular upstream contraction on the 3D dimensional polymer extrudate swell has been further investigated in follow-up work [62]. It has been demonstrated that increasing the die length induces a smaller height swell ratio but a larger width swell ratio, contributing to a larger anisotropy degree of swelling. The swelling area is however not affected so much, which highlights that one cannot use this macroscopic characteristic to quantify the anisotropy of swelling.

This need for a 3D approach was also highlighted by Spanjaards *et al.* [168] who proposed a transient 3D FEM to predict the extrudate swell from flow domains having sharp edges, considering the differential PTT and Giesekus consitutive model with general material parameters. Fig. 2-14 presents that for a square die higher Wi numbers result in an increasing swell of the extrudate middle and edge height. As the

Wi number increases to a critical value, the sharp edges seem to disappear gradually in the extrudate. Notably this extra information is lacking in the corresponding 2D modelling but meaningful for industrial applications.

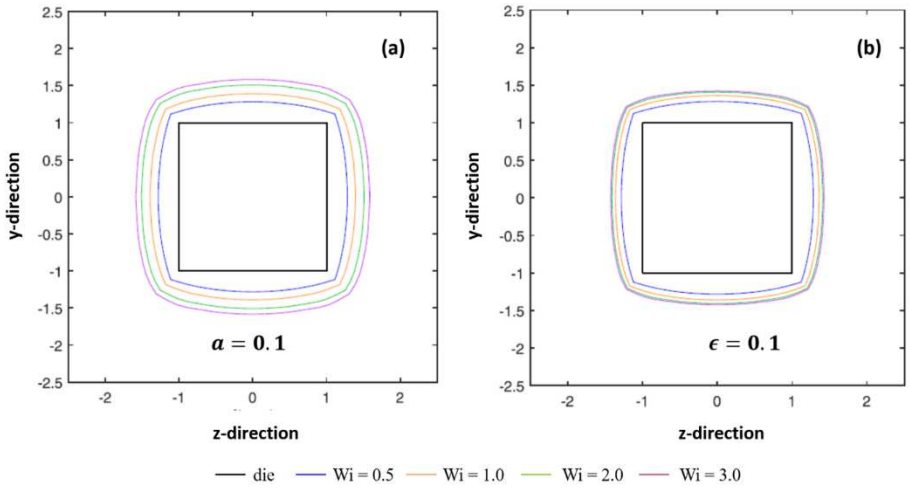


Figure 2-14. (a) Extrudate swell from a square die with increasing Wi number and material parameter α = 0.1 for the Giesekus model; (b) material parameter ε = 0.1 for PTT model, Copyright 2019 [168]. Reproduced with permission from Elsevier Ltd.

Furthermore, Mu *et al.* [33, 40] pointed out that the DEVSS algorithm incorporating the inconsistent Streamline-upwind scheme improves the calculation stability of 3D simulation on extrudate swell of LDPE flows in combination with the PTT constitutive model based on the penalty finite element method. The effect of geometrical characteristics on the extrudate swell of LDPE melts through an annular die was revealed by evaluating the amount of extrudate area swell, which can now be seen as insufficient to illustrate the 3D swell characteristic [33]. It was concluded that a smaller die contraction angle, a longer parallel length and intermedium ratio of the outer to the inner diameter are in favor of an optimal flow channel design. A preliminary study on the viscoelastic flow and swell phenomenon from a hollow

profile extrusion die was implemented, which appeared more complicated than the annular flow channel [40]. It was found that the distortion of the profile extrudate is not very significant and the introduction of the pre-parallel zone can be feasible regarding the die design strategy.

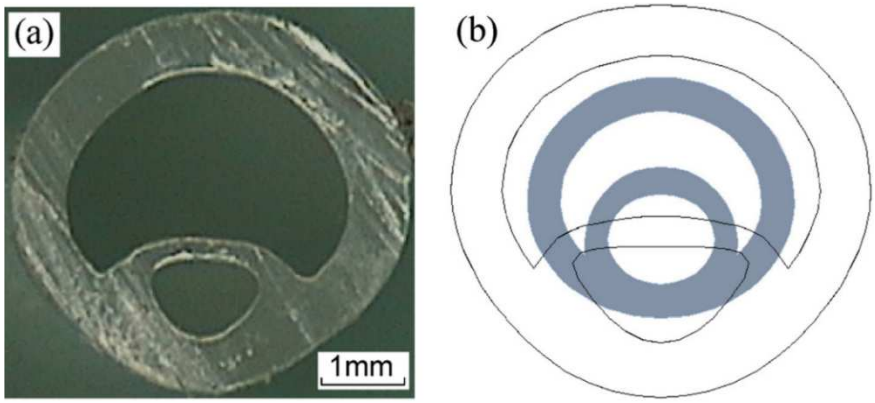


Figure 2-15. (a) Cross section of the extrudate. (b) simulated final extrudate contour in black line compared with the die exit in gray color, Copyright 2015 [45]. Reproduced with permission from Elsevier Ltd.

A final example is the work of Tian *et al.* [45] who employed the molecular-based DCPP model to study the extrudate swell of viscoelastic melts from a hollow profile possessing multiple lumens and uneven thickness by 3D modeling configurations. They pointed out the importance of the micro size effect on the viscosity of fluids thus on the anisotropic swelling behavior, so that they incorporated a size factor to the calculation of the Newtonian-contribution viscosity. A satisfactory agreement between the simulated extrudate size and the experimental data has been attained, as shown in Fig. 2-15. Several extrudate swell ratios have been defined to exhibit the anisotropic extrudate swell characteristics. Besides that, they investigated the sensitivity of the material parameters on the anisotropic extrudate swell and pointed

out the necessity to establish the die design theory for micro profile dies based on numerical modeling.

2.6. Reverse engineering: model-based die design for a controlled swelling for complex geometries

With the aim of obtaining extrudate product with a desired 3D profile, it is of great importance to determine the corresponding die design *a priori*, which is denoted as an inverse extrusion problem or reverse engineering [168]. For industrial applications, die design is strongly dependent on the knowledge of the experienced designers. A trial and error approach is applied for most present design procedures and the typical sequence involves the following steps: (i) initial design, (ii) manufacturing and (ii) experimental balancing [169]. It thus involves a usage of large amounts of time and resource costs, especially regarding the optimization of complex geometry profiles. Shortening this development process is a regular target for companies to enable substantial economic benefits and to support innovation from both an academic and industrial research angle. To tackle this problem more efficiently numerical modelling has been extensively investigated in recent years with commercial or publicly available softwares such as Ansys Polyflow, OpenFOAM and Dieflow [49, 110, 169-176]. Currently the status can be mainly summarized according to two methodologies: (i) achieving exit flow uniformity or balancing at the die exit by the modification of the upstream flow channel or design variables, such as the cross section of the flow channel, parallel zone or die land [171, 175, 177], as shown in Fig. 2-16(a) and (b) [169]; (ii) using the desired extrudate shape as a constraint for the integration of the kinematic equations for the free surface flow by modifying the die lips. For example,

a solution algorithm is implemented in the Polyflow program for a reverse extrusion problem [49, 178-180].

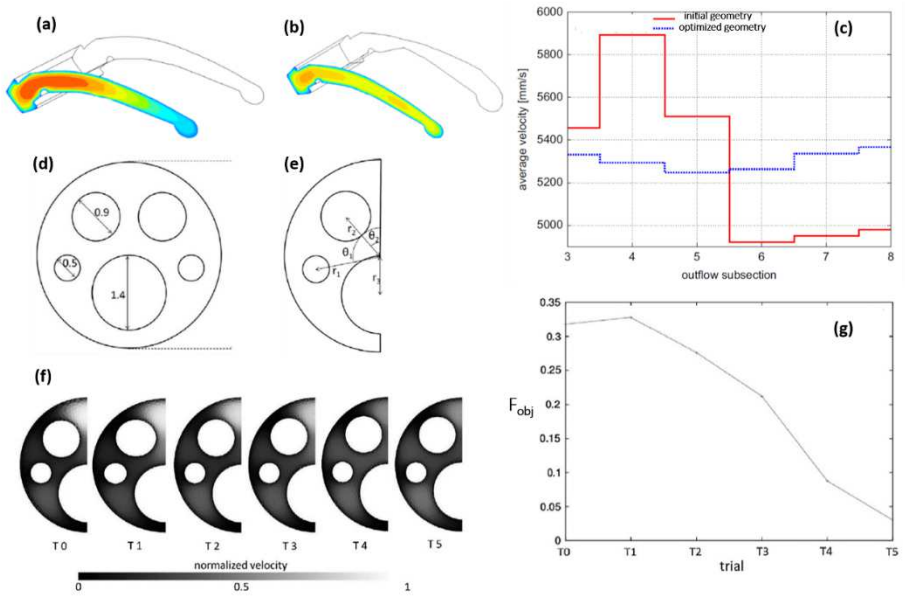


Figure 2-16. (a) and (b): Exit velocity profiles for parallel die and die optimized using conical widening or narrowing, Copyright 2010 [169]. Reproduced permission from Elsevier Ltd; (c) Average velocity of each outflow subsection of the slit die (width=100 mm and height= 1.5 mm), Copyright 2012 [177]. Reproduced with permission from Elsevier Ltd. (d) and (e): the geometry profiles of the Catheter cross-section covered as case study, Copyright 2013 [171]; (f) the velocity distribution at the die outflow for different trials: T0: the original die profile; T1: r_2 varies from 0.9 mm to 0.95 mm; T2: r_2 varies from 0.95 to 0.9 mm, θ_2 varies from 45° to 43°; T3: r_2 varies from 0.9 to 0.95 mm; T4: θ_2 varies from 43° to 40°; T_5: r_3 varies from 0.7 to 0.65 mm, Copyright 2013 [171]; (g) the corresponding objective function evolution in consecutive trials, Copyright 2013 [171]. These subfigures (d), (e), (f) and (g) are reproduced with permission from Elsevier Ltd.

One main difference between the two methodologies for die design is the exclusion of the free surface motion for the first strategy. This drives researchers to use a general

non-Newtonian constitutive model, such as the Bird-Carreau model, to capture the shear-thinning behavior of the flow, assuming that the elasticity does not significantly affect the flow kinematics within the die, but mainly influences the swelling behavior outside the die [174, 177]. Furthermore, for this first methodology, various types of objective functions have been defined concerning the partitioning of velocity contributions or flow rate. Such functions become close to 0 if for all the subsections of the die the bulk average velocity is reached [110, 171, 174]. This implies the target of homogeneous flow at the die exit through typically the automatic optimization of the geometry parameterization combined with the computer aided design (CAD) software, thereby minimizing the swelling outside the die. For instance, Elgeti *et al.* [177] subdivided the extrusion die outflow into subsections and computed the difference between the local maximal velocity, max(V_{sub}), and the average maximal bulk velocity $\bar{V}_{max}$:

$$J = \sum(\max(V_{sub}) - \bar{V}_{max})^2 \qquad (2\text{-}11)$$

These authors indicated that the value of the function strongly relies on the flow distribution in the outflow cross section, with a smaller value implying here a more uniform flow distribution.

More in detail the shape optimization framework depends on two separate executing components, namely the optimization driver and the flow solver, and works by changing the state information between each other. Consequently, an updated mesh pattern is produced according to the given design parameters accompanied by an updated evaluation of the objective function. This information is delivered to the optimization driver, which feeds back the updated design parameters. Fig. 2-16(c) depicts the average velocities in various outflow subsections for the initial geometry and the optimized geometry of a slit die. It is presented that geometry optimization

facilitates a much more uniform average velocity profile. It is thus expected to significantly prohibit the extrudate swell after the flow emerges the die exit.

To further illustrate the practical use of the reverse engineering strategy focus is on some typical test cases in what follows. For example, Nóbrega *et al.* [171, 175, 181, 182] systematically investigated the design of profile extrusion dies by employing the strategy of adjusting the flow balance at die exit using in-house numerical modelling codes, which were verified against typical viscoelastic flow benchmark problems, such as the flow around a cylinder. For example, they used the code to numerically optimize the die design for producing PP material for a medical catheter profile, whose geometry parameters of the cross section are shown in Fig. 2-16(d) and (e) [171]. The cross section of the catheter was subdivided into four section parts. To evaluate the quality of the flow distribution in each subsection, an objective function was defined:

$$F_{obj} = \sum_i^{i=4} F_{obj,i} = \sum_i^{i=4} \left\| 1 - \frac{\bar{V}_i}{\bar{V}} \right\| \frac{A_i}{A} \qquad (2\text{-}12)$$

in which $\bar{V}_i$ is the average flow velocity in a certain subsection, and A_i and A are the area size of the corresponding subsection and the entire outlet.

Fig. 2-16 (f) presents the velocity distribution contour in the whole outflow cross section for each trial of the geometry optimization. It should be noted that each new trial starts with the results from the previous case with parameter changes for r_1, r_2, r_3, θ_1 and θ_2 as shown in Fig. 2-16(e). An almost uniform velocity is observed on the entire outlet section for the fifth trial T_5. It is seen in Fig. 2-16 (g) that the objective function F_{obj} value decreases from 0.32 to 0.03, indicating that the final flow balancing increased significantly and the extrudate with the designed profile is attained to a first approximation. Unfortunately, these authors did not provide an experimental validation of the extrudate product by this modeling die design.

Another example can be found in the work of Debbaut *et al.* [49] who reported the algorithm and detailed simulations for the 3D inverse extrusion regarding a complicated extrudate profile considering the multi-mode DCPP constitutive model in a comprehensive way from an industrial viewpoint using the Polyflow solver. The industrial extrusion profile including the die lip is depicted in Fig. 2-17 alongside the targeted final extrudate profile. The largest simulated deviation from the extrudate is located at the edge of the die lip, indicating the corresponding largest swelling after die exit. For a given flow rate the die computed lips might not be properly adopted to produce the same extrudate at a different flow rate, since the compensation for swelling from the die lips depends on the processing conditions as well. In spite of this discussion, it can be claimed that this study can be extended toward other geometric cases or (viscoelastic) models.

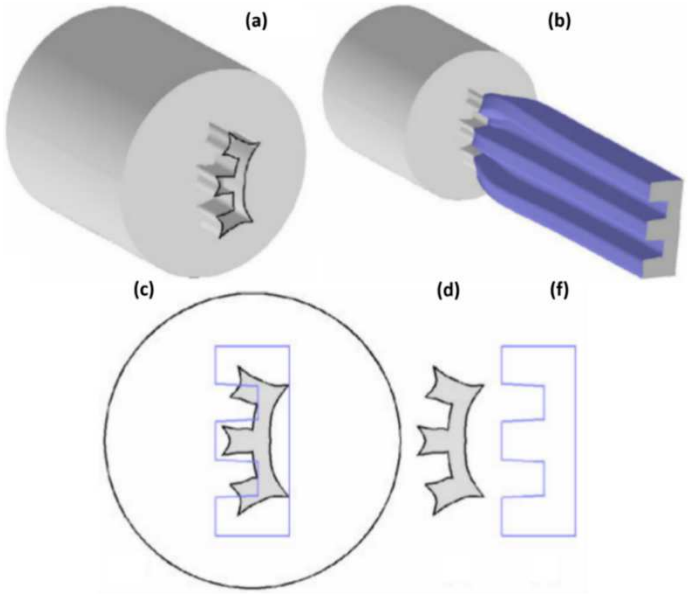


Figure 2-17. Computational domain for industrially relevant profile extrusion: (a) die land; (b) same but including the extrudate; (c) cross sections in front view with a cylindrical entry; (d)

die lips and (e) targeted extrudate profile, Copyright 2008 [49]. Reproduced with permission from Maney on behalf of the institute of materials, minerals and mining.

In addition, Kovalenko *et al.* and Pepliński *et al.* [179, 180] applied the Polyflow solver to investigate the inverse extrusion problem of HDPE polymer melt to provide an assistance for die design. However, for simplicity, the general non-Newtonian constitutive model by Bird-Carreau has been used to reshape the die lip to obtain the desired extrudate profile. Overall, it can be expected that a viscoelastic constitutive model, such as the Gieseskus model, PTT model and Pom-pom based model, should be ideally implemented to address this issue no matter which design approach is applied. As Szarvasy *et al.* [174] stated, the remaining deviation between the product produced based on the modelling guidance from the desired product by means of homogenizing the outflow distribution might likely come from the inherent limitations of the applied non-Newtonian models. Despite that the more simplified viscoelastic models represent quite well the flow in the die land more complex shapes require a more dedicated approach. Specifically, for profiles with various wall thicknesses, die lands with varying dimension sizes apply different deformation histories in flow subsections at which the normal stress change or extensional effect induced by the converging or diverging flow regions should not be omitted. Therefore, advanced numerical 3D modeling based on further developed thus more fundamental viscoelastic constitutive models will be of great significance in the design and flow optimization community in the near future.

2.7. Conclusions

Starting from fundamental principles, the mechanism of extrudate swell of polymer melts has been discussed. The main focus has been on the velocity reorganization

behavior and the stress and strain relaxation of the deformation history, including shear and extensional deformations once the flow emerges the die exit. The normal stress effect for polymer melts contributes to a more robust velocity reorganization, resulting in a significantly large swelling compared to general Newtonian or even non-Newtonian fluids. Such insights have been mainly obtained by focusing on more conventional polymers sometimes in combination with a compounding step to achieve the extrusion of composite materials.

Two classes of measurement methodologies for extrudate swell have been identified, being the offline and online method, and the pros and cons of each method have been discussed. It has been additionally highlighted that the swelling is influenced by processing parameters such as the shear rate and temperature, geometry parameters of the flow channels, molecular characteristics as well as the properties of the filler particles. A joint optimization provides a good guidance to control the swelling behavior and thus to relate the design and synthesis of polymers to the bulk-processing phenomenon of extrudate swell.

In a historical view, the prediction for the swelling behavior of polymer melts through capillary and slit dies has been initially covered by using relatively simply semi-empirical equations, such as the well-known Tanner equation. The semi-empirical based descriptions can however not predict the final swell ratio precisely, especially for polymers with strong viscoelastic properties because they do not consider the die exit effect. Regarding the more recently developed numerical simulations, the common differential PTT constitutive model and integral K-BKZ model have been intensively discussed, because a satisfactory agreement between modeling results and experimental data concerning extrudate swell has been reported for both. In any case, the accurate measurements of the nonlinear viscoelastic rheological raw data are of

great significance to more fundamentally tune the parameters of these viscoelastic models in the future. Furthermore, the Rolie-Poly model shows a promising potential in predicting the swelling for polymers with high dispersity.

It has been further highlighted that a full appreciation of extrudate die swell requires that viscoelastic models are combined with 3D numerical simulations to obtain the actual flow profiles in a given geometry. The discrepancy between experimental results and the commonly used simplified 2D simulations can at least be partially attributed to the ignoring of the 3D or wall effect on extrudate swell. Focus should be here on the consideration of differential or molecular-based constitutive models, although a challenge remains modeling divergence at high Wi numbers.

This need of a 3D interpretation becomes also clear upon reviewing the current methodologies for die design with complex shapes in an industrial context. The first methodology is based on homogenizing the outflow distribution to minimize the swelling behavior after die exit and the second methodology relies on compensating the extrudate swell by modifying the die lips. The challenging task is here to incorporate more fundamental viscoelastic models into the die optimization algorithms but avoiding a too high computational cost.

REFERENCES

1. Miller, E. and J.P. Rothstein, *Control of the sharkskin instability in the extrusion of polymer melts using induced temperature gradients.* Rheologica acta, 2004. **44**(2): p. 160-173.
2. Wieme, T., et al., *The relevance of material and processing parameters on the thermal conductivity of thermoplastic composites.* Polymer Engineering & Science, 2018. **58**(4): p. 466-474.
3. Breitenbach, J., *Melt extrusion: from process to drug delivery technology.* European journal of pharmaceutics and biopharmaceutics, 2002. **54**(2): p. 107-117.
4. Tian, H., et al., *Effect of die lip geometry on polymer extrudate deformation in complex small profile extrusion.* Journal of Manufacturing Science and Engineering, 2017. **139**(6): p. 061005.
5. Aarts, A.C.T., *Analysis of the flow instabilities in the extrusion of polymeric melts*. 1997: Technische Universiteit Eindhoven.
6. Duan, L., et al., *Designing formulation variables of extrusion-based manufacturing of carbon black conductive polymer composites for piezoresistive sensing.* Composites Science and Technology, 2019. **171**: p. 78-85.
7. Newman, S. and Q.A. Trementozzi, *Barus effect in filled polymer melts.* Journal of Applied Polymer Science, 1965. **9**(9): p. 3071-3089.
8. Robertson, B., *Understanding Extrudate Swell: From Theoretical Rheology to Practical Processing*. 2019, Durham University.
9. Schreiber, H., A. Rudin, and E. Bagley, *Separation of elastic and viscous effects in polymer melt extrusion.* Journal of Applied Polymer Science, 1965. **9**(3): p. 887-892.
10. Metzner, A., *Historical comments on stress relaxation following steady flows through a duct or orifice.* Transactions of the Society of Rheology, 1969. **13**(4): p. 467-470.
11. Kishi, N. and H. Iizuka, *The barus effect of polymer melts.* Journal of Polymer Science Part C: Polymer Letters, 1964. **2**(4): p. 399-402.
12. Tanner, R., *A theory of die-swell.* Journal of Polymer Science Part B: Polymer Physics, 1970. **8**(12): p. 2067-2078.
13. Thien, N.P. and R.I. Tanner, *A new constitutive equation derived from network theory.* Journal of Non-Newtonian Fluid Mechanics, 1977. **2**(4): p. 353-365.
14. Luo, X.L. and R. Tanner, *Finite element simulation of long and short circular die extrusion experiments using integral models.* International journal for numerical methods in engineering, 1988. **25**(1): p. 9-22.
15. Luo, X.-L. and R. Tanner, *A streamline element scheme for solving viscoelastic flow problems. Part I. Differential constitutive equations.* Journal of non-newtonian fluid mechanics, 1986. **21**(2): p. 179-199.
16. Tanner, R.I., *A theory of die-swell revisited.* Journal of non-newtonian fluid mechanics, 2005. **129**(2): p. 85-87.

17. Tanner, R., *A new inelastic theory of extrudate swell.* Journal of Non-Newtonian Fluid Mechanics, 1980. **6**(3-4): p. 289-302.
18. Larson, R.G. and P.S. Desai, *Modeling the rheology of polymer melts and solutions.* Annual Review of Fluid Mechanics, 2015. **47**: p. 47-65.
19. Eggen, S. and E.L. Hinrichsen, *Swell and distortions of high-density polyethylene extruded through capillary dies.* Polymer Engineering & Science, 1996. **36**(3): p. 410-424.
20. Han, C.D. and K.U. Kim, *Influence of reservoir diameter on the melt elasticity in capillary flow.* Polymer Engineering & Science, 1971. **11**(5): p. 395-400.
21. Richardson, S., *The die swell phenomenon.* Rheologica Acta, 1970. **9**(2): p. 193-199.
22. Behzadfar, E., et al., *Extrudate swell of HDPE melts: I. Experimental.* Journal of Non-Newtonian Fluid Mechanics, 2015. **225**: p. 86-93.
23. Konaganti, V.K., et al., *Non-isothermal extrudate swell.* Physics of Fluids, 2016. **28**(12): p. 123101.
24. Huang, D.C. and J.L. White, *Extrudate swell from slit and capillary dies: an experimental and theoretical study.* Polymer Engineering & Science, 1979. **19**(9): p. 609-616.
25. Meissner, J., *Basic parameters, melt rheology, processing and end-use properties of three similar low density polyethylene samples.* Pure and Applied Chemistry, 1975. **42**(4): p. 551-612.
26. Yang, B. and L.J. Lee, *Effect of die temperature on the flow of polymer melts. Part II: Extrudate swell.* Polymer Engineering & Science, 1987. **27**(14): p. 1088-1094.
27. Anand, J. and I. Bhardwaj, *Die swell behaviour of polypropylene—An experimental investigation.* Rheologica Acta, 1980. **19**(5): p. 614-622.
28. Koopmans, R., *Extrudate swell of high density polyethylene. Part II: Time dependency and effects of cooling and sagging.* Polymer Engineering & Science, 1992. **32**(23): p. 1750-1754.
29. Jay, P., et al., *The reduction of viscous extrusion stresses and extrudate swell computation using slippery exit surfaces.* Journal of non-newtonian fluid mechanics, 1998. **79**(2): p. 599-617.
30. Huang, H.X. and J.C. Li, *Fast online acquisition and analysis for parison swell and sag in blow molding.* Journal of applied polymer science, 2006. **101**(4): p. 2399-2406.
31. Koopmans, R., *Extrudate swell of high density polyethylene. Part I: Aspects of molecular structure and rheological characterization methods.* Polymer Engineering & Science, 1992. **32**(23): p. 1741-1749.
32. Liang, J.-Z., J. Yang, and C.-Y. Tang, *Die-swell behavior of PP/Al (OH) 3/Mg (OH) 2 flame retardant composite melts.* Polymer testing, 2010. **29**(5): p. 624-628.
33. Mu, Y., G. Zhao, and C. Zhang, *Numerical investigation of die geometry effect on LDPE annular extrudate swell.* Journal of applied polymer science, 2010. **117**(1): p. 91-109.

34. Konaganti, V.K., et al., *Extrudate swell of a high-density polyethylene melt: II. Modeling using integral and differential constitutive equations.* Journal of Non-Newtonian Fluid Mechanics, 2015. **225**: p. 94-105.
35. Caswell, B. and M. Viriyayuthakorn, *Finite element simulation of die swell for a Maxwell fluid.* Journal of Non-Newtonian Fluid Mechanics, 1983. **12**(1): p. 13-29.
36. Bush, M., R. Tanner, and N. Phan-Thien, *A boundary element investigation of extrudate swell.* Journal of non-newtonian fluid mechanics, 1985. **18**(2): p. 143-162.
37. Mitsoulis, E., *Three-dimensional non-Newtonian computations of extrudate swell with the finite element method.* Computer methods in applied mechanics and Engineering, 1999. **180**(3-4): p. 333-344.
38. Goublomme, A., B. Draily, and M. Crochet, *Numerical prediction of extrudate swell of a high-density polyethylene.* Journal of non-Newtonian fluid mechanics, 1992. **44**: p. 171-195.
39. Crochet, M. and R. Keunings, *Die swell of a Maxwell fluid: numerical prediction.* Journal of Non-Newtonian Fluid Mechanics, 1980. **7**(2-3): p. 199-212.
40. Mu, Y., et al., *Finite-Element Simulation of Polymer Flow and Extrudate Swell Through Hollow Profile Extrusion Die with the Multimode Differential Viscoelastic Model.* Advances in Polymer Technology, 2013. **32**(S1).
41. Béraudo, C., et al., *A finite element method for computing the flow of multi-mode viscoelastic fluids: comparison with experiments.* Journal of non-newtonian fluid mechanics, 1998. **75**(1): p. 1-23.
42. McLeish, T. and R. Larson, *Molecular constitutive equations for a class of branched polymers: The pom-pom polymer.* Journal of Rheology, 1998. **42**(1): p. 81-110.
43. Clemeur, N., R. Rutgers, and B. Debbaut, *Numerical simulation of abrupt contraction flows using the Double Convected Pom–Pom model.* Journal of non-newtonian fluid mechanics, 2004. **117**(2-3): p. 193-209.
44. Ganvir, V., et al., *Extrudate swell of linear and branched polyethylenes: ALE simulations and comparison with experiments.* Journal of Non-Newtonian Fluid Mechanics, 2011. **166**(1): p. 12-24.
45. Tian, H., et al., *Study on extrudate swell of polypropylene in double-lumen micro profile extrusion.* Journal of Materials Processing Technology, 2015. **225**: p. 357-368.
46. Ansari, M., E. Mitsoulis, and S.G. Hatzikiriakos, *Capillary extrusion and swell of a HDPE melt exhibiting slip.* Advances in Polymer Technology, 2013. **32**(S1).
47. Ahmed, R., R. Liang, and M. Mackley, *The experimental observation and numerical prediction of planar entry flow and die swell for molten polyethylenes.* Journal of non-newtonian fluid mechanics, 1995. **59**(2-3): p. 129-153.
48. Huang, S.X. and C.J. Lu, *Stress relaxation characteristics and extrudate swell of the IUPAC-LDPE melt.* Journal of non-newtonian fluid mechanics, 2006. **136**(2): p. 147-156.

49. Debbaut, B. and T. Marchal, *Numerical simulation of extrusion process and die design for industrial profile, using multimode pom–pom model.* Plastics, rubber and composites, 2008. **37**(2-4): p. 142-150.
50. Den Doelder, C. and R. Koopmans, *The effect of molar mass distribution on extrudate swell of linear polymers.* Journal of Non-Newtonian Fluid Mechanics, 2008. **152**(1): p. 195-202.
51. Konaganti, V., et al., *Extrudate swell of high density polyethylenes in slit (flat) dies.* International Polymer Processing, 2016. **31**(2): p. 262-272.
52. Tang, D., et al., *Evaluating the exit pressure method for measurements of normal stress difference at high shear rates.* Journal of Rheology, 2020. **64**(3): p. 739-750.
53. Kiriakidis, D. and E. Mitsoulis, *Viscoelastic simulations of extrudate swell for an HDPE melt through slit and capillary dies.* Advances in Polymer Technology, 1993. **12**(2): p. 107-117.
54. Russo, G. and T.N. Phillips, *Numerical prediction of extrudate swell of branched polymer melts.* Rheologica acta, 2010. **49**(6): p. 657-676.
55. Aloku, G.O. and X.-F. Yuan, *Numerical simulation of polymer foaming process in extrusion flow.* Chemical Engineering Science, 2010. **65**(12): p. 3749-3761.
56. Liang, J. and J. Ness, *The melt die-swell behaviour during capillary extrusion of LDPE/PP blends.* Polymer testing, 1998. **17**(3): p. 179-189.
57. Chiu, W.Y. and G.D. Shyu, *Die swell from capillary die and slit die: a theoretical study.* Journal of applied polymer science, 1988. **35**(4): p. 847-862.
58. Normandin, M., et al., *Three-dimensional extrudate swell experimental and numerical study of a polyethylene melt obeying a memory-integral equation.* Journal of non-newtonian fluid mechanics, 1999. **87**(1): p. 1-25.
59. Tang, D., et al., *Isothermal flow of neat polypropylene through a slit die and its die swell: Bridging experiments and 3D numerical simulations.* Journal of Non-Newtonian Fluid Mechanics, 2019. **266**: p. 33-45.
60. Ariffin, A., Z. Ariff, and S. Jikan, *Evaluation on extrudate swell and melt fracture of polypropylene/kaolin composites at high shear stress.* Journal of Reinforced Plastics and Composites, 2011. **30**(7): p. 609-619.
61. Tang, D., et al., *Three-dimensional flow simulations for polymer extrudate swell out of slit dies from low to high aspect ratios.* Physics of Fluids, 2019. **31**(9): p. 093103.
62. Tang, D., et al., *The impact of upstream contraction flow on three-dimensional polymer extrudate swell from slit dies.* Journal of Non-Newtonian Fluid Mechanics, 2020, **282**: 104337.
63. Huang, J.C. and K.S. Leong, *Shear viscosity, extensional viscosity, and die swell of polypropylene in capillary flow with pressure dependency.* Journal of applied polymer science, 2002. **84**(6): p. 1269-1276.
64. Sombatsompop, N., *Extrudate swell and texture of PS, LDPE, ABS, PVC melts and their blends in extrusion capillary flow using a magnetic die.* Journal of applied polymer science, 2002. **86**(2): p. 509-517.
65. Intawong, N.T. and N. Sombatsompop, *A parallel coextrusion technique for simultaneous measurements of radial die swell and velocity profiles of a*

polymer melt in a capillary rheometer. Polymer Engineering & Science, 2004. **44**(10): p. 1960-1969.

66. Robertson, B., et al., *Theoretical prediction and experimental measurement of isothermal extrudate swell of monodisperse and bidisperse polystyrenes.* Journal of Rheology, 2017. **61**(5): p. 931-945.
67. Lee, W.S. and H.Y. Ho, *Experimental study on extrudate swell and die geometry of profile extrusion.* Polymer Engineering & Science, 2000. **40**(5): p. 1085-1094.
68. Utracki, L., Z. Bakerdjian, and M.R. Kamal, *A method for the measurement of the true die swell of polymer melts.* Journal of Applied Polymer Science, 1975. **19**(2): p. 481-501.
69. Liang, J., et al., *Melt extrudate swell behavior of multi-walled carbon nanotubes filled-polypropylene composites.* Polymer Composites, 2017 2017, 38: 2433-2439. **38**: p. 2433.
70. Liang, J.Z., et al., *Extrudate swell behavior of polypropylene composites filled with microencapsulated red phosphorus.* Journal of Applied Polymer Science, 2013. **129**(6): p. 3497-3501.
71. Wong, A.C. and A.C. Wong, *Extrudate swell ratio characteristics of CaCO3 added linear low density polyethylene.* Polymer Testing, 2018. **71**: p. 262-271.
72. Liang, J.-Z., *Effects of particle size on melt viscoelastic properties during capillary extrusion of glass bead-filled LDPE composites.* Journal of Thermoplastic Composite Materials, 2006. **19**(6): p. 703-713.
73. Mitsoulis, E. and S. Hatzikiriakos, *Annular extrudate swell of a fluoropolymer melt.* International Polymer Processing, 2012. **27**(5): p. 535-546.
74. Hulsen, M.A., R. Fattal, and R. Kupferman, *Flow of viscoelastic fluids past a cylinder at high Weissenberg number: stabilized simulations using matrix logarithms.* Journal of Non-Newtonian Fluid Mechanics, 2005. **127**(1): p. 27-39.
75. Baaijens, F.P., *Mixed finite element methods for viscoelastic flow analysis: a review.* Journal of Non-Newtonian Fluid Mechanics, 1998. **79**(2): p. 361-385.
76. Rueda, M.M., et al., *Rheology and Applications of Highly Filled Polymers: A review of current understanding.* Progress in Polymer Science, 2016.
77. Sombatsompop, N. and N. Intawong, *Extrudate swell and flow analysis of polystyrene melt flowing in an electro-magnetized die in a single screw extruder.* Polymers for advanced technologies, 2005. **16**(7): p. 505-514.
78. Yarusso, B.J., *Exit and entrance flows of non-Newtonian fluids in parallel slits.* Journal of non-newtonian fluid mechanics, 1991. **40**(1): p. 103-117.
79. Limtrakarn, W., et al., *Circular Die Swell Evaluation of LDPE Using Simplified Viscoelastic Model.* King Mongkut's University of Technology North Bangkok International Journal of Applied Science and Technology, 2013. **6**(3): p. 59-68.
80. Ganvir, V., et al., *Prediction of extrudate swell in polymer melt extrusion using an Arbitrary Lagrangian Eulerian (ALE) based finite element method.* Journal of Non-Newtonian Fluid Mechanics, 2009. **156**(1): p. 21-28.

81. Nair, K., et al., *Rheological behavior of short sisal fiber-reinforced polystyrene composites.* Composites Part A: Applied Science and Manufacturing, 2000. **31**(11): p. 1231-1240.
82. Liang, J., et al., *Melt extrudate swell behavior of multi-walled carbon nanotubes filled-polypropylene composites.* Polymer Composites, 2015.
83. Müllner, H.W., J. Eberhardsteiner, and W. Fidi, *Rheological characterization of the die swell phenomenon of rubber compounds.* Polymer Testing, 2007. **26**(8): p. 1041-1048.
84. Intawong, N.T. and N. Sombatsompop, *Experimental studies on radial extrudate swell and velocity profiles of flowing PS melt in an electro-magnetized die of an extrusion rheometer.* Polymer Engineering & Science, 2004. **44**(12): p. 2298-2307.
85. Sombatsompop, N. and N.-T. Intawong, *A comparative study on extrudate swell ratio of polystyrene in a capillary rheometer and a single screw extruder.* Polymer testing, 2005. **24**(8): p. 948-952.
86. Hatzikiriakos, S.G., *Wall slip of molten polymers.* Progress in Polymer Science, 2012. **37**(4): p. 624-643.
87. Migler, K., H. Hervet, and L. Leger, *Slip transition of a polymer melt under shear stress.* Physical review letters, 1993. **70**(3): p. 287.
88. Laun, H.M., *Capillary rheometry for polymer melts revisited.* Rheologica acta, 2004. **43**(5): p. 509-528.
89. Kraynik, A. and W. Schowalter, *Slip at the wall and extrudate roughness with aqueous solutions of polyvinyl alcohol and sodium borate.* Journal of Rheology, 1981. **25**(1): p. 95-114.
90. Brzoskowski, R., et al., *Air-lubricated die for extrusion of rubber compounds.* Rubber chemistry and technology, 1987. **60**(5): p. 945-956.
91. Pladis, P., D. Meimaroglou, and C. Kiparissides, *Prediction of the Viscoelastic Behavior of Low-Density Polyethylene Produced in High-Pressure Tubular Reactors.* Macromolecular Reaction Engineering, 2015. **9**(3): p. 271-284.
92. Sombatsompop, N. and R. Dangtangee, *Effects of the actual diameters and diameter ratios of barrels and dies on the elastic swell and entrance pressure drop of natural rubber in capillary die flow.* Journal of applied polymer science, 2002. **86**(7): p. 1762-1772.
93. La Mantia, F., D. Curto, and D. Acierno, *The rheological behaviour of HDPE/LDPE blends. II. Die swell and normal stresses.* Acta polymerica, 1984. **35**(1): p. 71-73.
94. Romanini, D. and G. Pezzin, *Relation between extrudate swelling of polypropylene and molecular weight.* Rheologica Acta, 1982. **21**(6): p. 699-704.
95. Dangtungee, R. and P. Supaphol, *Melt rheology and extrudate swell of titanium (IV) oxide nanoparticle-filled isotactic polypropylene: Effects of content and surface characteristics.* Polymer Testing, 2008. **27**(8): p. 951-956.
96. Aral, B.K. and D.M. Kalyon, *Viscoelastic material functions of noncolloidal suspensions with spherical particles.* Journal of Rheology, 1997. **41**(3): p. 599-620.

97. Wagner, A., R. Yazici, and D.M. Kalyon, *Extrudate swell behavior of glass fiber filled polyamide 6.* Polymer composites, 1996. **17**(6): p. 840-849.
98. Duan, L., et al., *Facile and low-cost route for sensitive stretchable sensors by controlling kinetic and thermodynamic conductive network regulating strategies.* ACS applied materials & interfaces, 2018. **10**(26): p. 22678-22691.
99. Gnanasekaran, K., et al., *A unified view on nanoscale packing, connectivity, and conductivity of CNT networks.* Advanced Functional Materials, 2019. **29**(13): p. 1807901.
100. George, J. and H. Ishida, *A review on the very high nanofiller-content nanocomposites: Their preparation methods and properties with high aspect ratio fillers.* Progress in Polymer Science, 2018. **86**: p. 1-39.
101. Wieme, T., et al., *Effect of Matrix and Graphite Filler on Thermal Conductivity of Industrially Feasible Injection Molded Thermoplastic Composites.* Polymers, 2019. **11**(1): p. 87.
102. Luo, W., et al., *Thermal, electrical and rheological behavior of high-density polyethylene/graphite composites.* Iranian Polymer Journal, 2015. **24**(7): p. 573-581.
103. Rueda, M.M., et al., *Rheology and applications of highly filled polymers: A review of current understanding.* Progress in Polymer Science, 2017. **66**: p. 22-53.
104. Bee, S.-L., et al., *Polymer nanocomposites based on silylated-montmorillonite: A review.* Progress in Polymer Science, 2018. **85**: p. 57-82.
105. Stabik, J., *Influence of filler particle geometry on die swell.* International Polymer Processing, 2004. **19**(4): p. 350-355.
106. Minagawa, N. and J.L. White, *The influence of titanium dioxide on the rheological and extrusion properties of polymer melts.* Journal of Applied Polymer Science, 1976. **20**(2): p. 501-523.
107. Mendelson, R., F. Finger, and E. Bagley. *Die swell and recoverable shear strain in polyethylene extrusion*. in *Journal of Polymer Science Part C: Polymer Symposia*. 1971. Wiley Online Library.
108. Liang, J.-Z., *Estimation of die-swell ratio for polymer melts from exit pressure drop data.* Polymer testing, 2000. **20**(1): p. 29-31.
109. Kar, K.K. and J.U. Otaigbe, *Numerical analysis and experimental studies on the role of rheological properties in effecting die swell of low density polyethylene, polypropylene and polystyrene: A predictive model based on Newtonian fluid.* Journal of Elastomers & Plastics, 2001. **33**(4): p. 297-336.
110. Jabbari, M., et al., *Multiphysics modelling of manufacturing processes: A review.* Advances in mechanical engineering, 2018. **10**(5): p. 1687814018766188.
111. Al-Muslimawi, A., H. Tamaddon-Jahromi, and M. Webster, *Simulation of viscoelastic and viscoelastoplastic die-swell flows.* Journal of Non-Newtonian Fluid Mechanics, 2013. **191**: p. 45-56.
112. Huang, S.-x., et al., *Rheological characterizations and extrudate swell predictions of an LDPE melt by two KBKZ-type constitutive equations.* Journal of Hydrodynamics, Ser. B, 2010. **22**(5): p. 915-919.

113. Comminal, R., et al., *Numerical simulation of the planar extrudate swell of pseudoplastic and viscoelastic fluids with the streamfunction and the VOF methods.* Journal of Non-Newtonian Fluid Mechanics, 2018. **252**: p. 1-18.
114. Wagner, M., *Analysis of time-dependent non-linear stress-growth data for shear and elongational flow of a low-density branched polyethylene melt.* Rheologica Acta, 1976. **15**(2): p. 136-142.
115. Papanastasiou, A., L. Scriven, and C. Macosko, *An integral constitutive equation for mixed flows: viscoelastic characterization.* Journal of Rheology, 1983. **27**(4): p. 387-410.
116. Musil, J. and M. Zatloukal, *Historical review of secondary entry flows in polymer melt extrusion.* Polymer Reviews, 2019. **59**(2): p. 338-390.
117. Song, J.H. and J.Y. Yoo, *Numerical simulation of viscoelastic flow through a sudden contraction using a type dependent difference method.* Journal of non-newtonian fluid mechanics, 1987. **24**(2): p. 221-243.
118. Ahn, Y.C. and M.E. Ryan, *A finite difference analysis of the extrudate swell problem.* International journal for numerical methods in fluids, 1991. **13**(10): p. 1289-1310.
119. Di, Y., S. Iannace, and L. Nicolais, *Thermal behavior and morphological and rheological properties of polypropylene and novel elastomeric ethylene copolymer blends.* Journal of applied polymer science, 2002. **86**(13): p. 3430-3439.
120. Normandin, M., et al., *Finite element and stream-tube formulations for flow computations—two-dimensional applications.* Mathematics and computers in simulation, 2002. **60**(1-2): p. 129-134.
121. Schoonen, J.F., et al., *A 3D numerical/experimental study on a stagnation flow of a polyisobutylene solution.* Journal of non-newtonian fluid mechanics, 1998. **79**(2-3): p. 529-561.
122. Xue, S.-C., N. Phan-Thien, and R. Tanner, *Numerical study of secondary flows of viscoelastic fluid in straight pipes by an implicit finite volume method.* Journal of Non-Newtonian Fluid Mechanics, 1995. **59**(2-3): p. 191-213.
123. Yamamoto, T., et al., *Three-dimensional viscoelastic flows through a rectangular channel with a cavity.* Journal of non-Newtonian fluid mechanics, 2003. **114**(1): p. 13-31.
124. Oliveira, P.J. and F. Pinho, *Plane contraction flows of upper convected Maxwell and Phan-Thien–Tanner fluids as predicted by a finite-volume method.* Journal of Non-Newtonian Fluid Mechanics, 1999. **88**(1-2): p. 63-88.
125. Mompean, G. and M. Deville, *Unsteady finite volume simulation of Oldroyd-B fluid through a three-dimensional planar contraction.* Journal of Non-Newtonian Fluid Mechanics, 1997. **72**(2-3): p. 253-279.
126. Marchal, J. and M. Crochet, *A new mixed finite element for calculating viscoelastic flow.* Journal of Non-Newtonian Fluid Mechanics, 1987. **26**(1): p. 77-114.
127. Brasseur, E., et al., *The time-dependent extrudate-swell problem of an Oldroyd-B fluid with slip along the wall.* Journal of Rheology, 1998. **42**(3): p. 549-566.

128. Rajagopalan, D., et al., *Comparison of numerical simulations and birefringence measurements in viscoelastic flow between eccentric rotating cylinders.* Journal of Rheology, 1992. **36**(7): p. 1349-1375.
129. Guénette, R. and M. Fortin, *A new mixed finite element method for computing viscoelastic flows.* Journal of non-newtonian fluid mechanics, 1995. **60**(1): p. 27-52.
130. Bird, R.B., R.C. Armstrong, and O. Hassager, *Dynamics of polymeric liquids. Vol. 1: Fluid mechanics.* 1987.
131. Crochet, M.J., *Numerical simulation of viscoelastic flow: a review.* Rubber chemistry and technology, 1989. **62**(3): p. 426-455.
132. Debbaut, B., J. Marchal, and M. Crochet, *Numerical simulation of highly viscoelastic flows through an abrupt contraction.* Journal of Non-Newtonian Fluid Mechanics, 1988. **29**: p. 119-146.
133. Chang, P.-W., T.W. Patten, and B.A. Finlayson, *Collocation and galerkin finite element methods for viscoelastic fluid flow—I.: Description of method and problems with fixed geometry.* Computers & Fluids, 1979. **7**(4): p. 267-283.
134. Chang, P.-W., T.W. Patten, and B.A. Finlayson, *Collocation and galerkin finite element methods for viscoelastic fluid flow—II. Die swell problems with a free surface.* Computers & Fluids, 1979. **7**(4): p. 285-293.
135. Luo, X.-L. and R. Tanner, *A streamline element scheme for solving viscoelastic flowproblems part II: integral constitutive models.* Journal of Non-Newtonian Fluid Mechanics, 1986. **22**(1): p. 61-89.
136. Oldroyd, J.G., *On the formulation of rheological equations of state.* Proceedings of the Royal Society of London. Series A. Mathematical and Physical Sciences, 1950. **200**(1063): p. 523-541.
137. Musarra, S. and R. Keunings, *Co-current axisymmetric flow in complex geometries: numerical simulation.* Journal of non-newtonian fluid mechanics, 1989. **32**(3): p. 253-268.
138. Crochet, M. and R. Keunings, *Finite element analysis of die swell of a highly elastic fluid.* Journal of Non-Newtonian Fluid Mechanics, 1982. **10**(3-4): p. 339-356.
139. Xue, S.-C., N. Phan-Thien, and R. Tanner, *Three dimensional numerical simulations of viscoelastic flows through planar contractions.* Journal of Non-Newtonian Fluid Mechanics, 1998. **74**(1): p. 195-245.
140. Schoonen, J., *Determination of rheological constitutive equations using complex flows.* 1998: Technische Universiteit Eindhoven Eindhoven.
141. Mompean, G., et al., *Numerical prediction of three-dimensional time-dependent viscoelastic extrudate swell using differential and algebraic models.* Computers & fluids, 2011. **44**(1): p. 68-78.
142. Thais, L., L. Helin, and G. Mompean, *Numerical simulation of viscoelastic flows with Oldroyd-B constitutive equations and novel algebraic stress models.* Journal of non-newtonian fluid mechanics, 2006. **140**(1-3): p. 145-158.
143. Souvaliotis, A. and A. Beris, *An extended White–Metzner viscoelastic fluid model based on an internal structural parameter.* Journal of Rheology, 1992. **36**(2): p. 241-271.

144. Phan-Thien, N., *A nonlinear network viscoelastic model.* Journal of Rheology, 1978. **22**(3): p. 259-283.
145. Alves, M.A., F.T. Pinho, and P.J. Oliveira, *Study of steady pipe and channel flows of a single-mode Phan-Thien–Tanner fluid.* Journal of non-newtonian fluid mechanics, 2001. **101**(1-3): p. 55-76.
146. Mu, Y., et al., *Modeling and simulation of three-dimensional planar contraction flow of viscoelastic fluids with PTT, Giesekus and FENE-P constitutive models.* Applied Mathematics and Computation, 2012. **218**(17): p. 8429-8443.
147. Carrot, C., et al., *Experimental validation of non linear network models*, in *Rheology Series*. 1996, Elsevier. p. 141-198.
148. Konaganti, V.K., et al., *The effect of damping function on extrudate swell.* Journal of Non-Newtonian Fluid Mechanics, 2016. **236**: p. 73-82.
149. Goublomme, A. and M. Crochet, *Numerical prediction of extrudate swell of a high-density polyethylene: further results.* Journal of non-newtonian fluid mechanics, 1993. **47**: p. 281-287.
150. Kajiwara, T., et al., *Numerical simulation of converging flow of polymer melts through a tapered slit die.* Journal of non-newtonian fluid mechanics, 1993. **48**(1-2): p. 111-124.
151. Azaiez, J., R. Guénette, and A. Ait-Kadi, *Numerical simulation of viscoelastic flows through a planar contraction.* Journal of non-newtonian fluid mechanics, 1996. **62**(2-3): p. 253-277.
152. Verbeeten, W.M., G.W. Peters, and F.P. Baaijens, *Differential constitutive equations for polymer melts: The extended Pom–Pom model.* Journal of rheology, 2001. **45**(4): p. 823-843.
153. Clemeur, N., R.P. Rutgers, and B. Debbaut, *On the evaluation of some differential formulations for the pom-pom constitutive model.* Rheologica acta, 2003. **42**(3): p. 217-231.
154. Graham, R.S., et al., *Microscopic theory of linear, entangled polymer chains under rapid deformation including chain stretch and convective constraint release.* Journal of Rheology, 2003. **47**(5): p. 1171-1200.
155. Likhtman, A.E. and R.S. Graham, *Simple constitutive equation for linear polymer melts derived from molecular theory: Rolie–Poly equation.* Journal of Non-Newtonian Fluid Mechanics, 2003. **114**(1): p. 1-12.
156. Doi, M. and S.F. Edwards, *The theory of polymer dynamics*. Vol. 73. 1988: oxford university press.
157. Cao, Y., et al. *An Analysis of Die Swell with Rolie-Poly Model*. in *2015 3rd International Conference on Machinery, Materials and Information Technology Applications*. 2015. Atlantis Press.
158. Robertson, B., et al., *Polymer extrudate-swell: From monodisperse melts to polydispersity and flow-induced reduction in monomer friction.* Journal of Rheology, 2019. **63**(2): p. 319-333.
159. Fierens, S., et al., *Analytical and advanced kinetic models for characterization of chain-growth copolymerization: the state-of-the-art.* Reaction Chemistry & Engineering, 2018. **3**(2): p. 128-145.
160. Alexander M. Mood , F.A.G., Duane C. Boes, *Introduction to the Theory of Statistics*. 3 ed. 1974: McGraw Hill. 577.

161. Mitsoulis, E., *50 years of the K-BKZ constitutive relation for polymers.* ISRN Polymer Science, 2013. **2013**.
162. Bernstein, B., E. Kearsley, and L. Zapas, *A study of stress relaxation with finite strain.* Transactions of the Society of Rheology, 1963. **7**(1): p. 391-410.
163. Kaye, A., *Non-Newtonian flow in incompressible fluids.* 1962, College of Aeronautics Cranfield.
164. Wagner, M., *A constitutive analysis of uniaxial elongational flow data of low-density polyethylene melt.* Journal of Non-Newtonian Fluid Mechanics, 1978. **4**(1-2): p. 39-55.
165. Rajagopalan, D., R.C. Armstrong, and R.A. Brown, *Comparison of computational efficiency of flow simulations with multimode constitutive equations: integral and differential models.* Journal of non-newtonian fluid mechanics, 1993. **46**(2-3): p. 243-273.
166. Phan-Thien, N., *Influence of wall slip on extrudate swell: a boundary element investigation.* Journal of non-newtonian fluid mechanics, 1988. **26**(3): p. 327-340.
167. Liang, J., et al., *Melt extrudate swell behavior of multi-walled carbon nanotubes filled-polypropylene composites.* Polymer Composites, 2017. **38**(11): p. 2433-2439.
168. Spanjaards, M., M. Hulsen, and P. Anderson, *Transient 3D finite element method for predicting extrudate swell of domains containing sharp edges.* Journal of Non-Newtonian Fluid Mechanics, 2019. **270**: p. 79-95.
169. Sienz, J., A. Goublomme, and M. Luege, *Sensitivity analysis for the design of profile extrusion dies.* Computers & structures, 2010. **88**(9-10): p. 610-624.
170. Agassant, J.-F. and M.R. Mackley, *A personal perspective on the use of modelling simulation for polymer melt processing.* International Polymer Processing, 2015. **30**(1): p. 121-140.
171. Gonçalves, N., O. Carneiro, and J. Nóbrega, *Design of complex profile extrusion dies through numerical modeling.* Journal of Non-Newtonian Fluid Mechanics, 2013. **200**: p. 103-110.
172. Hopmann, C., et al. *Improving the automated optimization of profile extrusion dies by applying appropriate optimization areas and strategies*. in *AIP Conference Proceedings*. 2014. AIP.
173. Siegbert, R., et al., *Individualized production in die-based manufacturing processes using numerical optimization.* The International Journal of Advanced Manufacturing Technology, 2015. **80**(5-8): p. 851-858.
174. Szarvasy, I., et al., *Computer aided optimisation of profile extrusion dies: definition and assessment of the objective function.* International Polymer Processing, 2000. **15**(1): p. 28-39.
175. Carneiro, O., et al., *Computer aided rheological design of extrusion dies for profiles.* Journal of materials processing technology, 2001. **114**(1): p. 75-86.
176. Pittman, J., *Computer-aided design and optimization of profile extrusion dies for thermoplastics and rubber: a review.* Proceedings of the Institution of Mechanical Engineers, Part E: Journal of Process Mechanical Engineering, 2011. **225**(4): p. 280-321.

177. Elgeti, S., et al., *Numerical shape optimization as an approach to extrusion die design.* Finite Elements in Analysis and Design, 2012. **61**: p. 35-43.
178. Legat, V. and J.M. Marchal, *Die design: an implicit formulation for the inverse problem.* International journal for numerical methods in fluids, 1993. **16**(1): p. 29-42.
179. Kovalenko, K., V. Sivetskii, and A. Sokol'skii, *Design of an extrusion die for plastic profiles.* Chemical and Petroleum Engineering, 2014. **49**(9-10): p. 675-678.
180. Pepliński, K. and A. Mozer, *Design of extrusion die for plastic profile using ansys polyflow software.* Journal of Polish CIMAC, 2011. **6**(3): p. 221-226.
181. Carneiro, O. and J. Nobrega, *Recent developments in automatic die design for profile extrusion.* Plastics, Rubber and Composites, 2004. **33**(9-10): p. 400-408.
182. Carneiro, O., et al., *Flow balancing in extrusion dies for thermoplastic profiles: part II: influence of the design strategy.* International Polymer Processing, 2003. **18**(3): p. 307-312.

Chapter 3

Flow of neat polypropylene through a slit die and its die swell: bridging experiments and 3D numerical simulations

The relevance of 3D numerical simulations for the isothermal flow of neat polypropylene through a slit die and the subsequent swelling upon die exit is highlighted based on the finite element method using the ANSYS Polyflow software package. The input parameters of (i) the generalized Newtonian constitutive model with the Cross law viscosity function and (ii) the multimode viscoelastic Phan-Thien-Tanner (PTT) constitutive model are estimated from rheological data obtained with rotational and capillary rheometers. Model validation is performed based on die pressure and real time experimental HD imaging for 3D die swell characterization. The evolution of the swell ratios in both width and height directions is investigated downstream the die exit. By employing the generalized Newtonian constitutive model with the Cross law viscosity function, the swell ratios are highly underestimated, and this discrepancy becomes more significant as the flow rate increases. It is demonstrated that the PTT based swell ratio in the width direction increases in a much lower rate than the swell ratio in the height direction until equilibrium is achieved in both directions. Therefore, the distance from the die exit in which the final extrudate shape is obtained strongly depends on the die width, which is ignored in conventional 2D numerical simulations. The findings are underpinned through a detailed analysis of the simulated 3D stress and velocity field distributions.

3.1. Introduction

Extrusion is one of the most important processing methods used for several industrial applications [1-3]. For the proper design of extrusion, a quantitative understanding of the viscoelastic behavior of polymer melts is fundamental. The complicated extrudate deformation behavior outside the die exit during free surface flow, which is generally known as die or extrudate swell, results in a difficulty in obtaining a final manufacturing product with the desired stability [4]. Therefore, it is of great significance to figure out the extrudate behavior in view of the die design and processing control.

It is commonly accepted that the polymer extrudate deformation problem is dependent on the material properties and flow history related to the channel geometry [5, 6]. However, the flow behavior in the channel is a typical "black box" problem. Numerical modeling is a good choice to have insight into the flow pattern [7-9]. Since Luo and Tanner [10, 11] simulated the flow behavior of low density polyethylene (LDPE) melts through capillary dies using the more realistic differential Phan-Thien-Tanner (PTT) constitutive model or the Kaye-Bernstein-Kearsley-Zapas (K-BKZ) integral constitutive model instead of the pragmatic but unrealistic differential Maxwell constitutive model based on a streamline element scheme, the attention of the researchers on the extrusion flow problem has been moved to the former models. During the last decades, a great progress has been made in that respect [12-16] . For instance, Luo and Tanner [12] simulated the flow behavior of LDPE melt through long and short capillary dies with a conical contraction ratio of 1:4 using the multi-mode integral K-BKZ model. A quantitative agreement between simulation and experimental results was obtained for both cases for an apparent shear

rate up to 10 s^{-1}. Hatzikiriakos *et al.* [17-20] reported several numerical studies of the flow behavior of HDPE melts through capillary dies including wall slippage and extrudate swell using the multi-mode integral model. Similar achievements have also been made by utilizing the multi-mode differential model [13, 15, 21, 22]. Béraudo *et al.* [13] investigated the complex flow behavior of polyethylene melts through convergent flow channels with the PTT model. They found that the computations agreed well with experiments. For the extrudate swell problem, a good agreement was achieved only for long dies, but not for short dies. In addition, Azaiez *et al.* [23] studied both linear and nonlinear properties of polymer solutions using several single-mode differential models and concluded that the single-mode instead of multi-mode model is normally unable to accurately capture that behavior.

It is additionally often put forward that the flow pattern can be considered as a 2D axisymmetric or planar flow if the melt flows through a cylindrical channel or rectangular channel, respectively. In the case of the former one, it should be accurate as long as the flow remains steady [24-27]. As for the latter one, previous researchers preferred to model the flow behavior inside and outside the die exit with a 2D configuration of the flow channel assuming that the ratio of width to height (W/H) is infinite leading to much less computational cost and facilitating the numerical convergence [28-31].

However, the W/H ratio of the rectangular flow channel is usually finite experimentally. Because of the side wall effect of the flow channel, the flow behavior along the width direction could not be totally the same, which means the velocity gradient in that direction never always vanishes. Researchers reported the side wall effect on the flow behavior of planar flow through a contraction channel [32, 33].

Therefore, for flow emerging the rectangular die, apart from the extrudate size, it can be expected that the extrudate shape also deforms because of the swell behavior in the width direction, increasing difficulty in the die design. Konaganti *et al.* [34] studied the swelling behavior of high density polyethylene (HDPE) melt from a series of slit dies with different geometries. From experimental results, they concluded that the swelling in the height direction is predominant in comparison with that in the width direction. However, due to the 2D configuration used in their simulation study, they only predicted the extrudate height swelling. From the experimental results, it is found that if the height swell ratio of HDPE extrudate from the slit die with a width/height ratio of 36 was around 1.75 at a shear rate of 40 s^{-1}, width swell ratio was as high as 1.46, which means that the width swell behavior is relevant and can thus likely not be neglected. Hence, in general, 2D numerical simulations cannot accurately capture the whole complicated swelling behavior.

It is therefore not surprising that in recent years, more attention has been given to extrudate swell problems based on a full 3D simulation [35-40]. Normandin *et al*. [36] compared the 3D numerical to the experimental results of extrudate swell of a PE melt through a square die using a memory-integral model. A good agreement between experimental and numerical data was achieved for points at the middle side plane, while there are some discrepancies for the data at the corner. They attributed it to the geometrical singularity in 3D flow situations. In addition, the anisotropic dimensions of the extrudate after the square die were also shown. Mu *et al.* [37-39] studied the extrudate swell of LDPE melt for a series of extrusion dies, using a multimode PTT model with a penalty finite element method in 3D configuration. The effect of die geometry on swell behavior was discussed in detail. Mu *et al.* [38] also compared the flow behavior of LDPE melt in the 3D planar flow channel predicted

by a series of differential constitutive models, such as the PTT, Giesekus and Finite Extensible Nonlinear Elastic Dumbbell-Peterlin (FENE-P) constitutive model. The flow velocity field and stress field obtained by the simulations showed satisfactory agreement with experimental observations, but the extrudate swelling problem was not accounted for. To the best of the authors' knowledge, very limited combined experimental and modeling reports regarding a comprehensive understanding of the extrudate swell of the viscoelastic flow through a slit die considering both height and width swell have been conducted, which is essential for the die optimization design. Therefore, a more detailed 3D numerical simulation combined with experimental validation is still necessary to figure out this issue in an industrial context.

In this contribution, the main objective is to provide insight into the complicated flow behavior of the isothermal polymer melts both inside and outside a slit die, selecting polypropylene (PP) as reference polymer at 200 °C. Therefore, a full 3D numerical simulation study of flow behavior for an isothermal extrusion process is carried out to provide detailed results, using two types of constitutive models, namely the generalized Newtonian constitutive model with the Cross law viscosity function and the viscoelastic multi-mode differential PTT model. To reduce the computational cost, the pressure field is calculated within the corresponding 2D simulation configuration. Pressure and extrudate swell measurements by a real-time method are used to validate the numerical simulations. The swell behavior in both width and height direction of extrudate is discussed, and the difference of swell behavior in the corresponding two directions known as inhomogeneous extrudate swell behavior is noted. The possible mechanism is revealed based on the investigation of velocity and stress field distributions.

3.2. 3D modelling principles

3.2.1. Governing equations

With the assumption that the incompressible polymer melt is under steady, isothermal and creeping laminar flow conditions due to the much low Reynolds number of polymer flow [41], the mathematical model applied in this study includes the following continuity and momentum conservation equations in vector notation:

Continuity equation: $$\nabla \cdot \mathbf{v} = 0 \quad (3\text{-}1)$$

Momentum equation $$-\nabla p + \nabla \cdot \boldsymbol{\tau} = 0 \quad (3\text{-}2)$$

where $\boldsymbol{v}$ is the velocity vector, ρ the material density, p the hydrostatic pressure, and $\boldsymbol{\tau}$ the extra stress tensor. It is important noting that the effects of gravity are neglected, which seems to be a reasonable assumption considering the high melt viscosity of the polymer [16].

Two types of numerical constitutive models, namely the viscous Cross law model and the viscoelastic PTT model are considered in the present work to investigate the rheological behavior of neat PP. Focus is on these two models as the PTT model is claimed to be able to capture the viscoelastic properties of polymer melt including the shear thinning and elongational thinning behavior in the high strain rate range, while the Cross law provides an insight into the role of purely viscous properties of the flow through a slit die in that strain rate range [20].

3.2.1.1. Cross law model

For a generalized Newtonian flow stress tensor $\boldsymbol{\sigma}$ defined as:

$$\sigma = 2\eta \boldsymbol{D} \qquad (3\text{-}3)$$

where η is shear-dependent non-Newtonian viscosity, while $\boldsymbol{D}$ means the rate of deformation tensor of fluid dependent on shear rate, which obeys the following form:

$$\boldsymbol{D} = \frac{\nabla v + (\nabla v)^T}{2} \qquad (3\text{-}4)$$

where ∇v and $(\nabla v)^T$ are velocity gradient and transpose of velocity gradient separately. For the Cross law model, the viscosity, η can be written as:

$$\eta = \frac{\eta_0}{1+(\lambda \dot{\gamma})^m} \qquad (3\text{-}5)$$

Where η_0 is the zero shear viscosity for the fluid, λ is the relaxation time, and m means the cross law factor.

3.2.1.2. PTT constitutive model

For the differential viscoelastic constitutive model, the extra stress tensor $\boldsymbol{\tau}$ can be divided into a purely viscous part $\boldsymbol{\tau_N}$ and a viscoelastic part $\boldsymbol{\tau_p}$, which could be calculated by the basic viscoelastic constitutive equations.

In comparison with a single mode PTT model, a multi-mode PTT model with a relaxation time spectrum tends to obtain more accurate simulation results [29]. This model is expressed as:

$$\boldsymbol{\tau_p} = \sum_{i=1}^{N} \boldsymbol{\tau_{pi}} \qquad (3\text{-}6)$$

$$exp\left[\frac{\varepsilon_i \lambda_i}{\eta_i}\boldsymbol{tr}(\boldsymbol{\tau_{pi}})\right]\boldsymbol{\tau_{pi}} + \lambda_i\left[(1-\frac{\xi_i}{2})\overset{\frown}{\boldsymbol{\tau_{pi}}} + \frac{\xi_i}{2}\overset{\frown}{\boldsymbol{\tau_{pi}}}\right] = 2\eta_i\mathbf{D} \qquad (3\text{-}7)$$

Where the two non-linear parameters, ε_i and ξ_i, control extensional and shear behavior of polymer fluid, respectively, and $\overset{\frown}{\boldsymbol{\tau_{pi}}}$ and $\overset{\frown}{\boldsymbol{\tau_{pi}}}$ denote upper and lower convected derivatives of $\boldsymbol{\tau_{pi}}$, defined by:

$$\overset{\frown}{\boldsymbol{\tau_{pi}}} = \frac{D\boldsymbol{\tau_{pi}}}{Dt} - (\boldsymbol{\tau_{pi}}\cdot\nabla\mathbf{v} + (\nabla\mathbf{v})^T\cdot\boldsymbol{\tau_{pi}}) \qquad (3\text{-}8)$$

$$\overset{\frown}{\boldsymbol{\tau_{pi}}} = \frac{D\boldsymbol{\tau_{pi}}}{Dt} + (\boldsymbol{\tau_{pi}}\cdot\nabla\mathbf{v} + (\nabla\mathbf{v})^T\cdot\boldsymbol{\tau_{pi}}) \qquad (3\text{-}9)$$

3.2.2. Geometry and boundary conditions

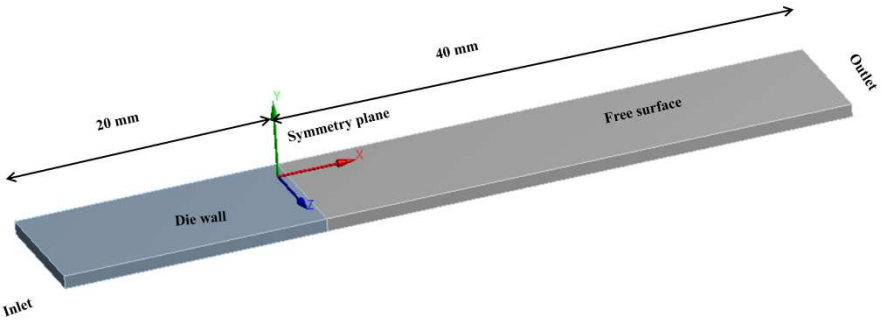


Figure 3-1. Schematic diagram of the 3D flow domain in and out of the slit die.

Based on the extrusion processing, a 3D flow domain of the slit die is developed in Figure 3-1. Considering the symmetry of the geometry, a quarter of the extrusion flow domain is computed in order to reduce the computational cost. The associated boundary conditions in Fig. 3-1 are presented. At the inlet, the flow with a certain flow rate enters. On the die walls, a non-slip condition is assumed for simplicity: v_n = v_t = 0 (mm/s). On the symmetry planes, usual symmetry conditions are applied: v_n = 0 (mm/s), f_t = 0 (N). Leaving the die exit, the melt develops a free motion which is

unknown a priori. Surface tension is not considered, therefore a zero normal force condition is implemented at it. Then, the line kinematic condition, $v \cdot n = 0$ is solved. At the outlet of the flow domain, the force conditions are set: $f_t = f_n = 0$ (N). It should be noticed that the subscript t and n in the above equations represent the tangential and normal component of the velocity and force, respectively. $\boldsymbol{n}$ is the normal vector to the free surface. In addition, because of the computational cost, the corresponding 2D simulation pattern is used to calculate the pressure value in the die channel.

3.2.3. Details on finite element calculations

A flow solver (POLYFLOW version, ANSYS, 18.0) based on a finite element algorithm with the discrete elastic viscous stress splitting (DEVSS) method combined with the streamline upwind (SU) scheme to improve the numerical calculation stability is employed to solve the governing equations and constitutive models described above. In addition, to ensure numerical accuracy, an interpolation method of quadratic velocity and linear pressure are used despite increasing the computational cost and memory requirements when compared with other interpolation methods. An evolutionary scheme is applied on the volumetric flow rate to gradually improve the non-linearity problem of the calculations, since it is not possible to obtain a solution from an initial linear solution by extrapolation [6].

Three mesh patterns with different densities carried out within the Ansys meshing package are shown in Figure 3-2. The arrangement of meshes/grids is that the denser grids are employed near the die exit singularity while larger grids are used in other flow regions. Fig. 3-2 shows the three different meshes, being Mesh 2 and Mesh 3 more refined meshes. More detailed information on the three meshes can be found in Table 3-1. Fig. 3-3a presents the normal stress difference $N_{xy}(\tau_{xx}-\tau_{yy})$ along the top

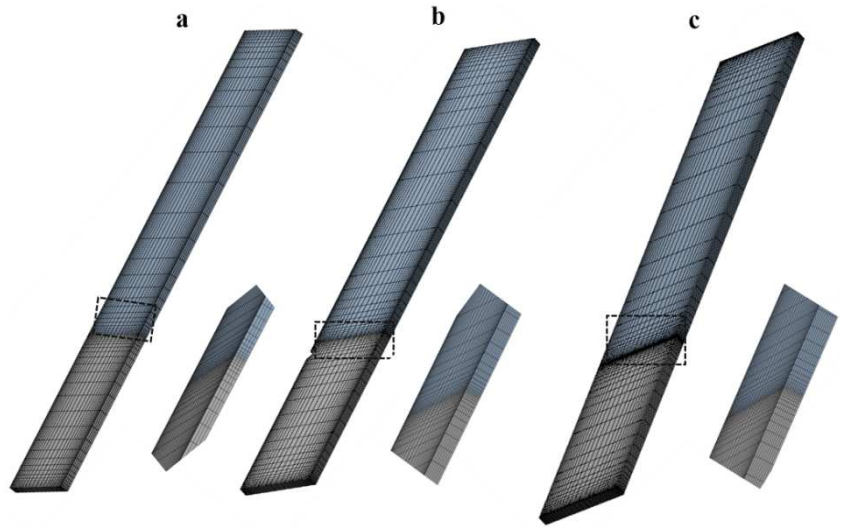


Figure 3-2. Three different meshes with increased refinement levels: (a) Mesh 1, (b) Mesh 2, and (c) Mesh 3.

die wall and the extrudate surface direction at 620 mm^3/s. It is found that refining the mesh pattern does not change the N_{xy} value along the top wall before the flow approaches the die exit. At the die exit, the stress singularity phenomenon is observed. Refining the mesh density around the die exit increases the stress singularity value, which is depicted by Kenuings [42], but does not affect the die swell behavior after the die, as described in Fig. 3-3b. This figure compares the area swell ratio of PP extrudate with different flow rates using material parameters of the PTT model in Table 3-2. It is shown that area swell ratio values predicted by PTT model based on mesh 1 are larger than those based on Mesh 2 and Mesh 3. However, the simulation results based on Mesh 2 and Mesh 3 are almost the same and the differences are < 1% in the flow rate range. Mesh 2 and Mesh 3 have sufficient nodes to capture the velocity and pressure profiles in comparison with Mesh 1 [43]. Therefore, Mesh 2 is selected in the subsequent study considering the computational cost.

Table 3-1. Description of the finite elements meshes used for the current computation.

Mesh	Element	Nodes
1	6032	7965
2	15600	18141
3	22500	25916

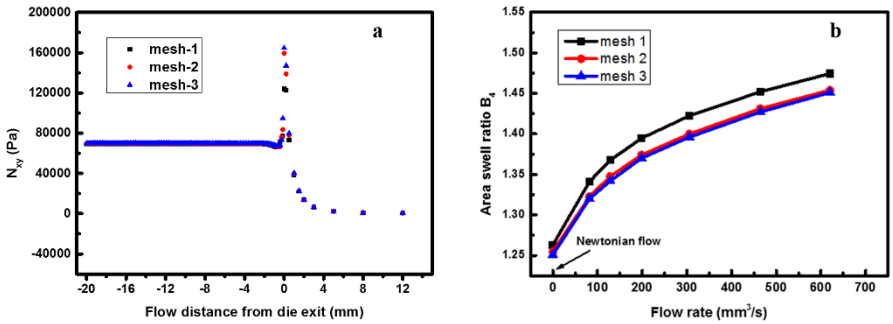


Figure 3-3. (a) the normal stress difference $N_{xy}(\tau_{xx}-\tau_{yy})$ along the top die wall and the extrudate surface direction at 620 mm^3/s; (b) the simulated area swell ratios based on the three meshes for different flow rates. PTT model is used to show that Mesh 2 is sufficient.

3.3. 3D modelling principles

3.3.1. Rheological measurements and parameter tuning for PTT and Cross law model

The commercial Polypropylene (PP 575P) investigated in this study was purchased from the SABIC company in Germany, whose density and melt flow rate were 905 kg/m^3 and 10.5 g/10min (2.16 kg) at 230 ^oC measured according to ISO 1133 method. Measurements in dynamic oscillatory mode and steady shear mode were carried out using a strain-controlled rotational rheometer (ARES, TA Instruments, USA) separately at 200 ^oC. The frequency sweep was conducted in an angular velocity range

of 0.1-500 rad/s and the steady tests were performed within a shear rate range from 0.01-5 s^{-1}. The disk samples with a diameter of 25 mm and a thickness of 1 mm were prepared using a standard compression processing.

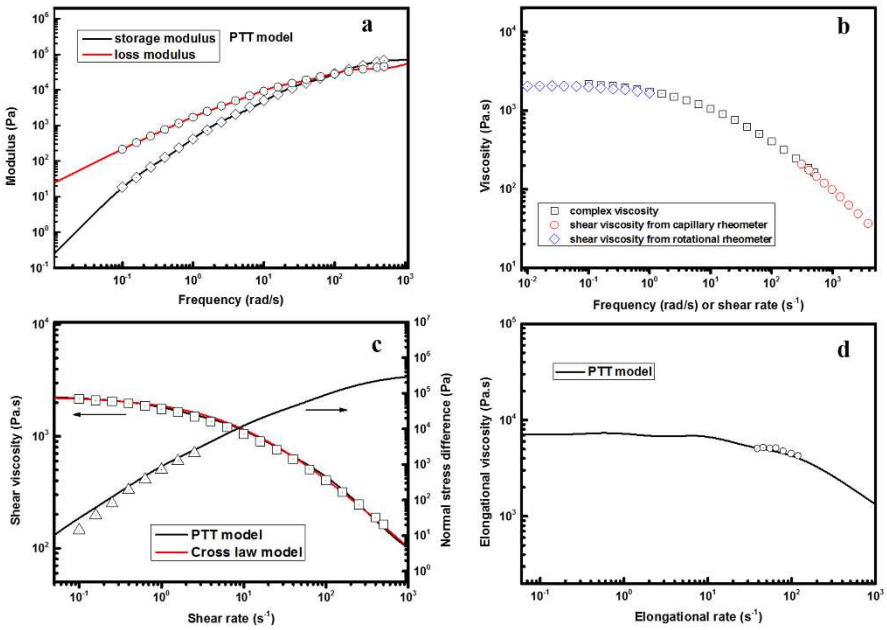


Figure 3-4. (a) the experimentally recorded linear viscoelastic properties of PP melt; (b) a comparison between the measured complex viscosity and shear viscosity; (c) shear viscosity and normal stress difference; (d) elongational viscosity; the symbols represent the experimental data and the lines additionally describe the tuning results with the Cross law and PTT model (material parameters in Table 3-2).

The fitting of the linear viscoelastic data with the PTT model with a 4-mode relaxation time spectrum is presented in Figure 3-4. The parameters η_i and λ_i are shown in Table 3-2. The non-linear parameters of the PTT model can be obtained by fitting the shear viscosity and normal stress difference data. Cox-Merz rule states a formula relating shear viscosity $\eta(\dot{\gamma})$ and complex viscosity $\eta^*(\omega)$ [44], which is often used to obtain shear viscosity in a wide shear rate range. Several previous reports have

proved that Cox-Merz rule is valid in terms of linear neat PP melt [45-47]. In Figure 3-4(b), the shear viscosity from a rotational rheometer in the low shear rate range and from a capillary rheometer Rosand RH7 (Malvern Instruments Ltd., UK) in the high shear rate range are compared with the complex viscosity, and it agrees well to this Cox-Merz rule:

$$\eta(\dot{\gamma}) = \eta^*(\omega) \mid \dot{\gamma} = \omega \qquad (3\text{-}10)$$

In addition, the entrance pressure drops measured by the capillary rheometer are used to calculate the elongational viscosities with the Cogswell method [48, 49]. In Fig. 3-4(c) and (d), by tunning the experimental results, the non-linear parameters ϵ_i and ξ_i of PTT model are extracted and shown in Table 3-2. It is important to note that to obtain these parameters it is assumed no strain-hardening behavior at low elongational rates and strain-thinning behavior at high elongational rates, as observed in Fig. 3-4(d). This seems to be a reasonable assumption considering the trends reported in the literature for general linear polymer melts [19, 29]. The material parameters for the Cross law model are also represented in Table 3-2. The parameters are comparable to literature data [50].

Neat PP flow was extruded from a single screw extruder (P. Brabender 19 with a diameter of 19 mm, L/D of 25) with a slit die (length: 160 mm, height: 2 mm, and width: 20 mm) at a processing temperature of 200 °C to investigate the flow behavior in and out of the die. A volumetric flow rate range of 196–869 mm^3/s was chosen to investigate the effect of flow rate on the flow behavior. The pressures were measured by two pressure sensors mounted at the positions 140 mm (P1) and 40 mm (P2) upstream from the exit separately.

Table 3-2. Materials parameters for PTT model and cross law model at 200 °C.

PTT model									
Materials	Mode	λ_i (s)		η_i (pa.s)		ε_i		ξ_i	
	1	λ_1	0.01	η_1	536	ε_1	0.17	ξ_1	0.16
	2	λ_2	0.1	η_2	816	ε_2	0.18	ξ_2	0.2
Neat PP	3	λ_3	1	η_3	707	ε_3	0.27	ξ_3	0.2
	4	λ_4	10	η_4	220	ε_4	0.4	ξ_4	0.3
Cross law									
		η_0		λ	m				
		2248.3		0.096	0.67				

The extrudate swell measurements were conducted using two HD cameras (LOGITECH Webcam Brio 4K) connected with the computers, so that a real -time measurement came true. First, we needed to fix each camera as close as possible to the die lip, then the glass rule reference was used to set a reference scale for the lateral (width) direction and transversal (height) direction of the slit die, respectively. The evolutions of the dimensions of the extrudate in height and width direction are analysed using the known reference tip. The schematic for the swell measurement is shown in Fig. 3-5a–c. The 2D schematic diagram of the cross section of the die is shown in Fig. 5d. Swelling ratio (*B*) is defined as the ratio between the dimension of extrudate and die exit. To investigate the swelling anisotropy of the extrudate, we defined several swelling ratios, B_1, B_2, and B_3, which denote the swelling in the width, the edge height, and the middle height of the extrudate:

$$B_1 = \frac{\mathrm{w-extrudate}}{\mathrm{w_{-die}}},\ B_2 = \frac{\mathrm{H_1-extrudate}}{\mathrm{H_{1-die}}} \text{ and } B_3 = \frac{\mathrm{H_2-extrudate}}{\mathrm{H_{2-die}}} \quad (3\text{-}11)$$

In addition, the area swelling ratio (*S*) of the extrudate cross section B_4 is defined as:

$$B_4 = \frac{S_{-extrudate}}{S_{-die}} \qquad (3\text{-}12)$$

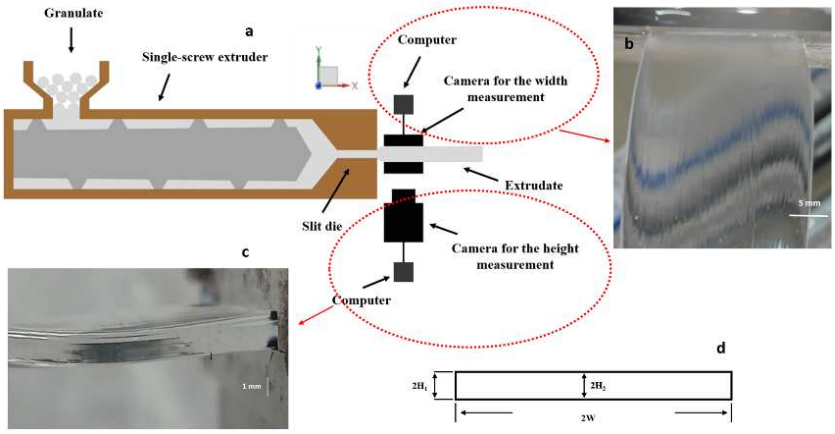


Figure 3-5. (a) schematic of experimental setup to measure die swell; (b) the extrudate profile from bottom view; (c) the extrudate profile from side view; and (d) the cross section of the slit die. Based on these measurements: Eqs. (3-11) and (3-12) are obtained.

3.4. Results and discussion

3.4.1. Pressure and profiles

Figure 3-6 compares the pressure values from experiment measurement and numerical prediction by the PTT and Cross law model. It is shown in Fig. 3-6(a) that pressure values increase with the flow rate, as expected. Both PTT model and Cross law model can be used to predict very well the pressure values in two different positions in the slit die channel. Fig. 3-6(b) displays the simulated pressure profiles of the centerline flow as a function of x-position at a flow rate of 620 mm^3/s. In the slit die, there is very small difference in the two pressure profiles. This indicates that shear viscosity is predominantly responsible for the hydrodynamic pressure, and the viscoelastic constitutive model is not necessary considering its high computational

cost, at least for this process characteristic [51]. When the flow leaves the die, the exit pressure value of PTT flow is however slightly higher than that of Cross law flow. This can be ascribed to the elastic properties captured by the PTT model. The deviation in pressure profiles after the die exit indicates significant different extrudate behavior for two types of flows, which will be highlighted in the next subsection.

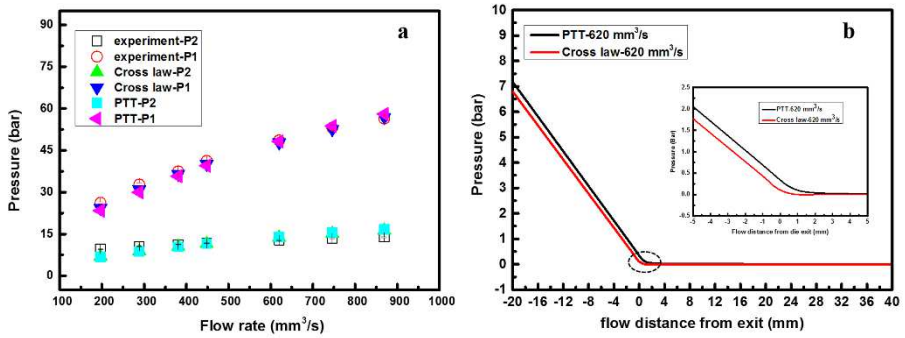


Figure 3-6. (a) A comparison between the pressure values from experiment and predictions by PTT and Cross law model at different flow rates (P1 and P2 denote the pressure value at 140 mm and 40 mm upstream from the exit, respectively); (b) the pressure profile along the centerline flow by PTT model and cross law model at 620 mm^3/s; both models are representative although the PTT model highlights a slightly higher pressure at the die exit.

3.4.2. Anisotropic extrudate swell

As for the extrudate swell behavior for a polymer melt, a typical character is that the extrudate continuously evolves from the die exit. Fig. 3-7(a) represents the experimental evolution of the extrudate width profile at different flow rates. It is shown that the width swell ratio firstly increases quickly until the distance of 10 mm after the die exit, then it increases slowly with a further distance to a constant value. It is presented that the agreement between predictions from the PTT model and the

experiment is good, in contrast, it is shown that Cross law model underestimates significantly the swelling ratio, and the difference increases with flow rate, which is opposite to what really happens to the extrusion of viscoelastic melts. Fig. 3-7(b) displays the experimental evolution of the edge height profiles of the extrudate melt along the flow direction. In contrast with the swell behavior in the width direction, the edge height decreases instead. The cross law model over-predicts the decreasing behavior. We attribute this to the velocity redistribution behavior of the flow after die exit as confirmed below [5]. The PTT model takes into consideration the elastic properties of PP melts, which compensates that decrease.

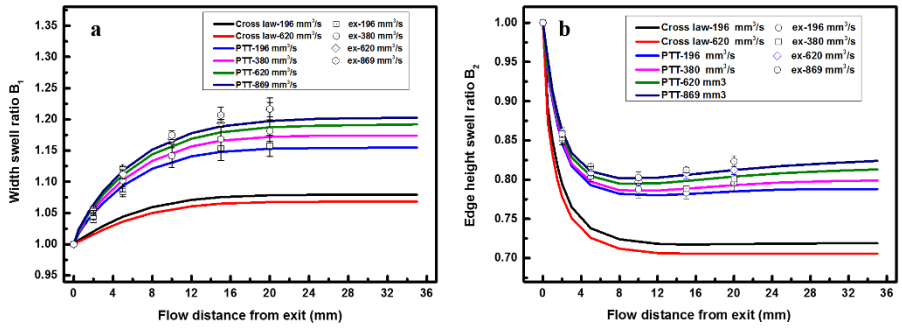


Figure 3-7. Extrudate profile for B_1 (a) and B_2 (b) with the axial distance from the die exit at different flow rates (Eq. (3-10)); the curves represent simulation results while the symbols correspond to experimental data at distances of 2, 5, 10, 15, and 20 mm from the die exit, respectively; only the PTT model is representative.

A representative evolution of the extrudate cross section profiles for PTT flow and Cross law flow after the die exit with a flow rate of 196 mm^3/s gives a direct insight into the variation of extrudate shape in Fig. 3-8(a) and (b). Different from the evolution behavior of the extrudate width profile in Fig. 3-7(a), it is of interest to find that the middle height of the extrudate predicted by both Cross law and PTT model

seems not monotonously to increase with flow distance. For example, for the PTT model, in Fig. 3-8(c), at around 5 mm away from the exit, the extrudate middle height increases to the maximum value. Then with further distance, it starts decreasing more or less until a constant value. In Fig. 3-8(c), an increase of the flow rate of PTT flow seems to make the ripple extrudate swell ratio B_3 profile more smooth. For Cross law flow, the similar phenomenon is observed. In addition, it is easy to note that for both types of theoretical calculations, the swell behavior in the extrudate width direction appears slower than that in the height direction at a given flow rate.

Generally, the area swell ratio of the extrudate cross section is another factor which is thought as a comprehensive evaluation of the swelling behavior. Fig. 3-9(a) compares the evolution of area swell ratio as a function of flow distance at different flow rates. It depicts that at low flow rates, the smallest difference of area swell ratio between PPT and Cross law flow is observed. Increasing the flow rate makes a larger growing rate of area swell ratio B_4 for PTT flow, while it results in a further final equilibrium swell position where B_4 value begins to be constant. This variation trend is in quantitative agreement with a previous report [34]. In order to further explore the dependence of the extrudate swell on the axial distance from die exit, here we define an accomplishing swell ratio:

$$C_r = \frac{S_{ar} - 1}{S_{ar-f} - 1} \qquad (3\text{-}13)$$

S_{ar} means the area swell ratio at a certain distance after the die exit and Sar−f means the area swell ratio at the final equilibrium position for all flows. As shown in Fig. 3-9(b), just after the die exit (before the distance of 5 mm), the C_r values for both PTT

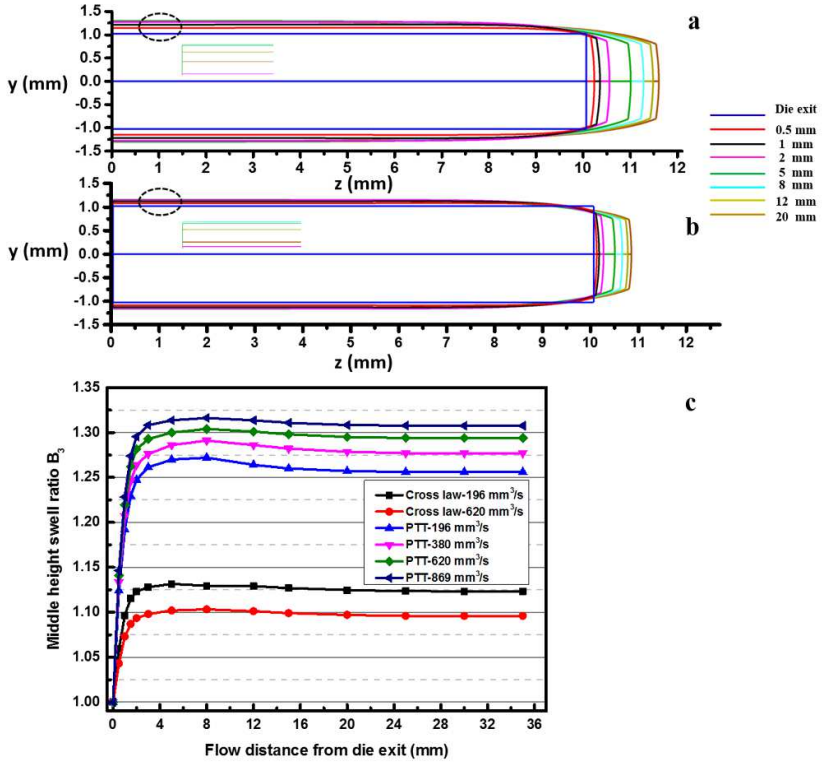


Figure 3-8. (a) the theoretical evolution of the cross section of extrudate along the distance from die exit at a flow rate of 196 mm^3/s for PTT flow and (b) Cross law flow; (c) the middle height swelling ratio B_3 (Eq. (3-10)) of extrudate by PTT and Cross law model with different flow rates.

and Cross law flow decrease with the flow rate at a same distance, which might be mainly attributed to the larger average axial velocity of extrudate with larger flow rate. Within a same flow rate, although Cross law flow has a larger average extrudate axial velocity from die exit in comparison with PTT flow (shown in Fig. 3-10 below), PTT flow has a smaller C_r value in contrast, due to the larger stress relaxation time for PTT flow. Therefore, it is expected that PTT flow with the largest flow rate shows the smallest C_r value among all the flows at the same flow distance from the die exit. Within further flow distance, all extrudates accomplish swelling behavior gradually.

In fact, it is found that at a distance of 10 mm, except PTT flow with 620 mm^3/s, the swell behavior has been completed at least 90% for all flows.

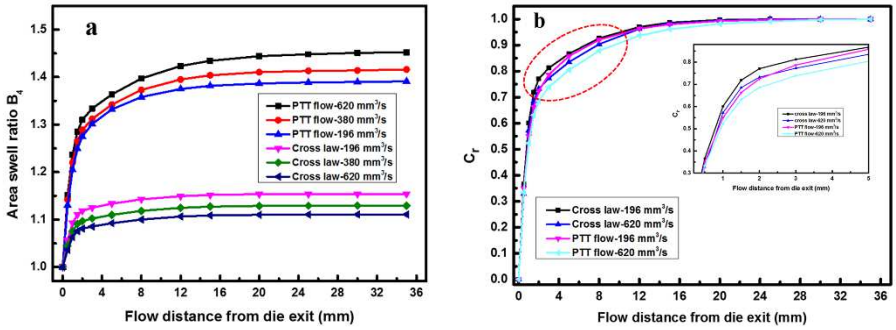


Figure 3-9. (a) the theoretical evolution of the swelling of the area size of extrudate cross section along the axial distance from the die exit; (b) the accomplishing swell ratio (C_r; Eq. (3-12)) of extrudate area with different flow rates.

S_{ar} means the area swell ratio at a certain distance after the die exit and Sar−f means the area swell ratio at the final equilibrium position for all flows. As shown in Fig. 3-9(b), just after the die exit (before the distance of 5 mm), the C_r values for both PTT and Cross law flow decrease with the flow rate at a same distance, which might be mainly attributed to the larger average axial velocity of extrudate with larger flow rate. Within a same flow rate, although Cross law flow has a larger average extrudate axial velocity from die exit in comparison with PTT flow (shown in Fig. 3-10 below), PTT flow has a smaller C_r value in contrast, due to the larger stress relaxation time for PTT flow. Therefore, it is expected that PTT flow with the largest flow rate shows the smallest C_r value among all the flows at the same flow distance from the die exit. Within further flow distance, all extrudates accomplish swelling behavior gradually. In fact, it is found that at a distance of 10 mm, except PTT flow with 620 mm^3/s, the swell behavior has been completed at least 90% for all flows.

3.4.3. Non-uniformity in v_x distributions

Generally, velocity distribution and normal stress are considered as two important factors to influence the swell behavior [37, 52-54]. It is of great interest to investigate the distribution of axial velocity v_x along the flow direction (x direction), transversal direction (y direction) and lateral direction (z direction). Fig. 3-10(a) shows the centerline velocity profile along the axial direction (v_x) for flows with different flow rates. For normalizing the axial velocity, all velocities are divided by the corresponding global mean velocity at the same flow rate. As it is shown, the v_x value keeps constant until the flow is close to the die exit. In Fig. 3-10(b), it is found that the v_x rearrangement starts occurring at a distance upstream the die exit. Near the die exit, the PTT flow shows a sudden small increase in v_x in comparison with Cross law flow. A similar result was reported by Yarusso [55], who attributed this behavior to the normal stress effect of polymer flow. Although there is a little difference between the v_x profile for PTT flow and Cross law flow inside the die, a significant variation is noticed in the downstream die exit. The v_x value of the balanced PTT flow is lower than that of the Cross law flow provided a same flow rate and the difference increases with increasing flow rate. This is likely due to the significantly different swell behavior for the two types of flows. A larger amount of swell behavior leads to a lower final v_x value. Tian *et al*. [5] pointed out that velocity rearrangement and elastic recovery leading to die swell behavior take place simultaneously. This means that increasing the elastic properties of flows increases the velocity rearrangement degree to some extent after the die exit, while increasing the viscous properties has an opposite effect.

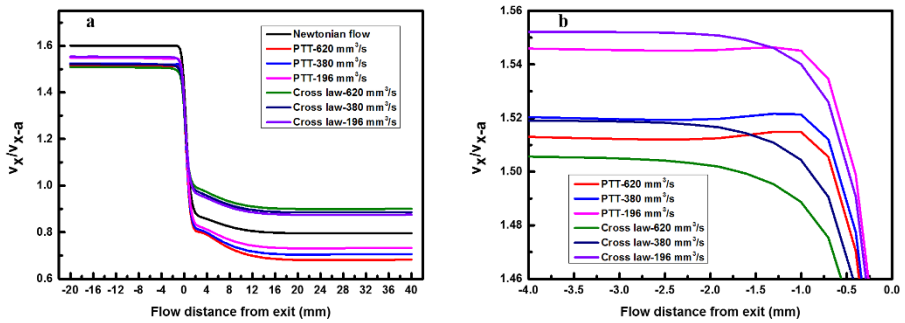


Figure 3-10. The centerline distribution of v_x along the flow direction x for the Newtonian, PTT and Cross law flow at different flow rates; normalization with respect the global mean velocity at the same flow rate. (b) is the inset of (a).

Fig. 3-11 compares the v_x distribution of PTT and Cross law flow along y and z direction separately with various flow rates at the die exit and a distance of 10 mm from the die exit where the flow is considered as fully developed. For a better comparison, the y and z axes are scaled by its corresponding dimension of the flow cell. In Fig. 3-11(a), (b), and (c), it appears that the v_x profiles of PTT and Cross law flow at the fully developed region almost do not display any difference along both height and width direction. When the flow approaches the die exit, with increasing flow rate, the deviation of the velocity profiles between both flows starts occurring because non-linear rheological behavior of viscoelastic flow imposes additional influence on the flow field, especially at a higher flow rate [31]. It is noted that the v_x profile along the z direction keeps constant until $z/2W$ reaches to 0.35, which is much flatter than the velocity profile along the y direction. Therefore, for Cross law flow a larger height swell ratio B_3 is obtained compared with width swell ratio B_1 at a same flow rate in Figs. 3-7 and 3-8. Compared to Newtonian flow, the velocity profiles of both types of flows at the fully developed flow region are blunted in Fig. 3-11(d), and the deviation increases when the flow rate grows. With increasing flow rate, the fully

developed flow is closer to a flow with a uniform velocity profile which requires less velocity rearrangement, therefore the swell ratios decrease for Cross law flow in Fig. 3-9. It implies that the contribution of viscous axial velocity rearrangement to the final swelling of polymer melt decreases with flow rate.

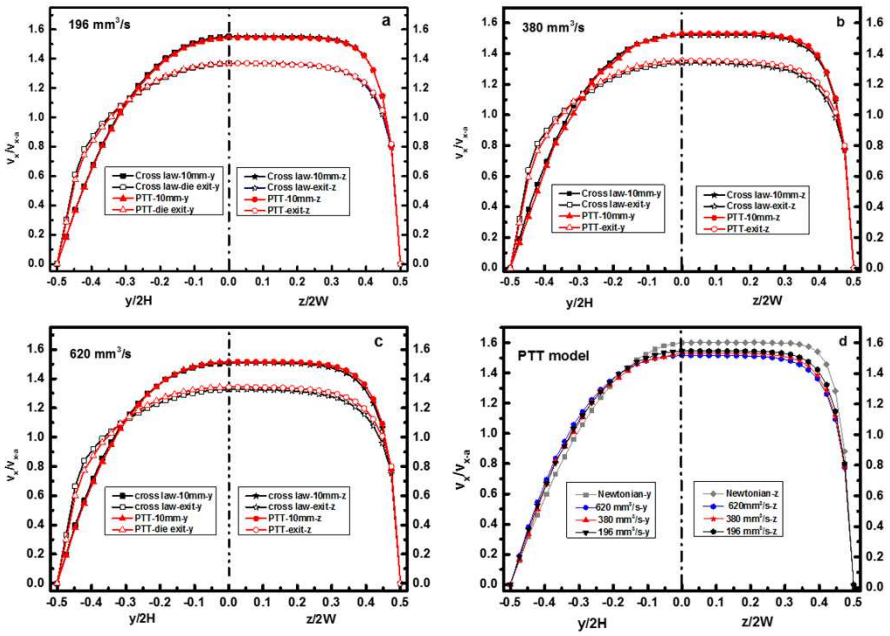


Figure 3-11. (a) axial velocity profile of PTT flow and Cross law flow separately along the height (left side) and the width (right side) at x= −10 mm (solid symbols) and x=0 (open symbols) at flow rate of 196 mm^3/s, (b) 380 mm^3/s, and (c) 620 mm^3/s; (d) a comparison of axial velocity profile of PTT flow with various flow rates along the height at x= −10 mm.

A representative comparison about the evolution of v_x for Cross law and PTT flow separately at different cross sections before and after the die exit is displayed in Fig. 3-12. It is shown that the v_x rearrangement takes place more slowly for PTT flow than Cross law flow, and greater velocity reduces for the former, which is depicted by Yarusso [55]. For example, when the flow approaches to the distance of 1 mm after

die exit, v_x along the y direction almost becomes constant in the whole cross section for Cross law flow, while obvious difference in v_x for PTT flow can be noted, which is attributed to the elastic properties of PTT flow. In addition, for PTT flow, when the distance reaches 2 mm, there is a maximum velocity in the flow layer near the free surface instead of the centerline layer in y direction, which seems not to be observed in Cross law flow. This results in a damping effect on the swelling behavior in that direction. Furthermore, along the y direction, the v_x arrange-ment is faster than that in the z direction, which leads to the inhomogeneous swelling behavior in both directions. Therefore, the slower v_x rearrangement behavior along the z direction determines the final equilibrium position, although v_x profile along the z direction is much flatter than that in the y direction. Clearly, the side wall effect cannot be neglected under an assumption of no slip in this study.

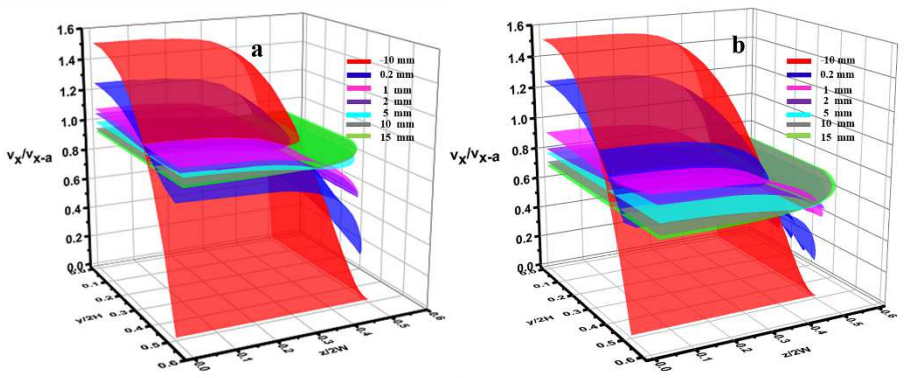


Fig. 3-12. (a) the evolution of the distribution of v_x for Cross law flow and (b) PTT flow at different cross sections before and after the die exit at 620 mm^3/s.

3.4.4. Non-uniformity in stress distributions

When polymer fluid flows in the channel, it experiences large shear and extentional deformations. The calculated fully developed stresses by PTT model (shear stress

component τ_{xy}, τ_{xz} and normal stress τ_{xx}, τ_{yy} and τ_{zz}) at one cross section of the flow channel with the flow rate of 620 mm^3/s are shown in Fig. 3-13. It exhibits that both confining walls have an influence on the stress field. τ_{xy} is typical linear as a function of the height of slit die. Along the z direction, when approaching the side wall, a sharp decrease of τ_{xy} is noted. Nonzero value of τ_{xz} is observed along the width direction due to the nonzero velocity gradient, which is thought to be zero in 2D simulation. The maximum value of τ_{xz} is smaller than that of τ_{xy} due to the lower velocity gradient on the side wall in comparison with that on the top wall (see Fig. 3-11). As for the normal stress components, nonzero value of τ_{xx} is noticed along z direction because of the shear rate perpendicular to *xy*-plane [56]. In contrast with τ_{xx}, the values of τ_{yy} and stress τ_{zz} of the flow in the vicinity of top die wall and side wall are negative separately. That can be attributed to the confining effect of the die walls, leading to compression flow there. In addition, it should be pointed out that the numerical value of τ_{xx} is at least one order of magnitude larger than τ_{yy} and τ_{zz} on the die wall, indicating τ_{xx} plays a dominant role in determining the elastic properties of polymer melt. The existence of τ_{xx} on the side wall with the same magnitude comparable to τ_{xx} on the top wall might imply the necessity of the consideration of side wall effect for the comprehensive understanding of extrudate behavior outside die.

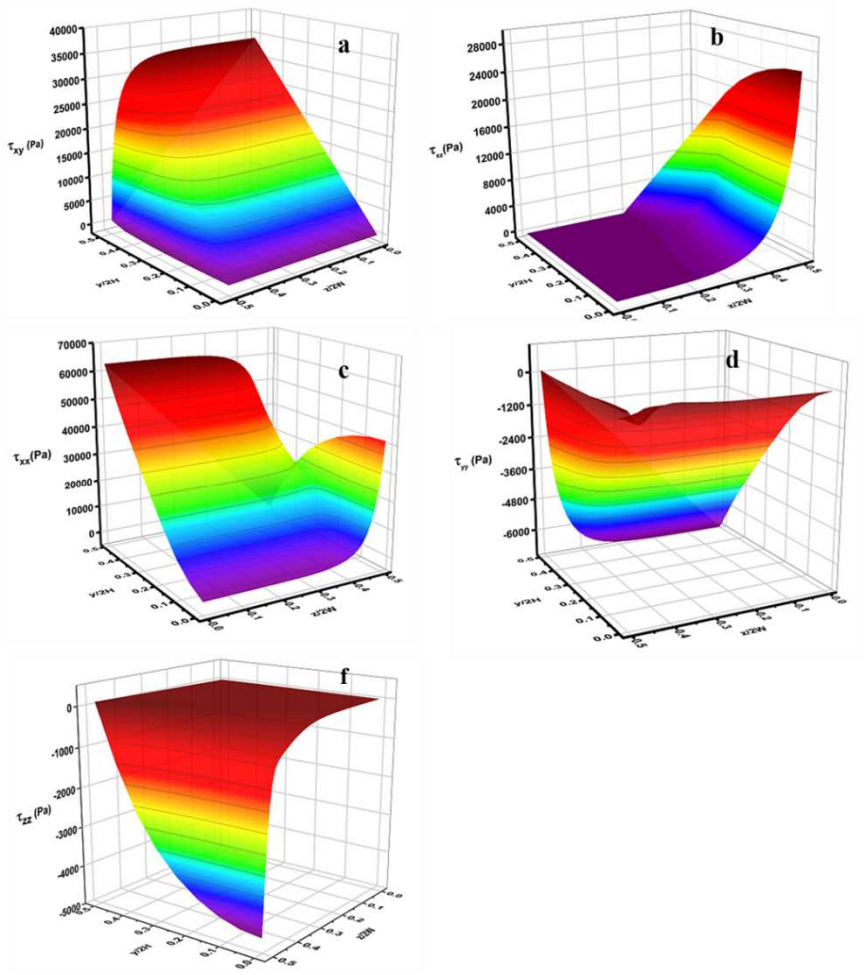


Figure 3-13. Stress component τ_{xy}, τ_{xz}, τ_{xx}, τ_{yy} and τ_{zz} distribution at the cross section of the fully developed flow at 620 mm^3/s.

Comminal *et al.* [52] pointed out the complex relaxation behavior of normal stress leads to extrudate swell. Figure 3-14 shows the τ_{xx} distribution contours of the extrudate cross sections at different distances from die exit by PTT model at 620 mm^3/s. It shows that when the flow leaves die exit, τ_{xx} relaxes quickly in both y and z directions. Just after die exit, in the center of the flow, negative τ_{xx} values are observed. That coincides to the simulation result of Comminal et al. [52]. Liang et al.

[57] thought the equilibrium conformations of macromolecular chains might be disturbed due to the applied shear and extension from the flow field. From a viewpoint of microscopic polymer chain, extrudate swell is a result of the behavior of polymer chains, recoiling along flow direction but growing in radical and lateral directions as flow leaves die exit. Negative τ_{xx} in flow after die exit is mainly resulted from the recoil behavior of the deformed flow macromolecules chains [57].

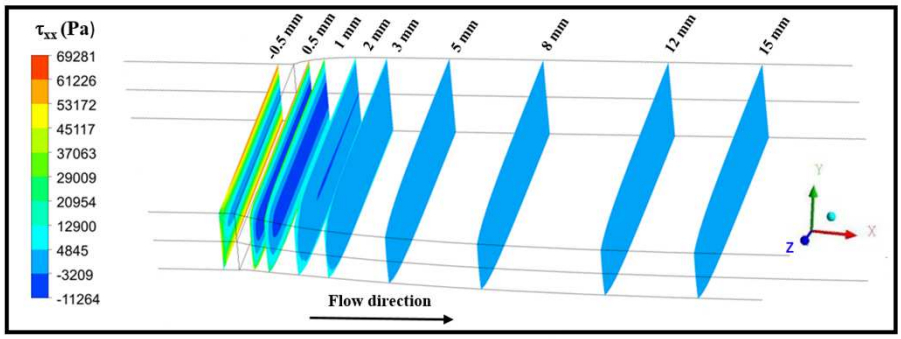


Figure 3-14. τ_{xx} distribution at the cross sections of flow at several distances from die exit at 620 mm^3/s. Results for PTT model.

In principle, the normal stress effect causing extrudate swell of PTT flow is characterized by normal stress difference [57]. Therefore, a comparison between the normal stress difference $N_{xy}(\tau_{xx} - \tau_{yy})$ and $N_{xz}(\tau_{xx} - \tau_{zz})$ profiles along the top die wall and free surface layer direction in middle plane z=0, and the side die wall and free surface layer direction in middle plane y=0 is shown in Figure 3-15a. Obviously, an increase in the flow rate leads to a significant increase in normal stress difference value, resulting in higher swell ratios. N_{xy} along the top die wall is significantly larger than N_{xz} along the side wall at a given flow rate. Hence, a larger swell ratio B_3 is obtained compared to B_2 in the discussion above. The relaxation of both N_{xy} and N_{xz} occurring closer to the die exit for low flow rate further explains the general trend for

swell behavior [34]. The progressively relaxation behavior of normal stress difference along top free surface layer and side free surface layer of extrudate separately is presented in Fig. 3-15b. It depicts when the extrudate approaches a distance of 3 mm from die exit, N_{xz} value in lateral free surface layer becomes larger in contrast. That means the relaxation rate of N_{xz} along lateral side free surface direction is slower than N_{xy} along top free surface layer even to further distance. We attribute it to the difference of stress distribution of the fully developed flow in two directions as shown in Fig. 3-13. Larger shear stress results in a larger deformation of polymer macromolecules, and part of the deformation energy is stored in polymer molecules. When flow leaves die exit, the deformed polymer molecules tend to re-equilibrium the internal energy in a form of elastic recovery by recoiling [58]. To achieve stress equilibrium state, the macromolecular chains with larger deformations tend to coil a bit faster, which causes a higher normal stress difference relaxation rate correspondingly. Considering the normal stress difference can be thought as the 'driving force' to cause extrudate swell, as a result, the swelling behavior in width direction seems to delay a little in comparison with that in height direction.

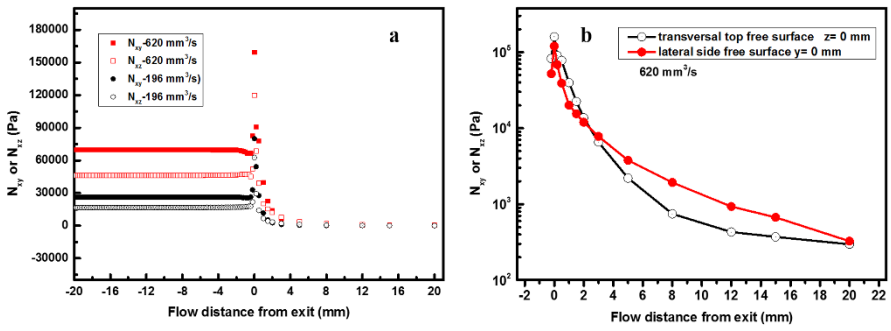


Figure 3-15 (a) comparison of normal stress difference N_{xy} along the radial top wall and the top free surface layer (solid symbols), and N_{xz} along the side wall and the lateral free surface

layer (open symbols) at 620 mm^3/s and 196.4 mm^3/s; (b) close view of the relaxation behavior of normal stress difference N_{xy} along the radial top free surface (middle plane (z=0), solid symbols), and N_{xz} along the lateral side free surface layer (middle plane (y=0), open symbols) after die exit at 620 mm^3/s.

3.4.5. Non-uniformity for radial velocity (v_y) and lateral velocity (v_z)

A comparison between distribution contours of the velocity component v_y in the center-plane z=0 mm, and velocity component v_z in the center-plane y=0 mm of PTT flow at 620 mm^3/s is carried out in Fig. 3-16. It is depicted that when the flow is in the die channel, both vanishing v_y and v_z components exist. Emerging from the die exit, they show different variation trends. Fig. 3-17 represents the evolutions of v_z and v_y in the side free surface layer and the top free surface layer separately. It is seen that v_z increases quickly, then it decreases to a small value gradually. While for v_y a much faster decreasing rate follows the initial significant increase after die exit. This can be attributed to the faster relaxation rate of normal stress difference and the rearrangement rate of axial velocity v_x from the approximated Poiseuille to a plug flow in extrudate transversal direction (y) as discussed above. In addition, it displays that if v_y decreases to zero, v_z still keeps positive. In order to match material balance (the mass conservation), the transversal flow might be in the reverse direction (negative v_y). Reconsidering to Fig. 3-8, therefore it is not difficult to understand why the middle height of the extrudate increases quickly to the maximum value at the beginning, then it decreases more or less. This indicates that the final equilibrium swelling position is determined by the swell behavior in the width direction to some extent although the swell ratio value is smaller than that in the height direction. Clearly, it confirms that

fully taking into consideration the side wall effect is necessary for a better understanding for the swelling behavior of flows through a rectangular flow channel.

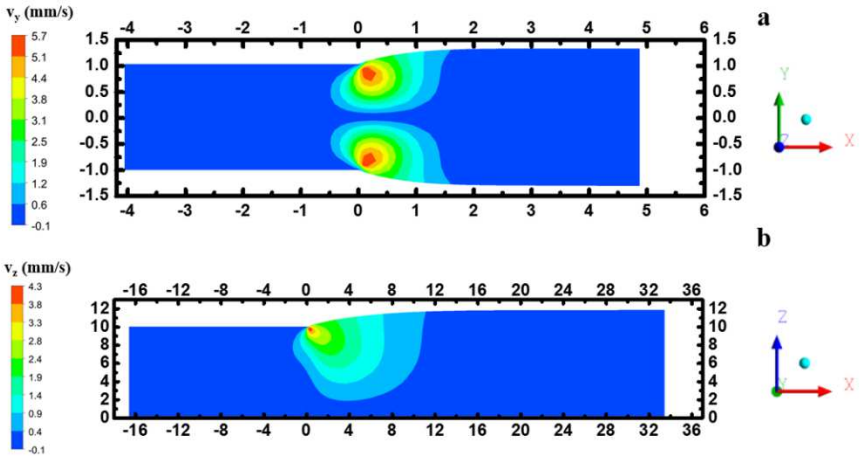


Figure 3-16. Distribution of (a) v_z in the $x-y$ plane (z=0), and (b) v_y in the $x-z$ plane (y=0). PTT model at a flow rate of 620 mm^3/s.

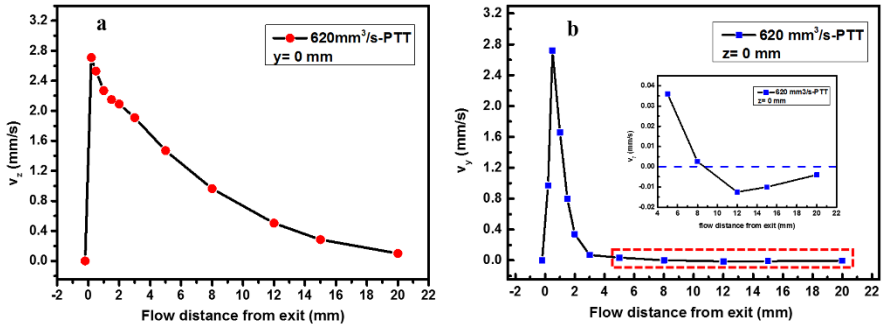


Figure 3-17. (a) v_z and (b) v_y on the free surface side layer and top layer separately along the flow distance from the die exit. Obtained from Figure 3-16.

3.5. Conclusions

In this study, the isothermal flow of neat PP at 200 °C through a slit die and upon subsequent swelling is investigated by extrusion experiments and 3D numerical

simulations. Two types of constitutive models are employed to perform the numerical simulations, namely the generalized Newtonian constitutive model with the Cross law viscosity function and the viscoelastic multi-mode PTT model. The pressure profiles predicted by both models inside the die agree well with experimental data obtained for all flow rates evaluated. The slightly larger exit pressure predicted by the PTT model compared to that of Cross law model causes different extrudate swell behavior, which is successfully compared to experimental results for extrudate swell through real-time measurements. This comparison indicates that the PTT model is able to capture the complex swell behavior observed, while the Cross law model highly under-predicts that.

The swell behavior in both height and width directions depend on the distance from the die exit and both swell ratios increase with the flow rate, which is not captured by simulation results obtained with the Cross law model. In addition, obvious different swell behavior in the height and the width direction of extrudate is noted. The swell ratio in the width direction increases in a much lower rate than the swell ratio in the height direction until equilibrium is achieved in both directions. Therefore, the distance from the die exit in which the final extrudate shape is obtained strongly depends on the die width, which is not captured by the more conventional 2D simulations.

The mechanism for the previous phenomenon is investigated regarding the velocity field and stress field distributions. It is indicated that different flow rearrangement behavior including the axial velocity redistribution behavior and the normal stress difference relaxation behavior in the corresponding direction of the extrudate outside the die simultaneously are responsible for that phenomenon.

Overall, the present work demonstrates that a detailed 3D simulation is necessary for a comprehensive understanding of the complicated extrudate swell behavior from a slit die for the die optimization design and that reliable rheological data are indispensable to be fed to such as simulation tool.

REFERENCE

1. Breitenbach, J., *Melt extrusion: from process to drug delivery technology.* European journal of pharmaceutics and biopharmaceutics, 2002. **54**(2): p. 107-117.
2. Sauceau, M., et al., *New challenges in polymer foaming: A review of extrusion processes assisted by supercritical carbon dioxide.* Progress in Polymer Science, 2011. **36**(6): p. 749-766.
3. Wieme, T., et al., *The relevance of material and processing parameters on the thermal conductivity of thermoplastic composites.* Polymer Engineering & Science, 2018. **58**(4): p. 466-474.
4. Gifford, W., *Compensating for die swell in the design of profile dies.* Polymer Engineering & Science, 2003. **43**(10): p. 1657-1665.
5. Tian, H., et al., *Study on extrudate swell of polypropylene in double-lumen micro profile extrusion.* Journal of Materials Processing Technology, 2015. **225**: p. 357-368.
6. García-Rejón, A., R. DiRaddo, and M. Ryan, *Effect of die geometry and flow characteristics on viscoelastic annular swell.* Journal of non-newtonian fluid mechanics, 1995. **60**(2-3): p. 107-128.
7. Srivastva, D. and A. Nikoubashman, *Flow Behavior of Chain and Star Polymers and Their Mixtures.* Polymers, 2018. **10**(6): p. 599.
8. Hertel, D., R. Valette, and H. Münstedt, *Three-dimensional entrance flow of a low-density polyethylene (LDPE) and a linear low-density polyethylene (LLDPE) into a slit die.* Journal of Non-Newtonian Fluid Mechanics, 2008. **153**(2-3): p. 82-94.
9. Vergnes, B. and J. Agassant, *Die flow computations: A method to solve industrial problems in polymer processing.* Advances in Polymer Technology, 1986. **6**(4): p. 441-455.
10. Luo, X.-L. and R. Tanner, *A streamline element scheme for solving viscoelastic flow problems. Part I. Differential constitutive equations.* Journal of non-newtonian fluid mechanics, 1986. **21**(2): p. 179-199.
11. Luo, X.-L. and R. Tanner, *A streamline element scheme for solving viscoelastic flowproblems part II: integral constitutive models.* Journal of Non-Newtonian Fluid Mechanics, 1986. **22**(1): p. 61-89.
12. Luo, X.L. and R. Tanner, *Finite element simulation of long and short circular die extrusion experiments using integral models.* International journal for numerical methods in engineering, 1988. **25**(1): p. 9-22.
13. Béraudo, C., et al., *A finite element method for computing the flow of multi-mode viscoelastic fluids: comparison with experiments.* Journal of non-newtonian fluid mechanics, 1998. **75**(1): p. 1-23.
14. Caswell, B. and M. Viriyayuthakorn, *Finite element simulation of die swell for a Maxwell fluid.* Journal of Non-Newtonian Fluid Mechanics, 1983. **12**(1): p. 13-29.
15. Ganvir, V., et al., *Prediction of extrudate swell in polymer melt extrusion using an Arbitrary Lagrangian Eulerian (ALE) based finite element method.* Journal of Non-Newtonian Fluid Mechanics, 2009. **156**(1): p. 21-28.

16. Konaganti, V.K., et al., *Extrudate swell of a high-density polyethylene melt: II. Modeling using integral and differential constitutive equations.* Journal of Non-Newtonian Fluid Mechanics, 2015. **225**: p. 94-105.
17. Konaganti, V.K., et al., *The effect of damping function on extrudate swell.* Journal of Non-Newtonian Fluid Mechanics, 2016. **236**: p. 73-82.
18. Ansari, M., S.G. Hatzikiriakos, and E. Mitsoulis, *Slip effects in HDPE flows.* Journal of Non-Newtonian Fluid Mechanics, 2012. **167**: p. 18-29.
19. Ansari, M., E. Mitsoulis, and S.G. Hatzikiriakos, *Capillary extrusion and swell of a HDPE melt exhibiting slip.* Advances in Polymer Technology, 2013. **32**(S1).
20. Mitsoulis, E. and S. Hatzikiriakos, *Annular extrudate swell of a fluoropolymer melt.* International Polymer Processing, 2012. **27**(5): p. 535-546.
21. Russo, G. and T.N. Phillips, *Spectral element predictions of die-swell for Oldroyd-B fluids.* Computers & Fluids, 2011. **43**(1): p. 107-118.
22. Guénette, R. and M. Fortin, *A new mixed finite element method for computing viscoelastic flows.* Journal of non-newtonian fluid mechanics, 1995. **60**(1): p. 27-52.
23. Azaiez, J., R. Guenette, and A. Ait-Kadi, *Entry flow calculations using multi-mode models.* Journal of non-newtonian fluid mechanics, 1996. **66**(2-3): p. 271-281.
24. Eggen, S. and E.L. Hinrichsen, *Swell and distortions of high-density polyethylene extruded through capillary dies.* Polymer Engineering & Science, 1996. **36**(3): p. 410-424.
25. Barrera, M., et al., *Melt flow index on high molecular weight polyethylene: A comparative study of experiments and simulation.* Journal of materials processing technology, 2006. **174**(1-3): p. 171-177.
26. Ganvir, V., et al. *Numerical and Experimental Studies on Extrudate Swell of Linear and Branched Polyethylenes.* in *AIP Conference Proceedings*. 2008. AIP.
27. Kajiwara, T., et al., *Numerical simulation of extrudate swell problem and evaluation of applicability of viscoelastic constitutive models 1. A study on axisymmetric extrudate swell from a straight die.* Nihon Reoroji Gakkaishi, 2001. **29**(1): p. 47-52.
28. Russo, G. and T.N. Phillips, *Numerical prediction of extrudate swell of branched polymer melts.* Rheologica acta, 2010. **49**(6): p. 657-676.
29. Kiriakidis, D. and E. Mitsoulis, *Viscoelastic simulations of extrudate swell for an HDPE melt through slit and capillary dies.* Advances in Polymer Technology, 1993. **12**(2): p. 107-117.
30. Azaiez, J., R. Guénette, and A. Ait-Kadi, *Numerical simulation of viscoelastic flows through a planar contraction.* Journal of non-newtonian fluid mechanics, 1996. **62**(2-3): p. 253-277.
31. Xue, S.-C., N. Phan-Thien, and R. Tanner, *Three dimensional numerical simulations of viscoelastic flows through planar contractions.* Journal of Non-Newtonian Fluid Mechanics, 1998. **74**(1): p. 195-245.

32. Kajiwara, T., et al., *Numerical simulation of converging flow of polymer melts through a tapered slit die.* Journal of non-newtonian fluid mechanics, 1993. **48**(1-2): p. 111-124.
33. Sirakov, I., et al., *Three-dimensional numerical simulation of viscoelastic contraction flows using the Pom–Pom differential constitutive model.* Journal of non-newtonian fluid mechanics, 2005. **126**(2): p. 163-173.
34. Konaganti, V., et al., *Extrudate swell of high density polyethylenes in slit (flat) dies.* International Polymer Processing, 2016. **31**(2): p. 262-272.
35. Xingming, X., et al., *Numerical simulation of viscoelastic extrudate swell through elliptical ring die.* Chinese Journal of Chemical Engineering, 2011. **19**(1): p. 10-17.
36. Normandin, M., et al., *Three-dimensional extrudate swell experimental and numerical study of a polyethylene melt obeying a memory-integral equation.* Journal of non-newtonian fluid mechanics, 1999. **87**(1): p. 1-25.
37. Mu, Y., G. Zhao, and C. Zhang, *Numerical investigation of die geometry effect on LDPE annular extrudate swell.* Journal of applied polymer science, 2010. **117**(1): p. 91-109.
38. Mu, Y., et al., *Modeling and simulation of three-dimensional planar contraction flow of viscoelastic fluids with PTT, Giesekus and FENE-P constitutive models.* Applied Mathematics and Computation, 2012. **218**(17): p. 8429-8443.
39. Mu, Y., et al., *Finite-Element Simulation of Polymer Flow and Extrudate Swell Through Hollow Profile Extrusion Die with the Multimode Differential Viscoelastic Model.* Advances in Polymer Technology, 2013. **32**(S1).
40. Mu, Y., et al., *Measurement and simulation of low-density polyethylene extrudate swell through a circular die.* Polymer International, 2009. **58**(5): p. 475-483.
41. Agassant, J. and J. Villemaire. *Rheology for polymer processing: an overview of the present knowledge and some open problems*. in *Makromolekulare Chemie. Macromolecular Symposia*. 1988. Wiley Online Library.
42. Keunings, R., *Simulation of viscoelastic fluid flow.* 1987.
43. Aloku, G.O. and X.-F. Yuan, *Numerical simulation of polymer foaming process in extrusion flow.* Chemical Engineering Science, 2010. **65**(12): p. 3749-3761.
44. Gleissle, W. and B. Hochstein, *Validity of the Cox–Merz rule for concentrated suspensions.* Journal of rheology, 2003. **47**(4): p. 897-910.
45. Mobuchon, C., et al., *Shear and extensional properties of short glass fiber reinforced polypropylene.* Polymer composites, 2005. **26**(3): p. 247-264.
46. Li, S., P.K. Järvelä, and P.A. Järvelä, *Melt rheological properties of polypropylene–maleated polypropylene blends. II. Dynamic viscoelastic properties.* Journal of applied polymer science, 1999. **71**(10): p. 1649-1656.
47. Kim, K.J., et al., *Effects of stearic acid coated talc, CaCO3, and mixed talc/CaCO3 particles on the rheological properties of polypropylene compounds.* Journal of applied polymer science, 2004. **93**(5): p. 2105-2113.

48. Hatzikiriakos, S.G., et al., *Rheological characterization of polyethylene terephthalate resins using a multimode Phan-Tien-Tanner constitutive relation.* Rheologica acta, 1997. **36**(5): p. 568-578.
49. Guillet, J., et al., *Experimental and numerical study of entry flow of low-density polyethylene melts.* Rheologica acta, 1996. **35**(5): p. 494-507.
50. Nam, G., J. Yoo, and J. Lee, *Effect of long-chain branches of polypropylene on rheological properties and foam-extrusion performances.* Journal of Applied Polymer Science, 2005. **96**(5): p. 1793-1800.
51. Doerpinghaus, P.J. and D.G. Baird, *Pressure profiles along an abrupt 4: 1 planar contraction.* AIChE journal, 2003. **49**(10): p. 2487-2498.
52. Comminal, R., et al., *Numerical simulation of the planar extrudate swell of pseudoplastic and viscoelastic fluids with the streamfunction and the VOF methods.* Journal of Non-Newtonian Fluid Mechanics, 2018. **252**: p. 1-18.
53. Min, K.H. and C. Kim, *Simulation of particle migration in free-surface flows.* AIChE journal, 2010. **56**(10): p. 2539-2550.
54. Debbaut, B. and T. Marchal, *Numerical simulation of extrusion process and die design for industrial profile, using multimode pom–pom model.* Plastics, rubber and composites, 2008. **37**(2-4): p. 142-150.
55. Yarusso, B.J., *Exit and entrance flows of non-Newtonian fluids in parallel slits.* Journal of non-newtonian fluid mechanics, 1991. **40**(1): p. 103-117.
56. Bogaerds, A.C., et al., *3D viscoelastic analysis of a polymer solution in a complex flow.* Computer methods in applied mechanics and engineering, 1999. **180**(3-4): p. 413-430.
57. Liang, J.-Z., *Melt die-swell behavior of polyoxymethylene blended with ethylene-vinyl acetate copolymer and high-density polyethylene.* Polymer Testing, 2018. **68**: p. 213-218.
58. Rueda, M.M., et al., *Rheology and applications of highly filled polymers: A review of current understanding.* Progress in Polymer Science, 2017. **66**: p. 22-53.

Chapter 4

Three-dimensional simulations for polymer extrudate swell out of slit dies from low to high aspect ratios

The impact of the slit die geometry and the polymer melt flow characteristics on the extrudate swell behavior, which is a key extrusion operating parameter, is highlighted. Three-dimensional (3D) numerical simulations based on the finite element method are compared with their conventional 2D counterparts at the same apparent shear rates using ANSYS Polyflow software. The rheological behavior is described by the differential multi-mode PTT constitutive model, with polypropylene as reference. It is shown that increasing the aspect ratio of the die geometry (width/height ratio variation from 1 to 20) contributes to a significant change of the 3D extrudate deformation (relative changes of 10% in several directions; absolute changes up to 30%) and delays the equilibrium axial position (up to a factor 10). High aspect ratios induce a switch to contract flow (swell ratio < 1) for the edge height swell. The 3D extrudate swell strongly deviates from the 2D simplified case due to the die effect near the wall, even for higher aspect ratios. The initially large swell behavior is followed by a small shrinkage flow in the *middle height direction which cannot be captured by the 2D counterpart. The findings are supported by a comprehensive analysis of the velocity and stress fields in and out of the slit dies.*

4.1. Introduction

Extrusion is a polymer forming operation under melt conditions that is widely applied for industrial applications [1-5]. It is usually observed that the dimensions of the extrudate coming out of the extruder are larger than the dimensions of the extruder orifice. This phenomenon is denominated as extrudate or die swell and is a key process control parameter in view of product stability [6]. Investigating the swell behavior upon flow exit only through experimental methods is not optimal and time consuming [7, 8]. Hence, to obtain additional insights numerical flow simulations are recommended. Such simulations have the advantage of tracking the varying trend of velocity and stress fields for different processing conditions [9-12].

Essential is the choice of the constitutive equation to grasp the viscoelastic properties of the fluids. Early studies were carried out using the basic Maxwell viscoelastic constitutive model [13]. However, this model cannot capture realistic or non-linear viscoelastic properties of polymer fluids, such as shear-thinning and elongation-thinning behavior in the high strain rate region [14]. Some more realistic constitutive models have therefore been proposed, such as the integral Kaye-Bernstein-Kearsley-Zapas (KBKZ) constitutive model [15-19], the differential Phan-Thien-Tanner (PTT) model [20-26] and the Giesekus model [25, 27]. Among them, the integral KBKZ model and the differential PTT model seem suited due to the possibility of describing the shear and elongational properties of polymer melts independently [14, 28-30].

A variety of geometrical characteristics, including the die entrance angle, the length/diameter (or thickness) ratio, the width/thickness ratio, and the out/inner diameter ratio, have already theoretically shown to play an important role in determining the final thus equilibrated extrudate swell behavior [23, 24, 27, 31-33].

For example, Garcia *et al*. [32] systematically studied the effect of the channel geometry and inclination angle on the annular extrudate swell from the diverging, converging and straight annular die, considering the integral constitutive KBKZ model for two-dimensional (2D) isothermal high density polyethylene (HDPE) flow. They concluded that both the thickness and diameter swell are very sensitive to the die geometry. Mu *et al*. [24] simulated in detail the impact of the die geometrical parameters on the 3D annular extrudate swell for isothermal low density polyethylene (LDPE) flow, including the effect of the die contraction angle, the ratio of parallel length to inner radius, and the ratio of outer to inner radius. More recently, Hatzkiriakos *et al.* conducted 2D simulations with varying length/diameter and width/height (or equivalently width/thickness) ratio mainly with the KBKZ model to figure out the relevance of the die geometry [31, 33, 34]. These authors indicated that increasing the length/diameter ratio decreases the extrudate swell in agreement with their experimental results.

It should be realized that in many cases the 3D flow pattern during and after extrusion is simplified into isothermal 2D flow to lower the computational cost and in favor of numerical convergence [26, 33, 35-38]. For example, for planar flow configurations, 2D simulations imply an infinite width/height (W/H) or aspect ratio. However, the aspect ratios of flow channels are in reality finite and thereby a deviation is expected between the experimental observations and 2D simulations, which is referred to as the 3D or edge effect [28, 39-42]. For example, Clemeur *et al.* [40] showed a mismatch with the observed isochromatic birefringence (an optical property which is related to the stress difference of flow) of a polymer solution in slit dies for the simplified isothermal 2D simulations with varying aspect ratio, which enlarged by increasing the flow rate. Schoonen [28, 43] found that decreasing the aspect ratio for polyisobutylene

(PIB) flow in a rectangular flow channel from 8 to 2 resulted in an increase of the discrepancy between isothermal 2D and 3D simulations. For instance, the difference between the simulated first normal stress difference of the PIB solution and that of the 2D one at the same apparent shear rate is only 11% for an aspect ratio of 8 but increases to 30% for an aspect ratio of 2.

Nevertheless, the 3D effect on the polymer extrudate swell behavior is typically not studied, as one focuses mainly on the flow at the end of the extruder equipment. In our recent work [44], we carried out comprehensive isothermal 3D simulations of the extrudate swell behavior of neat polypropylene (PP) flow from a slit die at 200 ^{o}C with fixed dimensions (aspect ratio of 10). We highlighted that the distance from the die exit, within which the final extrudate shape is obtained, strongly depends on the swell behavior in the width direction, indicating that 3D effects must be considered for optimization of the die design. Moreover, the die swell simulations results were experimentally confirmed by 3D imaging, considering experimentally verified PTT input model parameters.

In the present study, we further focus on the dependence of PP extrudate swell behavior on the geometric characteristics, specifically the aspect ratio of the slit die. Consequently, 3D simulations of PP melt with different aspect ratios have been conducted using the PTT model as previously tuned. The computational results are compared to those obtained from the corresponding 2D simulations with the aim at assessing the relevance of the 3D effect. A significant discrepancy of the swell behavior between the two modelling configurations is reported. The corresponding flow velocity and stress fields are further discussed in detail to illustrate the mechanism for this discrepancy. A parametric study regarding the key parameters of

the PTT model is additionally included to clarify the influence of the polymer rheological properties on the 3D effect of the flow channels.

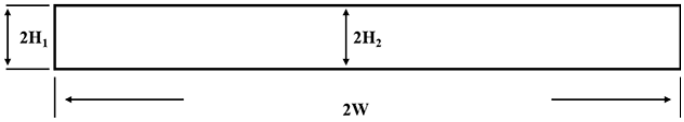


Figure 4-1. The cross section of a slit die (case of an aspect ratio of 10). Four swell ratios can be defined, as mathematically represented by Eq. 4-1 and Eq. 4-2. They relate to swelling for the width direction, the edge height direction, the middle height direction, and the area swelling.

4.2. Modelling principles

4.2.1. Geometric parameters

Figure 4-1 depicts the 2D schematic diagram of the cross section of a slit die with an aspect ratio of 10. Several swell ratios can be defined as the ratios between the dimensions of the extrudate and the die. To identify a possible anisotropic extrudate swell behavior, three such ratios B_1, B_2 and B_3 are needed, denoting the swelling in the extrudate width, edge height and middle height direction (Figure 3-1), respectively [44]:

$$B_1 = \frac{W_{-extrudate}}{W_{-die}},\ B_2 = \frac{H_{1-extrudate}}{H_{1-die}} \text{ and } B_3 = \frac{H_{2-extrudate}}{H_{2-die}} \qquad (4\text{-}1)$$

Additionally, B_4 is defined as the swell ratio of the area size (S) of the extrudate cross section and the slit die:

$$B_4 = \frac{S_{-extrudate}}{S_{-die}} \qquad (4\text{-}2)$$

4.2.2. Governing equations

In this work, we assume that the incompressible polymer fluid is under isothermal, steady and creeping laminar flow conditions without gravity effects, and the applied governing equations include the following continuity and momentum equations in vector notation [44, 45]:

$$\nabla \cdot \mathbf{v} = 0 \qquad (4\text{-}3)$$

$$-\nabla p + \nabla \cdot \boldsymbol{\tau} = 0 \qquad (4\text{-}4)$$

in which ρ is the material density, v the velocity vector, p the hydrostatic pressure, and $\boldsymbol{\tau}$ the extra stress tensor. For the polymer melts, the constitutive model associating the extra stress with the velocity or velocity gradients is essential to solve the set of equations [18].

4.2.2.1. PTT constitutive model

The extra stress tensor, for the viscoelastic constitutive model, $\boldsymbol{\tau}$, is split into a purely viscous part, $\boldsymbol{\tau_N}$, and a viscoelastic part, $\boldsymbol{\tau_p}$. $\boldsymbol{\tau_N}$ is solved by the generalized Newtonian flow model [44], while $\boldsymbol{\tau_p}$ is calculated by the basic viscoelastic constitutive equations in terms of the differential (or integrated) constitutive model. Regarding a time spectrum of *N* relaxation modes, the viscoelastic stress tensor, $\boldsymbol{\tau_p}$, is calculated as a sum of N individual $\boldsymbol{\tau_{pi}}$ contributions, which is expressed as:

$$\boldsymbol{\tau_p} = \sum_{i=1}^{N} \boldsymbol{\tau_{pi}}, \qquad (4\text{-}5)$$

Each individual contribution τ_{pi} is revealed by the PTT constitutive equation, as it shows a good ability to describe the rheological properties of the PP melt including

the shear-thinning behavior and the extensional-thinning in the high strain rate range as demonstrated in our previous work.[44] This PTT model is written as:

$$exp\left[\frac{\varepsilon_i \lambda_i}{\eta_i} tr(\tau_{pi})\right]\tau_{pi} + \lambda_i\left[(1-\frac{\xi_i}{2})\overset{\sim}{\tau_{pi}} + \frac{\xi_i}{2}\overset{\frown}{\tau_{pi}}\right] = 2\eta_i \boldsymbol{D} \quad (4\text{-}6)$$

in which, λ_i and η_i are the relaxation time and shear viscosity, determining the linear rheological properties of melts. The non-linear parameters, ε_i and ξ_i, control the extensional and shear behavior of fluids. $\overset{\sim}{\tau_{pi}}$ and $\overset{\frown}{\tau_{pi}}$ correspond to the upper and lower convected time derivatives of τ_{pi}. $\boldsymbol{D}$ represents the deformation tensor rate, which is defined as:

$$\boldsymbol{D} = \frac{\nabla v + (\nabla v)^T}{2} \quad (4\text{-}7)$$

with ∇v and $(\nabla v)^T$ the velocity gradient and transpose of the velocity gradient.

For the polypropylene in this study the material parameters of the multi-mode PTT constitutive model are extracted from the good fitting of the linear and non-linear rheological properties as described in Figure 3-4 in Chapter 3. The corresponding parameters are shown in Table 3-1 in Chapter 3, which are comparable to a previous report [46].

For illustration purposes, a sensitivity analysis of the non-linear material parameters ξ_3 and ε_3 of the PTT model regarding rheological properties is shown in Figure 4-2. In comparison with the parameter ξ_3, increasing ε_3 not only increases the first normal stress difference $N_{xy}(\tau_{xx}-\tau_{yy})$ but also significantly increases the elongational viscosity. On the other way, ξ_3 mainly has a significant influence on the second normal stress difference $Nyz(\tau_{yy}-\tau_{zz})$ component.

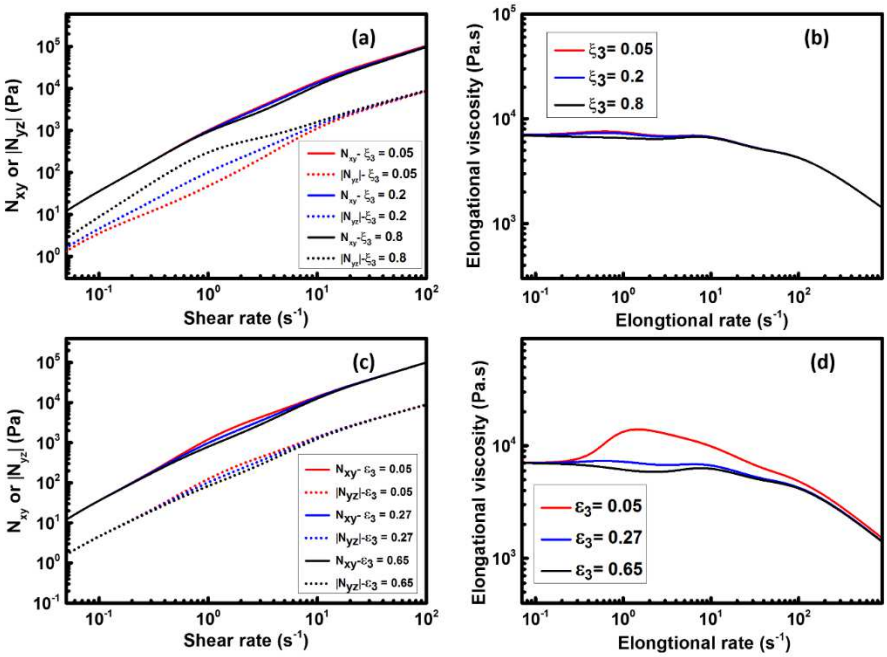


Figure 4-2. Effect of the material parameter ξ_3 ((a)-(b)) and ε_3 ((c)-(d)) on the normal stress difference N_{xy} and $|N_{yz}|$ and the elongational viscosity as functions of shear and elongational rate.

Table 4-1. Material parameters of PP for PTT model at 200 °C from Chapter 3. In Fig. 4-2 the relevance of such this model is highlighted by a sensitivity analysis of the non-linear material parameters ξ_3 and ε_3.

PTT model									
Material	Mode	λ_i (s)		η_i (Pa.s)		ε_i		ξ_i	
	1	λ_1	0.01	η_1	536	ε_1	0.17	ξ_1	0.16
	2	λ_2	0.1	η_2	816	ε_2	0.18	ξ_2	0.2
Neat PP	3	λ_3	1	η_3	707	ε_3	0.27	ξ_3	0.2
	4	λ_4	10	η_4	220	ε_4	0.4	ξ_4	0.3

4.2.3. General geometry and boundary conditions

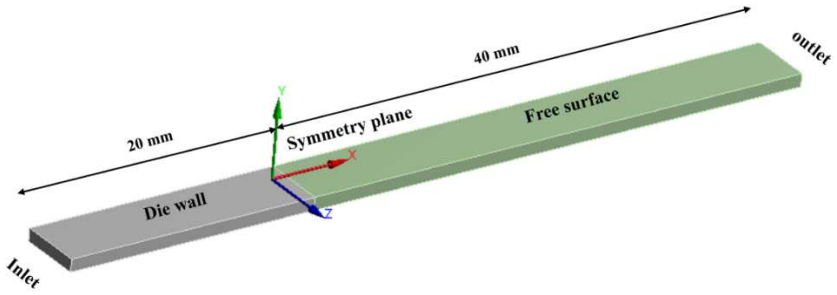


Figure 4-3. 3D flow domain of a slit die profile (list see Table 4-2). One quarter is considered for all simulations due to symmetry (l_1= 20mm and l_2= 40mm).

The 3D flow domain for a given W/H ratio is shown in Fig. 4-3. Due to the symmetry only one quarter of the flow channel is considered for all simulations to reduce the computational cost. The geometrical parameters for different flow channels (varying aspect ratio) are shown in Table 4-2 .The general boundary conditions are set as reported in previous work [44]. At the inlet, a fully developed flow is assumed due to the long die length for the experimental comparison (160 mm; aspect ratio of 10). At the die walls, a non-slip condition for the velocity field is prescribed, which indicates that the flow velocity vanishes: $v_n = v_t = 0$ (mm/s). Outside the die exit, a free surface flow is developed, which is unknown a priori. The force conditions $f_t = f_n = 0$ (N) are set at the outlet of the flow domain, with the subscript n and t representing the normal and tangential component of the force and velocity.

4.2.4. Method of 2D and 3D numerical solution for various aspect ratios

To solve the conservation and constitutive equations above, a flow solver (POLYFLOW version, ANSYS version 18.0) is applied based on the finite element

algorithm. A discrete elastic viscous stress splitting (DEVSS) combined with the streamline-upwind (SU) scheme is used to improve the numerical calculation stability [9, 33, 37, 42, 47]. This is done as there is a geometric singularity near the die exit where an abrupt change for the flow occurs from the non-slip to the free surface boundary condition. The DEVSS method adds a purely viscous term into the momentum equation based on velocity unknowns and removes an equivalent contribution based on rate-of-deformation unknowns to maintain the constitutive equation [48]. In addition, we apply an interpolation method on the velocity and pressure by quadratic and linear functions. An evolutionary scheme is performed on the volumetric flow rate to advance the solution from almost purely Newtonian to the viscoelastic flow with high non-linear rheological properties.

Table 4-2. Geometrical parameters for flow channels with various aspect ratios; link to Fig. 4-2; Q_1 and Q_2 correspond to $\dot{\gamma}_a$=15 and 48 s^{-1}, which are maintained as target values in line with the work of Clemeur *et al* [37] .

Aspect ratio (W/H)	Width ($2W$) (mm)	Height ($2H$) (mm)	l_1 (mm)	l_2 (mm)	Q_1 (mm^3/s)	Q_2 (mm^3/s)
1	2	2	20	40	13	42
1.5	3	2	20	40	22	69
2	4	2	20	40	31	98
5	10	2	20	40	91	288
10	20	2	20	40	196	620
20	40	2	20	40	405	1280

The height of each slit die is fixed at 2 mm and the aspect ratio includes values of 1, 1.5, 2, 5, 10 and 20 (see Table 4-1). The mesh sizes used in both *x* and *y* coordinates (shown in Figure 4-3) of the geometry model with different aspect ratios are maintained at the same level in all 3D simulations [40, 42, 49]. A mesh grid that progressively adds more elements toward the exit singularity is utilized, while larger

mesh elements are applied in the flow region away from the singularity [50]. These elements are shown in Fig. B-1 in the Appendix B. The analysis of the mesh independence for the swell simulations can be found in Table B1 in the Appendix B.

To quantify the effect of the die geometry on the flow behavior, the results obtained from different geometry configurations are compared at a constant $\dot{\gamma}_a$ value as in the work of Clemeur *et al*. [37]. Generally, the dimensionless Weissenberg number (*Wi*) is adopted to evaluate the viscoelasticity level involved in polymer flows [9, 37]:

$$Wi = \dot{\gamma}_a \lambda_m \qquad (4\text{-}8)$$

in which λ_m is the viscoelastic average relaxation time for the polymer fluid:

$$\lambda_m = \frac{\sum_{i=1}^{N} \eta_i \lambda_i}{\sum_{i=1}^{N} \eta_i} \qquad (4\text{-}9)$$

and $\dot{\gamma}_a$ is an apparent shear rate in the slit die with no slip [51]:

$$\dot{\gamma}_a = \frac{6Q}{2W*(2H)^2} \qquad (4\text{-}10)$$

It should be noted that Eq. (4-10) works well only if W/H is larger than 10 [37, 52], which is thus not the case for most considered aspect ratios in the present work. In contrast, if the aspect ratio decreases to smaller values such as 1 and 2, this equation is too approximative to calculate $\dot{\gamma}_a$. Therefore, for each simulation case where formally Newtonian flow is extruded from a slit die with a certain W/H ratio, the flow rate value applied in the Polyflow software is modified to make sure that the final apparent shear rates are the same. The values of 15 and 48 s^{-1} are considered for $\dot{\gamma}_a$ (see last two columns in Table 4-2 for *Q* values).

For the simplified 2D pattern, the discretization of the mesh pattern in the *x*-*y* plane is the same as that of all 3D counterparts to avoid some difference only arising from the

mesh discretization (Fig. B-2 in the Appendix B) [37, 40]. The interpolation methods for all unknown physical fields such as velocity and pressure variables for all 2D and 3D cases are the same.

To further demonstrate the relevance of the simulation results, focus is also on the comparison with the analytical solution proposed by Tanner to evaluate the swell ratio of the 2D simplified planar viscoelastic flow based on stress analysis [53, 54]:

$$B_3 = 0.19 + (1 + \frac{{S_w}^2}{3})^{1/4} \qquad (4\text{-}11)$$

in which S_w indicates a half of the ratio of the first normal stress difference to the shear stress on the die wall. The swell ratio predicted with Eq. (4-11) plugging in the simulated value of S_w is around 1.28 at $\dot{\gamma}_a$= 48 s^{-1}. This is slightly smaller than the numerically simulated value of 1.31 for the simplified 2D flow in this study and can be related to the ignoring of the stress singularity in Tanner's equation. This equation is only based on a physical analysis of the die-swell problem, with a combination of two characteristic properties of viscoelastic materials: recoiling and the existence of the normal stress difference [53]. Overall, the good match indicates the reasonability of the numerical simulations in this study for sure in the context of identifying trends regarding the relevance of the aspect ratio.

4.3. Results and discussions

4.3.1 Effect of aspect ratio on the 3D die swell characteristics

An important characteristic of the PP extrudate swell behavior is the continuous evolution when the flow emerges the die exit [18]. Figure 4-4 depicts the variations of the predicted extrudate profiles with an aspect ratio range from 1 to 20 at $\dot{\gamma}_a$= 48

(top row) and 15 (bottom row) s^{-1}. The associated Q values are given in Table 4-1. For the aspect ratio of 10, previously recorded experimental data have been included as well [44]. Good agreement between simulation and experimental results is observed. As shown in Figure 4(a) and (c), increasing the aspect ratio results in a decrease in the width swell ratio B_1, but a larger distance to obtain an equilibrium swelling. In Figure 4-4(b) and (d), the evolution of the swelling behavior of the extrudate edge height (swell ratio B_2 in Figure 4-1) is compared, as only accessible with 3D simulations. It is shown that a higher aspect ratio is able to strongly change the flow pattern along the extrudate edge height ultimately with "negative" swelling or contract flow ($B_2 < 1$). For an aspect ratio of 1, a significant swelling is noted since the B_2 value sharply increases to around 1.15, which seems similar to the results for linear low density polyethylene (LLDPE) extrudate from a cubic die [55]. Increasing slightly the aspect ratio from 1 to 1.5 leads to a significant drop in the B_2 value. As the aspect ratio increases further (5, 10 and 20), a contract flow in the edge height direction is observed.

In Figure 4-5, the corresponding changes in the middle height swell ratio B_3 are plotted (symbols) against the axial distance ($\dot{\gamma}_a$ = 48 (top row) and 15 (bottom row) s^{-1}). Clearly, the values are different from the B_2 values. Anisotropy of extrudate swell behavior is thus observed in all directions (see Table 4-3). A comparison with the die swell behavior of the corresponding "ideal" 2D flow is depicted as well in Fig. 4-5 (grey lines). A larger aspect ratio results in a smaller final equilibrium height swell ratio B_3, which is similar to the results of Konaganti *et al.*[33] In a short distance downstream the die exit, significant deviations between the 2D and 3D simulations are obtained, as made even clearer in the lower graphs. Specifically, the 3D values are

larger than the 2D ones at the same locations, which is more pronounced for $\dot{\gamma}_a$ = 48 s^{-1}.

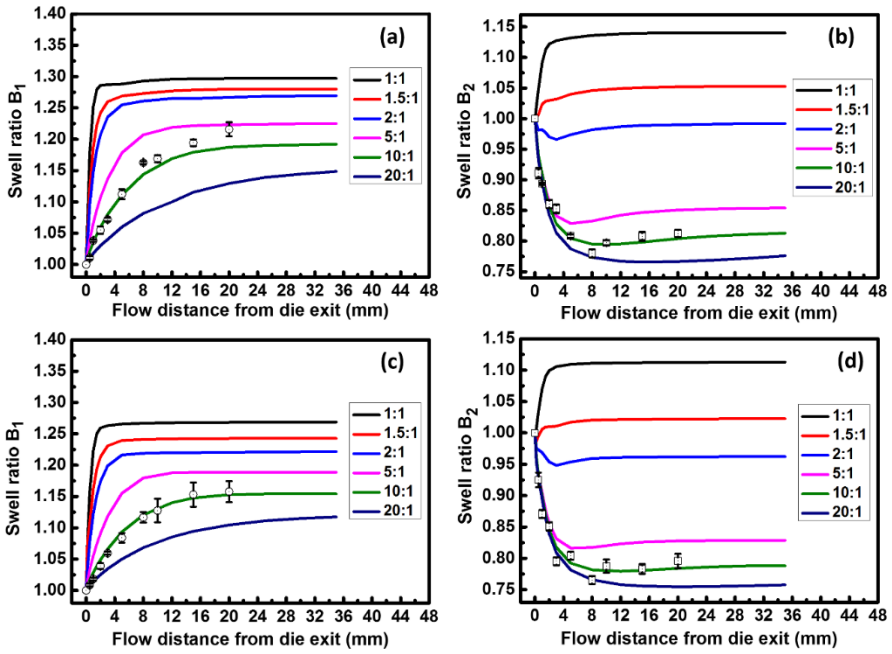


Figure 4-4. Comparison of the predicted extrudate profiles through slit dies with different aspect ratios (from 1:1 to 20:1; W/H; 200 °C; Table II) at $\dot{\gamma}_a$ = 48 s^{-1} (top) and 15 s^{-1} (bottom): width swell ratio B_1 (a) and (c) and edge height swell ratio B_2 (b) and (d) (Eq. 4-1; PTT parameters from Table 1). Symbols indicate the experimental data for aspect ratio of 10 [44].

Before the distance of *e.g.* 2 mm, the deviations increase with the flow distance with larger discrepancies between the two models specially for low aspect ratios ($\leq$ 2). After *ca.* 2 mm away from the die exit, interestingly, the swell ratio B_3 keeps almost constant for an aspect ratio of 1 (with the same final value as for B_1; 1.3; see Table 4-3). For the other flow cells, it does not grow monotonously with the flow distance. Instead, an extrudate shrinkage behavior following the fast initial swelling is observed until the final equilibrium swelling positions in Figs. 4-5(b) and (d). For instance,

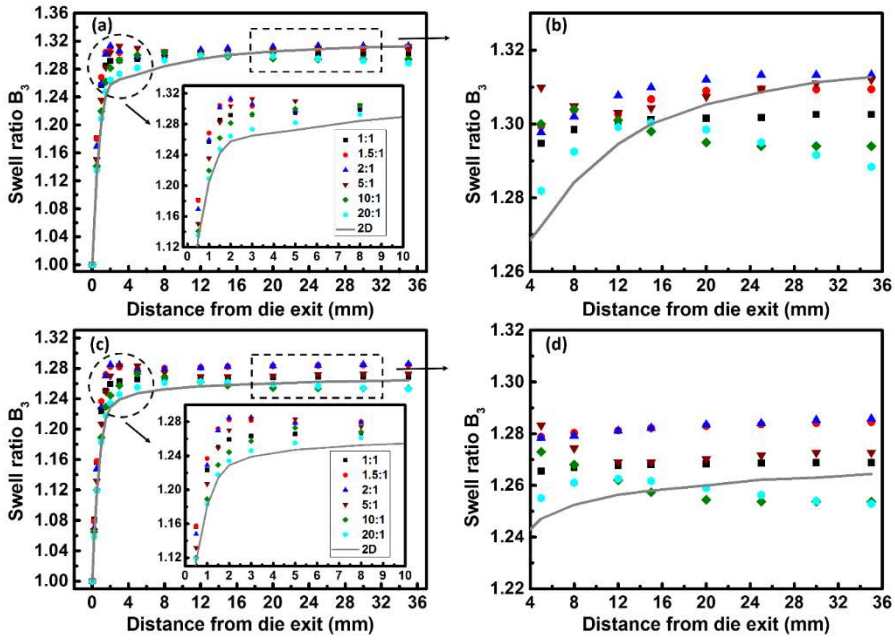


Figure 4-5. (a) Evolution of the predicted middle height swell ratio B_3 (Eq. (1)) of PP extrudate (200 °C; Table II) for the simplified 2D (line) and 3D flows (symbols) at $\dot{\gamma}_a$ = 48 s^{-1} (top row; (a) full image; (b) zoom in) and $\dot{\gamma}_a$ = 15 s^{-1} (bottom row; (c) full image; (d) zoom in); PTT parameters from Table 4-1.

within a short distance after the exit, the swell behavior with an aspect ratio of 20 agrees well with that for the 2D flow. Then, with a further distance, a deviation is noticed because of the "secondary" shrinkage flow in the middle height direction (see also right extra subplots). More generally, the secondary shrinkage flows (symbols at higher positions in Fig. 4-5) in the middle height direction cannot be observed in the simplified steady 2D viscoelastic flow over the whole swell evolution. In addition, the differences of the swell ratio at various aspect ratios tend to become smaller with further flow distance. This can be attributed to the rather similar viscoelastic behavior of flows as the apparent shear rates are maintained the same for various aspect ratios. Such feature mainly determines the final equivalent swell ratio according to Eq. 4-11.

Overall, the mismatches of the 2D modeling results highlight the effect of the side confining wall on the flow field (as confirmed in the next section) and thus the need of 3D simulations with both increases and decreases for swelling ratios along the distance.

Table 4-3. Final (f) values for B_1, B_2 and B_3 at $\dot{\gamma}_a$ = 48 s^{-1} (200 °C; PP extrudate; Table 4-2). Also given are the differences; ΔB_{31} is essential in the secondary shrinkage explanation.

Aspect ratio	Final $B_{1,f}$	Final $B_{2,f}$	Final $B_{3,f}$	$\Delta B_{32,f} = B_{3,f} - B_{2,f}$	$\Delta B_{31,f} = B_{3,f} - B_{1,f}$
1:1	1.3	1.145	1.3	0.155	0
1.5:1	1.284	1.06	1.309	0.249	0.025
2:1	1.26	0.99	1.31	0.32	0.05
5:1	1.22	0.86	1.31	0.45	0.09
10:1	1.19	0.81	1.294	0.484	0.104
20:1	1.15	0.78	1.288	0.508	0.138
2D	0	1.314[a]	1.314	0[a]	1.314

[a]not calculated but a consequence of the 2D assumption.

This less detailed information with 2D models and the absence of shrinkage is in agreement with the general trends in most modeling studies [26, 56, 57]. An exception is the modelling work of Comminal *et al*., [53] which reported a small secondary shrinkage in the extrudate height direction after the initial swelling for the 2D planar viscoelastic flow. Relaxation of the negative normal stress component, τ_{yy}, on the extrudate surface layer was put forward as the trigger. Recently, Toukhtarian *et al*. [58] also revealed a shrinkage flow following the extrudate swell for 2D simplified transient planar Newtonian flow upon varying the die gap. It is attributed to the

increasing volumetric flow rate because of the sudden decrease in the die gap. In the present work, it seems thus logical to assume that these triggers are absent (or counteracted) and an explanation needs to be sought in the 3D effect. In this respect, our previous 3D simulations for a die with fixed dimensions (aspect ratio of 10) pointed out that the swell ratio in the extrudate width direction increases in a much lower rate than the swell ratio in the height direction until an equilibrium is reached in both directions [44].

To obey the volumetric conversation a shrinkage flow is therefore expected in the extrudate height direction with several influencing factors. One factor is the difference of the final equilibrium width swell ratio B_1 and the final middle height swell ratio B_3 with a higher aspect ratio resulting in a larger difference, as shown in Table 4-3. Another factor is the different growing rate of both swell ratios with the flow distance. For example, for an aspect ratio of 1, no shrinkage flow is observed because the final B_1 is equal to the final B_3 (with a small drop for the final B_2). Increasing the aspect ratio results not only in a smaller final B_1 than B_3, but also in a smaller growing rate of B_1. Therefore, the synergistic effect of the aforementioned factors contributes to the secondary shrinkage flow in the height direction. In contrast, for the “ideal” 2D planar flow, the width of the flow channel is assumed to be infinite. This implies that the difference between B_1 and B_3 is too large (last column in Table 4-3) to induce secondary shrinkage flow in the (middle) height direction, taking into account that contract flow at the edge cannot be accounted for in such modeling.

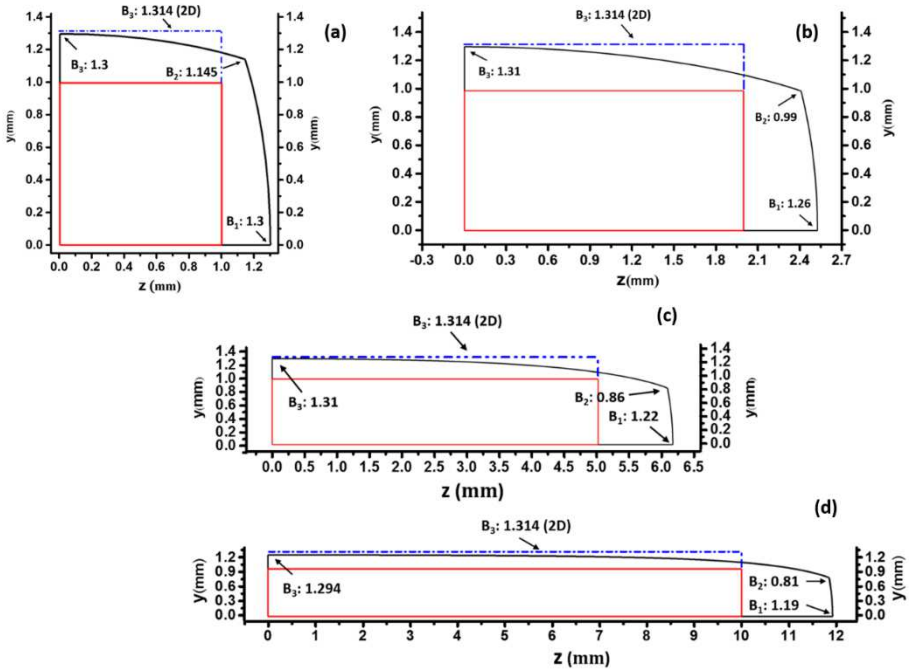


Figure 4-6. Comparison of the final extrudate profiles (full black lines) from slit dies (full red lines) with different aspect ratios: (a): 1:1, (b): 2:1, (c): 5:1 and (d): 10:1 (Table II) at $\dot{\gamma}_a$ = 48 s^{-1}. For a comparison, also the simplified 2D results are included (dashed blue lines). Note that only one quarter is shown due to symmetry. Absolute changes up to 30% and relative changes in various directions of 10% can be observed.

A global view of the final PP extrudate shapes (full black lines) from various dies (full red lines) is found in Figure 4-6 ($\dot{\gamma}_a$=48 s^{-1}). In agreement with the analysis of the evolution profiles of the extrudate swell ratio (Fig. 4-5 and Fig. 4-6 and Table 4-3) on an overall basis, higher aspect ratios result in a larger anisotropy degree of extrudate swell ratio upon considering jointly the height and width direction variations. Absolute variations up to 30% and relative variations of *e.g.* 10% can be identified, which explains the significant variation of the evolution of the area swell ratio B_4, shown in Fig. B-3 in the supplementary material. For example, this ratio decreases

from 1.55 to 1.417 by increasing the aspect ratio from 1 to 20. Additionally, in any case, the 3D description is needed as illustrated by the deviation with the 2D simulation results (blue dashed lines) in Figure 4-6.

4.3.2. Relation aspect ratio and velocity fields

4.3.2.1. Axial velocity component $\boldsymbol{v_x}$

It is expected that the changes to the velocity field by varying the aspect ratios of the flow channels affect the extrudate swell behavior. Figure B-2, B-3 and B-4 in the supplementary material shows that as the aspect ratio increases, the velocity profile of the central flow along the width direction differs gradually from its analogue along the height direction. For very high aspect ratios (e.g. 10 and 20) the velocity profile (*y* direction) overlaps the 2D flow profile. This means that in these die geometries, the 3D effect on the flow behavior in the *x*-*y* plane (*z*=0 mm) in the die can be ignored.

However, as shown in Figure 4-7, it is not safe to conclude that the 3D effect on the extrudate swell behavior out of the flow cell can be neglected as well. Figure 4-7(a) compares the velocity profiles of the centerline flow along the flow direction with different aspect ratios at $\dot{\gamma}_a = 48\ s^{-1}$. The axial velocity v_x is scaled by the corresponding 2D average velocity value $v_{xa\text{-}2D}$. A strong effect of the aspect ratio on the v_x rearrangement behavior is observed. In agreement with the swelling data, increasing the aspect ratio causes a larger final equilibrium v_x value. It is therefore not surprising that the simplified 2D flow has the largest equilibrium v_x, since there is no swell behavior in the width direction. For small aspect ratios ($\leq$2), the v_x rearrangement behavior accomplishes within a short distance. From Figure 4-7(b), it follows that a higher aspect ratio postpones the position where the departure of the v_x profile from

that of 2D flow starts. For the aspect ratio of 20, the v_x rearrangement behavior is almost the same as that of the 2D flow until a distance of around 6 mm after the exit. Then v_x continues to drop slowly in the former case.

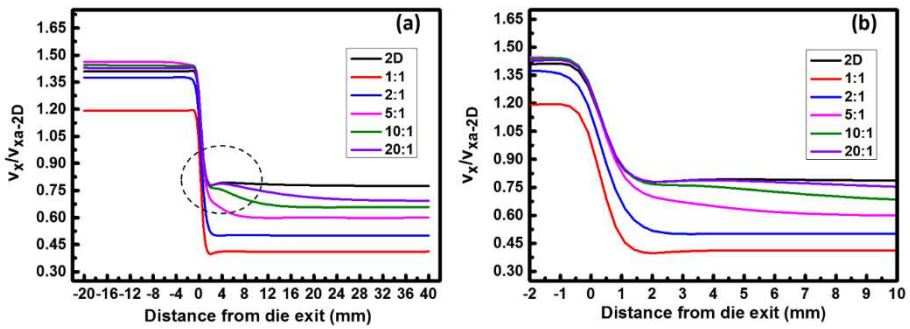


Figure 4-7. Velocity profiles of centerline PP flow (y=0 and z =0 mm) at $\dot{\gamma}_a$= 48 s^{-1} (Table 4-2) through the dies with different aspect ratios along the flow direction x. Right: zoom in.

4.3.2.2 Velocity components v_y and v_z

Due to the flow reorganization, the velocity components v_y and v_z in the transversal (y) and lateral (z) direction separately increase sharply from a vanishing value just upon exiting the die, as shown in Figure 4-8. Subplots (a) and (b) show the variations of v_y along the extrudate free surface flow layer in the central plane (z=0 mm) for 2D modelling and 3D flow with an aspect ratio of 1 and 20 at $\dot{\gamma}_a$= 48 s^{-1}. For an aspect ratio of 1, v_y falls fast to zero in comparison with the other two modelling cases. Seen in the inset in Figure 4-8(a), the v_y curves for 2D flow and 3D flow with an aspect ratio of 20 are almost the same, which correspond to the same swell behavior of the extrudate middle height for these two modelling cases in Figure 4-5. For the former case, v_y remains positive while it decreases to a negative value after a distance of x=15 mm for the latter case. This accounts for the secondary shrinkage flow in the middle height direction for the aspect ratio of 20 in Figure 4-5.

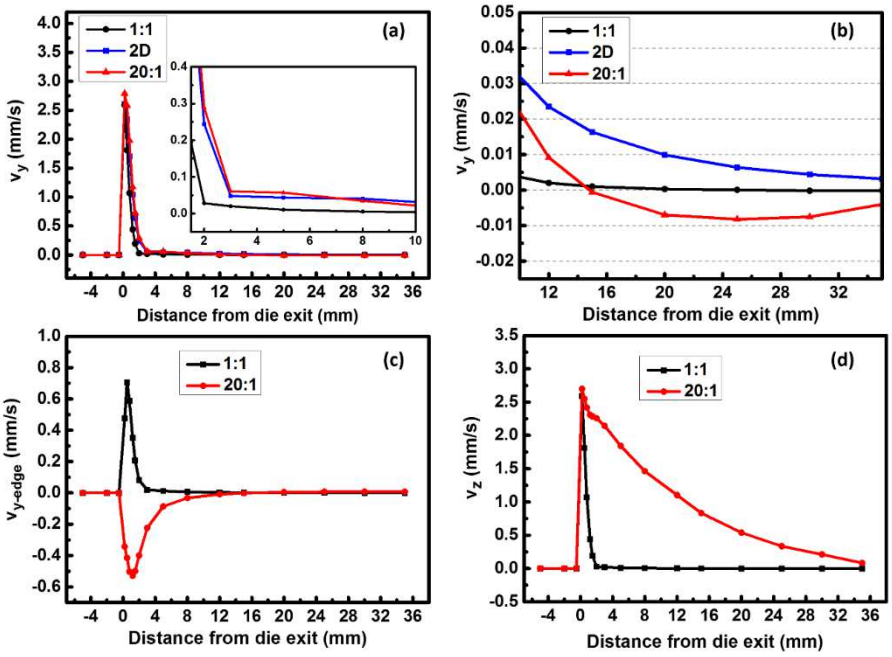


Figure 4-8. (a) Velocity component v_y along the die wall and free surface flow layer direction in the middle plane z=0 mm for low and high aspect ratio with 3D model, including a comparison with the ideal 2D flow; (b) is a close view of FIG. 8(a)). (c) velocity $v_{y\text{-}edge}$ along the flow cross-line between the side and top flow plane of extrudate free surface; (d) velocity component v_z along the side die wall and free surface flow layer in the middle plane y=0 mm. v_y, $v_{y\text{-}edge}$ and v_z codetermine the variations of extrudate middle height, edge height and width separately at $\dot{\gamma}_a = 48\ s^{-1}$.

Fig. 4-8(c) shows the velocity $v_{y\text{-}edge}$ along the flow cross-line between the side and top flow planes of the extrudate free surface layers for modelling cases with an aspect ratio of 1 and 20. These velocity changes determine the swell behavior in the extrudate edge height direction. It is interesting to observe that the $v_{y\text{-}edge}$ values have different signs, namely positive for an aspect ratio of 1 but negative for a value of 20. Therefore, swell (B_2>1) and shrinkage behavior B_2<1) can be observed for the two cases in Fig. 4-4(b), respectively. Fig. 4-8(d) presents the variations of the velocity component v_z

along the extrudate side (free surface direction in the plane y=0 mm. It follows that the decreasing of v_z for an aspect ratio of 1 is significantly faster than that for an aspect ratio of 20.

4.3.3. Relation between aspect ratio and stress field

Generally, the normal stress relaxation development is also responsible for the evolution of the swell behavior of polymer fluids [44, 53, 59]. Figure B-5 in the supplementary material shows the calculated fully developed stress components at x= -10 mm (shear stresses: τ_{yx} and τ_{zx}; normal stress differences (N_{xy} (τ_{xx}-τ_{yy}) and N_{xz} (τ_{xx}-τ_{zz})) for all 3D and 2D flows at $\dot{\gamma}_a$ = 48 s^{-1}. The related variations further confirm the 3D aspect due to the side confining wall. Figure 4-9(a) compares N_{xy} profiles for 3D flows with various aspect ratios and the corresponding 2D flow along the die wall and free surface direction in the symmetry planes. The calculated N_{xy} profiles agree with the general trend in literature[18, 26, 60] with significantly different normal stress relaxation behavior due to the aspect ratio. Figs. 4-9(b) and (c) give a close view of the stress relaxation away the die exit. For an aspect ratio of 1, a faster relaxation behavior is exhibited compared to that of the 2D counterpart, explaining the larger growing rate of the swell ratio B_3, and also the faster equilibrium swell positioning in Fig. 4-5. As the axial flow velocity with low aspect ratio is smaller than that of the simplified 2D flow (Fig. 4-7), a longer time to reach the same distance, therefore leading to a larger influence of the normal stress relaxation. Hence, the middle height swell ratio B_3 increases much faster in comparison with the 2D counterpart in Fig. 4-5. In contrast, the situation is less dynamic for high aspect ratios (5 and 20). The stress relaxation of an aspect ratio of 20 is expected to agree better with that of the simplified 2D flow, but still shows a bit faster relaxation.

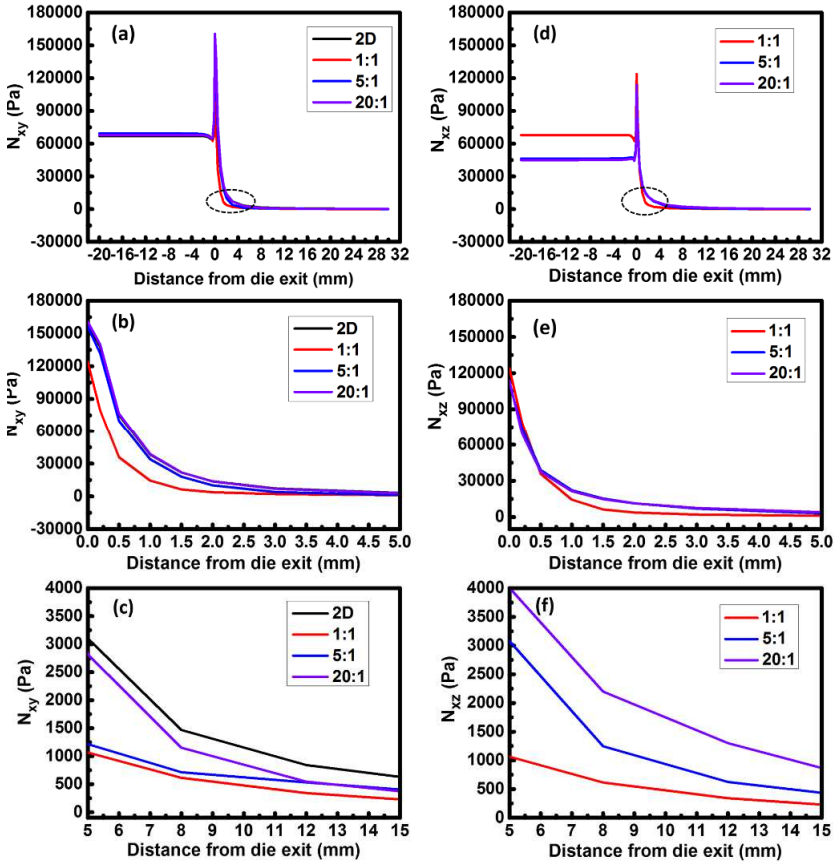


Figure 4-9. Comparison of normal stress difference N_{xy} (top row; (a)-(c); (a): full image; (b) and (c): close view) and N_{xz} (down row; (d)-(f); (d): full image; (e) and (f): close view) along the wall and free surface layer at $\dot{\gamma}_a = 48\ s^{-1}$.

Similarly, Fig. 4-9(d) compares the relaxation of N_{xz} along the extrudate surface layer direction in the x-z plane (y=0 mm), which is related to the swell behavior in the extrudate width direction. It is interesting to note that although the flow with an aspect ratio of 1 has a much larger N_{xz} before die exit (see Fig. B-5), it shows a faster normal stress relaxation. Besides the smaller axial velocity in Fig. 4-7, the relatively faster relaxation of the largely-deformed polymer chains due to a larger deformation is involved as well. Increasing the aspect ratio slows down the N_{xz} relaxation, thereby

leading to a delayed influence on the swell behavior in the width direction. Hence, in an industrial context the distance between the cooling system (*e.g.* water tank) and the die exit should be longer for a die with a large aspect ratio to minimize remaining internal stress, which can lead to a higher product quality.

4.3.4. Parametric study regarding non-linear PTT parameters

The PTT parameters in Table 4-1 reflect the polymer melt rheological properties, which have an influence on the flow behavior in and out of the die [9]. In essence, the parameters ε_i and ξ_i (*i* the mode) predominantly determine the extensional and shear behavior of polymer melts. The parameter ξ_i is also related to the second normal stress difference (N_{yz}; τ_{yy}- τ_{zz}) that controls the polymer backbone slippage for the non-affine motion of the surrounding continuum [9, 20, 37]. Due to the difficulty in measuring N_{yz} data [61] , the effect of N_{yz} on the extrudate behavior of the polymer melts is a point of attention. Konaganti *et al.* [34] highlighted that the effect of N_{yz} is very limited on the extrudate swell behavior and therefore they ignored this effect by considering zero ξ_i values for the multi-mode PTT model to describe the rheological properties of the HDPE melt. On the other hand, Carrot *et al*. [14] reported that a real agreement of the extensional and shearing behavior of the polymer melts cannot be achieved by using a single ε_i or ξ_i parameter. Also, our previous work on PP melts with a fixed aspect ratio indicates that both parameters are needed. Hence, it is worthwhile to further explore their relevance [44].

For simplicity, in this parametric study, the linear parameters (λ_i and η_i) are maintained constant in Table 4-1. The aspect ratio of the flow channel is fixed at 10 and $\dot{\gamma}_a$ = 48 s^{-1}. Preliminary screening showed that the parameter ε and ξ of Mode 4 or

Mode 1 (the longest and shortest relaxation time) cannot have an obvious influence on the extrudate swell. For Mode 4, the reason is likely that most elastic energy stored in the deformed polymer molecular chains has faded away before such long relaxation time, at least at the selected $\dot{\gamma}_a$. For Mode 1, the selected deformation rate is simply not covered by Mode 1 of PTT model, which is mainly used to control the rheological properties of the melt at a rather high shear rate range. This is in agreement with literature data [28]. Therefore, the impact of the PTT parameters of Mode 3 and Mode 2 on the extrudate swell behavior is only focused on.

Figure 4-10 depicts the simulated width and height swell ratio B_1 and B_3 with the ξ range of 0.05 to 0.8 in individual Mode 3 (top row; Fig. 4-2(a)-(c)) and Mode 2 (bottom row; Fig. 4-2(d)-(f)) for 3D and 2D configurations. Note that the values in Table 4-1 are inside this range and are denoted as reference values for simplicity. Figure 4-10(a) shows that the width swell ratio B_1 strongly depends on ξ_3, with a larger ξ_3 resulting in smaller B_1. For B_3 in Figure 4-10(b), increasing ξ_3 from 0.2 to 0.8 decreases the swell ratio B_3 as well, consistent with the report of Goublomme *et al*. [62]. However, decreasing ξ_3 from 0.2 to 0.05 results in a smaller B_3 value, which is attributed to the strong "secondary" shrinkage flow in the latter case. Goublomme *et al*. [62] reported that N_{yz} has a major influence on the swell ratio, but also mentioned that a modest decrease of the uniaxial extensional viscosity caused by changing the material parameter should not be ignored. Consistent with this statement, it is found in Figure 4-2 that a larger ξ value results in a rather slight decrease of *Nxy* and elongational viscosity values. In contrast, $|N_{yz}|$ increases significantly.

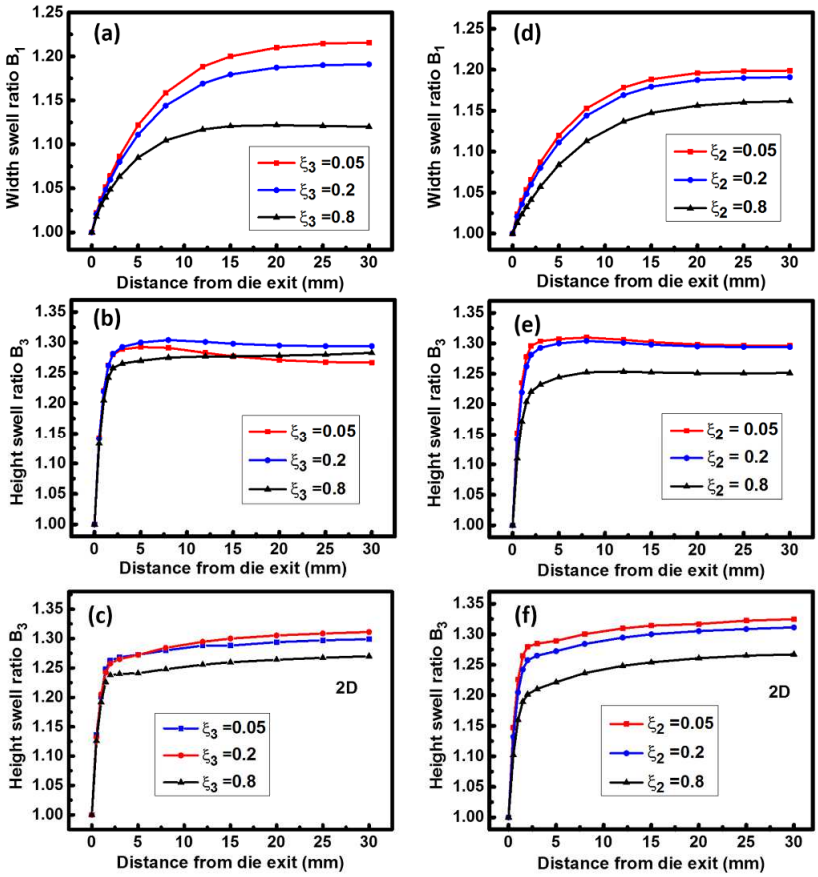


Figure 4-10. Effect of the parameter ξ in mode 3 ((a)-(c)) and mode 2 ((d)-(f)) of PTT model (other parameters as in Table I) on the extrudate swell ratio B_1 and B_3 with 3D ((a)-(b) and (d)-(e)) and 2D ((c) and (f)) simulations (aspect ratio of 10).

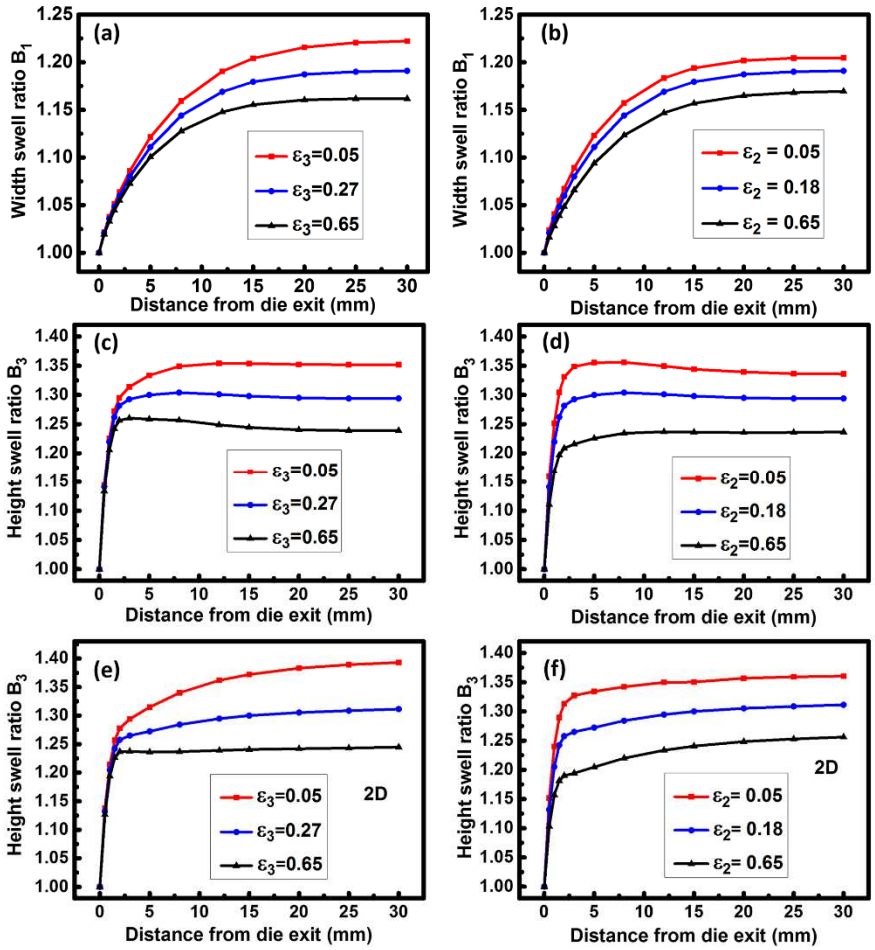


Figure 4-11. Effect of the parameter ε in mode 3 ((a),(c) and (e)) and mode 2 ((b), (d) and (f) and) of the PTT model on the extrudate width swell ratio B_1 and height swell ratio B_3 with 3D ((a), (b), (d) and (e)) and 2D ((c) and (f)) simulations. Other parameters as in Table 4-1.

Additionally, as mentioned above, B_3 profiles for ξ_3 = 0.05 and 0.8 in Fig. 4-10(b) are rather different. The significant shrinkage flow follows the initially large swell behavior in the former case, which cannot be observed in the latter. This indicates that the 3D effect of the geometric channels on the extrudate height swell behavior depends on the material parameters of PTT model as well. It is important to realize

that for ξ_3 = 0.05 and 0.8, the difference between the final B_3 and B_1 value is 0.05 and 0.16, respectively. This again confirms that the difference between the swell behavior in the (middle) extrudate height and width direction significantly contributes to the secondary shrinkage flow in the extrudate height direction (*cf.* Table 4-3). For the simplified 2D flow in Figure 4-10(c), the B_3 value increases monotonically with the flow distance without a shrinkage flow.

The material parameter ε shows a large influence on the elongational viscosity during melt deformations shown in Figure 4-2, and in case it starts to vanish, the elongational viscosity becomes unbounded [63]. Fig. 4-11(a), (b), (d) and (e) compare the calculated extrudate swell ratios with various ε_2 (bottom row) and ε_3 (top row) values from 0.05 to 0.65. It is shown that both the width swell ratio B_1 and the height swell ratio B_3 decrease with increasing ε value. To achieve a uniform velocity for each flow layer out of the die, the velocity difference between two flow layers leads to an extensional effect on the flow layers near the die exit, especially the flow layer close to the die wall. Formally increasing the ε value decreases the elongational viscosity of the polymer flow, indicating larger extensional effect applied on the polymer molecules until the flow becomes stable. Therefore, the shrinkage of the flow streamline outside the die is expected, explaining the decrease of swell ratio B_1 and B_3. In addition, a comparison of the results in Fig. 4-11(b) and (e) shows that the secondary shrinkage flow at a larger distance in the extrudate height direction is related to the ε values and cannot be observed in the 2D flow for which increases are always obtained. These effects are shown in Fig. 4-11(c) and (f), confirming the relevance of material parameters for detailed 3D simulations.

4.4. Conclusion

The influence of the slit die geometry on the extrudate flow behavior of neat PP melt with aspect ratios ranging from 1 to 20 is investigated via numerical simulations, considering the differential viscoelastic multi-mode PTT model with parameters taken from literature. To verify the impact of the die geometry, the 3D simulation results are compared to the simplified 2D case considering constant apparent shear rates. In any case, the 3D model is needed as die swell/shrinkage is multidimensional with absolute variations up to 30% and relative variations of *ca*. 10%. Hence, future process control and die design should be based on 3D interpretations.

Increasing the aspect ratio decreases the width swell ratio B_1 and the edge height swell ratio B_2 and leads to a shift in the onset of the axial equilibrium swelling position to a further distance. The edge height swell ratio B_2 can become even negative, leading to a contraction flow. The middle height swell ratio B_3 profiles for the 3D flow significantly deviate from that of the 2D simulation. Just after the die exit the B_3 values are larger than the 2D value and then a decrease of the B_3 values occurs, except for the aspect ratio of 1, for which a 2D model is irrelevant. This phenomenon of a secondary shrinkage is not eliminated even if the aspect ratio is increased to the highest value of 20.

The mechanism for the above phenomenon is illustrated by the flow velocity and stress fields. A significant deviation of the 3D configurations from the corresponding 2D one inside and outside the die is generally noted. Increasing the aspect ratio of the flow cells narrows the discrepancy but cannot vanish the 3D effect. For sure the deviation out of the die still cannot be neglected, even if the flow behavior in the die (*y* direction) seems almost the same as that of the 2D flow with an aspect ratio higher

than 2. The larger axial velocity v_x for a larger aspect ratio outside the die contributes to a slower normal stress relaxation, thereby a slower swell behavior delaying the swelling equilibrium position. This is also in agreement with the variations of the other velocity components v_y and v_z.

A parametric study reveals that the width swell ratio B_1 largely decreases with increasing ξ which is related to the second normal stress difference. An increasing ε controlling the elongational viscosity decreases both the width well ratio B_1 and the height swell ratio B_3. In addition, the secondary shrinkage flow becomes large with decreasing ξ but still cannot be observed in the corresponding 2D flow. This implies that the 3D effect on the extrudate swell behavior depends not only on the geometric characteristics of the flow channel but also on the melt material parameters. From this perspective, the impact of the 3D effect on the extrudate swell behavior is expected to vary if the polymer melts are modified or are combined with fillers. Such variations will be included in future work by the authors.

REFERENCES

1. Wieme, T., et al., *The relevance of material and processing parameters on the thermal conductivity of thermoplastic composites.* Polymer Engineering & Science, 2018. **58**(4): p. 466-474.
2. Wieme, T., et al., *Effect of Matrix and Graphite Filler on Thermal Conductivity of Industrially Feasible Injection Molded Thermoplastic Composites.* Polymers, 2019. **11**(1): p. 87.
3. Velayudhan, S., et al., *Extrusion of hydroxyapatite to clinically significant shapes.* Materials Letters, 2000. **46**(2-3): p. 142-146.
4. Miller, E. and J.P. Rothstein, *Control of the sharkskin instability in the extrusion of polymer melts using induced temperature gradients.* Rheologica acta, 2004. **44**(2): p. 160-173.
5. Ebrahimi, M., et al., *Melt fracture of linear low-density polyethylenes: Die geometry and molecular weight characteristics.* Physics of Fluids, 2018. **30**(5): p. 053103.
6. Beverly, C. and R. Tanner, *Numerical analysis of extrudate swell in viscoelastic materials with yield stress.* Journal of Rheology, 1989. **33**(6): p. 989-1009.
7. Sirisinha, C., *A review of extrudate swell in polymers.* J. Sci. Soc, Thailand, 1997. **23**: p. 259-280.
8. Liang, J., et al., *Melt extrudate swell behavior of multi-walled carbon nanotubes filled-polypropylene composites.* Polymer Composites, 2015.
9. Tian, H., et al., *Study on extrudate swell of polypropylene in double-lumen micro profile extrusion.* Journal of Materials Processing Technology, 2015. **225**: p. 357-368.
10. Neves, N., A. Pontes, and A. Pouzada, *Experimental validation of morphology simulation in glass fibre reinforced polycarbonate discs.* Journal of reinforced plastics and composites, 2001. **20**(6): p. 452-465.
11. Ferrás, L., et al., *A numerical and theoretical study on viscoelastic fluid slip flows.* Physics of Fluids, 2017. **29**(5): p. 053102.
12. Barborik, T. and M. Zatloukal, *Effect of heat transfer coefficient, draw ratio, and die exit temperature on the production of flat polypropylene membranes.* Physics of Fluids, 2019. **31**(5): p. 053101.
13. Caswell, B. and M. Viriyayuthakorn, *Finite element simulation of die swell for a Maxwell fluid.* Journal of Non-Newtonian Fluid Mechanics, 1983. **12**(1): p. 13-29.
14. Carrot, C., et al., *Experimental validation of non linear network models*, in *Rheology Series*. 1996, Elsevier. p. 141-198.
15. Huang, S.X. and C.J. Lu, *Stress relaxation characteristics and extrudate swell of the IUPAC-LDPE melt.* Journal of non-newtonian fluid mechanics, 2006. **136**(2): p. 147-156.
16. Goublomme, A., B. Draily, and M. Crochet, *Numerical prediction of extrudate swell of a high-density polyethylene.* Journal of non-Newtonian fluid mechanics, 1992. **44**: p. 171-195.
17. Huang, S.-x., et al., *Rheological characterizations and extrudate swell predictions of an LDPE melt by two KBKZ-type constitutive equations.* Journal of Hydrodynamics, Ser. B, 2010. **22**(5): p. 915-919.

18. Konaganti, V.K., et al., *The effect of damping function on extrudate swell.* Journal of Non-Newtonian Fluid Mechanics, 2016. **236**: p. 73-82.
19. Konaganti, V.K., et al., *Non-isothermal extrudate swell.* Physics of Fluids, 2016. **28**(12): p. 123101.
20. Thien, N.P. and R.I. Tanner, *A new constitutive equation derived from network theory.* Journal of Non-Newtonian Fluid Mechanics, 1977. **2**(4): p. 353-365.
21. Sugeng, F., N. Phan-Thien, and R. Tanner, *A Study of Non-Isothermal Non-Newtonian Extrudate Swell by a Mixed Boundary Element and Finite Element Method.* Journal of Rheology, 1987. **31**(1): p. 37-58.
22. Mu, Y., et al., *Measurement and simulation of low-density polyethylene extrudate swell through a circular die.* Polymer International, 2009. **58**(5): p. 475-483.
23. Mu, Y., et al., *Modeling and simulation of three-dimensional extrusion swelling of viscoelastic fluids with PTT, Giesekus and FENE-P constitutive models.* International Journal for Numerical Methods in Fluids, 2013. **72**(8): p. 846-863.
24. Mu, Y., G. Zhao, and C. Zhang, *Numerical investigation of die geometry effect on LDPE annular extrudate swell.* Journal of applied polymer science, 2010. **117**(1): p. 91-109.
25. Azaiez, J., R. Guénette, and A. Ait-Kadi, *Numerical simulation of viscoelastic flows through a planar contraction.* Journal of non-newtonian fluid mechanics, 1996. **62**(2-3): p. 253-277.
26. Béraudo, C., et al., *A finite element method for computing the flow of multi-mode viscoelastic fluids: comparison with experiments.* Journal of non-newtonian fluid mechanics, 1998. **75**(1): p. 1-23.
27. Tanoue, S. and Y. Iemoto, *Effect of die gap width on annular extrudates by the annular extrudate swell simulation in steady-states.* Polymer Engineering & Science, 1999. **39**(11): p. 2172-2180.
28. Schoonen, J., *Determination of rheological constitutive equations using complex flows*. 1998: Technische Universiteit Eindhoven Eindhoven.
29. Guillet, J., et al., *Comparison between experimental data and numerical models*, in *Rheology Series*. 1996, Elsevier. p. 285-336.
30. Tomkovic, T., E. Mitsoulis, and S.G. Hatzikiriakos, *Contraction flow of ionomers and their corresponding copolymers: Ionic and hydrogen bonding effects.* Physics of Fluids, 2019. **31**(3): p. 033102.
31. Behzadfar, E., et al., *Extrudate swell of HDPE melts: I. Experimental.* Journal of Non-Newtonian Fluid Mechanics, 2015. **225**: p. 86-93.
32. García-Rejón, A., R. DiRaddo, and M. Ryan, *Effect of die geometry and flow characteristics on viscoelastic annular swell.* Journal of non-newtonian fluid mechanics, 1995. **60**(2-3): p. 107-128.
33. Konaganti, V., et al., *Extrudate swell of high density polyethylenes in slit (flat) dies.* International Polymer Processing, 2016. **31**(2): p. 262-272.
34. Konaganti, V.K., et al., *Extrudate swell of a high-density polyethylene melt: II. Modeling using integral and differential constitutive equations.* Journal of Non-Newtonian Fluid Mechanics, 2015. **225**: p. 94-105.
35. Verbeeten, W.M., G.W. Peters, and F.P. Baaijens, *Numerical simulations of the planar contraction flow for a polyethylene melt using the XPP model.* Journal of Non-Newtonian Fluid Mechanics, 2004. **117**(2-3): p. 73-84.

36. Mitsoulis, E. and I. Argyropaidas, *Numerical simulation of contraction and expansion flows of Langmuir monolayers.* Journal of Non-Newtonian Fluid Mechanics, 2009. **157**(3): p. 163-174.
37. Clemeur, N., R. Rutgers, and B. Debbaut, *Numerical simulation of abrupt contraction flows using the Double Convected Pom–Pom model.* Journal of non-newtonian fluid mechanics, 2004. **117**(2-3): p. 193-209.
38. Ahmed, R., R. Liang, and M. Mackley, *The experimental observation and numerical prediction of planar entry flow and die swell for molten polyethylenes.* Journal of non-newtonian fluid mechanics, 1995. **59**(2-3): p. 129-153.
39. Bogaerds, A.C., et al., *3D viscoelastic analysis of a polymer solution in a complex flow.* Computer methods in applied mechanics and engineering, 1999. **180**(3-4): p. 413-430.
40. Clemeur, N., R. Rutgers, and B. Debbaut, *Numerical evaluation of three dimensional effects in planar flow birefringence.* Journal of non-newtonian fluid mechanics, 2004. **123**(2-3): p. 105-120.
41. Xue, S.-C., N. Phan-Thien, and R. Tanner, *Three dimensional numerical simulations of viscoelastic flows through planar contractions.* Journal of Non-Newtonian Fluid Mechanics, 1998. **74**(1): p. 195-245.
42. Omowunmi, S. and X.-F. Yuan, *Modelling the three-dimensional flow of a semi-dilute polymer solution in microfluidics—on the effect of aspect ratio.* Rheologica acta, 2010. **49**(6): p. 585-595.
43. Schoonen, J.F., et al., *A 3D numerical/experimental study on a stagnation flow of a polyisobutylene solution.* Journal of non-newtonian fluid mechanics, 1998. **79**(2-3): p. 529-561.
44. Tang, D., et al., *Isothermal flow of neat polypropylene through a slit die and its die swell: Bridging experiments and 3D numerical simulations.* Journal of Non-Newtonian Fluid Mechanics, 2019. **266**: p. 33-45.
45. Aloku, G.O. and X.-F. Yuan, *Numerical simulation of polymer foaming process in extrusion flow.* Chemical Engineering Science, 2010. **65**(12): p. 3749-3761.
46. Rodríguez, L.F.C., *Modification of the PTT Model and its Application for the Predictions of Elongational Viscosity of Polypropylenes-Edición Única.*
47. Saramito, P. and J. Piau, *Flow characteristics of viscoelastic fluids in an abrupt contraction by using numerical modeling.* Journal of non-newtonian fluid mechanics, 1994. **52**(2): p. 263-288.
48. Guénette, R. and M. Fortin, *A new mixed finite element method for computing viscoelastic flows.* Journal of non-newtonian fluid mechanics, 1995. **60**(1): p. 27-52.
49. Xue, S.-C., N. Phan-Thien, and R. Tanner, *Numerical study of secondary flows of viscoelastic fluid in straight pipes by an implicit finite volume method.* Journal of Non-Newtonian Fluid Mechanics, 1995. **59**(2-3): p. 191-213.
50. Ansari, M., S.G. Hatzikiriakos, and E. Mitsoulis, *Slip effects in HDPE flows.* Journal of Non-Newtonian Fluid Mechanics, 2012. **167**: p. 18-29.
51. Baird, D.G., *First normal stress difference measurements for polymer melts at high shear rates in a slit-die using hole and exit pressure data.* Journal of Non-Newtonian Fluid Mechanics, 2008. **148**(1-3): p. 13-23.
52. Macosko, C.W. and R.G. Larson, *Rheology: principles, measurements, and applications.* 1994.

53. Comminal, R., et al., *Numerical simulation of the planar extrudate swell of pseudoplastic and viscoelastic fluids with the streamfunction and the VOF methods.* Journal of Non-Newtonian Fluid Mechanics, 2017.
54. Tanner, R.I., *A theory of die-swell revisited.* Journal of non-newtonian fluid mechanics, 2005. **129**(2): p. 85-87.
55. Normandin, M., et al., *Three-dimensional extrudate swell experimental and numerical study of a polyethylene melt obeying a memory-integral equation.* Journal of non-newtonian fluid mechanics, 1999. **87**(1): p. 1-25.
56. Ganvir, V., et al., *Prediction of extrudate swell in polymer melt extrusion using an Arbitrary Lagrangian Eulerian (ALE) based finite element method.* Journal of Non-Newtonian Fluid Mechanics, 2009. **156**(1): p. 21-28.
57. Ganvir, V., et al., *Extrudate swell of linear and branched polyethylenes: ALE simulations and comparison with experiments.* Journal of Non-Newtonian Fluid Mechanics, 2011. **166**(1): p. 12-24.
58. Toukhtarian, R., et al., *Modeling polymer extrusion with varying die gap using Arbitrary Lagrangian Eulerian (ALE) method.* Physics of Fluids, 2018. **30**(9): p. 093103.
59. Tanner, R., *A theory of die-swell.* Journal of Polymer Science Part B: Polymer Physics, 1970. **8**(12): p. 2067-2078.
60. Al-Muslimawi, A., H. Tamaddon-Jahromi, and M. Webster, *Simulation of viscoelastic and viscoelastoplastic die-swell flows.* Journal of Non-Newtonian Fluid Mechanics, 2013. **191**: p. 45-56.
61. Dealy, J.M. and R.G. Larson, *Nonlinear Viscoelasticity*, in *Structure and Rheology of Molten Polymers*. 2006, Carl Hanser Verlag GmbH & Co. KG. p. 329-413.
62. Goublomme, A. and M. Crochet, *Numerical prediction of extrudate swell of a high-density polyethylene: further results.* Journal of non-newtonian fluid mechanics, 1993. **47**: p. 281-287.
63. Karapetsas, G. and J. Tsamopoulos, *Steady extrusion of viscoelastic materials from an annular die.* Journal of Non-Newtonian Fluid Mechanics, 2008. **154**(2-3): p. 136-152.

Chapter 5

The impact of upstream contraction flow on three-dimensional polymer extrudate swell from slit dies

The relevance of upstream contraction for extrudate swell behavior of polymer melts is numerically investigated for slit dies with an aspect ratio of 10 and a length-to-height ratio ranging from 2.5 to 40. Three-dimensional (3D) flow simulations are performed with ANSYS Polyflow software at different flow rates and 200°C, selecting polypropylene as melt and the differential multimode Phan-Thien-Tanner (PTT) constitutive model to describe the viscoelastic behavior. It follows that decreasing the die length results in opposite trends for the swell ratio in the relevant directions: the width swell ratio decreases up to 28%, the middle height swell ratio increases up to 55% and the edge height contraction increases with 37%, all highlighting the 3D anisotropy of the extrudate swell deformation. In contrast, especially for low flow rates, the area swell ratio remains almost unchanged and cannot be used to capture the anisotropic swelling behavior. This is predominantly attributed to the similar relative redistribution degree of the axial velocity (v_x). An analysis of the transversal (v_y) and lateral velocity (v_z) combined with the stress field variation is performed as well to fully relate the anisotropy extrudate swell behavior to the various die lengths. The current study thus further completes the understanding of the relation of slit die design parameters and 3D extrudate flow under isothermal conditions.

5.1. Introduction

Extrusion is one of the most important material forming operations widely considered in the polymer industry. Examples of processes in which polymer extrusion is employed include blow molding, and sheet, pipe and profile extrusion [1-7]. In extrusion, the phenomenon of die swell, *i.e.* the shape variation of the extrudate swell out of die exit, is of particular interest, as it is an important controlling factor to obtain a desired product profile. Different variables determine this die swell, including the processing conditions, the viscoelastic properties of the polymer melt, and the deformation history [8-11].

It should be stressed that the deformation history can already be relevant upon the die entry with generally a converging flow transition region between the barrel and the die entrance. In this region, the flow cross-section decreases, and a significant contraction deformation is applied to the flowing melt. Stemming from its much more complex flow behavior with extensional and shear flow taking place together, contraction flow is considered as a benchmark for evaluating the capability of constitutive models and numerical methods to capture the viscoelastic behavior of polymer melts or solutions [12, 13].

As a consequence, there have been numerous publications related to contraction flow, covering both experimental and numerical results [14-31]. For example, in a recent review, Musil *et al.* [22] pointed out that the converging flow transition region is the key trigger for polymer melt stagnation or secondary flow. Contraction leads to developing downstream flow, which exhibits considerable exit pressure therefore codetermining the extrudate swell behavior. Previous studies have often focused on flows through capillary or slit dies, which were considered as axisymmetric or planar

flows, respectively [5, 23-26]. Already in the 1970s, Han *et al.* [24] experimentally observed that increasing the contraction ratio, *i.e.* the ratio between the reservoir diameter and the die (inlet) diameter leads to an increase of the die swell of high density polyethylene (HDPE) melt through a capillary die. In the 1980s, Tanner and Luo [23, 27, 28] published seminal works on the simulation of extrudate swell of a highly viscoelastic low density polyethylene (LDPE) melt for both long and short capillary dies, using the integral Kaye-Bernstein-Kearsley-Zapas (KBKZ) model and the streamline finite element method (SFEM). It has been reported that by shortening the die length, the extrudate swell ratio increases. These improved models can capture general trends of more realistic flows at higher Weissenberg numbers or apparent shear rates. Hatzikiriakos, Mitsoulis and co-workers have put forward several contributions in which the effects of an upstream contraction flow on the extrudate swell behavior have been investigated for capillary and slit dies by using integral or differential viscoelastic models [5, 9, 12, 29, 32]. These authors discussed the applicability and limitations of various rheological models and numerical formulations to grasp polymer extrudate swell [5]. Recently, Robertson *et al.* [11, 33] theoretically predicted the extrudate swell of axisymmetric constricted polystyrene melts with a variation in the broadness of the molar mass distribution, using the Rolie-Poly constitutive model. A more pronounced swelling for shorter dies at higher shear rates is noted, due to the larger contribution of unrelaxed chains thus chain stretching.

Notably, most numerical simulations for extrudate die swell rely on a two-dimensional (2D) model for simplifying the calculations. However, in practice all die dimensions are finite, *e.g.* the width-to-height or aspect ratio of a common slit die is finite, and the shape of the upstream contraction or transition region is irregular [34, 35], so that it is likely that polymer melt flow in these regions cannot be simplified by

a 2D geometry model. Indeed in our previous work, first focusing on an aspect ratio of 10 and later on aspect ratios between 1 and 20, we highlighted already the relevance of 3D characteristics of the extrudate swell behavior of polypropylene (PP) melts at 200 °C through slit dies, considering the case of fully developed flow by selecting a sufficiently long experimental die length [36, 37]. For any aspect ratio, a significant change in the 3D extrudate deformation is reported, with absolute variations up to 30% in all Cartesian directions and relative variations up to 10% in individual such directions. However, a developing flow is expected before the die exit if the slit die length reduces to a certain value, further complicating the 3D swell behavior. Considering the anisotropy swell behavior in the extrudate width and height directions it is thus interesting to study the potential of 3D effects induced by the contraction flow for different slit die lengths. This type of research is further supported by taking into account that there are only limited reports available on this matter. Moreover, from an economic point of view, one wants to minimize the material amount and the complexity of a die set-up and thus control the die length for a given contraction configuration.

Therefore, in the present work, we investigate how the length of a slit die with a fixed aspect ratio affects extrudate swell behavior by its unavoidable connection with a given upstream contraction region in which the cross-section is still variable. Focus is on the gradual transformation from developing flow to fully developed flow before the die exit by formally increasing the length of the die part with a constant cross-section. In the finite element method based simulations, as conducted with POLYFLOW software, this length is varied from 5 to 80 mm, considering the multimode Phan-Thien-Tanner (PTT) model for PP melt at 200 °C with its parameters previously tuned based on rheological data [36], and an upstream contraction region

of length 35 mm. A comprehensive comparison of the swelling behavior in the extrudate width and height directions is carried out as a function of the former length accompanied by an analysis of the associated stress and velocity fields.

5.2. Modelling principles

5.2.1. Geometric parameters

Fig. 5-1 shows the 2D schematic diagram of the cross section of the end of a slit die, selecting an aspect ratio of 10. To account for the anisotropy of the swell behavior three swell ratios are defined:

$$B_1 = \frac{w_{-extrudate}}{w_{-die}},\ B_2 = \frac{H_{1-extrudate}}{H_{1-die}} \text{ and } B_3 = \frac{H_{2-extrudate}}{H_{2-die}} \qquad (5\text{-}1)$$

They correspond to the swelling in the extrudate width, edge height and middle height direction [36]. It is important to note that already for fully developed flow, significant difference between the edge height ($D_{1\text{-extrudate}}$) and the middle height ($D_{2\text{-extrudate}}$) of the extrudate can be expected due to the extrudate anisotropy swell behavior [37]. In addition, the swell ratio B_4 is defined as the ratio of the area size (S) of the extrudate cross section and the die:

$$B_4 = \frac{S_{-extrudate}}{S_{-die}} \qquad (5\text{-}2)$$

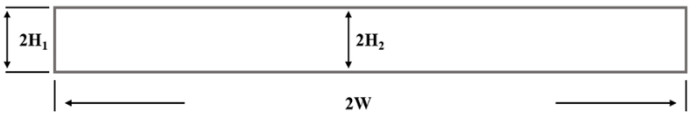


Figure 5-1. Cross section of the end of a slit die with an aspect ratio of 10. Four swell ratios are defined, as mathematically represented by Eq. 5-1 and 5-2. They denote the swelling in the width direction, in the edge height direction, in the middle height direction and for the area; example of a complete die shown in Fig. 5-2.

5.2.2. Governing equations

In this work, the incompressible polymer melt is considered under steady and isothermal creeping laminar flow conditions at 200 °C. The inertial force is neglected due to the consideration of a flowing viscoelastic melt with a sufficiently low Reynold number. Since we only consider the extrudate swell behavior up to a maximal distance of 20 mm (die height: 2 mm) after the die exit in experiments, gravity and surface tension effects of the melts can be ignored as well [36, 38].

$$\nabla \cdot \mathbf{v} = 0 \qquad (5\text{-}3)$$

$$-\nabla p + \nabla \cdot \boldsymbol{\tau} = 0 \qquad (5\text{-}4)$$

in which $\boldsymbol{v}$ is the velocity vector, ∇ is the Hamiltonian operator p is an isotropic contribution to the total stress commonly called pressure and $\boldsymbol{\tau}$ the extra stress tensor.

The set of equations above is coupled with the constitutive model relating the extra stress to the velocity gradient. For a viscoelastic constitutive model, the extra stress tensor $\boldsymbol{\tau}$ is split into a purely viscous part $\boldsymbol{\tau_N}$ and a viscoelastic part $\boldsymbol{\tau_p}$. The former is solved by the generalized Newtonian flow model [36, 39], while the latter is calculated by a viscoelastic constitutive model. For a time spectrum of *N* relaxation modes, the viscoelastic stress tensor $\boldsymbol{\tau_p}$ is a sum of *N* individual $\boldsymbol{\tau_{pi}}$ contributions, which are calculated by the differential PTT model [36, 40]:

$$\boldsymbol{\tau_p} = \sum_{i=1}^{N} \boldsymbol{\tau_{pi}} \qquad (5\text{-}5)$$

$$exp\left[\frac{\varepsilon_i \lambda_i}{\eta_i} \boldsymbol{tr}(\boldsymbol{\tau_{pi}})\right] \boldsymbol{\tau_{pi}} + \lambda_i \left[(1 - \frac{\xi_i}{2}) \overset{\sim}{\boldsymbol{\tau_{pi}}} + \frac{\xi_i}{2} \overset{\frown}{\boldsymbol{\tau_{pi}}}\right] = 2\eta_i \boldsymbol{D} \qquad (5\text{-}6)$$

in which λ_i and η_i are the *i*th relaxation time and viscosity, describing the linear rheological properties of polymer melts. The non-linear ε_i and ξ_i parameters determine the extensional and shear behavior of fluids, respectively. ξ_i which allows for the backbone slippage for the non-affine motion of the surrounding continuum is also related to the second normal stress difference [37, 39]. $\overset{\frown}{\boldsymbol{\tau}_{pi}}$ and $\overset{\smile}{\boldsymbol{\tau}_{pi}}$ correspond to the lower and upper convected time derivatives of $\boldsymbol{\tau_{pi}}$, and *D* is the deformation tensor rate, defined as:

$$\overset{\smile}{\boldsymbol{\tau}_{pi}} = \frac{D\boldsymbol{\tau_{pi}}}{Dt} - (\boldsymbol{\tau_{pi}} \cdot \nabla\mathbf{v} + (\nabla\mathbf{v})^T \cdot \boldsymbol{\tau_{pi}}) \qquad (5\text{-}7)$$

$$\overset{\frown}{\boldsymbol{\tau}_{pi}} = \frac{D\boldsymbol{\tau_{pi}}}{Dt} + (\boldsymbol{\tau_{pi}} \cdot \nabla\mathbf{v} + (\nabla\mathbf{v})^T \cdot \boldsymbol{\tau_{pi}}) \qquad (5\text{-}8)$$

$$\boldsymbol{D} = \frac{\nabla v + (\nabla v)^T}{2} \qquad (5\text{-}9)$$

where ∇v and $(\nabla v)^T$ are the velocity gradient and the transpose of the velocity gradient, respectively.

Table 5-1. Phan-Thien-Tanner material parameters of PP at 200 °C. Reproduced from Table 3-2 in Chapter 3.

Parameters								
Mode	λ_i (s)		η_i (Pa.s)		ε_i		ξ_i	
1	λ_1	0.01	η_1	536	ε_1	0.17	ξ_1	0.16
2	λ_2	0.1	η_2	816	ε_2	0.18	ξ_2	0.2
3	λ_3	1	η_3	707	ε_3	0.27	ξ_3	0.2
4	λ_4	10	η_4	220	ε_4	0.4	ξ_4	0.3

The material parameters of the multi-mode PTT constitutive model for the PP melt (200 °C) are extracted by adjusting the linear and non-linear rheological properties. The corresponding parameters are shown in Table 3-2 in Chapter 3, which are comparable to a previous report [41].

5.2.3. General geometry and boundary conditions

For illustration purposes, the 3D flow domain considering a die length l_2 of 80 mm for the part with a constant cross-section is shown in Figure 5-2(a) alongside the preceding converging flow region with a fixed length l_1 of 35 mm. The associated contraction ratio, *i.e.* the ratio of the cross-section (S) of the upstream inlet and the die entry, is 1.256. The converging part of the die geometry starts from a circular cross-section with a diameter of 8 mm and ends with a slit geometry (width 20 mm, thickness 2 mm). Due to the symmetry, only one quarter of the flow channel is considered to reduce the computational cost. A length l_3 is foreseen for the free surface flow and the flow rate is 160 or 620 $mm^3\ s^{-1}$. The left side (projected) view of the considered geometry is shown in Fig. 5-2(b), where the details regarding the geometry configuration can be found in detail.

An overview of all the geometrical characteristics for the flow channels with a die length-to-height ratio ranging from 2.5 to 40 is provided in Table 5-2. The main variable in each case is l_2, which is crucial to control the degree of developing flow after the entry flow deformations. The general boundary conditions are as in previous work [36]. A nonslip condition for the velocity field is set on the die walls. A zero normal force condition is implemented at it as well. Outside the die exit, a free surface flow is formed, which is unknown a priori. Then, the line kinematic condition $\boldsymbol{v}\cdot\mathbf{n} = 0$ is solved, with $\boldsymbol{n}$ the normal vector to the free surface. Vanishing forces are applied at the outlet of the flow domain.

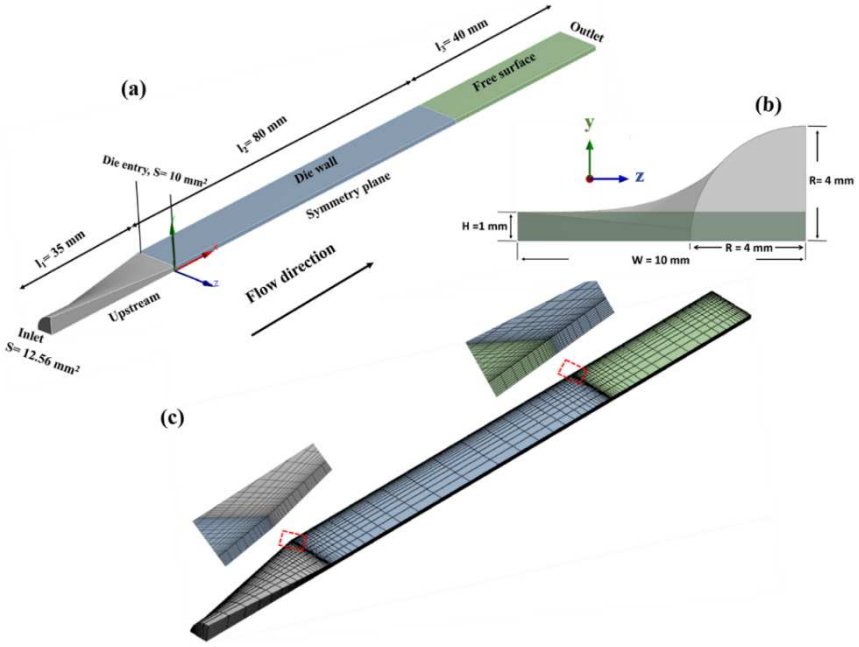


Figure 5-2. (a) 3D flow domain of the slit die as connected to the upstream contraction part and change in a free surface flow upon die exit (focus here on Case E in Table 5-2: l_1= 35 mm, l_2= 80 mm, aspect ratio of 10), and l_3= 40 mm); (b) Mesh patterns for 3D geometries; only quarter is considered for all simulations due to symmetry.

An overview of all the geometrical characteristics for the flow channels with a l_2-to-height ratio ranging from 2.5 to 40 is provided in Table 5-2. The main variable in each case is l_2, which is crucial to control the degree of developing flow after the entry flow deformations. The general boundary conditions are shown in previous work [36]. A nonslip condition for the velocity field is set on the die walls. Vanishing forces are applied at the outlet of the flow domain.

5.2.4. Method of 3D numerical solution

A flow solver (POLYFLOW version, ANSYS version 18) based on the finite element algorithm is utilized to solve the conservation and constitutive equations above. Accounting for the stress singularity around the die entry and die exit, the discrete elastic viscous stress splitting (DEVSS) method combined with the streamline upwind (SU) scheme is used to stabilize the numerical calculations [5, 9, 37, 42]. Additionally, we perform an interpolation method on the velocity and pressure with quadratic and linear functions. Due to the intrinsic complexity in obtaining a solution from an initial linear solution directly, an initial Newtonian solution with the flow rate as the evolution parameter is employed [21].

Table 5-2. Geometrical parameters and mesh information for flow channels with various die lengths l_2 (cf. Fig. 5-2); the l_2-to-height ratio varies from 2.5 to 40; the aspect ratio of the die in the part with constant cross section is fixed at 10 (cf. Fig. 5-1). Case E corresponds to a case of fully developed flow for the selected flow rates.

Case	Width (2W) (mm)	Height (2H) (mm)	l_1 (mm)	l_2 (mm)	l_3 (mm)	Mesh elements	Mesh nodes
A	20	2	35	5	40	9984	12087
B	20	2	35	20	40	10800	13104
C	20	2	35	40	40	11040	13392
D	20	2	35	60	40	11640	14112
E	20	2	35	80	40	11880	14400

Mesh arrangements used in the upstream and free surface region are maintained at the same level for all flow cases. For the flow region inside the die, the mesh sizes in both *y* and *z* coordinates are also maintained almost at the same level in each case. Fig. 5-2(b) shows the general mesh arrangements with a l_2 of 80 mm. A mesh grid that

progressively adds more elements upon approaching the die entry and exit singularity is used, while mesh elements with larger size are applied in the flow region away from the singularity [30, 37].

5.3. Results and discussion

5.3.1. Extrudate swell

The typical character of polymer extrudate swell is its continuous evolution after the die exit until an equilibrium is reached [43]. For a slit die, anisotropic swell behavior is expected due to inherent difference in the die dimensions with common aspect ratios well above 1 [37]. Figure 5-3 presents the evolution profiles of the swell behavior for PP melt at 200 °C in three extrudate directions, namely the extrudate width (B_1), the edge height (B_2), and the middle height (B_3) direction (Eq. 5-1) with flow rates of 620 (top layer) and 196 (bottom layer) $mm^3\,s^{-1}$. Our previous results for fully developed ("FD") flow inside a die with a large length (160 mm with respect to the studied operating conditions) are also included for comparison as black full lines (simulation results) and black open circles (experimental data) [37]. A further validation regarding other slit die dimensions is outside the scope of the present work, taking into account the non-trivial nature of such die assembly and the predictive strength of simulation tools with material parameters in Table 5-1 determined based on dedicated rheological analysis.

It follows from Fig. 5-3 that the width swell ratio B_1 increases significantly at each axial position with the die length l_2 increasing from 5 to 20 mm. As l_2 increases to 40 mm, a further increase of l_2 only leads to a rather small increase in B_1 value, with ultimately (for l_2 equal to 80 mm onwards) a reaching of the asymptotic value for the

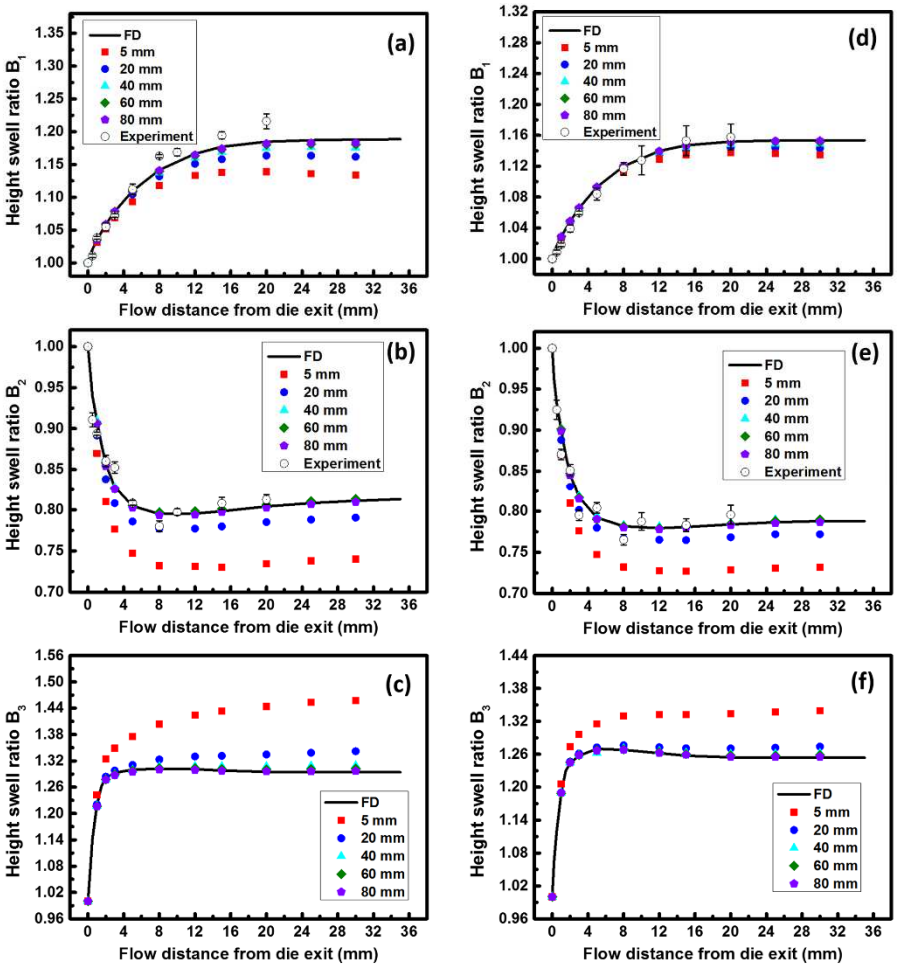


Figure 5-3. The evolution profile of the swell behavior in the extrudate width (B_1), edge height (B_2), and middle height direction (B_3) (Eq. 5-1) for polypropylene (PP) melts from slit dies at 200 °C with various die lengths l_2 (5 mm, 20 mm, 40 mm, 60 mm, and 80 mm; full details in Table 5-2) at a flow rate of 620 $mm^3\ s^{-1}$ (top row: (a)-(c)) and 196 $mm^3\ s^{-1}$ (bottom row: (d)-(e)). The black full lines (simulations) and black open symbols (experimental data) are from our previous work with a sufficiently large l_2 (>> 80 mm) and indicate the swell behavior of a fully developed (FD) flow [37].

FD flow. This confirms the assumption of the fully developed flow before the die exit in our previous work with a die length of 160 mm in the experimental set-up long

enough for the contraction flow to fully develop after the extensional deformations through the converging region [36, 37]. In the same fashion as the width swell ratio B_1, the edge height swell ratio B_2 presents an increasing tendency with a longer l_2 at each axial position, although displaying decreasing trends for contract flow for each l_2. In addition, a smaller flow rate contributes to a smaller difference of both swelling ratios among the cases with various l_2 values. This is due to a longer residence time with a lower flow rate inside the die, which shortens the critical l_2 for the formation of fully developed flow.

Table 5-3. The relative ratio of each type of swell ratio (Eq. (5-10) for i=1,..,4) for different die lengths (l_2 values in Table 5-2)) at 620 and 196 $mm^3\ s^{-1}$. Negative and positive values indicate a decrease and increase for the corresponding swell behavior for the case of l_2= 80 mm.

	Cr_1		Cr_2		Cr_3		Cr_4	
	Flow rate (mm^3s^{-1})							
Die length	620	196	620	196	620	196	620	196
60 mm	-1.1%	-1.0%	-1.8%	-0.9%	1.9%	1.4%	-0.5%	-0.3%
40 mm	-4.3%	-3.0 %	-1.6%	-1.5%	5%	1.4%	-1.3%	-0.9%
20 mm	-12.9%	-7.2%	9.7%	6.5%	15.7%	7.6%	-3%	-1.9%
5 mm	-28.1%	-13.5%	37.3%	25.4%	55.0%	34.3%	-4.8%	-2.4%

Opposed to the variations for B_1 and B_2, increasing l_2 causes a significant decrease in the middle height swell ratio B_3 at each axial position, as shown in Figure 5-3 (c) and (f). For example, for l_2 equal to 5 mm the final B_3 value is 1.46, whereas this value sharply drops to 1.34 as l_2 increases to 20 mm. This behavior for B_3 is in agreement with previous (2D) reports [9, 12, 29, 44, 45] and relates to the variation of the

elasticity of polymer melts. Due to the fading memory effect of a polymer melt, longer residence times inside the die lead to a smaller B_3 value [44]. A closer inspection of Fig. 5-3 also reveals that for a l_2 of 5 and 20 mm, B_3 monotonously increases with the axial distance. In contrast, for the FD flow, a "secondary" shrinkage flow (black line) following the initial significant swell behavior is observed [37]. The reason is the much larger difference between the swell ratio B_1 and B_3 in both former cases, leading to larger anisotropy for the extrudate swell behavior. This can be for instance illustrated by following additional ratios:

$$C_{ri} = \frac{B_{i,f} - B_{i,f-80}}{B_{i,f-80} - 1} \ (i\text{=1, 2, 3 or 4}) \qquad (5\text{-}10)$$

in which $B_{i,f}$ indicates the large (equilibrated/final) time swell ratio for the selected l_2 and $B_{i,f-80}$ represents the corresponding swell ratio with a reference l_2 of 80 mm reflecting the FD case. It follows from the first six columns in Table 5-3 that the maximum C_r increases/decreases are obtained by reducing l_2 from 80 mm to 5 mm at 620 $mm^3\ s^{-1}$. Values of *ca.* 30, 40, and 55% result for C_{r1}, C_{r2}, and C_{r3}, with thus a large *ca.* 25% variation between C_{r1} and C_{r3}, highlighting a discrepancy of the swell behavior in the width and middle height direction. In contrast for higher l_2 values this difference between C_{r1} and C_{r3} is only *ca.* 1-5%. Increasing the contraction ratio is expected to even further increase the anisotropy degree of the extrudate swell.

For a too short die, thus a too low l_2 value, on the molecular level a higher degree of unrelaxed axial elongational deformation is established if the contraction flow cannot be fully minimized. In other words, the axial stretching effect stemming from the converging streamline is predominantly responsible for the larger anisotropy extrudate swell discussed above. This statement is supported by our previous work in

which a larger difference between B_1 and B_3 is obtained upon decreasing the parameter ε_3 in Table 5-1 related to a higher elongational viscosity [37], as also reconfirmed in Subsection 5.2.3.

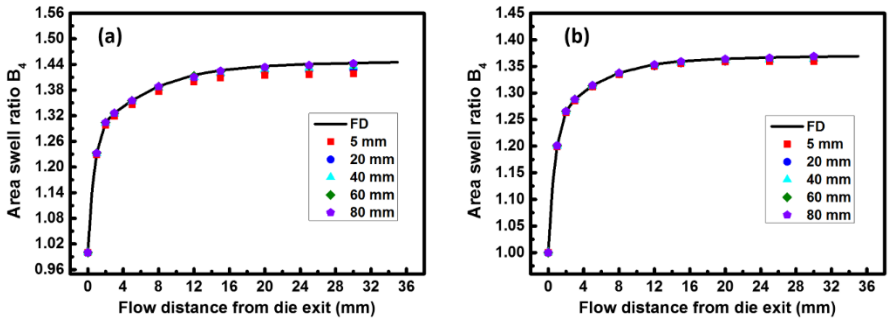


Figure 5-4. The evolution profile of the area swell behavior (Eq. 5-4) for polypropylene (PP) melts from slit dies at 200 °C with various die lengths l_2 (5 mm, 20 mm, 40 mm, 60 mm and 80 mm; full details in Table 5-2) at (a) a flow rate of 620 $mm^3\ s^{-1}$ and (b) 196 $mm^3\ s^{-1}$. The black full lines are from our previous work (l_2 >> 80 mm) and indicate the swell behavior of a fully developed (FD) flow [37].

In Figure 5-4, it is surprising to note that l_2 has no obvious influence on B_4, especially for the case of the lower flow rate (Fig. 5-4(b)) and the higher l_2 values (upper symbols in Figure 5-4(a) and (b)). Instead of the large deviation for the other three types of swell ratio B_1, B_2 and B_3 mentioned above (*cf.* Figure 5-3), a relatively unchanged B_4 value is observed upon increasing l_2 from 5 to 80 mm, as also confirmed in the last two columns shown in Table 5-2 with Cr_4 values below 5%. These observations for slit dies based on 3D simulations disagree with the general varying trend for polymer extrudate area swell behavior through a capillary or annular die [12, 44, 46]. Although reducing l_2 increases the middle height swell ratio B_3, the decrease of the width swell ratio works as a compromise. Hence, a focus on only the area swell behavior is in general not recommended to quantify the 3D anisotropy of extrudate swell.

5.3.2. Stress and velocity fields

5.3.2.1. Relation between the die length and stress fields

The presence of normal stresses is a specific characteristic of viscoelastic behavior of polymer melts in comparison with Newtonian or purely viscous melts. As the flow approaches the die entry, due to the non-constant cross-section, a strong extensional deformation of the polymer melt occurs, resulting in a dramatic increase in the axial normal stress component τ_{xx}, followed by the stress relaxation after the die entry, as shown in Figure 5-5 for three l_2 values (5, 20 and 80 mm). It can be seen in Figure 5-5(a) that until the flow reaches the die entry, l_2 has no influence on τ_{xx}. However, as shown in Fig. 5-5(b), upon approaching the die exit, the magnitude of τ_{xx} is significantly larger for a l_2 of 5 mm as compared with the coinciding cases of 20 and 80 mm, highlighting that too short dies lead to stronger variations in die swell, at least in a given direction shown in Fig. 5-3. Hence, the stronger flow deviations for lower l_2 values are also reflected in the τ_{xx} variations.

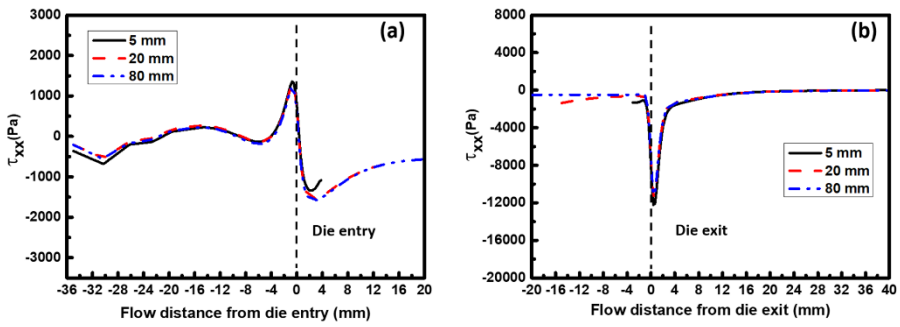


Figure 5-5. The normal stress component τ_{xx} profile of the center flow layer (y=z=0 mm) along the flow distance (so axial position) away (a) from the die entry and (b) from the die exit for a flow rate of 620 mm^3 s^{-1}; PP melt flow at 200 °C; model parameters: Table 5-1; details on conditions: Table 5-2. Focus on three l_2 values from Table 5-2.

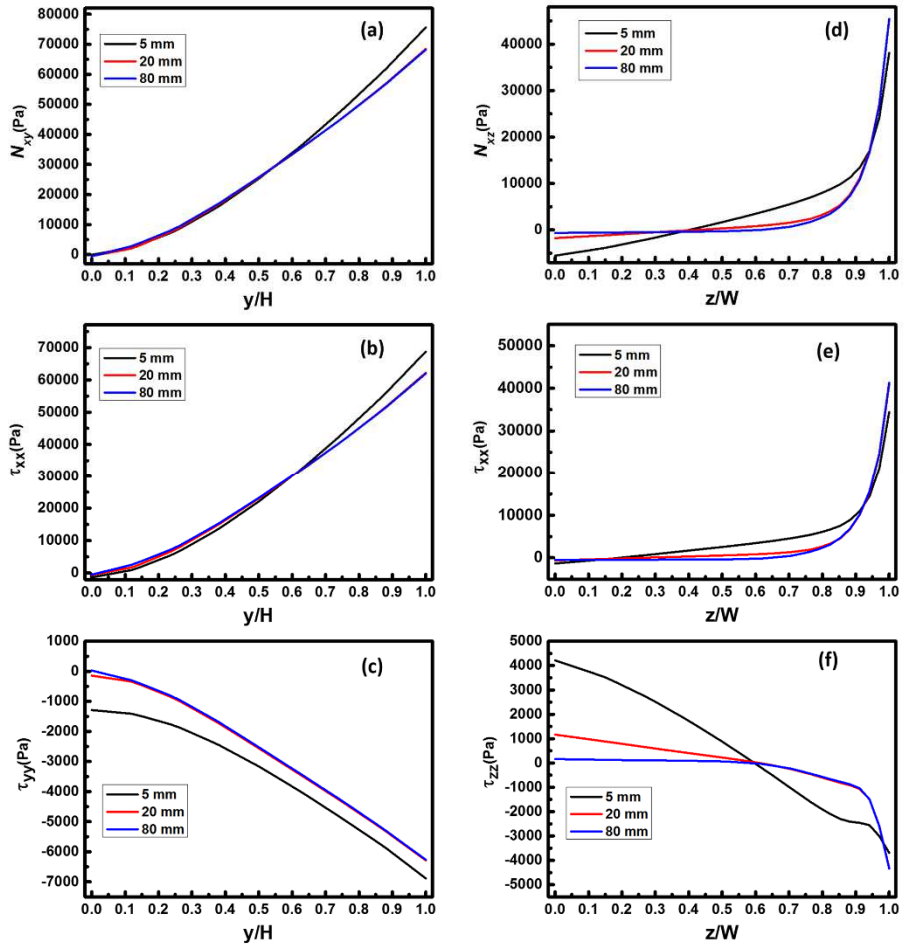


Figure 5-6. The distributions of the normal stress components (a) N_{xy}(τ_{xx}-τ_{yy}), (b) τ_{xx} and (c) τ_{yy} along the height direction (y direction central, plane z=0 mm); and the normal stress components (d) N_{xz}(τ_{xx}-τ_{zz}), (e) τ_{xx} and (f) τ_{zz} along the width direction (z direction, central plane y=0 mm) with a flow rate of 620 mm^3 s^{-1} at the location of 3 mm before the die exit with various l_2 values ranging from 5 to 80 mm; PP melt flow at 200 °C; model parameters: Table 5-1; details on conditions: Table 5-2.

Fig. 5-6(a) and (d) compare the normal stress differences N_{xy} (τ_{xx}-τ_{yy}) and N_{xz} (τ_{xx}-τ_{zz}) along the middle height (*y* direction; *z*=0 mm) and width directions (*z* direction; *y*=0 mm) at the location of 3 mm before the die exit with l_2 values of 5, 20 and 80 mm at a flow rate of 620 mm^3 s^{-1}. For comparison, the *y* and *z* values are scaled by the corresponding dimension of the flow geometry and the individual normal stresses are

given in Figs. 5-6(b), (c), (e), and (f). A significantly different influence resulting from the l_2 variation is observed on the distributions of N_{xy} and N_{xz}, respectively. In Fig. 5-6(a), the N_{xy} value near the die wall is positive and declines significantly upon increasing l_2 from 5 to 20 mm but varies not much in vicinity of the central flow as a function of l_2. Further increasing l_2 to 80 mm does not affect much N_{xy} at any position, with in any case a decrease of N_{xy} toward the central flow. In contrast, looking at the N_{xz} values, a substantial magnitude increase in the flow region close to the die wall can be observed for all l_2 values but a strong decrease is obtained toward the middle region ($\frac{z}{W}$ = 0.3 to 0.9) with even negative values, as shown in Fig. 5-6(d). This decrease is more gradual for a l_2 of 5 mm but also longer going on with thus more negative values toward the center flow. At the edge, however, there is a weaker effect for a smaller l_2 so that the less pronounced B_1 (width) variation in Figure 5-3 for decreasing l_2 can be explained.

The individual normal stress components for the further interpretation of Fig. 5-6(a) and (b) are given in Fig. 5-6(b), (c), (e), and (f). In Fig. 5-6(b) and (c), both the absolute value of τ_{xx} and τ_{yy} increase more near the die wall with a lower l_2 which indicates a stronger axial (x) elongational force and transversal (y) compression force, respectively. This again confirms the relation between l_2 and B_3. However, the opposite trend can be found in Fig. 5-5 and Fig. 5-6(e) and (f), which indicates a weaker axial (x) elongational force and lateral (z) compression force close to the die wall, again confirming the relation between l_2 and B_1. In addition, a significantly larger lateral elongational force (z direction) applied on the center flow is observed in Fig. 5-6 (f), due to a larger τ_{zz} value upon reducing l_2.

In a final stage one can also focus at complete cross sections so without a restriction for *y* or *z*, as in Figure 5-5 and 5-6 at least one of those directions is vanishing. In this respect, Fig. C-1, C-2 and C-3 in the supplementary material reveal more details on the evolution of the normal stress components distributions on the flow cross section plane at different flow distances, namely 3 mm before the die exit and 2 mm, 5 mm and 10 mm after the exit. The l_2 value is 5, 20 or 80 mm. For l_2=5 mm, the magnitude of τ_{xx} in vicinity of the center flow increases significantly at the flow distance of 2 mm after the die exit in Fig. C-1(d) in comparison with that in Fig. C-1(a) (3 mm before the die exit). This again indicates a larger compression force in that region. A close inspection reveals that the flow region close to the top die wall in Fig. C-1(a) with the largest τ_{xx} value is also extended to the side edge corner in Fig. C-1(d) as well. The same phenomenon can be noted for l_2=20 mm and l_2=80 mm in Fig. C-1, which can be attributed to the axial velocity v_x redistribution behavior as fully addressed in Fig. 7.

Fig. C-2(d)-(l) (all results after the die exit) show that at the edge corner negative τ_{yy} values always result, indicating that a compression force is applied to that flow region. Therefore, a contraction flow is observed in the edge height direction in Fig. 5-3 (B_2 < 1). This is specifically true upon decreasing the die length to 5 mm, leading to the smallest B_2 values in Fig. 5-3 for the shortest die length. Furthermore, Fig. C-3(d)-(f) depict that negative τ_{zz} values ultimately result near the side corner of the extrudate, indicating a damping effect on the width swell behavior. This region is colored in blue and is more clearly developing for l_2 equal to 5 mm, explaining the lowest B_3 values in Fig. 5-3 for the shortest die length.

5.3.2.2. Relation between die length and velocity redistributions

Figure 5-7 compares the axial velocity distribution on the cross section of the die entry, the die exit, and the extrudate at a distance of 40 mm away from die exit for l_2 values ranging from 5 to 80 mm at a flow rate of 620 mm^3 s^{-1}. In Fig. 5-7(a), (d) and (g), it is shown that l_2 does not influence the axial velocity distribution (v_x) at the die entry even though there is a sharp increase in v_x at the die entry due to a large elongational force, which can also be seen in Fig. 5-7(j) displaying the complete v_x profile for the centerline flow only (y=z=0 mm). For the die exit increasing l_2 from 5 to 20 and ultimately 80 mm makes the velocity distribution more uniform, especially along the width (z) direction (Figs. 5-7 (b), (e) and (h)). (Fig. 5-7 (d), (e) and (f)) consistent with the stress distribution profiles in Fig. C-1, C-2 and C-3.

Furthermore, qualitatively similar extrudate velocities are obtained at 40 mm away from the die exit, as shown by almost same colors in Figs. 5-7(c), (f) and (i), particularly for the case of 20 mm and 80 mm, as also clear from the final decays in Fig. 5-7(j). In other words, a similar degree of the v_x redistribution behavior is completed regardless of the l_2 value for these contraction flows at a given flow rate. This is consistent with the very similar area swell ratios in Fig. 5-4. The extrudate area swell ratio behavior is mainly determined by the redistribution degree of the axial velocity, which induces the velocity redistribution behavior in the transversal and lateral direction in return [38].

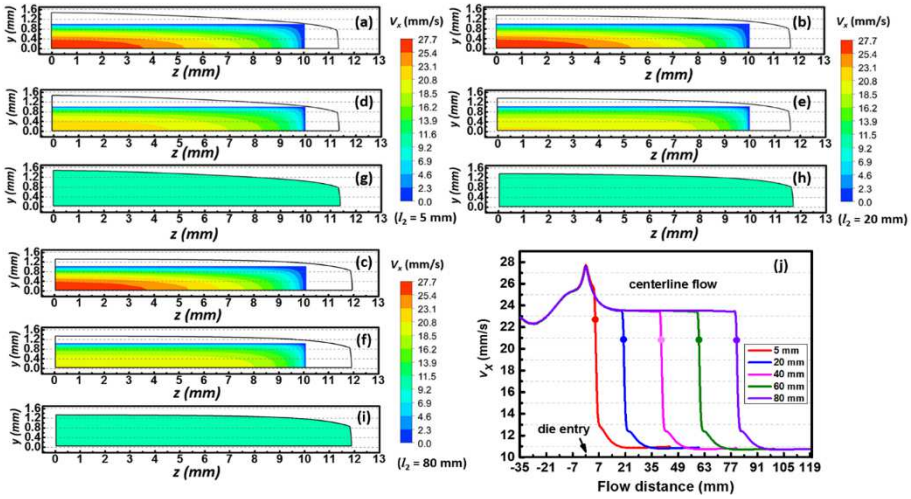


Figure 5-7. Axial velocity (v_x) distributions in the cross section of die entry (a, d and g), the die exit (b, e and h), and the extrudate 40 mm from the die exit (c, f and i) covering die length l_2 values of 5, 20 mm and 80 mm and for comparison always the die swell shape at the aforementioned 40 mm as a black line; (j) the axial velocity profile of the central flow along the flow direction (y=0, z=0 mm) for l_2 values of 5, 20, 40, 60 and 80 mm; flow rate of 620 $mm^3\ s^{-1}$. Die exit points are highlighted by spheres in the same color as the line; PP melt flow at 200 °C; model parameters: Table 1; details on conditions: Table 5-2.

Fig. 5-8 compares the profiles of the velocity component v_y of the flow streamline at y=0.4 mm (z=0 mm)of and the velocity component v_z of the flow streamline at z=4 mm (y=0 mm) along the flow distance for l_2 values of 5 mm and 80 mm. The two streamlines are denoted as (x, 0.4, 0) and (x, 0, 4), respectively. It is found that when the flow goes through the upstream contraction region, negative v_y and positive v_z results indicate a compression and extensional force applied to the flow streamlines of (x, 0.4, 0) and (x, 0, 4), respectively. For the case of a l_2 value of 5 mm, a non-vanishing v_z is observed just before the die exit in comparison with that for the l_2 value of 80 mm. This corresponds to the much larger elongational stress τ_{zz} for the flow

layer shown in Fig. 5-6(f). In the *y* direction (red line) the impact seems to be much less, and a similar overall behavior is noted.

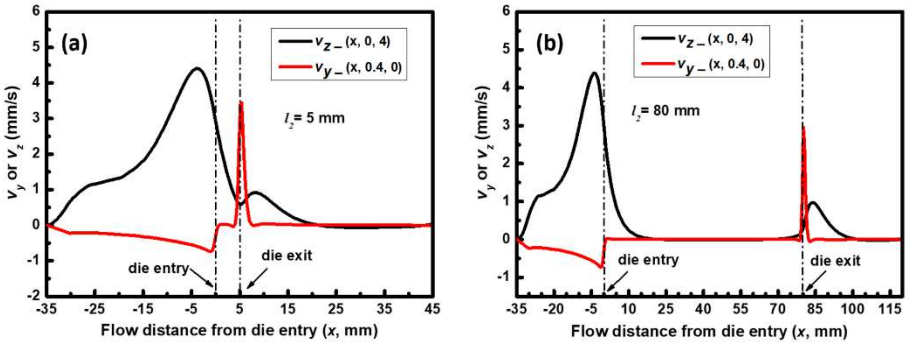


Figure 5-8. The transversal velocity (v_y) profile at the central flow streamline of y=0.4 mm ((x, 0.4, 0)) and the lateral velocity (v_z) profile at the flow streamline of z=4 mm ((x, 0, 4)) along the flow distance for the case of die length l_2 of 5 mm (a) and 80 mm (b) at the flow rate of 620 $mm^3 s^{-1}$; PP melt flow at 200 °C; model parameters: Table 1; details on conditions: Table 5-2.

Figure 5-9 shows the variation trends of the transversal v_y and lateral v_z velocity components along the free surface flow layers (so out of the die) for l_2 values of 5, 20 and 80 mm. The general trend observed is that v_z has a much lower damping rate after the die exit than v_y, which is consistent with our previous report [36]. In Fig. 5-9(a), a larger v_y for a l_2 value of 5 mm at the same axial position is observed compared to the other two l_2 values. In contrast, the flow coming out of a die with l_2 equal to 80 mm has the largest v_z value along the free surface flow layer, as shown in Figure 5-9(b). This explains the previously mentioned opposite varying tendency of the extrudate swell behavior in extrudate width and height directions upon varying l_2 (*cf.* Fig. 5-3). In addition, in the subplot of Fig. 5-9 (a), a negative value for v_y is only observed for a l_2 of 80 mm. This confirms the occurring of a small shrinkage flow after the initial swelling behavior in the middle height direction [37].

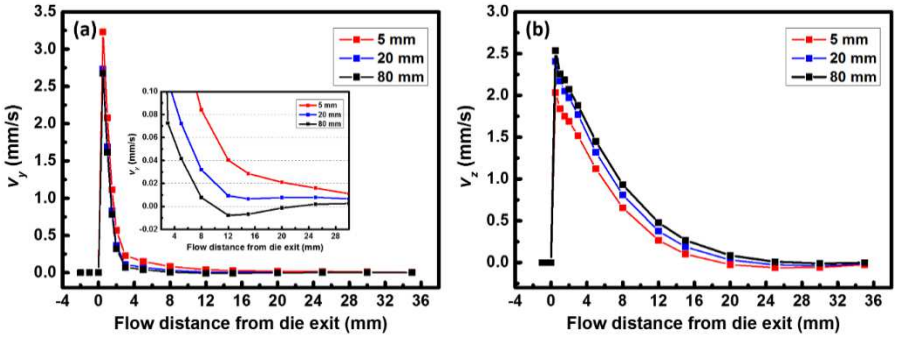


Figure 5-9. (a) Velocity component v_y along the die wall and the free surface flow layer direction in the middle plane z=0 mm and (b) velocity component v_z along the side wall and free surface in the middle plane y=0 mm for different l_2 values (5 mm, 20 mm and 80 mm) at a flow rate of 620 mm^3 s^{-1}; PP melt flow at 200 °C; model parameters: Table 5-1; details on conditions: Table 5-1.

5.3.3. Parametric study of the extrudate swell

As discussed above and specifically illustrated in Fig. 5-5, a strong axial elongational effect is applied to flow melts with a converging flow region. Considering ε predominantly controlling the extensional viscosity, it is interesting to study the effect of this parameter in the multimode PTT model combined with the die length effect on the extrudate swell behavior. Figure 5-10 therefore demonstrates a sensitivity analysis of the material parameter ε_3 on the anisotropy swell behavior with respect to the cases of l_2= 80 mm (subplots a-c) and l_2= 5 mm (subplots d-f) at a flow rate of 620 mm^3/s. These results complement our sensitivity analysis for the fully developed case, as covered in previous work [37].

Decreasing ε_3 from 0.65 to 0.05 (l_2= 80 mm) facilitates increasing the three types of the extrudate swell ratio B_1, B_2 and B_3, as shown in Fig. 5-10(a)-(c). This agrees well with the corresponding variations of the extrudate swell behavior for the fully devel-

oped flow thus with a sufficiently large l_2 >> 80 mm in our previous work [37], again highlighting the relevance of the threshold value of 80 mm as put forward in the present work. For example, with the parameter ε_3 of 0.05, the final width B_1 and

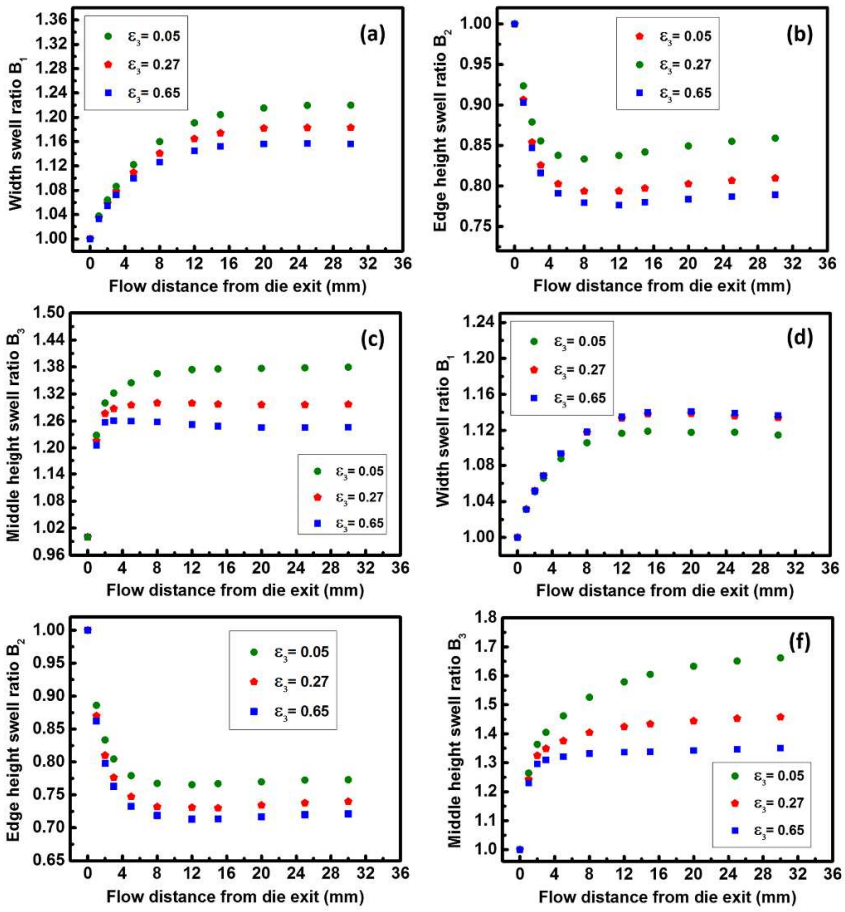


Figure 5-10. Effect of parameter ε_3 in mode 3 of PTT model on three types of the extrudate swell behavior of PP flow at the flow rate of 620 mm^3/s regarding the cases of l_2= 80 mm (a-c) and l_2= 5 mm (d-f). The red solid symbols indicate the results obtained from the original ε_3= 0.27 parameters in Table 5-1. Green and blue symbols represent the cases of ε_3= 0.05 and ε_3= 0.65.

middle height swell ratio B_3 are 1.22 and 1.38 with l_2= 80 mm, and 1.23 and 1.36 for the fully developed flow. As the die length decreases to 5 mm (Fig. 5-10(d)-(f)) a significant sensitivity is again confirmed, specifically for lower ε_3 values. A smaller ε_3 formally indicates a larger branching degree and thus a larger extensional viscosity [37]. It follows that decreasing ε_3 from the original value of 0.27 in Table 5-1 to 0.05 results in the swell ratio B_3 growing sharply from 1.47 to 1.66, as shown in Fig. 5-10(f). In contrast, an increase of 0.08 of the swell ratio B_3 is noted in Fig. 10(c) with l_2 = 80 mm.

Note that the width swell ratio B_1 in Fig. 5-10(d) shows a small decreasing tendency as the parameter ε_3 decreases from 0.27 to 0.05 with l_2 = 5 mm, which is opposite to the case with l_2 = 80 mm in Fig. 5-10(a). The reason is the aforementioned large swell behavior in the middle height direction (Fig. 5-10(f)), which significantly limits the swell behavior in the extrudate width direction to maintain mass conservation. Overall it can thus be concluded that ε_3 determines the level of swelling anisotropy. In other words, for a polymer melt with a low ε_3 one needs to pay more attention to the optimization of the l_2 design parameter.

5.4. Conclusions

Three-dimensional effects of upstream contraction flow on polymer extrudate swell from slit dies are investigated through numerical simulations for different flow rates and thus residence times. By increasing the die length l_2 from low to high values the middle height swell ratio significantly decreases until a constant value is approached for sufficiently long dies in which fully developed flow is achieved. Conversely, the width swell and edge height ratio increase upon increasing l_2. The area extrudate swell

ratio is however only affected to a limited extent, especially for lower flow rates. This implies that an identification of possible anisotropy should in general not be based on the area swell ratio. Furthermore, a method to obtain an extrudate product with a less uneven profile is to elongate the die, especially for polymer melts that experience large extensional deformations.

The l_2 value does not significantly affect the normal stress distribution until the polymer flow reaches the die entry through the contraction flow channel. Downstream the die entry, a significantly larger magnitude of the normal stresses τ_{xx} and τ_{yy} in the flow region close to the top of the die wall is observed upon decreasing l_2, indicating larger extensional and compression forces being applied to the flowing melt. However, an oppositely varying trend is noted regarding τ_{xx} and τ_{zz} in vicinity of the side wall of the die, further highlighting the relevance of 3D simulations in which the side wall effects are fully accounted for. Out of the die exit, the big difference of the stress redistribution behavior caused by the variations of the die length l_2 is shown to demonstrate the corresponding anisotropy swell behavior mentioned above.

The similar final extrudate average axial velocity regardless of the l_2 value is consistent with the similar area swell ratios and implies a similar axial velocity redistribution behavior. In addition, the evolution of the transversal velocity v_y and lateral velocity v_z components after the die exit directly reveal the opposite varying trend of the corresponding swell behavior in the extrudate middle height and width direction with increasing l_2 value.

Our study shows that a method to obtain an extrudate product with a less uneven extrudate profile could be made by properly elongating the die, especially for polymer melts that experience large extensional deformations. However, from the view of an

industrial aspect, at the same time the pressure drop will increase and so does the potential viscous dissipation thus the possible polymer degradations. Therefore, a compromise combined with both aspects seems to be necessary for the application of the extrusion processing.

REFERENCES

1. Lee, W.S. and H.Y. Ho, *Experimental study on extrudate swell and die geometry of profile extrusion.* Polymer Engineering & Science, 2000. **40**(5): p. 1085-1094.
2. Wieme, T., et al., *The relevance of material and processing parameters on the thermal conductivity of thermoplastic composites.* Polymer Engineering & Science, 2018. **58**(4): p. 466-474.
3. Wieme, T., et al., *Effect of Matrix and Graphite Filler on Thermal Conductivity of Industrially Feasible Injection Molded Thermoplastic Composites.* Polymers, 2019. **11**(1): p. 87.
4. Huang, H.X. and J.C. Li, *Fast online acquisition and analysis for parison swell and sag in blow molding.* Journal of applied polymer science, 2006. **101**(4): p. 2399-2406.
5. Konaganti, V.K., et al., *Extrudate swell of a high-density polyethylene melt: II. Modeling using integral and differential constitutive equations.* Journal of Non-Newtonian Fluid Mechanics, 2015. **225**: p. 94-105.
6. Drabek, J., M. Zatloukal, and M. Martyn, *Effect of molecular weight on secondary Newtonian plateau at high shear rates for linear isotactic melt blown polypropylenes.* Journal of Non-Newtonian Fluid Mechanics, 2018. **251**: p. 107-118.
7. Chougale, S., et al., *Non-isothermal analysis of extrusion film casting using multi-mode Phan-Thien Tanner constitutive equation and comparison with experiments.* Rheologica Acta, 2018. **57**(6-7): p. 493-503.
8. Tian, H., et al., *Study on extrudate swell of polypropylene in double-lumen micro profile extrusion.* Journal of Materials Processing Technology, 2015. **225**: p. 357-368.
9. Konaganti, V., et al., *Extrudate swell of high density polyethylenes in slit (flat) dies.* International Polymer Processing, 2016. **31**(2): p. 262-272.
10. Spanjaards, M., M. Hulsen, and P. Anderson, *Transient 3D finite element method for predicting extrudate swell of domains containing sharp edges.* Journal of Non-Newtonian Fluid Mechanics, 2019. **270**: p. 79-95.
11. Robertson, B., et al., *Theoretical prediction and experimental measurement of isothermal extrudate swell of monodisperse and bidisperse polystyrenes.* Journal of Rheology, 2017. **61**(5): p. 931-945.
12. Kiriakidis, D. and E. Mitsoulis, *Viscoelastic simulations of extrudate swell for an HDPE melt through slit and capillary dies.* Advances in Polymer Technology, 1993. **12**(2): p. 107-117.
13. Comminal, R., et al., *Vortex behavior of the Oldroyd-B fluid in the 4-1 planar contraction simulated with the streamfunction–log-conformation formulation.* Journal of Non-Newtonian Fluid Mechanics, 2016. **237**: p. 1-15.
14. Clemeur, N., R. Rutgers, and B. Debbaut, *Numerical simulation of abrupt contraction flows using the Double Convected Pom–Pom model.* Journal of non-newtonian fluid mechanics, 2004. **117**(2-3): p. 193-209.

15. Boger, D., *Viscoelastic flows through contractions.* Annual review of fluid mechanics, 1987. **19**(1): p. 157-182.
16. Saramito, P. and J. Piau, *Flow characteristics of viscoelastic fluids in an abrupt contraction by using numerical modeling.* Journal of non-newtonian fluid mechanics, 1994. **52**(2): p. 263-288.
17. Debbaut, B., J. Marchal, and M. Crochet, *Numerical simulation of highly viscoelastic flows through an abrupt contraction.* Journal of Non-Newtonian Fluid Mechanics, 1988. **29**: p. 119-146.
18. Tomkovic, T., E. Mitsoulis, and S.G. Hatzikiriakos, *Contraction flow of ionomers.* Journal of Non-Newtonian Fluid Mechanics, 2018. **262**: p. 131-141.
19. Tomkovic, T., E. Mitsoulis, and S.G. Hatzikiriakos, *Contraction flow of ionomers and their corresponding copolymers: Ionic and hydrogen bonding effects.* Physics of Fluids, 2019. **31**(3): p. 033102.
20. Schoonen, J., *Determination of rheological constitutive equations using complex flows.* 1998: Technische Universiteit Eindhoven Eindhoven.
21. García-Rejón, A., R. DiRaddo, and M. Ryan, *Effect of die geometry and flow characteristics on viscoelastic annular swell.* Journal of non-newtonian fluid mechanics, 1995. **60**(2-3): p. 107-128.
22. Musil, J. and M. Zatloukal, *Historical review of secondary entry flows in polymer melt extrusion.* Polymer Reviews, 2019. **59**(2): p. 338-390.
23. Luo, X.L. and R. Tanner, *Finite element simulation of long and short circular die extrusion experiments using integral models.* International journal for numerical methods in engineering, 1988. **25**(1): p. 9-22.
24. Han, C.D. and K.U. Kim, *Influence of reservoir diameter on the melt elasticity in capillary flow.* Polymer Engineering & Science, 1971. **11**(5): p. 395-400.
25. Goublomme, A., B. Draily, and M. Crochet, *Numerical prediction of extrudate swell of a high-density polyethylene.* Journal of non-Newtonian fluid mechanics, 1992. **44**: p. 171-195.
26. Béraudo, C., et al., *A finite element method for computing the flow of multi-mode viscoelastic fluids: comparison with experiments.* Journal of non-newtonian fluid mechanics, 1998. **75**(1): p. 1-23.
27. Luo, X.-L. and R. Tanner, *A streamline element scheme for solving viscoelastic flow problems. Part I. Differential constitutive equations.* Journal of non-newtonian fluid mechanics, 1986. **21**(2): p. 179-199.
28. Luo, X.-L. and R. Tanner, *A streamline element scheme for solving viscoelastic flowproblems part II: integral constitutive models.* Journal of Non-Newtonian Fluid Mechanics, 1986. **22**(1): p. 61-89.
29. Kiriakidis, D., et al., *A study of stress distribution in contraction flows of anb LLDPE melt.* Journal of non-newtonian fluid mechanics, 1993. **47**: p. 339-356.
30. Ansari, M., S.G. Hatzikiriakos, and E. Mitsoulis, *Slip effects in HDPE flows.* Journal of Non-Newtonian Fluid Mechanics, 2012. **167**: p. 18-29.
31. Mompean, G. and M. Deville, *Unsteady finite volume simulation of Oldroyd-B fluid through a three-dimensional planar contraction.* Journal of Non-Newtonian Fluid Mechanics, 1997. **72**(2-3): p. 253-279.

32. Ansari, M., E. Mitsoulis, and S.G. Hatzikiriakos, *Capillary extrusion and swell of a HDPE melt exhibiting slip.* Advances in Polymer Technology, 2013. **32**(S1).
33. Robertson, B., *Understanding Extrudate Swell: From Theoretical Rheology to Practical Processing*. 2019, Durham University.
34. Sunwoo, K.B., et al., *Three-dimensional viscoelastic simulation of coextrusion process: comparison with experimental data.* Rheologica Acta, 2002. **41**(1-2): p. 144-153.
35. Sirakov, I., et al., *Three-dimensional numerical simulation of viscoelastic contraction flows using the Pom–Pom differential constitutive model.* Journal of Non-Newtonian Fluid Mechanics, 2005. **126**(2-3): p. 163-173.
36. Tang, D., et al., *Isothermal flow of neat polypropylene through a slit die and its die swell: Bridging experiments and 3D numerical simulations.* Journal of Non-Newtonian Fluid Mechanics, 2019. **266**: p. 33-45.
37. Tang, D., et al., *Three-dimensional flow simulations for polymer extrudate swell out of slit dies from low to high aspect ratios.* Physics of Fluids, 2019. **31**(9): p. 093103.
38. Tian, H., et al., *Effect of die lip geometry on polymer extrudate deformation in complex small profile extrusion.* Journal of Manufacturing Science and Engineering, 2017. **139**(6): p. 061005.
39. Xue, S. C., N. Phan-Thien, and R. Tanner, *Numerical study of secondary flows of viscoelastic fluid in straight pipes by an implicit finite volume method.* Journal of Non-Newtonian Fluid Mechanics, 1995. **59**(2-3): p. 191-213.
40. Phan-Thien, N., *A nonlinear network viscoelastic model.* Journal of Rheology, 1978. **22**(3): p. 259-283.
41. Rodríguez, L.F.C., *Modification of the PTT Model and its Application for the Predictions of Elongational Viscosity of Polypropylenes-Edición Única.*
42. Guénette, R. and M. Fortin, *A new mixed finite element method for computing viscoelastic flows.* Journal of non-newtonian fluid mechanics, 1995. **60**(1): p. 27-52.
43. Konaganti, V.K., et al., *The effect of damping function on extrudate swell.* Journal of Non-Newtonian Fluid Mechanics, 2016. **236**: p. 73-82.
44. Behzadfar, E., et al., *Extrudate swell of HDPE melts: I. Experimental.* Journal of Non-Newtonian Fluid Mechanics, 2015. **225**: p. 86-93.
45. Liang, J. and J. Ness, *The melt die-swell behaviour during capillary extrusion of LDPE/PP blends.* Polymer testing, 1998. **17**(3): p. 179-189.
46. Mu, Y., G. Zhao, and C. Zhang, *Numerical investigation of die geometry effect on LDPE annular extrudate swell.* Journal of applied polymer science, 2010. **117**(1): p. 91-109.

Chapter 6

Evaluating the exit pressure method for measurements of normal stress difference at high shear rates by 3D modelling

A challenge for polymer rheology is the reliable determination of shear dependent first normal stress difference (N_1 values) at high shear rates (>10 s^{-1}). Here we evaluate the correctness of the commonly applied exit pressure method focusing on polypropylene, and high and low density polyethylene melts at 200°C. It is demonstrated that the linear extrapolation of pressure values toward the die exit, which is a key step in the application of the exit pressure method, is affordable to determine N_1 values despite that these extrapolated exit pressure values are characterized by a relative deviation of 25-40%. The validity of the exit pressure method is further supported by an excellent match with rheological data from the Laun rule (exponent close to 0.7) and a representative simulation of extrudate swelling data in the width and height direction, considering tuned parameters for the Phan-Thien-Tanner (PTT) constitutive model. Also, the absence of significant viscous heating effect near the die exit is highlighted based on numerical analysis.

6.1. Introduction

A good understanding of the viscoelastic properties of polymer melts is of great importance to design and control polymer flow for processing methods such as extrusion and injection molding [1-4]. In polymer rheology most focus has been on the melt behavior in simple flow configurations. For fluids undergoing steady shear flow, e.g. with *x* being the axial direction as is the case for the slit die mounted to an extruder in Fig. 6-1, the stress components can be related to three well-defined material functions that are depending on the shear rate $\dot{\gamma}$ thus the velocity profile: (i) the shear/dynamic viscosity η, (ii) the first normal stress coefficient Ψ_1, and (iii) the second normal stress coefficient Ψ_2 [5]. These material functions are rheometric functions that can be determined based on measurements of the shear stress (σ_{xy}), the first normal stress difference N_1 ($\sigma_{xx} - \sigma_{yy}$)), and the second normal stress difference N_2 ($\sigma_{yy} - \sigma_{zz}$) as function of $\dot{\gamma}$ [6].

Such rheological measurements can be challenging as conventional rotational rheometers are characterized by an effective upper limit that rarely surpasses frequencies of 10^3 s^{-1} for polymer solutions and 10 s^{-1} for polymer melts, due to "melt" edge fracture [7, 8]. This type of measurements fails to meet the industrial requirements because most applications with polymer melts are carried out at $\dot{\gamma}$ values significantly higher than 10-10^3 s^{-1}. This explains why a capillary rheometer is widely employed for the viscosity or shear stress measurement in the high $\dot{\gamma}$ range, although a cone-partitioned plate rheometer facilitates access to higher $\dot{\gamma}$ [9]. In any case, for normal stress measurements, high accuracy at high $\dot{\gamma}$ still remains a vital issue. In the present work, focus is on the reliable determination of N_1 values.

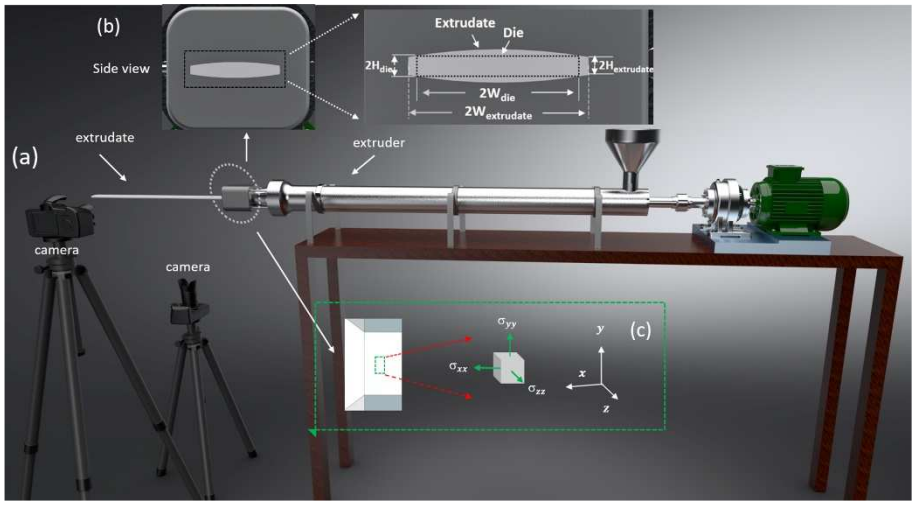


Figure 6-1. (a) Principle of extrudate flow from a slit die mounted on an extruder, hence, die swell; (b) zoom of the die cross section; (c) the associated normal stresses for an infinitesimally small unit to define the first ($N_1 = \sigma_{xx} - \sigma_{yy}$) and second ($N_2 = \sigma_{yy} - \sigma_{zz}$) normal stress difference. The present work focuses on the reliable determination of N_1.

To measure N_1, most commonly a continuous in-line exit pressure method is considered [10], in which focus is on the pressure value at the end of the die (Figure 6-1). This exit pressure value cannot be directly measured as it is impossible to mount a pressure transducer exactly at the die exit. Instead the exit pressure needs to be obtained according to extrapolations of measured pressure profiles along the axial flow (x) direction to the die exit [3, 11]. Compared with the capillary rheometer, the major advantages of a slit rheometer include not only to directly obtain the pressure gradient along the flow distance without in principle a Bagley correction or entry effect but also a direct measurement of N_1 in comparison with a combination of N_1 and N_2 values with a capillary rheometer [7, 12].

It should be admitted that since its inception in the early 1960s the exit pressure method has been controversial [10]. As the exit pressure is much smaller than the

pressure readings in the die channel (*e.g.* $\leq$2% of the starting value) [10, 11], small pressure fluctuations because of a viscous heating effect, pressure-dependent viscosities and sensitivities of the pressure transducers might render a significant influence on the exit pressure. For example, Lodge *et al.* [13] questioned the exit pressure method as means of a N_1 measurement because they obtained negative exit pressure values upon extrapolation. In addition, another disagreement in the field is regarding the assumption of fully developed shear flow down to the exit by ignoring the flow disturbance caused by the velocity rearrangement behavior. Specifically the magnitude of error or whether these flow perturbation effects can be ignored is unclear [14].

For example, Boger *et al.* [7] comprehensively studied the exit pressure theory including an extra term corresponding to the flow disturbance near the die exit in the analytic derivations. They pointed out that a detailed understanding of the velocity rearrangement profile is necessary before using the exit pressure method for flowing fluids with low Reynold (Re) number. Furthermore, Baird *et al.* [3] reported that the normal stress difference data from the exit pressure method agree with that from the rotational rheometer at low $\dot{\gamma}$ (<10 s^{-1}), but an obvious difference is reported at relatively high $\dot{\gamma}$. The results of Han *et al.* [15-19] on the other hand strongly support the use of the exit pressure method with the assumption of fully developed flow down to die exit based on experimental observations. These authors compared the normal stress difference data of several polymer melts and solutions as measured by the exit pressure method with those measured by a rotational rheometer, and found a rather good agreement [16]. The experimental measurements presented by Chan *et al.* [10] and two-dimensional (2D) numerical simulations performed by Tuna *et al.* [14] further support the work of Han *et al.* However, Choplin *et al.* [20, 21] dismissed the

validity of the exit pressure method for determining N_1 under the fully developed flow assumption. They reported a significant deviation of the two pressure readings closest to the exit from the presumed linear pressure profile for a polyisobutylene (PIB) solution in a capillary die, especially at higher shear stresses. These authors attributed the discrepancy to the velocity rearrangement or viscous dissipation near the exit.

It is thus clear that a further investigation on the validity of the exit pressure method to determine N_1 is still worthwhile. In the present work, a combined experimental and three-dimensional (3D) flow modeling study is presented to better quantify the relation of $\dot{\gamma}$ and the success of the exit pressure method. It should be stressed that 3D numerical modeling, as only been performed more recently, is able to have a detailed insight into the flow behavior especially close to the die exit and outside the die defining the extrudate swell behavior [22, 23]. For example, in our previous work, we highlighted that for polypropylene (PP) melt at 200 °C increasing the aspect ratio of a slit die strongly influences the swelling behavior in the three directions and delays the establishment of the equilibrium swelling position. 3D die swell experimental and simulated data are thus additional responses to study the relation of $\dot{\gamma}$ and normal stress differences, therefore opening a new pathway for validation of experimental techniques such as the exit pressure method.

In the present work, a combined experimental and three-dimensional (3D) flow modeling study is presented to better quantify the relation of $\dot{\gamma}$ and the success of the exit pressure method, considering polypropylene (PP), low density polyethylene (LDPE), high density polyethylene (HDPE), and PP composite with 20% graphite fillers (PP/20GP) as melting materials. 3D numerical modeling, as only performed more recently, allows a detailed insight into the flow behavior especially close to the

die exit [22-25]. 3D experimental and simulated data on extrudate swelling are thus additional responses to study the relation of $\dot{\gamma}$ and normal stress differences, therefore opening a new pathway for validation of experimental techniques.

In a first step, we compare the N_1 values as obtained by the exit pressure method with those following from conventional rotational rheometric analysis and the empirical Laun rule [26]. In a second step, the 3D numerical simulations for the extrudate swell behavior are validated against experimental observations, with the viscoelastic material parameters tuned based on literature and N_1 data. In a third step, the exit pressure values with and without the assumption of fully developed flow down to die exit are numerically compared to elucidate the possible contribution of velocity redistributions, thereby the effect on the exit pressure method. In a final step, we numerically focus on the possible impact of a viscous heating effect.

6.2. Materials and experimental characterization

6.2.1. Materials

Four polymer melts, namely polypropylene (PP, SABIC 575P) melt, low density polyethylene (LDPE, Lyondellbasell Lupolen 2420H) melt, high density polyethylene (HDPE, SABIC B5933) melt, and PP melt with mass 20% graphite fillers (PP/20GP, Asbury 3807) were used with a set temperature of 200 °C. For the pure polymer melts, pellets were directly available. The PP/20GP composite pellets were in contrast made in-house employing twin-screw extrusion with a screw rotational rate of 90 rpm and a processing temperature window of 160–210 ^{o}C and using a chopping machine. The polymer melts were all extruded from a single screw extruder (P. Brabender 19 with a screw diameter D_s of 19 mm, L_s/D_s of 25; L_s: screw length) combined with a slit die

(die length: 220 mm, die height (H_{die} in Fig. 6-1(b)): 2 mm, and die width (W_{die} in Fig. 6-1(b)): 20 mm) at a screw speed of 10–120 rpm at 200 °C. Important characteristics of the polymer materials are listed in Table 6-1.

6.2.2. Mass flow rate and pressure measurements

The mass flow rates are obtained by collecting extrudates in a given time period. Three pressure transducers were mounted along the die length direction and the distances from the die exit are 20 mm (measurement of P_1 value), 120 mm (measurement of P_2 value), and 170 mm (measurement of P_3 value). Before the pressure measurement, calibration was carried out for each transducer.

Table 6-1. Material characteristics.

Material	Density ($g \cdot cm^{-3}$; 25 °C)	Zero-shear rate viscosity (Pa·s; 200 °C)	Power law index
LDPE	0.924	8.49×10^3	0.42
HDPE	0.959	5.12×10^4	0.43
PP	0.905	2.24×10^3	0.60
PP/20GP	0.965	4.12×10^4	0.42

6.2.3. Conventional rheological measurements

An ARES (TA, Discovery HR-3, US) rheometer was used to perform the temperature-dependent rheological measurements of polymer melts at 180, 200 and 230 °C. The dynamic small amplitude oscillatory measurements were performed with a frequency sweep in an angular velocity (ω) range of 0.1–500 rad s^{-1}. The steady shear mode tests were carried out within a small shear rate range of 0.01–5 s^{-1} to avoid melt edge

fracture. The data was corrected for non-linearity of the shear rate dependent on the radius. Disk samples with a diameter of 25 mm and a thickness of 2 mm were made using compression.

To enable an evaluation of conventional analysis tools for normal stress differences, focus has been also on the determination of $N_1 - N_2$ by a parallel plate geometry mode [12, 27]. For polymers, generally it holds that $N_1 > 0$ but $N_2 < 0$, and $|N_1| \approx 10$ $|N_2|$ [27, 28]. The $|N_2|/|N_1|$ value for both HDPE and PP is claimed to be 0.1 (200 °C) [29, 30], which is consistent with our recent simulation results [24]. On the other hand, a value of 0.2 has been put forward for LDPE melt as this polymer is characterized by branched chains [28]. For composites, it has been pointed out that $|N_2|/|N_1|$ increases further [31, 32]. Consequently, the ratio is assumed to be 0.2. It should be stressed that these ratios are ball-park values and are fitting parameters in practice, implying the less fundamental nature of this determination method.

For comparison, the empirical Laun rule [26] is also utilized to assess N_1 through relating the dynamic moduli G' (storage modulus) and G'' (loss modulus) for simple steady shear flow in the conventional rheometer:

$$N_1(\dot{\gamma} = \omega) = 2G' \left[(1 + \left(\frac{G'(\omega)}{G''(\omega)}\right)^2\right]^a \qquad (6\text{-}1)$$

Originally the exponent α was given a value of 0.7, whereas later on various works reported values mainly ranging from 0 to 0.7 [3, 27, 33, 34]. In this work, for simplification and without loss of generality, we only adopt $\alpha = 0$ and 0.7, corresponding to a minimum and maximum N_1 by means of the Laun rule.

6.2.4. Slit die viscosity measurements

The shear viscosity η for a slit die under ideal laminar and isothermal conditions is given by the ratio of the shear stress at the wall (σ_w) and the shear rate at the wall ($\dot{\gamma}_w$). Considering the Rabinowitch correction it follows that [35]:

$$\sigma_w = \frac{H}{(1+e)} * \frac{\partial p}{\partial L} \qquad (6\text{-}2)$$

$$\dot{\gamma}_w = \dot{\gamma}_a * \left(\frac{2n+1}{3n}\right) = \left(\frac{6Q}{2W*(2H)^2}\right)\left(\frac{2n+1}{3n}\right) \qquad (6\text{-}3)$$

in which H is the half die height, e the ratio of die height to width, $\frac{\partial p}{\partial L}$ the pressure gradient along the flow direction, Q the volumetric flow rate, and W the half die width, $\dot{\gamma}_a$ the apparent shear rate, and n the power law index of the non-Newtonian melt which is defined as $n = d\ln\sigma_w / d\ln\dot{\gamma}_a$. The n values are given for completeness in Table 6-1. Therefore, the calculated $\dot{\gamma}_w$ value for the four polymer melts lies in a range of around 10 to 100 s^{-1} due to the single extrusion screw speed of 10-120 rpm used in this study.

6.2.5. Exit pressure method for measurement of first normal stress difference

The (conventional) exit pressure theory as used for measuring N_1 of polymer melt flow through a planar geometry is based on the macroscopic momentum balance theory [36]. More in detail, assuming that fully developed flow is remained until the die exit and that the inertial effect can be neglected due to a low Reynolds (*Re*) number, Han [16] and Davies *et al.* [37] derived the following analytic expression linking the exit pressure P_{ex} and N_1:

$$N_1 = P_{ex} + P_{ex}\frac{d\lg P_{ex}}{d\lg \sigma_w} \qquad (6\text{-}4)$$

Hence, the experimental determination of the relation between P_{ex} and σ_w is essential.

6.2.6. Extrudate swell measurement

Two high-definition cameras were used to capture the extrudate swell behavior from side and bottom view considering a slit die as depicted in Fig. 6-1. The details about the measurement method can be found in our previous work focusing solely on the swelling of PP flow in Chapter 3. Two swell ratios are considered in the present work, namely B_1 and B_2 corresponding to the swell ratio in the width and edge height direction of the extrudate:

$$B_1 = \frac{W_{-extrudate}}{L_{-die}} \qquad (6\text{-}5)$$

$$B_2 = \frac{H_{-extrudate}}{H_{-die}} \qquad (6\text{-}6)$$

6.3. Modelling principle for multidimensional flow characteristics

6.3.1. Details on the governing equations and constitutive model

In this work, most focus is on isothermal flow conditions, but also non-isothermal conditions are included to evaluate the relevance of viscous heating near the die exit. Assuming incompressible fluids under steady creeping laminar flow conditions without inertial effects and gravity force, the required continuity and momentum and energy equations are given by [33, 38]:

$$\nabla \cdot \boldsymbol{v} = 0 \qquad (6\text{-}7)$$

$$-\nabla p + \nabla \cdot \boldsymbol{\tau} = 0 \qquad (6\text{-}8)$$

$$\rho c_p \boldsymbol{v} \cdot \nabla T = k\nabla^2 T + \boldsymbol{\tau} : \nabla \boldsymbol{v} \qquad (6\text{-}9)$$

in which $\boldsymbol{v}$ represents the velocity vector**,** p the isotropic pressure, k the thermal conductivity and $\boldsymbol{\tau}$ the extra stress tensor.

6.3.1.1. Interpretation of the exit pressure theory

It should be further noted that the pressure value *P* corresponds to the normal force T_{yy} acting on an unit area surface of flow [12, 18]:

$$T_{yy}(x,y) = -p(x,y) + \tau_{yy}(x,y) \qquad (6\text{-}10)$$

in which $p(x,y)$ is the isotropic pressure and $\tau_{yy}(x,y)$ the extra normal stress. For fully developed flow, $|T_{yy}|$ is constant and expected to be much larger than $|\tau_{yy}|$, so that the contribution of T_{yy} only comes from $p(x,y)$. However, with flow disturbance near the die exit, it is no longer reasonable to ignore the contribution of τ_{yy} to the normal stress T_{yy} or the exit pressure [18]. Under such conditions the exit pressure P_{ex} needs to be updated:

$$-P_{ex} = T_{yy} = -\frac{1}{H}\int_0^H N_1\, dy - \frac{1}{H}\int_0^H y \frac{\partial \tau_{xy}}{\partial x} dy \qquad (6\text{-}11)$$

The second right term reveals the influence induced by the flow disturbance [3]. The detailed analysis can be found in the work of Boger *et al.* [7]. Differentiating with respect to σ_w, Eq. (11) can be rewritten as:

$$N_1 = P_{ex} + \tau_w \frac{\partial P_{ex}}{\partial \tau_w} + \frac{\partial}{\partial \tau_w}{\tau_w}^2 \frac{S}{H}\left(1 - \int_0^1 f(\theta, \tau_w, Re) d\theta\right) \qquad (6\text{-}12)$$

in which S is the length of the flow disturbance region and $\theta = x/S$ $(0 \le x \le S)$.

The determination of the integral term $\int_0^1 f(\theta, \tau_w, Re) d\theta$ is challenging, but in the absence of a velocity rearrangement effect f equals 1 [16], so that Eq. 6-12 reduces to Eq. 6-4. Upon using detailed (3D) simulations, one indirectly accounts for this functional form *f*. Hence, such 3D simulations allow to assess if the pressure variation differs from the linear ideal one.

6.3.1.2. PTT constitutive model to describe the viscoelastic behavior

The above system of conservation equations is not closed for non-Newtonian fluids due to the shear dependent extra stress $\boldsymbol{\tau}$ [39], which is for a viscoelastic constitutive model split into a purely viscous part, $\boldsymbol{\tau}_N$, and a viscoelastic part, $\boldsymbol{\tau}_p$. $\boldsymbol{\tau}_N$ is solved by the generalized Newtonian flow model and $\boldsymbol{\tau}_p$ is solved by the basic viscoelastic differential (or integrated) constitutive model [40, 41]. Note that $\boldsymbol{\tau}_p$ is calculated as a sum of *N* individual $\boldsymbol{\tau}_{pi}$ contributions:

$$\boldsymbol{\tau}_p = \sum_{i=1}^{N} \boldsymbol{\tau}_{pi}, \qquad (6\text{-}13)$$

with each individual contribution $\boldsymbol{\tau_{pi}}$ revealed by the differential Phan-Thien-Tanner (PTT) constitutive equation [24]:

$$\exp\left[\frac{\varepsilon_i \lambda_i}{\eta_i} \mathrm{tr}(\boldsymbol{\tau}_{pi})\right] \boldsymbol{\tau}_{pi} + \lambda_i \left[(1 - \frac{\xi_i}{2}) \overset{\frown}{\boldsymbol{\tau}_{pi}} + \frac{\xi_i}{2} \overset{\smile}{\boldsymbol{\tau}_{pi}}\right] = 2\eta_i \mathbf{D} \qquad (6\text{-}14)$$

in which λ_i and η_i are the ith (i=1, …, N) relaxation time and viscosity, representing the linear rheological properties of melts. The non-linear ξ_i and ε_i parameters (i=1, …, N) determine the shear and extensional behavior of melts. $\overset{\frown}{\boldsymbol{\tau}_{pi}}$ and $\overset{\smile}{\boldsymbol{\tau}_{pi}}$ are the ith (i=1, …, N) upper and lower convected time derivatives of $\boldsymbol{\tau}_{pi}$, and **D** is the deformation tensor rate.

6.3.1.3. Additional input for non-isothermal modelling

For the computations considering the viscous heating effect, non-isothermal flow simulations were carried out and compared to isothermal results (200 °*C*), applying the conservation equations of mass, momentum, and energy [42]. The temperature-dependent viscosity η is obtained with the Arrhenius temperature-shifting function [42, 43]:

$$\eta = \sum_{i=1}^{N} \eta_i exp\left[\frac{E}{R_g}\left(\frac{1}{T-T_a} - \frac{1}{T_r-T_a}\right)\right] \qquad (6\text{-}15)$$

with the reference temperature T_r equal to 200 ^oC and T_a the absolute zero temperature being 273.15 ^oC, E the activation energy, and R_g the universal gas constant. In addition, focus has been on the calculation of the Nahme number:

$$Na = \frac{\eta E U^2}{k R_g {T_r}^2} \qquad (6\text{-}16)$$

in which η is the nominal viscosity and U the average velocity in the die. For very low *Na* number, ones expect a negligible impact of temperature variations.

6.3.1.4. Geometry and boundary conditions

In agreement with previous work [25], the 3D flow domain is given in Fig. D-2 with one quarter of the flow channel considered for all simulations to reduce the computational cost due to the symmetry planes. Briefly, at the inlet, a fully developed flow with a certain flow rate is considered. At the die walls, a non-slip condition for the velocity field is prescribed: $v_n = v_t = 0$ (mm/s). A free surface flow developed outside the die exit is unknown a priori. Force conditions: $f_t = f_n = 0$ (N) are however

set at the outlet of the flow domain, with the subscript *n* and *t* representing the normal and tangential component of the force and velocity.

For the non-isothermal modeling approach, a temperature of 200 ºC is applied at the inlet and die wall and 2D simulations are considered to lower the computational cost. Zero heat flux *q* is set for simplicity on the free surface and die outlet [41] as we are in the present work only interested in the temperature variations very close to the die exit to evaluate the exit pressure method.

For the finite element mesh arrangement, we selected a mesh/grid pattern that progressively becomes more refined upon approaching the singularity at die exit. The grid consists of 12000 elements and 14364 nodes. The refined mesh pattern is shown in Fig. D-3 in the Appendix D, in which we create denser grids near the die exit and wall: 17000 elements and 19868 nodes. Fig. D-4 in the Appendix D shows the analysis of the mesh independence on two types of extrudate swell ratios (B_1 and B_2; Eq. 6-5 and 6-6) of HDPE melt at 200 °C at various shear rates so that the less refined mesh can be reliably used for reducing the computational cost.

6.3.1.5. Numerical method

To solve the system of equations above, a flow solver (POLYFLOW version 18, ANSYS version 18) is used on the basis of the finite element algorithm. We apply the interpolation functions on the velocity and pressure quadratic and linear, respectively. A discrete elastic viscous stress splitting (DEVSS) combined with the streamline-upwind (SU) scheme is applied to improve the calculation stability since a geometric singularity exists near the die exit, where a sharp change for the flow boundary condition occurs. In addition, an evolutionary scheme is utilized on the volumetric

flow rate to advance the solution to the viscoelastic flow with high non-linear rheological properties starting from almost purely Newtonian flow, in agreement with our previous work [24, 25].

6.4. Results and discussion

6.4.1. Measurement of die pressure profile and shear dependent viscosities

Fig. 6-2 shows the interpolated axial pressure profiles (dashed lines) for the 4 polymer melts at 200 °C obtained at five wall shear rates from pressure transducer measurements at 3 positions (P_1, P_2 and P_3 values), with the raw data in Table D-1 in Appendix D. In agreement with the work of Mazzanti *et al.* [44] (quasi-)linear pressure profiles are recorded upon interpolation with in each case a determination R^2 very close to 1, highlighting the correctness of the experimental set-up. The corresponding wall shear stresses can be calculated through the slopes of the linear pressure profiles using Eq. 6-2.

A closer inspection of the experimental data in Figure 6-2 reveals that the HDPE melt is characterized by the highest pressure values and changes. Hence, this polymer is most suited to study more in detail if locally pressure drops are altering. It can be deduced that the experimental pressure gradient for HDPE melt is becoming slightly larger toward the die exit. For example, an experimental deviation of 4% is observed at a shear rate of 76.7 s^{-1} as $(P_3 - P_2)/\Delta x$=1.06 bar·mm^{-1} whereas $(P_2 - P_1)/\Delta x$=1.1 bar·mm^{-1}. Padmanabhan *et al.* [11] reported that if the pressure is less than 350 bar, the effect of pressure on viscosity can be neglected. As pressure calibrations have been performed before the actual measurements, the slightly larger pressure gradient

for HDPE upon approaching the die exit might be attributed to a slightly decreasing viscosity from the viscous heating effect or limited polymer degradations.

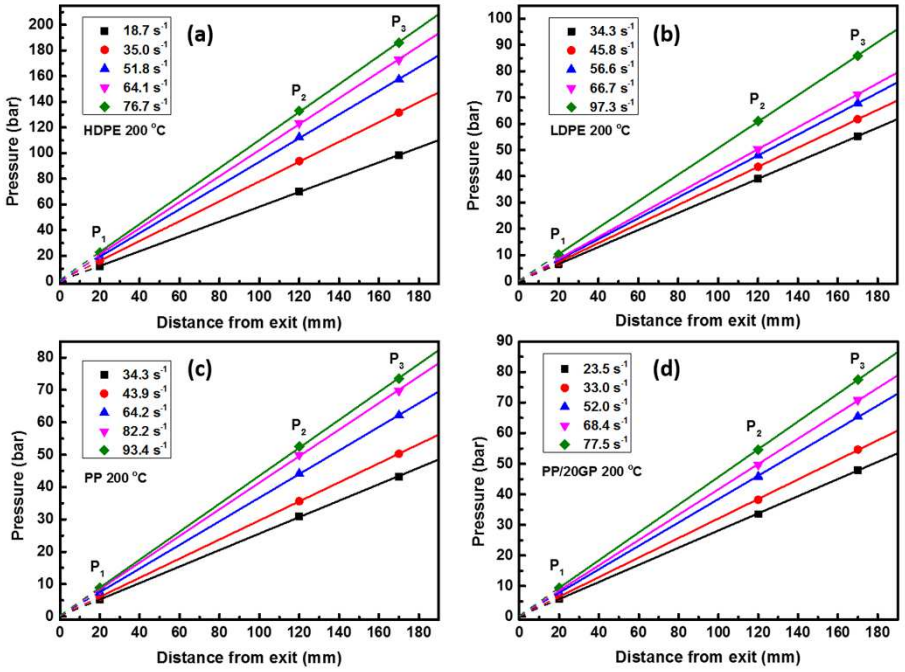


Figure 6-2. Lines: Fitted linear axial pressure profiles based on pressure transducer measurements (symbols) for (a) PP, (b) LDPE, (c) HDPE, and (d) PP/20GF polymer melts (material characteristics in Table 1) at 200°C at different wall shear rates (colors); the raw data and coefficients of determination are given in Table D1 in the Appendix D; extrapolations to die exit (x=0; dashed lines) lead to exit pressure values for the exit pressure method application in Figure 6-4; average error bar: < 0.7 bar.

Figure 6-3 compares complex (η^*) and real (η) viscosity values of the dynamic and steady shear test modes for the polymer melts at shear rates up to 500 s^{-1}, using rotational and slit rheometer analysis. A good agreement is observed between the shear (open symbols) and complex (filled symbols) viscosity data for neat PP (red),

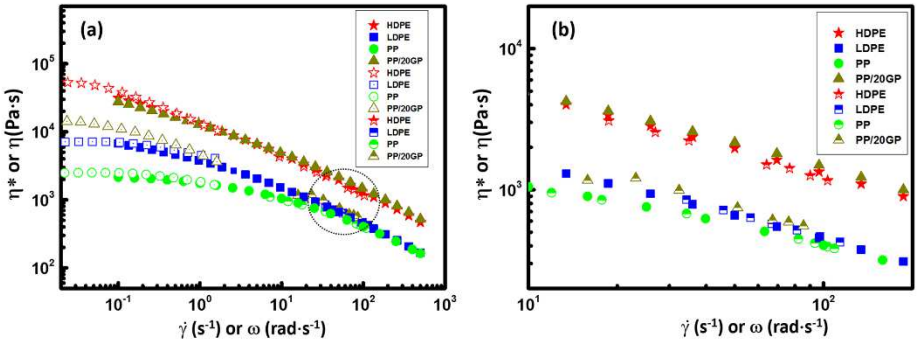


Figure 6-3. (a) A comparison between viscosity variations of HDPE (red), LDPE (blue), PP (green) and PP/20GP (brown) melts at 200 °C (material characteristics in Table 1): complex viscosity from rotational rheometer: filled symbols; shear viscosity also from rotational rheometer: open symbols; shear viscosity from inline slit die method: half-filled symbols; (b) zoom for indicated region (circle) in Figure 6-3(a) at larger shear rates/frequencies; except for the composite the Cox-Merz rule is obeyed for all polymers. Average error: < 40 Pa·s.

LDPE (blue) and HDPE (green) at low and high shear rate ranges, which indicates the validity of the Cox-Merz rule for these three melts [45]: $\eta^*(\omega) = \eta(\dot{\gamma})$. In contrast, for the PP/20GP composite, the shear viscosity data are much lower than the complex viscosity data, indicating the failure of the Cox-Merz rule for this more complex material. These results are consistent with previous reports [11, 46-50] and a possible reason is the deconstruction of the filler-matrix and filler-filler interactions by large strains applied on the flow melt in the non-linear viscoelastic region [49, 51]. As explained in Fig. D-4 in Appendix D, the yield stress contribution is only relevant at higher filler loadings (*e.g.* 40 m%) and at lower filler loading (*e.g.* 10 m%) the Cox-Merz rule still holds. Overall, the high R^2 values for Figure 6-2 and the applicability of the Cox-Merz rule for PP, HDPE and LDPE melt indicate that there is no major flaw during the pressure measurements for the neat polymers. Hence, a next logical

step is to determine conventional P_{ex} values (Eq. 6-4) for the 3 neat polymers thus assuming fully developed isothermal flow, as covered in the next section. For completeness, the method is also applied for the composite.

6.4.2. Determination of N_1 via the exit pressure method and through conventional rheological analysis

Eq. 6-2 indicates a linear variation of the pressure against the flow distance up to the actual die exit, assuming isothermal fully developed flow with pressure independent viscosities [13]. However, sometimes negative exit pressure values have been reported upon linear extrapolation of pressure die measurements but positive exit pressure values upon quadratic extrapolation [8, 10]. A slight curvature can be obtained in the pressure profile, which if existing is generally rather small to be visually perceptible. This curvature has been attributed to the entry effect leading to a developing flow in the vicinity of the transducers, a viscous heating effect of polymer flow, polymer degradation due to the too long residence times, a pressure-dependent viscosity, and even measurement errors [3, 8]. As already indicated above, the latter two effects can be ignored in the present work.

Fig. 6-4 shows the extrapolated exit pressure data (blue points) based on the die pressure data in Fig. 6-2 alongside the wall shear stresses (Eq. 6-2) in a double logarithmic plot, with the corresponding linear fits and associated equations also provided and a listing of the actual P_{ex} raw data in Table D-1 in Appendix D. The R^2 values are high in any case but the closest to 1 for the neat polymers. The slopes of the fitting lines in Fig. 6-4 are thus representing $d \lg P_{ex} / d \lg \sigma_w$ at higher shear rates so that with Eq. 6-4 the (conventional) N_1 values can be obtained at various (higher) wall shear rates.

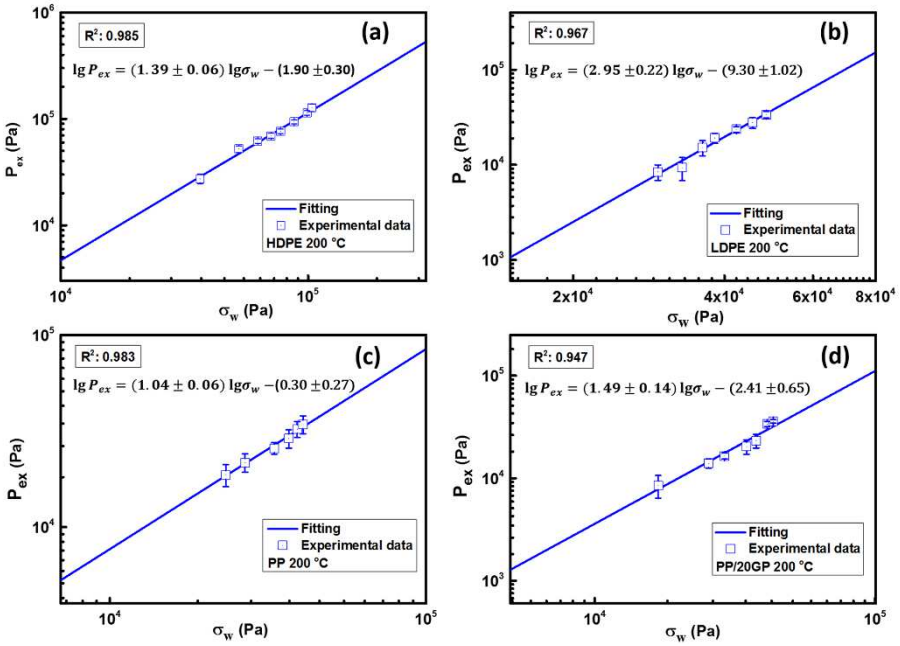


Figure 6-4. Exit pressure values (as extrapolated from Fig. 6-2; open blue symbols; so-called experimental P_{ex} values) versus the wall shear stresses σ_w (from Eq. 6-2) for (a) HDPE, (b) LDPE, (c) PP and (d) PP/20GP melt at 200 °C. Upon using Eq. (6-4) the N_1 values can be obtained as included in Fig. 5 (open blue symbols). Also given is the linear fit and its equation. The constant term is small so that in the limit of very small shear wall stresses very small P_{ex} values are obtained. Data from the composite are included for completeness despite that the Cox-Merz rule is not obeyed as indicated in Fig. 6-3(b).

Fig. 6-5 manifests besides these higher shear rate N_1 values as obtained by the slit rheometer (exit pressure method; label "E"; Eq. 6-4; blue open symbols) also the N_1 values based on application of the Laun rule (Eq. 6-1; label "L"; red/green line exponent α value of 0/0.7) as well as conventionally assessed lower shear rate N_1 values from the rotational rheometer (label "R"; details in the Subsection 6.5.3; full filled black symbols) as recorded at lower shear rate are also included.

It is observed in all subplots of Fig. 6-5 that the difference between the $N_{1\text{-}L}$ data for the case of α= 0 (red curves) and 0.7 (green curves) becomes larger with increasing shear rate. As shown in Fig. 6-5(a)-(c), for HDPE, LDPE and PP melts, except for the LDPE melt at the low shear rate range, $N_{1\text{-}R}$ variations are qualitatively similar as $N_{1\text{-}L}$ variations. This indicates the applicability of the empirical Laun rule for neat polymers, also bearing in mind the good match with $N_{1\text{-}E}$ variations at higher shear rates. An optimal exponent toward 0.7 is expected since the green curves are closer to the experimental data than the red curves, which agrees with Baird's work that $N_{1\text{-}E}$ values are larger than $N_{1\text{-}L}$ data with $\alpha = 0$ [3]. Hence, the exit pressure method seems indeed appropriate in measuring N_1 data for neat polymers, with at least the right magnitude order for neat PP, HDPE and LDPE melts at high shear rates. Moreover, the slight mismatch for LDPE at the lower shear rates might be attributed to the reason that only a ballpark value for $|N_2|/|N_1|$ has been utilized for the measured $N_{1\text{-}L}$ data, as explained above.

It further follows from Fig. 6-5(d) that the Laun rule (Eq. 6-1) fails for the PP/20GP melt, as the $N_{1\text{-}L}$ data are significantly larger than the $N_{1\text{-}R}$ data, even upon employing an α value of 0 and taking into account that the $N_{1\text{-}E}$ values appear to lie in the extrapolation region of $N_{1\text{-}R}$ data in different magnitude orders of shear rates. This observation is in line with the work of Winter [52] who suggested that the Laun rule might apply to Cox-Merz rule obeying materials only. As demonstrated in Fig. 6-3(b), the Cox-Merz rule is invalid for the composite material. Hence, based on the results in Fig. 6-2, Fig. 6-3, Fig. 6-3 and Fig. 6-5, an acceptable consistency is obtained for the neat polymers and for the composite it can only be postulated that the exit pressure method has potential, consistent with a previous report [15].

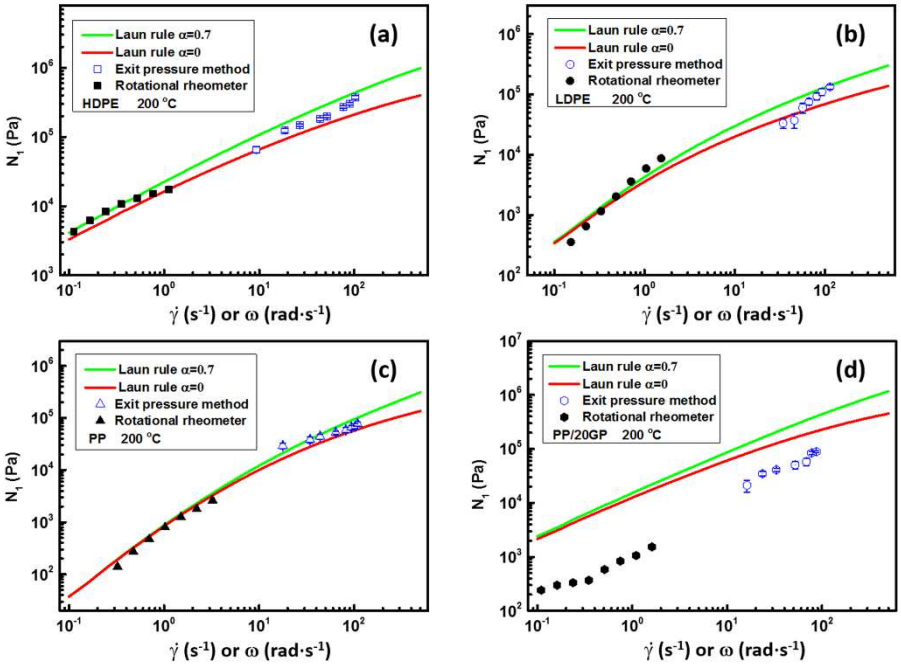


Figure 6-5. First normal stress difference N_1 for polymer melts at various shear rates/frequencies obtained from different methods: (a) LDPE; (b) HDPE; (c) PP and (d) PP/20GF melt (material properties in Table 6-1). Curves, black solid symbols and blue open symbols represent the $N_{1\text{-}L}$ data from Laun rule (Eq. 6-1) for exponent of 0 (red) and 0.7 (green), rotational rheometer ($N_{1\text{-}R}$; Subsection 6.2.3. and the exit pressure method (slit rheometer) ($N_{1\text{-}E}$; Eq. 6-4). For the neat melts the Laun rule can be applied to a first approximation (exponent close to 0.7). For all melts the $N_{1\text{-}E}$ and $N_{1\text{-}R}$ data are consistent.

6.4.3. Numerical analysis to evaluate the assumptions of the exit pressure method

It is clear from Figure 6-5 that a good match of N_1 data via the exit pressure method (Eq. 6-4) and the empirical Laun rule ((exponent α= 0.7); Eq. (6-1)) is obtained for neat polymer melts. To further confirm this interaction, in this modeling section, focus is on the 3D description of experimentally recorded extrudate swell data, which are

influenced by normal stress differences [53-55]. Furthermore, the simulations are adopted to study the impact of the velocity distribution and the viscous heating effect.

6.4.3.1. Determination and validation of PTT input parameters

In our previous work [24, 25], we highlighted the ability of the PTT model to describe 3D extrudate swell of PP melt at 200 °C from slit dies. The PTT parameters (Table D2 in Appendix D) followed from tuning to different types of rheological data. Figure 6-6(c) (purple curve) shows that the PTT predicted N_1 values for PP are in agreement with experimentally recorded values with the exit pressure method (Eq. 6-4) and a Laun-rule curve (Eq. 6-1) considering an α value of 0.7.

Table 6-2. PTT parameters for HDPE and LDPE melts at 200 °C (material characteristics in Table 6-1); those for PP are given in supplementary material and taken from Table 3-2 in Chapter 3.

	PTT model							
Materials	Mode	λ_i (s)		η_i (Pa.s)		ε_i		ξ_i	
HDPE	1	λ_1	0.005	η_1	890	ε_1	0.18	ξ_1	0.18
	2	λ_2	0.072	η_2	3882	ε_2	0.23	ξ_2	0.18
	3	λ_3	1.04	η_3	12977	ε_3	0.23	ξ_3	0.23
	4	λ_4	15	η_4	33595	ε_4	0.25	ξ_4	0.3
LDPE	1	λ_1	0.005	η_1	325	ε_1	0.2	ξ_1	0.15
	2	λ_2	0.063	η_2	1123	ε_2	0.22	ξ_2	0.16
	3	λ_3	0.794	η_3	3290	ε_3	0.20	ξ_3	0.22
	4	λ_4	10	η_4	2950	ε_4	0.05	ξ_4	0.4

This good linkage of the PTT based modeling approach with the exit pressure method as well as the Laun-rule curve is further confirmed in Fig. 6-6(a) and (b) for HDPE and LDPE melts still at 200 °C. The good tuning of the rheological parameters for both polymer melts, as conducted in the present work, is presented in Fig. D-5 in Appendix D. The corresponding PTT model parameters for these PE melts are given in Table 6-2.

6.4.3.2. Comparison between extrudate swell simulations and experimental data

Figure 6-7(a) and (b) compare the evolution of the simulated extrudate swell behavior of the extrudate width (B_1; Eq. 6-5) for HDPE and LDPE melts with the experimental data at various shear rates. A good agreement is observed in terms of B_1, which increases with the shear rate and flow distance away from the die exit. This is in agreement with literature general trends [30, 56, 57]. A significantly smaller increase of B_1 is noticed as the wall shear rate varies from 35 s^{-1} to 51.8 s^{-1} compared to the variation from 9.3 s^{-1} to 35 s^{-1}. This is similar to the predicted extrudate swell behavior for HDPE melt by Ansari *et al.* [33]. Furthermore, B_1 of the HDPE melt is larger than that of the LDPE melt, indicating the more significant elastic property for HDPE melt at the temperature of 200 °C. This can be specifically postulated as the corresponding shear rate is even lower for the former case.

Fig. 6-7(c) and (d) show the corresponding swell behavior at 200 °C of the extrudate height at the edge (B_2; Eq. 6-6). It follows that a 'negative' swelling or so-called contraction flow behavior (B_2 <1) is observed. This swell behavior highlights the strength of 3D simulations with a full preservation of mass and cannot be captured by

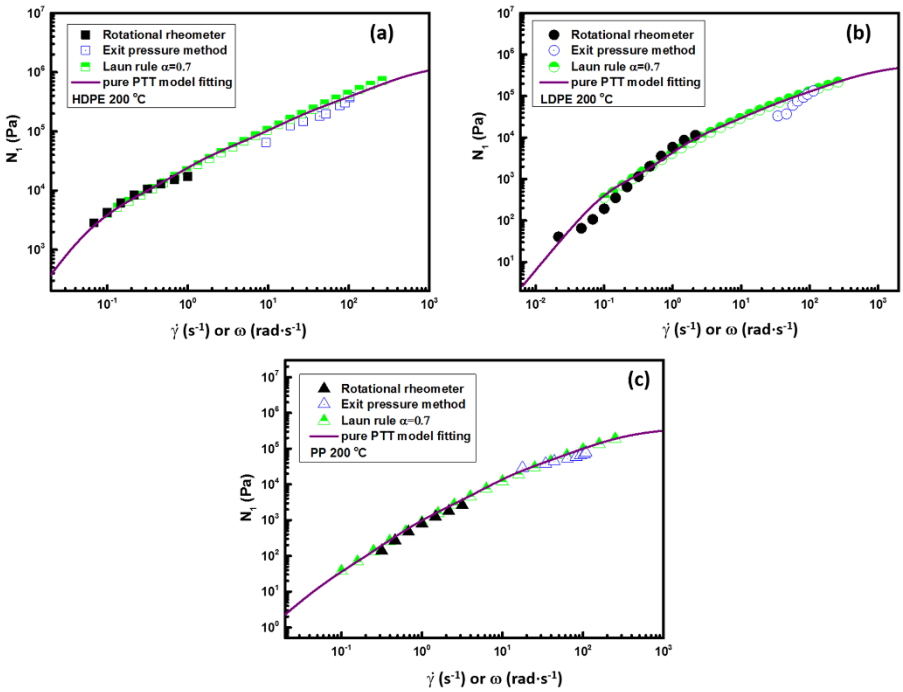


Figure 6-6. N_1 data of HDPE, LDPE and PP melts at 200 °C. Symbols indicate experimental data from the exit pressure method (Eq. 6-4; blue open symbols), rotational rheometer (cf. Subsection 6.3.3, black filled symbols), and the Laun rule (Eq. 6-1); green half-filled symbols; exponent of 0.7), while the purple curves correspond to overall fits with the PTT model. The obtained PTT parameters are highlighted in Table 6-2 (HDPE and LDPE) and Table 3-2 in Chapter 3. It follows that the PTT model curves are consistent with all data and thus also the data as recorded by the exit pressure method.

simplified two dimensional (2D) simulations [25]. A good agreement between the experimental data and simulation results can be noted again for both HDPE and LDPE melts. In Appendix D (Figure D-6) the similar agreement for the PP melt is included. Based on the numerical flow results regarding extrudate swell, it can thus be concluded that the N_1 values as following from the Laun rule (exponent of 0.7) and the exit pressure method (Eq. (6-4)) describe well the elastic properties of PP, HDPE and LDPE melts at 200 °C. This further supports the application of the conventional

exit pressure method, although a further validation can still be conducted with respect to its ideal flow assumptions, as covered below.

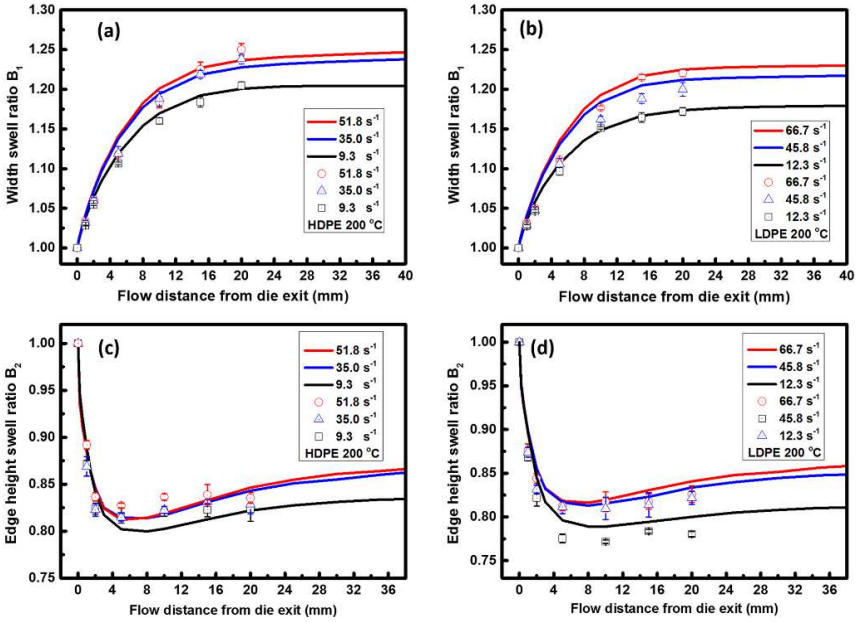


Figure 6-7. Simulated (curves; 3D isothermal simulations using the PTT model) and experimental (symbols) evolutions of the swell behavior in the extrudate width (B_1; Eq. 6-5; (a) and (b)) and edge height direction (B_2; Eq. 6-6; (c) and (d)) for HDPE and LDPE melts at 200 °C at different shear rates. Similar plots for PP melt are shown in Fig. 6-7 in the Chapter 3. Good descriptions are observed, further validating the relevance of Eq. 6-4.

6.4.3.3. Numerical evaluation of impact of flow disturbances near the die exit

To investigate the effect of flow disturbances near the die exit in Figure D-7 in the Appendix D, a numerical comparison is performed between the simulated exit pressure values as obtained by the detailed 3D modeling and those assuming simplified linear extrapolation. It is seen that the deviation between both types of simulations starts at around 1 mm before the die exit, which is in agreement with

literature stating disturbances at 1 or 2 times of the half die height (here H = 1 mm) [7, 18]. Furthermore, a sharp increase in the simulated pressure value very close to die exit is noted with the 3D model. This increase is related to a numerical stress singularity near the die exit, as shown in Figure 6-8 for the three neat melts and two wall shear rates. Note that for HDPE the stronger N_1 increases in Figure 6-8 are a consequence of the stronger pressure variations in Figure 6-2 and Fig. D-7 in the Appendix D, and the higher elasticities as discussed in Fig. 6-7.

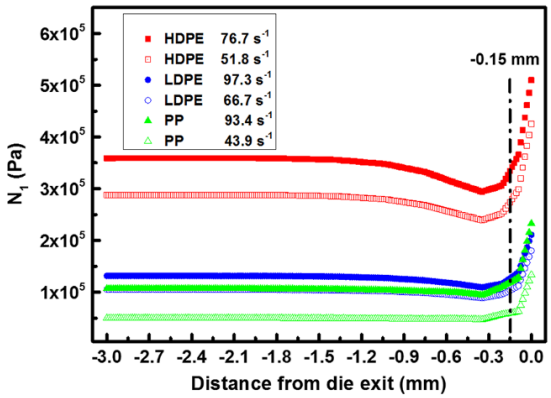


Figure 6-8. First normal stress difference N_1 along the die wall for LDPE and HDPE melts at lower and higher wall shear rates (colors) according to a detailed 3D model (with velocity redistribution) at 200 °C (material parameters in Table 6-1 and PTT model parameters in Table 6-2). The dashed line indicates the position at which we calculate the exit pressure value with the 3D full model so with velocity redistribution (so-called $P_{ex,r}$ value) in Fig. 6-8 to minimize the impact of a possible artificial effect [58].

The nature of exit singularity for viscoelastic models is still unclear as being a real physical phenomenon or an artificial prediction or a combination of both [58]. It has been indicated that mesh refinement enhances the intensity of the stress singularity [24, 58] and thereby results in a larger pressure values near the exit. This has been noticed in the present work as well with also a delay for the drastic increase taking

place in line with literature data [59]. Hence, it is recommendable to consider an intermediate solution and to deliver with a detailed flow modeling at least an underestimated but not an overestimated value of the exit pressure. Therefore, we evaluate the pressure value at the position where the N_1 value abruptly starts increasing. Fig. 6-8 displays that this position is around at a distance of 0.1-0.2 mm before the die exit. For uniformity, we fix this position at 0.15 mm before the die exit for all simulations. For clarity we denote this modeled exit pressure value as $P_{ex,r}$ as opposed to P_{ex} as based on Eq. 6-4 and thus extrapolation.

Importantly, this distance of 0.15 mm is in the extrapolated region in Fig. 6-2 and thus a natural question is to quantify the deviations between linearly extrapolated and actually calculated values accounting for velocity redistributions. Figure D-8 in the Appendix D shows that for all neat melts the flow disturbance in vicinity of the die exit leads to a significantly higher pressure value. The relative contribution stemming from the velocity redistribution R_v, which is defined as $(P_{ex,r} - P_{ex})/P_{ex,r}$ amounts to *ca*. 25-40%. Increasing the shear rate decreases slightly the value of R_v, which agrees with the report by Han [18].

These insights at first sight indicate that Eq. (6-4) is unsuited as there are significant deviations between P_{ex} and $P_{ex,r}$ values. However, it should be reminded that the actual goal is the reliable determination of N_1. Therefore, Figure 6-9 (top) presents the update of Fig. 6-4 for the two PE melts using simulated P_{ex} values as obtained from linear extrapolation of the 3D modeling results. We start here at a distance sufficiently away from the die exit to ensure the linearity according to the method. Similar slopes as in Fig. 6-4(a) and (b) are observed, indicating a limited effect on the N_1 determination. The latter is indeed confirmed in Fig. 6-9 (bottom) in which the lines from Fig. 6-9

(top) are used to obtain the corresponding N_1 values (red filled symbols) formally according to Eq. 6-4. It follows that these N_1 data are consistent with the N_1 data according to the green Laun-rule curve with an exponent α of 0.7. This highlights the relevance of the exit pressure method as these Laun rule data are in turn consistent with the N_1 values recorded based on the exit pressure method thus upon applying Eq. (6-4) with the actual experimental pressure profiles (*cf.* discussion Fig. 6-5). In addition, we show in Figure 6-9 (bottom) that the N_1 data for the PE melts as simulated by the detailed 3D model (evaluation at wall), thus employing the PTT model in the Polyflow software while considering velocity redistributions (purple open symbols), also agree with the Laun rule data. Hence, the assumption of fully developed flow down to the die exit is valid for the N_1 calculation by means of exit pressure method.

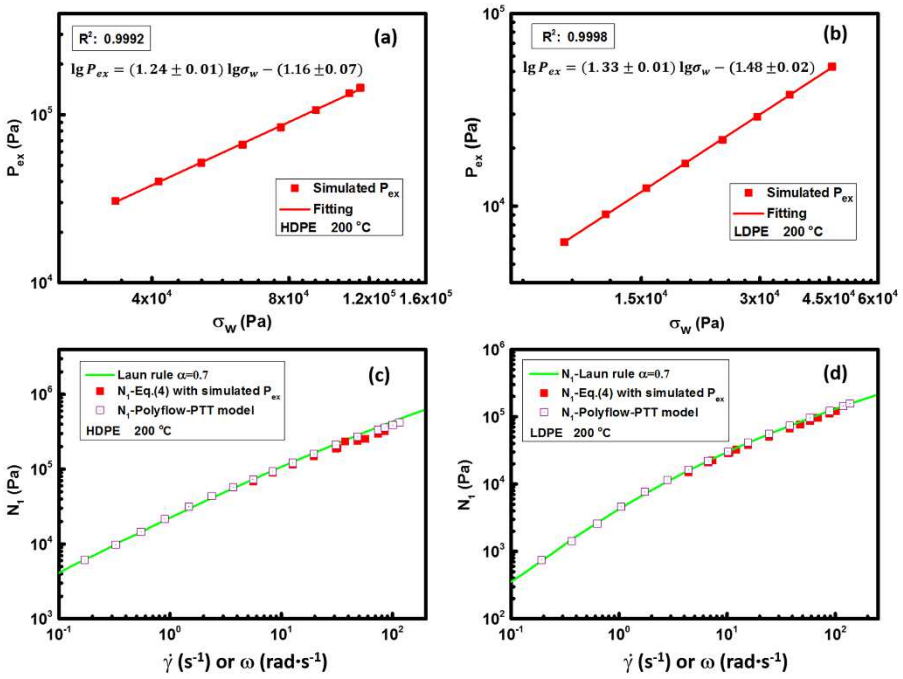


Figure 6-9. Top: Simulated exit pressure by linear extrapolation (sufficiently far away from the die exit) as a function of the simulated wall shear stress σ_w (a) LDPE and (b) HDPE at 200 °C; full red curve: linear fit. Bottom: comparison of the normal stress difference N_1 as obtained with

the full 3D model thus accounting for velocity distributions (purple open symbols; evaluation at wall), as calculated based on the simulated extrapolated P_{ex} in Fig. 6-9 (a) and (b) with Eq. (4) (red filled symbols) and as obtained based on the Laun rule with $\alpha = 0.7$ (green curves; consistent with experimental exit pressure values in Fig. 6-5).

6.4.4.3. Impact of viscous heating effect

The numerical analysis mentioned above is performed under isothermal flow conditions. However, the viscous heating effect of the viscoelastic flow might influence the temperature field inside the flow channel [43] thus affecting the pressure field. The fit of the temperature-dependent rheological properties of polymer melts is shown in Fig. D-9 in Appendix D, with the material parameters required presented in Table D-3 in Appendix D for the three polymer melts.

As explained in Fig. D-10 in Appendix D, flow simulations indicate a negligible effect of temperature gradients, implying a very low *N*a number. Indeed, for HDPE, LDPE and PP melt the *N*a number is 0.032, 0.035, and 0.09 at the highest shear rate, indicating a very weak viscous heating effect [33, 43]. Consequently, the N_1 measurements by means of the exit pressure method is thought to be free from this effect, at least considering the experimental ranges investigated in this work.

6.5. Conclusions

For neat polymer melts at 200 °C, we have comprehensively evaluated the exit pressure method via the slit rheometer to measure N_1 values at high shear rates, which cannot be obtained by a conventional rotational rheometer due to the melt edge fracture. In this method, the (quasi-)linear axial pressure profiles for the polymers at various wall shear rates are first extrapolated to the die exit, yielding the

corresponding exit pressure values, which in turn are related to the associated shear stresses to deliver N_1 values.

For these neat polymers, the shear viscosity data measured from the inline slit die method agree very well with those from the rotational rheometer at low shear rates as well as the associated measured complex viscosity data over a wide shear rate range, indicating the validity of the empirical Cox-Merz rule. The N_1 values at the shear-rate magnitude order of 10 to 100 s^{-1} as measured by the exit pressure method lie additionally in the value range calculated by the Laun rule with an exponent α of 0 and 0.7.

Extrudate swell behavior, which is related to normal stress differences, has been also utilized to further assess the validity of the exit pressure method for these neat polymer melts. 3D numerical simulations have been performed, using the differential viscoelastic multi-mode PTT model. The corresponding material parameters have been obtained by tuning the rheological functions including fitting the N_1 data obtained from the empirical Laun rule that are consistent with the exit pressure method based N_1 data. A good agreement between the predicted extrudate swell and experimental measurements for the neat polymer melts is observed, which further confirms that the exit pressure method is appropriate to determine N_1 values.

To address the disagreement in the field on the exit pressure method stemming from the skeptical assumption of fully developed flow down to die exit, we additionally compared the numerical exit pressure values in terms of accounting for the flow redistributions near the die exit or not doing so. Although the pressure contribution from velocity rearrangement near the die exit accounts for *ca*. 25-40% at various shear rates, this deviation diminishes in impact upon focusing on the actual simulated N_1

values, which are consistent with those by the exit pressure method. In addition, a negligible effect coming from viscous heating of polymer melts on the pressure field near the die exit has been demonstrated. Hence, the exit pressure method can be reliable utilized for the neat polymers studied.

Future work will be directed to also investigate composites. In this respect, the current study has already shown that Cox-Merz and Laun rule fail to describe the viscosity data for a PP composite. Even though the Laun rule fails, the N_1 values obtained with the exit pressure method appear to be in the extrapolation region of those obtained by the rotational rheometer. Hence, the exit pressure method seems to have also potential for more complex materials. Additional future work could focus on the evaluation at even higher shear rates.

REFERENCES

1. Tian, H., et al., *Study on extrudate swell of polypropylene in double-lumen micro profile extrusion.* Journal of Materials Processing Technology, 2015. **225**: p. 357-368.
2. Thiébaud, F. and J. Gelin, *Characterization of rheological behaviors of polypropylene/carbon nanotubes composites and modeling their flow in a twin-screw mixer.* Composites science and technology, 2010. **70**(4): p. 647-656.
3. Baird, D.G., *First normal stress difference measurements for polymer melts at high shear rates in a slit-die using hole and exit pressure data.* Journal of Non-Newtonian Fluid Mechanics, 2008. **148**(1-3): p. 13-23.
4. Robertson, B., et al., *Theoretical prediction and experimental measurement of isothermal extrudate swell of monodisperse and bidisperse polystyrenes.* Journal of Rheology, 2017. **61**(5): p. 931-945.
5. Jensen, E.A., *Measurements of first and second normal stress differences in a polymer melt.* Journal of Non-Newtonian Fluid Mechanics, 2008. **148**(1-3): p. 41-46.
6. Bird, R.B., R.C. Armstrong, and O. Hassager, *Dynamics of polymeric liquids. Vol. 1: Fluid mechanics.* 1987.
7. Boger, D.V. and M.M. Denn, *Capillary and slit methods of normal stress measurements.* Journal of Non-Newtonian Fluid Mechanics, 1980. **6**(3-4): p. 163-185.
8. Tuna, N. and B. Finlayson, *Exit pressure experiments for low density polyethylene melts.* Journal of Rheology, 1988. **32**(3): p. 285-308.
9. Konaganti, V.K., et al., *The effect of damping function on extrudate swell.* Journal of Non-Newtonian Fluid Mechanics, 2016. **236**: p. 73-82.
10. Chan, T., B. Pan, and H. Yuan, *An experimental study of exit pressures for polymer melts.* Rheologica Acta, 1990. **29**(1): p. 60-70.
11. Padmanabhan, M. and M. Bhattacharya, *In-line measurement of rheological properties of polymer melts.* Rheologica acta, 1994. **33**(1): p. 71-77.
12. Macosko, C.W. and R.G. Larson, *Rheology: principles, measurements, and applications.* 1994.
13. Lodge, A. and L. De Vargas, *Positive hole pressures and negative exit pressures generated by molten polyethylene flowing through a slit die.* Rheologica Acta, 1983. **22**(2): p. 151-170.
14. Tuna, N.Y. and B.A. Finlayson, *Exit pressure calculations from numerical extrudate swell results.* Journal of Rheology, 1984. **28**(2): p. 79-93.
15. Han, C.D., *Rheological properties of calcium carbonate-filled polypropylene melts.* Journal of Applied Polymer Science, 1974. **18**(3): p. 821-829.
16. Han, C.D., *On Silt-and Capillary-Die Rheometry.* Transactions of the Society of Rheology, 1974. **18**(1): p. 163-190.
17. Han, C.D. and L.H. Drexler, *The stress distribution of polymer melts in the exit region.* Transactions of the Society of Rheology, 1973. **17**(4): p. 659-665.

18. Han, C.D., *What is the role of "pressure" in the use of capillary and slit flows to determine the shear-rate dependent viscosity of a viscoelastic fluid?* Polymer Engineering & Science, 2008. **48**(6): p. 1126-1140.
19. Han, C., M. Charles, and W. Philippoff, *Rheological implications of the exit pressure and die swell in steady capillary flow of polymer melts. I. The primary normal stress difference and the effect of L/D ratio on elastic properties.* Transactions of the Society of Rheology, 1970. **14**(3): p. 393-408.
20. Carreau, P.J., L. Choplin, and J.R. Clermont, *Exit pressure effects in capillary die data.* Polymer Engineering & Science, 1985. **25**(11): p. 669-676.
21. Choplin, L. and P. Carreau, *Excess pressure losses in a slit.* Journal of Non-Newtonian Fluid Mechanics, 1981. **9**(1-2): p. 119-146.
22. Schoonen, J.F., et al., *A 3D numerical/experimental study on a stagnation flow of a polyisobutylene solution.* Journal of non-newtonian fluid mechanics, 1998. **79**(2-3): p. 529-561.
23. Sirakov, I., et al., *Three-dimensional numerical simulation of viscoelastic contraction flows using the Pom–Pom differential constitutive model.* Journal of Non-Newtonian Fluid Mechanics, 2005. **126**(2-3): p. 163-173.
24. Tang, D., et al., *Isothermal flow of neat polypropylene through a slit die and its die swell: Bridging experiments and 3D numerical simulations.* Journal of Non-Newtonian Fluid Mechanics, 2019. **266**: p. 33-45.
25. Tang, D., et al., *Three-dimensional flow simulations for polymer extrudate swell out of slit dies from low to high aspect ratios.* Physics of Fluids, 2019. **31**(9): p. 093103.
26. Laun, H., *Prediction of elastic strains of polymer melts in shear and elongation.* Journal of Rheology, 1986. **30**(3): p. 459-501.
27. Kádár, R., I.F. Naue, and M. Wilhelm, *First normal stress difference and in-situ spectral dynamics in a high sensitivity extrusion die for capillary rheometry via the 'hole effect'.* Polymer, 2016. **104**: p. 193-203.
28. Meissner, J., R. Garbella, and J. Hostettler, *Measuring normal stress differences in polymer melt shear flow.* Journal of Rheology, 1989. **33**(6): p. 843-864.
29. Mitsoulis, E., et al., *Flow Behavior of a Polypropylene Melt in Capillary Dies.* International Polymer Processing, 2018. **33**(5): p. 642-651.
30. Konaganti, V., et al., *Extrudate swell of high density polyethylenes in slit (flat) dies.* International Polymer Processing, 2016. **31**(2): p. 262-272.
31. Barnes, H.A., *A review of the rheology of filled viscoelastic systems.* Rheology reviews, 2003: p. 1-36.
32. Ohl, N. and W. Gleissle, *The second normal stress difference for pure and highly filled viscoelastic fluids.* Rheologica acta, 1992. **31**(3): p. 294-305.
33. Ansari, M., E. Mitsoulis, and S.G. Hatzikiriakos, *Capillary extrusion and swell of a HDPE melt exhibiting slip.* Advances in Polymer Technology, 2013. **32**(S1).
34. Wen, Y.H., et al., *An experimental appraisal of the Cox–Merz rule and Laun's rule based on bidisperse entangled polystyrene solutions.* Polymer, 2004. **45**(25): p. 8551-8559.

35. Laun, H.M., *Polymer melt rheology with a slit die.* Rheologica Acta, 1983. **22**(2): p. 171-185.
36. Lodge, A., *Elastic Liquids, Acad.* Press, New York-London, 1964.
37. Davies, J., J. Hutton, and K. Walters, *Theory for normal stresses in slits and capillaries.* Journal of Physics D: Applied Physics, 1973. **6**(18): p. 2259.
38. Mu, Y., et al., *Influence of die geometric structure on flow balance in complex hollow plastic profile extrusion.* The International Journal of Advanced Manufacturing Technology, 2017. **91**(1-4): p. 1275-1287.
39. Gujrati, P.D. and A.I. Leonov, *Modeling and simulation in polymers*. 2010: John Wiley & Sons.
40. Aloku, G.O. and X.-F. Yuan, *Numerical simulation of polymer foaming process in extrusion flow.* Chemical Engineering Science, 2010. **65**(12): p. 3749-3761.
41. Mitsoulis, E., et al., *Flow behavior of PP-polymer nanocomposites in injection molding hyperbolical dies.* Advances in Polymer Technology, 2018. **37**(8): p. 3045-3055.
42. Lee, K. and M. Mackley, *The significance of slip in matching polyethylene processing data with numerical simulation.* Journal of Non-Newtonian Fluid Mechanics, 2000. **94**(2): p. 159-177.
43. Ansari, M., S.G. Hatzikiriakos, and E. Mitsoulis, *Slip effects in HDPE flows.* Journal of Non-Newtonian Fluid Mechanics, 2012. **167**: p. 18-29.
44. Mazzanti, V. and F. Mollica, *In-line rheometry of polypropylene based Wood Polymer Composites.* Polymer Testing, 2015. **47**: p. 30-35.
45. Gleissle, W. and B. Hochstein, *Validity of the Cox–Merz rule for concentrated suspensions.* Journal of rheology, 2003. **47**(4): p. 897-910.
46. Mazzanti, V., F. Mollica, and N. El Kissi, *Rheological and mechanical characterization of polypropylene-based wood plastic composites.* Polymer Composites, 2015.
47. Köpplmayr, T., et al., *Influence of fiber orientation and length distribution on the rheological characterization of glass-fiber-filled polypropylene.* Polymer Testing, 2013. **32**(3): p. 535-544.
48. Clemeur, N., R. Rutgers, and B. Debbaut, *Numerical simulation of abrupt contraction flows using the Double Convected Pom–Pom model.* Journal of non-newtonian fluid mechanics, 2004. **117**(2-3): p. 193-209.
49. Hristov, V., E. Takacs, and J. Vlachopoulos, *Surface tearing and wall slip phenomena in extrusion of highly filled HDPE/wood flour composites.* Polymer Engineering & Science, 2006. **46**(9): p. 1204-1214.
50. Ansari, M., et al., *Rheology of Ziegler–Natta and metallocene high-density polyethylenes: broad molecular weight distribution effects.* Rheologica acta, 2011. **50**(1): p. 17-27.
51. Duan, L., et al., *Designing formulation variables of extrusion-based manufacturing of carbon black conductive polymer composites for piezoresistive sensing.* Composites Science and Technology, 2019. **171**: p. 78-85.
52. Winter, H.H., *Three views of viscoelasticity for Cox–Merz materials.* Rheologica acta, 2009. **48**(3): p. 241-243.

53. Comminal, R., et al., *Numerical simulation of the planar extrudate swell of pseudoplastic and viscoelastic fluids with the streamfunction and the VOF methods.* Journal of Non-Newtonian Fluid Mechanics, 2018. **252**: p. 1-18.
54. Rueda, M.M., et al., *Rheology and applications of highly filled polymers: A review of current understanding.* Progress in Polymer Science, 2017. **66**: p. 22-53.
55. Liang, J.-Z., *Melt die-swell behavior of polyoxymethylene blended with ethylene-vinyl acetate copolymer and high-density polyethylene.* Polymer Testing, 2018. **68**: p. 213-218.
56. Béraudo, C., et al., *A finite element method for computing the flow of multi-mode viscoelastic fluids: comparison with experiments.* Journal of non-newtonian fluid mechanics, 1998. **75**(1): p. 1-23.
57. Ganvir, V., et al., *Extrudate swell of linear and branched polyethylenes: ALE simulations and comparison with experiments.* Journal of Non-Newtonian Fluid Mechanics, 2011. **166**(1): p. 12-24.
58. Keunings, R., *Simulation of viscoelastic fluid flow.* 1987.
59. Spanjaards, M., M. Hulsen, and P. Anderson, *Transient 3D finite element method for predicting extrudate swell of domains containing sharp edges.* Journal of Non-Newtonian Fluid Mechanics, 2019. **270**: p. 79-95.

Chapter 7

From die swell for neat polymer melts to composite melts: a preliminary study

In this preliminary study, with the aim at grasping the rheological behavior of the die swell of polymer composites with various filler contents, a modified Phan-Thien-Tanner (PTT) model is proposed. To reduce the variables of the material parameters, we maintain the non-linear parameter constant in each mode of the PTT model. As a result, the viscosity parameter η_i and non-linear material parameters such as ε and ξ of PTT model are described as functions against the filler volumetric content. The anisotropic swelling behavior predicted by PTT model is presented for polypropylene(PP)/graphite composites. It is shown that the PTT model is less suited in capturing the anisotropic swelling behavior of PP composite with high volumetric content of graphite fillers. Also the relevance of slip-condition simulations is put forward.

7.1. Introduction

Extrusion, a polymer forming operation under melt conditions, is widely used in industrial applications [1-5]. Plastic profiles are applied today in large scales in industrial fields. Polymers such as polypropylene (PP), polyethylene (PE) and polyvinylidene (PVDF), owning advantages of distinguishing corrosion and light weight are an excellent substitute material for traditional materials (copper and alumina) in industrial applications such as for heat exchangers [6, 7].

In most cases, the low thermal conductivities (0.2-0.5 W/mK) of plastics cannot achieve the requirements of heat conducting for heat exchangers [7]. Generally, the solution to address this issue is most to add thermal conductive fillers (such as graphite [8, 9], Boron Nitride (BN) [10, 11] and Carbon fibers [12], *et al.*) to the polymer matrix to increase its thermal conductivity. However, adding filler induces an influence on the rheological and viscoelastic properties of polymer composite melts thus resulting in a processing difficulty, highlighting unstable flow behavior during the processing such as the extrudate swell [13-15], sharkskin [3, 16-18] and melt fracture phenomenon [16, 19] as the filler content increases to a critical value. Therefore, studying how the filler influences the rheological properties and thereby the processing behavior of polymer composites is an important research subject with the aim of controlling the processing conditions to obtain the desired product profiles.

It is generally put forward that additions of fillers into a polymer matrix suppress the swelling behavior [14, 15, 20-23]. Furthermore, filler characteristics seem to affect the swelling behavior such as the filler size, filler content and even the interaction between filler and matrix thus affecting the dispersion quality [14, 22]. For example, Stabik [24] found that larger aspect ratios of fillers lead to smaller extrudate swell,

while other factors such as the specific surface and mean diameter contribute less to the swelling of PE and polystyrene melts. However, to the best of the author's knowledge, there are very few studies addressing the issue of the anisotropic swelling behavior of polymer composites by a comprehensive 3D modelling method with for instance the well-established PTT model.

In our previous work [25-27], we extensively studied the processing behavior such as the extrudate swell behavior of neat polypropylene (PP-, high density polyethylene (HDPE) and low density polyethylene (LDPE) from a slit die by means of a combination of experimental observations and 3D numerical modelling mainly with the viscoelastic constitutive PTT model using the finite element method based POLYFLOW solver. Anisotropic swelling behavior depends here not only on the type of the polymer melt but also on the flow geometry characteristics such as the aspect ratio of the die and the length/height ratio within an upstream contraction region.

In this preliminary study, we evaluate the influences on the rheological properties of PP melt upon adding the graphite filler into polymer matrix. The question is how to relate the material parameters of the constitutive model to the rheological properties caused by addition of filler particles. It is important to mention that other filler characteristics such as the filler size and especially the interaction between the filler and matrix are not the scope of this preliminary study since focus is only on one type of filler. The objective of this study is to have an insight of the impact on the anisotropic extrudate swelling behavior of PP composites caused by adding filler particles via a comparison with experiments and simulations with the tuning material parameters of the PTT model. In addition, a modified PTT constitutive model by

establishing a function of the material parameters against the filler volumetric content of graphite filler is proposed.

7.2. Modelling principles

7.2.1. Geometric parameters

Figure 7-1 depicts the 2D schematic diagram of the cross section of a slit die with an aspect ratio of 10. Several swell ratios can be defined as the ratios between the dimensions of the extrudate and the die. To identify a possible anisotropic extrudate swell behavior, three such ratios B_1, B_2 and B_3 are needed, denoting the swelling in the extrudate width, edge height and middle height direction (Figure 7-1), respectively [27]:

$$B_1 = \frac{W_{-extrudate}}{W_{-die}},\ B_2 = \frac{H_{1-extrudate}}{H_{1-die}} \text{ and } B_3 = \frac{H_{2-extrudate}}{H_{2-die}} \qquad (7\text{-}1)$$

Additionally, B_4 is defined as the swell ratio of the area size (S) of the extrudate cross section and the slit die:

$$B_4 = \frac{S_{-extrudate}}{S_{-die}} \qquad (7\text{-}2)$$

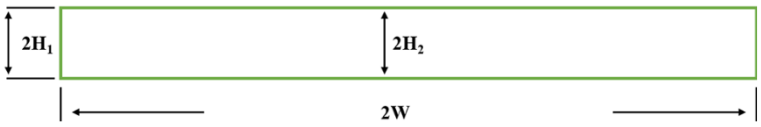


Figure 7-1. The cross section of a slit die (case of an aspect ratio of 10). Four swell ratios can be defined, as mathematically represented by Eq. 7-1 and Eq. 7-2. They relate to swelling for the width direction, the edge height direction, the middle height direction, and the area swelling.

7.2.2. PTT constitutive model

For the differential viscoelastic constitutive model, the extra stress tensor $\boldsymbol{\tau}$ can be divided into a purely viscous part $\boldsymbol{\tau_N}$ and a viscoelastic part $\boldsymbol{\tau_p}$, which can be calculated by the basic viscoelastic constitutive equations.

In comparison with a single mode PTT model, a multi-mode PTT model with a relaxation time spectrum enables more accurate simulation results [28]. This model is expressed as:

$$\boldsymbol{\tau_p} = \sum_{i=1}^{N} \boldsymbol{\tau_{pi}} \qquad (7\text{-}3)$$

$$exp\left[\frac{\varepsilon_i \lambda_i}{\eta_i} \boldsymbol{tr}(\boldsymbol{\tau_{pi}})\right] \boldsymbol{\tau_{pi}} + \lambda_i \left[(1 - \frac{\xi_i}{2}) \overset{\frown}{\boldsymbol{\tau_{pi}}} + \frac{\xi_i}{2} \overset{\frown}{\boldsymbol{\tau_{pi}}}\right] = 2\eta_i \mathbf{D} \qquad (7\text{-}4)$$

in which the two non-linear parameters, ε_i and ξ_i, mainly control extensional and shear behavior of polymer fluid, respectively, and $\overset{\frown}{\boldsymbol{\tau_{pi}}}$ and $\overset{\frown}{\boldsymbol{\tau_{pi}}}$ denote the upper and lower convected derivatives of $\boldsymbol{\tau_{pi}}$, defined by:

$$\overset{\frown}{\boldsymbol{\tau_{pi}}} = \frac{D\boldsymbol{\tau_{pi}}}{Dt} - (\boldsymbol{\tau_{pi}} \cdot \nabla \mathbf{v} + (\nabla \mathbf{v})^T \cdot \boldsymbol{\tau_{pi}}) \qquad (7\text{-}5)$$

$$\overset{\frown}{\boldsymbol{\tau_{pi}}} = \frac{D\boldsymbol{\tau_{pi}}}{Dt} + (\boldsymbol{\tau_{pi}} \cdot \nabla \mathbf{v} + (\nabla \mathbf{v})^T \cdot \boldsymbol{\tau_{pi}}) \qquad (7\text{-}6)$$

To figure out how the filler particles affect the rheological properties of the polymer, a modified PTT model is proposed to take into consideration the effect on the rheological behavior of polymer composite fluids, such as the filler size, filler shape (aspect ratio), filler content and the network between the filler and polymer matrix. As we mentioned above, in this preliminary study, the factor of the filler volumetric content denoted as *x* is only considered. To reduce the number of the variables of the

material parameters, the relaxation time λ_i is maintained constant for all polymer composites with a time range from 0.01 to 10 s. The function of the viscosity against the filler volumetric content is denoted as $\eta_i(x)$. Regarding the non-linear material parameter ξ_i and ε_i, we assume that the parameter is constant in each mode to reduce the number of variables. The corresponding material functions are denoted as $\xi(x)$ and $\varepsilon(x)$. As a consequence, a modifies PTT constitutive model is written as:

$$exp\left[\frac{\varepsilon(x)\lambda_i}{\eta_i}\boldsymbol{tr}(\boldsymbol{\tau_{pi}})\right]\boldsymbol{\tau_{pi}} + \lambda_i\left[(1-\frac{\xi(x)}{2})\overset{\sim}{\boldsymbol{\tau_{pi}}} + \frac{\xi(x)}{2}\overset{\frown}{\boldsymbol{\tau_{pi}}}\right] = 2\eta_i\mathbf{D} \quad (7\text{-}7)$$

7.2.3. Boundary conditions and numerical method

The 3D flow domain is given in Fig. D-2 with one quarter of the flow channel considered for all simulations to reduce the computational cost due to the symmetry planes. Briefly, at the inlet, a fully developed flow with a flow rate of 620 mm^3/s is considered. At the die walls, a non-slip condition for the velocity field is prescribed unless stated otherwise: $v_n = v_t = 0$ (mm/s). A free surface flow developed outside the die exit is unknown a priori. Force conditions: $f_t = f_n = 0$ (N) are set at the outlet of the flow domain, with the subscript n and t indicating the normal and tangential component of the force and velocity.

The flow solver (POLYFLOW version 18, ANSYS version 18) is used based on the finite element algorithm. We apply the interpolation functions on the velocity and pressure quadratic and linear, respectively. A discrete elastic viscous stress splitting (DEVSS) combined with the streamline upwind (SU) scheme is applied to improve the calculation stability due to the exit singularity. In addition, an evolutionary scheme is utilized on the volumetric flow rate to advance the solution to the viscoelastic flow

with high non-linear rheological properties starting from almost purely Newtonian flow, in agreement with our previous work [26, 27].

7.3. Material and characterizations

7.3.1. Materials

Polypropylene (PP, SABIC 575P) melt and graphite fillers (GP, Asbury 3807) were used in this study. For the pure polymer melts, pellets were directly available. The PP/graphite composite with various mass filler contents of 10%, 20% and 40%, corresponding to the volumetric filler content of 4.3%, 9.2% and 21.1% were in contrast made in-house employing the twin-screw extrusion, with a screw rotational rate of 90 rpm and a processing temperature window of 160–210 °C and using a chopping machine. The polymer melts were all extruded from a single screw extruder (P. Brabender 19 with a screw diameter D_s of 19 mm, L_s/D_s of 25; L_s: screw length) combined with a slit die (die length: 220 mm, die height (H_{die} in Fig. 7-1(a)): 2 mm, and die width (H_{die} in Fig. 1(a)): 20 mm) at a screw speed of 10–120 rpm at 200 °C.

7.3.2. Conventional rheological measurements

An ARES (TA, Discovery HR-3, US) rheometer was used to perform the temperature-dependent rheological measurements of polymer melts at 200 °C. The dynamic small amplitude oscillatory measurements were performed with a frequency sweep in an angular velocity (ω) range of 0.1–500 rad s^{-1}. The steady shear mode tests were carried out within a small shear rate range of 0.01–5 s^{-1} to avoid melt edge fracture. Disk samples with a diameter of 25 mm and a thickness of 2 mm were made using compression.

To enable an evaluation of conventional analysis tools for normal stress differences, focus has been also on the determination of $N_1 - N_2$ by a parallel plate geometry mode [29, 30]. For polymers, generally it holds that $N_1 > 0$ but $N_2 < 0$, and $|N_1| \approx 10\ |N_2|$ [29, 31]. The $|N_2|/|N_1|$ value for PP and PP with low filler content (4.3%) is claimed to be 0.1 (200 °C) [32, 33]. For composites, it has been pointed out that $|N_2|/|N_1|$ increases further [34, 35]. Consequently, the ratio is assumed to be 0.2 and 0.3 for PP/9.2GP and PP/21.1GP, respectively.

7.4. Results and Discussion

7.4.1 Rheological analysis and tuning of PTT model parameters with increasing filler content

Figure 7-2 compares the experimental rheological data including the storage modulus G', loss modulus G'', shear viscosity η_s and the first normal stress difference N_1 for PP (a and b) and PP composite with a graphite filler content of 4.3% (c and d), considering the parameters in Table 7.1. It is seen that an excellent agreement between the experimental measurements and the tuning data by PTT model is observed for both polymer melts with regarding to the linear rheological data such as G' and G''. As compared with a good prediction of the non-linear rheological data such as N_1 and shear viscosity data η_s for neat PP fluid, a very slight over-prediction of the N_1 by PTT model is noted, which might be attributed to the reason that only a ballpark value for $|N_2|/|N_1|$ has been utilized for calculating the N_1 data, as explained above. However, all the predictions by PTT model are highly acceptable in both cases.

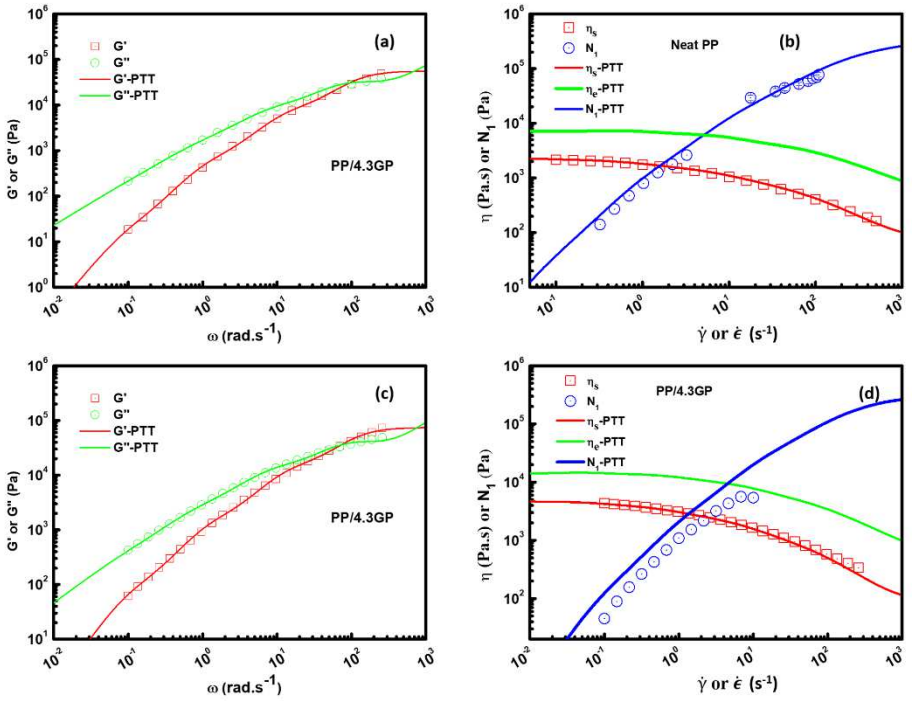


Figure 7-2. Experimental rheological data including the storage modulus G', loss modulus G'', and shear viscosity η_e and the first normal stress difference N_1 are shown for PP (a and b) and PP composite with graphite filler content of 4.3% (PP/4.3GP: c and d). The curves indicate the tuning corresponding rheological data by PTT model. With respect to PP/9.3GP composite, the N_1 data at high shear rate range is measured by means of exit pressure method explained in Chapter 6. The corresponding material parameters are shown in Table 7-1.

Figure 7-3 shows the varying trends of the rheological properties of PP/GP composites as the filler volumetric content increases further. As the filler volumetric content increases from zero up to 21.1%, it is found that the frequency where the G' value is equal to G'' value shifts to a lower range, which indicates stronger elastic properties caused by the addition of graphite fillers [8, 36]. In other words, adding filler into polymer matrix facilitates a transition from a fluid-like material to a solid-like one for

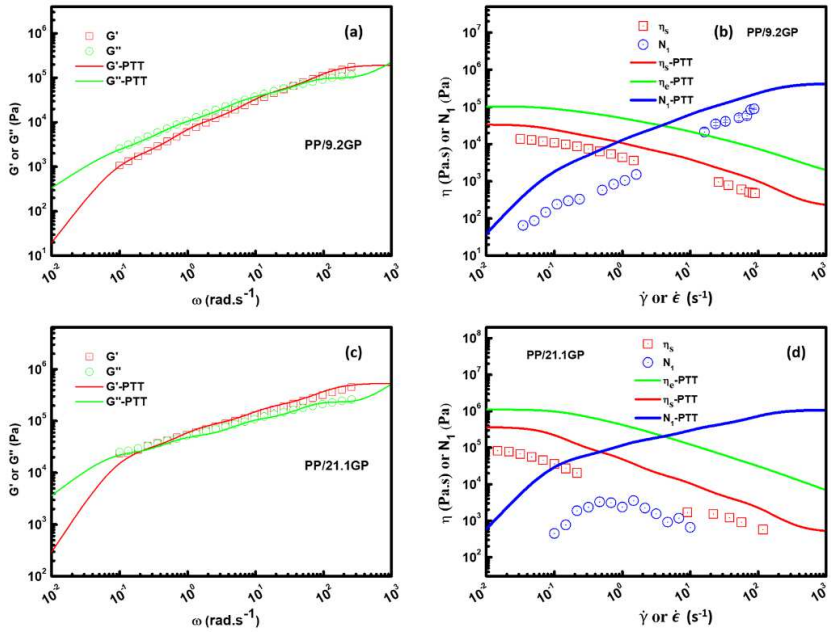


Figure 7-3. Experimental rheological data including the storage modulus G', loss modulus G'', and shear viscosity η_e and the first normal stress difference N_1 are shown for PP composite with graphite filler content of 9.2% (PP/9.2GP: a and b) and 21.1% (PP/21.1GP: c and d). The curves indicate the tuning corresponding rheological data by PTT model. With respect to PP/9.3GP composite, the N_1 data at high shear rate range is measured by means of exit pressure method explained in Chapter 6. The corresponding material parameters are shown in Table 7-1.

polymer melt at low strain rates in Fig. 7-3(a) and (c). In addition, the good prediction of the linear rheological data of G' and G'' for PP/9.2GP and PP/21.1GP composites indicate again the good predictive ability of PTT model. With respect to the non-linear rheological data such as N_1 and viscosity data, a more over-prediction is noted as the filler content from 4.3% in Fig. 7-2 grows to 9.2% and 21.1% in Fig. 7-3.

In our previous work [25], it is reported that the Cox-Merz rule is invalid as the graphite filler increases up to 9.2% and the possible reason for that should be the deconstruction of the filler-matrix and filler-filler interactions upon applying a large

strain. This factor is not accounted for by the viscoelastic constitutive PTT model. In addition, the significantly scattered N_1 data by rotational rheometer for PP/21.1GP composite in Fig. 7-3 indicates a severe melt fracture during the measurement experiments. Overall, there is a larger discrepancy between the PTT prediction and experimental data for the higher filler contents, while at least the right order of the magnitude value for both types of rheological data (symbols and curves) implies an acceptance of the PTT predictions with respect to all the rheological properties.

Table 7-1. Material parameters for Neat PP and PP composites with various graphite filler content.

	PTT model											
	Mode	λ_i		η_i		ε_i			ξ_i			
Neat PP	1	λ_1	0.01	η_1	536	ε_1	0.17		ξ_1	0.16		
	2	λ_2	0.1	η_2	816	ε_2	0.18		ξ_2	0.2		
	3	λ_3	1	η_3	707	ε_3	0.27		ξ_3	0.2		
	4	λ_4	10	η_4	220	ε_4	0.4		ξ_4	0.3		
PP/4.3GP	1	λ_1	0.01	η_1	670	ε_1	0.4		ξ_1	0.3		
	2	λ_2	0.1	η_2	1417	ε_2	0.4		ξ_2	0.3		
	3	λ_3	1	η_3	1590	ε_3	0.4		ξ_3	0.3		
	4	λ_4	10	η_4	970	ε_4	0.4		ξ_4	0.3		
PP/9.2GP	1	λ_1	0.01	η_1	1620	ε_1	0.65	*0.65 1.4*	ξ_1	0.7	*0.7*	*1.4*
	2	λ_2	0.1	η_2	4192	ε_2	0.65	*1.4 1.4*	ξ_2	0.7	*1.4*	*1.4*
	3	λ_3	1	η_3	9183	ε_3	0.65	*0.65 1.4*	ξ_3	0.7	*0.7*	*1.4*
	4	λ_4	10	η_4	18818	ε_4	0.65	*0.65 1.4*	ξ_4	0.7	*0.7*	*1.4*
PP/21.1GP	1	λ_1	0.01	η_1	3766	ε_1	0.9	*0.9 3*	ξ_1	0.95	*0.95*	*1.8*
	2	λ_2	0.1	η_2	12232	ε_2	0.9	*3 3*	ξ_2	0.95	*1.8*	*1.8*
	3	λ_3	1	η_3	58956	ε_3	0.9	*0.9 3*	ξ_3	0.95	*0.95*	*1.8*
	4	λ_4	10	η_4	292851	ε_4	0.9	*0.9 3*	ξ_4	0.95	*0.95*	*1.8*

Note: we investigate the sensitivity of parameter on the extrudate swell of PP/9.2GP and PP/21.1GP by changing the non-linear PTT model parameter ξ and ε as the PTT model cannot predict well the extrudate swell or rheological properties of PP composites with high filler content. The parameters in italic are chosen to compare with the original parameters in black. Attention should be paid that when we change the value of ξ parameter, the value of all the original ε value should be remained unchanged. We only studied the the sensitivity of the non-linear parameters on the rheological properties of polymer composites beacuse the linear parameter are necessary for a correct fitting of the rheological properties of by PTT model.

The corresponding material parameters for PTT model for different polymer composites with a graphite filler content ranging from 0 to 21.1% are shown in Table 7-1. Regarding the non-linear material parameter ξ_i, the material parameters are maintained constant in the four modes of PTT model for each polymer melt to decrease the number of the variables. The same consideration is taken for the parameter ε_i. It is expected that the values of the ξ_i and ε_i increase upon increasing the filler content. The reason can be explained that the rigid filler particles prohibit the entanglements amid polymer molecules, so that the entangled polymer chains can be easily disentangled once applying a small strain, thus resulting in a larger strain-thinning behavior [37].

In order to capture the varying trend of the material parameters against the filler content, it is of significance to establish a function relating the material parameter to the filler volumetric content *x*. As seen in Figure 7-4, the dependence of the viscosity parameter η_i in each mode on the filler content *x* is exhibited by a *log-log* plot. It should be mentioned that the data of viscosity parameter for neat PP with zero filler content (*x*=0) is not shown. It is interesting to note there is a perfect linearly increasing trend as the filler content increases, accompanied with a value of the determination factor R^2 high up to 0.995. The associated equation for η_i in each mode is shown in the corresponding subplot. All the equations can be rewritten and summarized by Equation 7-8:

$$\eta_i(x) = K_i * x^{a_i} \ (x > 0) \qquad (7\text{-}8)$$

The two constants K_i and α_i are listed in Table 7-2. It follows that larger values for both parameters of the viscosity function are observed in the order of $\eta_4(x)$, $\eta_3(x)$, $\eta_2(x)$ and $\eta_1(x)$. This indicates that the viscosity of polymer composites at

the low shear rate range thus corresponding to high relaxation time range (λ_i) is more sensitive to the addition of the graphite filler.

Table 7-2. The associated parameters for the equation of viscosity functions against the filler volumetric content for each mode of PTT model: $x > 0$.

	K_i	α_i
$\eta_1(x)$	$10^{4.32}$	1.08
$\eta_2(x)$	10^{5}	1.35
$\eta_3(x)$	$10^{6.3}$	2.27
$\eta_4(x)$	$10^{7.92}$	3.58

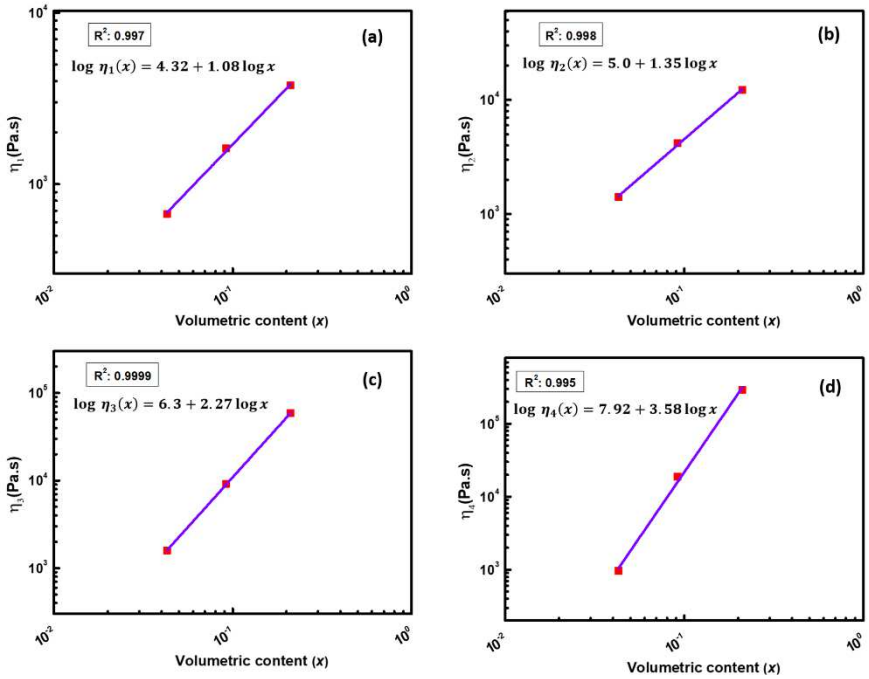


Figure 7-4. A comparison of the viscosity parameter $\eta_i(x)$ in each mode against the filler volumetric content (0, 4.3%, 9.2% and 21.1%). Lines indicate the fitting of the tuning material parameter (symbols) based on the rheological data of the polymer composite melts. Important to note that the material parameter for neat PP with x= 0 is not presented in each subfigure since both values of viscosity and volumetric filer content are plotted with a logarithm scale. The

associated equation for each viscosity against the filler content is shown in the subpicture, which is only valid with filler content $x > 0$.

Figure 7-5 shows the non-linear material parameters including ε_i and ξ_i for PP composites with various filler content. In Fig. 7-5(a), a linear increase of the ε_i value is observed as the filler volumetric content increases, indicating a stronger elongational thinning behavior. In addition, a similar varying trend is noted for the parameter ξ_i although with a lower value (0.883) of the determination factor R^2 as compared to that of the $\xi_i(x)$ function against the filler content (0.951) in Fig. 7-5(b). The associated equations are presented as:

$$\varepsilon(x) = 0.31 + 2.90x \qquad (7\text{-}9)$$

$$\xi(x) = 0.22 + 3.69x \qquad (7\text{-}10)$$

in which the constant 0.31 ± 0.04 and 0.22 ± 0.01 thus representing the intercept of the fitting line in Fig. 7-5 indicate the corresponding non-linear material parameters for neat PP shown in Table 7-1.

In summary, Eq. (7-7), Eq. (7-8), Eq. (7-9) and Eq. (7-10) compose the modified PTT model in this preliminary study. These equations are gathered below:

$$exp\left[\frac{\varepsilon_i(x)\,\lambda_i}{\eta_i} tr(\tau_{pi})\right]\tau_{pi} + \lambda_i\left[(1-\frac{\xi_i(x)}{2})\overset{\sim}{\tau_{pi}} + \frac{\xi_i(x)}{2}\overset{\frown}{\tau_{pi}}\right] = 2\eta_i(x)\,\boldsymbol{D} \quad (7\text{-}7)$$

$$\eta_i(x) = K_i * x^{a_i} \ (x > 0) \qquad (7\text{-}8)$$

$$\varepsilon(x) = 0.32 + 2.81x \qquad (7\text{-}9)$$

$$\xi(x) = 0.22 + 3.69x \qquad (7\text{-}10)$$

Comparing the present modified model with the one proposed by Thien *et al.* [38], it is seen that we establish three functions of the material parameters such as $\eta_i(x)$, $\varepsilon(x)$ and $\xi(x)$ against the filler volumetric content of graphite filler. This means that it might allow for obtaining the PTT material parameters for PP/GP composite with a certain filler content without knowing its experimental rheological data, which the original PTT model lacks. It is again important to mention that other filler characteristics such as the filler size and especially the interaction between the filler and matrix are not in the discussion scope of this preliminary study since focus is only on one type of the filler.

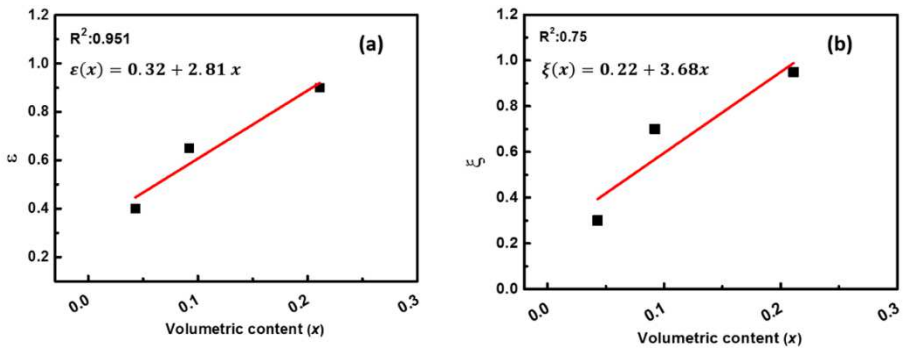


Figure 7-5. The dependence of the non-linear material parameter $\xi(x)$ and $\varepsilon(x)$ on the filler volumetric content. The red lines indicate the linear fitting of the non-linear material parameters for PP/GP composites tuned by PTT model. The associated equations are presented in each subplot.

7.4.2. Extrudate swell as a function of filler content

The typical character of polymer extrudate swell behavior is its continuous thus spatial and time dependent evolution after emerging the die exit. Fig.7-6 shows the evolution profile of the predicted extrudate swell behavior in the width and edge height direction of PP composites with various graphite filler volumetric contents at close to a flow

rate of 620 mm^3/s. For a comparison, the experimentally measured extrudate swell ratio for various polymer melts are shown as well in Fig. 7-6. It should be mentioned that the experimental measurements were carried out at a slightly different flows rate for each composite since we fixed the extrusion speed at 60 rpm. Due to the different densities and pellet sizes caused by the addition of graphite filler, it results in a flow rate of 620 mm^3/s for neat PP, 552.63 mm^3/s for PP/4.3GP composite, 510 mm^3/s for PP/9.2GP composite and 504.6 mm^3/s for PP/21.1GP composite.

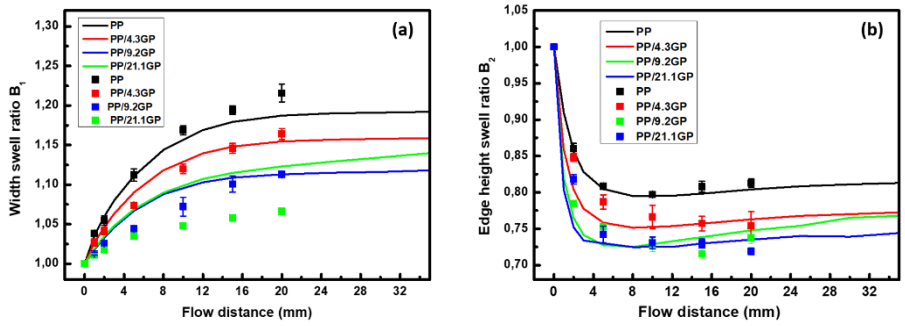


Figure 7-6. Comparison between the evolution of the simulated (curves) width swell ratio B_1 and edge height swell ratio B_2 of PP composite melt with various filler content at a simulated flow rate of 620 mm^3/s and the experimental measured swelling ratios of the extrudate (symbols) from the slit die as a function of the flow distance after the die exit. Attention should be paid that the experimental measurements were carried out at different flows rates for each composite since we fixed the processing condition at an extrusion speed of 60 rpm, thus resulting in 620 mm^3/s for neat PP, 552.63 mm^3/s for PP/4.3GP composite, 510 mm^3/s for PP/9.2GP composite and 504.6 mm^3/s for PP/21.1GP composite.

It is seen that the width swell ratio B_1 increases with the flow distance first, then reaches an equilibrium value with further increasing the flow distance. This is consistent with general reported trends [33, 39, 40]. It is expected that the experimentally measured extrudate swell ratio decreases with the addition of graphite

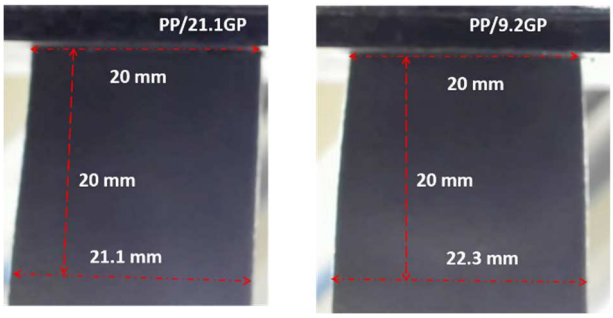


Figure 7-7. Images of the extrudate profiles of PP/21.1GP (a) and PP/9.2GP (b) composites from a slit die at an extrusion speed of 60 rpm, corresponding to a flow rate of 510 mm3/s and 504.6 mm^3/s respectively.

fillers [20]. For example, the width swell B_1 for neat PP at the flow rate of 620 mm^3/s is 1.20, which drops sharply to 1.11 as the volumetric filler content grows to 9.2% and further falls to 1.05 for PP/21.1 composite. The reason is explained that the rigid fillers prohibit the elastic recovery of the deformed polymer molecules thus decreasing the swelling behavior. However, a further simulated increase of the filler content to 21.1% results in a growing of the swell ratio B_1, which contrasts with the experiment results shown in Fig. 7-7. Furthermore, a significantly overpredicted width swell ratio B_1 of PP/21.1GP composite is observed in Fig. 7-6, which is not just to be attributed to a slight larger flow rate (620 mm^3/s) as a boundary condition applied in the simulation case as compared to that regarding the experiment (504.6 mm^3/s), based on another simulation case with exactly the same flow rate of 504.6 mm^3/s. Therefore, the PTT model appears not be able to reproduce the swelling behavior of polymer composite with a high volumetric content, considering the current material functions seems not fully take into account the rheological changes caused by adding graphite fillers. The reason might be attributed to the failure of the constitutive PTT model in covering the deconstructions of the network constructed by filler and matrix. On the other hand, a

high filler content might facilitate the occurring of the slippage thus resulting in a decreasing swell ratio [41], which is unaccounted for in this study.

Fig. 7-6(b) compares the swelling ratio of the extrudate height at the edge along the flow distance direction. As we reported before [26, 27], contraction flow behavior is noted as well although adding filler into the matrix. Increasing the filler content seems to contribute to a smaller swell ratio B_2 thus a larger contraction flow behavior. Hence, the need for 3D modeling remains. In addition, as compared with the width swell ratio B_1, the deviation between the predictions by PTT model and experimental measurements is insignificant even for the case of PP/21.1GP composite.

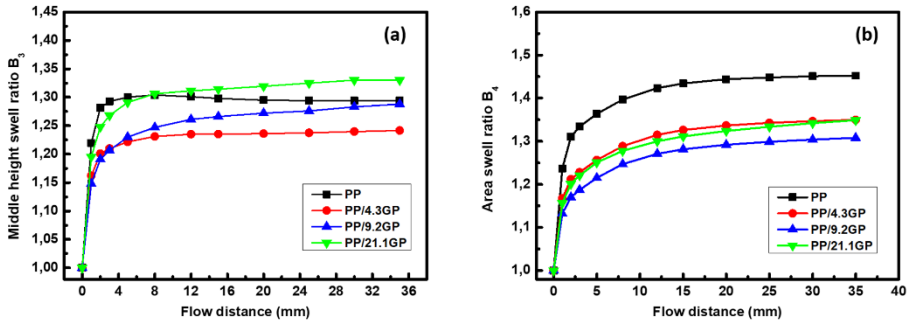


Figure 7-8. Comparison between the evolution of the simulated middle height swell ratio B_3 and area swell ratio B_4 (curves) of PP composite melt with various filler content at a flow rate of 620 mm^3/s.

In addition, Fig. 7-8 (a) presents the simulated swelling behavior of the extrudate height at the middle. Firstly, it is seen that a small increase in the filler content to 4.3% generally causes a decrease in the swell ratio B_3. However, further increasing the filler content in contrast leads to an increase of the swell ratio B_3 for PP/9.2GP and PP/21.1GP. Fig. 7-8(b) compares the evolution profiles of the area swelling behavior (B_4) for polymer composites. Due to both decrease of the swelling behavior in the height and width direction of the extrudate, the area swell ratio B_4 decreases as

expected with adding filler. However, increasing filler content from 9.2% to 21.1% again contributes to a larger area swell ratio B_4, which further indicates the failure of PTT model in modelling the extrudate swell behavior of polymer composite with high filler content, consistent with the observations in the swelling behavior in width direction shown above.

In previous work [42], it has been shown that the area swell behavior is however not affected so much if the upstream irregular contraction flow region is included, since there is an opposite swelling behavior in middle height and width direction. An increasing trend in the former case is obtained while a decreasing trend in the latter case is noticed. Clearly, this is different from what have been observed with the addition of filler particles into the matrix. This indicates more options for adjusting and controlling the extrudate swell behavior for polymer melt.

Fig. 7-9 exhibits the simulated extrudate profile for each polymer melt at the flow rate of 620 mm^3/s and the flow distance of 40 mm after the die exit. A direct insight is noted that the width swell ratio decreases first with adding filler content, then shows an increase trend with further addition of filler. In addition, here is the interest that the sharp corner in the PP extrudate seems to become less obvious as increasing the filler content and even disappears with filler content of 21.1%. The disappearing of the sharp edges disappears with further addition of fillers has also been put forward by Spanjaards *et al.* [43] with increasing the Weissenberg number (Wi) of melt, which is a strength of 3D modeling.

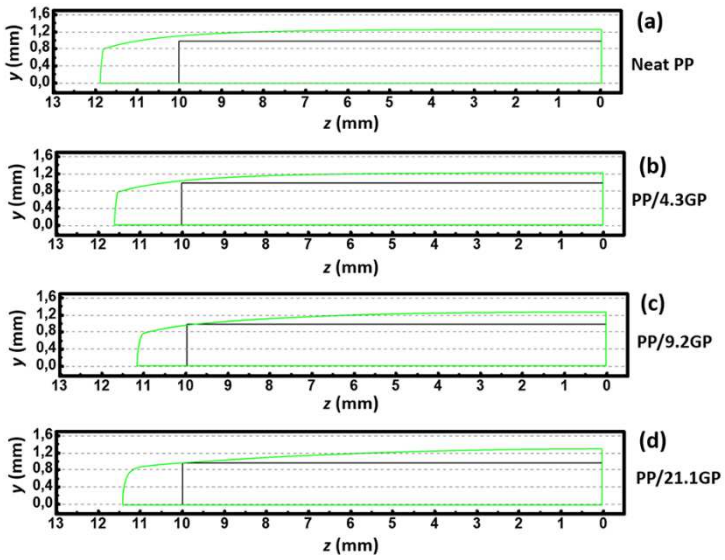


Figure 7-9. Profiles of the extrudate at a flow rate of 620 mm^3/s of PP composite melt with various filler content at the flow distance of 40 mm after the die exit: (a) neat PP, (b) PP/4.3GP, (c) PP/9.2GP, (d) PP/21.1GP. Black curves indicate the shape of the slit die while the green curves represent the extrudate profiles.

7.4.3. Theoretical evaluation regarding material parameters

Fig.7-10 shows the rheological analysis of PP/9.2GP and PP/21.1GP composites with varying the non-linear material parameters ε and ξ. It should be noted that the format N_1-ξ_2-1.4 in the legend of Fig. 7-10(a) indicates the value of 1.4 for the material parameter ξ in mode 2 of multi-mode PTT model. The format N_1-all-ξ-1.4 corresponds to the parameter ξ in each mode of multi-mode PTT model being 1.4. As a result, the term with the similar format in Fig. 7-10 (b), (c) and (d) has the same indication. Without special indications, these curves represent the rheological data with the original parameters shown in Table 7-1. For PP/9.2GP composite, it is seen that increasing ξ_2 value from 0.65 (original parameter in Table 7-1) to 1.4 seems slightly influences the shear viscosity data but increases the N_1 data. In addition, as for

elongational viscosity data, surprisingly, it is found that the elongational data can be fitted only at small range of the elongational rate less than 10 s^{-1} with Polymat used as the fitting tool. Furthermore, ifwe fix all ξ values at 1.8, an irregular fluctuated curve shape can be obtained not only for N_1 data but also for shear viscosity data. This might explain the divergence of the simulation calculation when we vary the shear parameter ξ from the original value in Table 7-1 to 1.8. In addition, we found that the maximum value for ξ should be smaller than 1, otherwise the abnormal fitting results of the rheological data will be obtained, resulting in the calculation divergence for the case of extrudate swell modelling. For completeness it is mentioned here that for Polyflow software there is a range for ξ parameter between 0 to 1, while for the parameter ε there is no obvious limit. Some reporters tended to fix the ξ value at zero, which results in an ultralarge ε value for PTT model [38], although it means an ignoring of the second normal stress difference N_2.

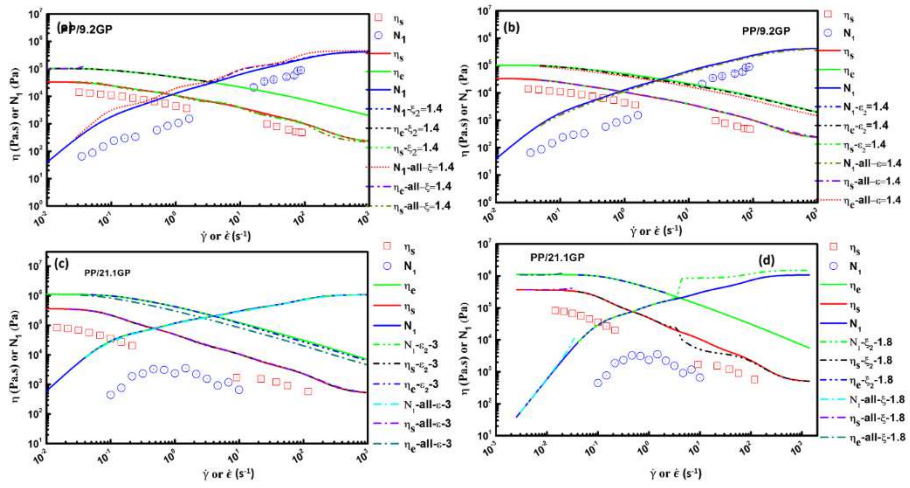


Fig.7-10. Rheological analysis of PP/9.2GP and PP/21.1GP composites with varying the non-linear material parameters ε and ξ. Notes should be made that the format N_1-ξ_2-3 corresponds to the value of 3 for the material parameter ξ in mode 2 of multi-mode PTT model. The format N_1-all-ξ-1.8 indicates that the parameter ξ in each mode of multi-mode PTT model is 1.8.

Without special indications, these curves represent the rheological data with the original parameters shown in Table 7-1.

For PP/21.1GP composite in Fig. 7-10(c), it is found that a large increase of the elongational parameter ε from the original value 0.9 in Table 7-1 to 3 leads to a decrease of the elongational viscosity but seems almost not to influence the shear viscosity data η_s and normal stress difference N_1. Fig. 7-10(d) compares the effect of the shear parameter ξ on the rheological data. It is interesting to note that there is an irregular sharp change for N_1 and shear viscosity data η_s as the ξ_2 increases from 0.9 to 1. When the parameter ξ in each mode is fixed at a value of 1.8, not only η_e but also η_s and N_1 can be fitted at the very small shear rate or elongational rate range less than 0.1 s^{-1}. This might be the reason why the corresponding numerical modelling of the extrudate swell of the PP/21.1 GP composite melt fails in this case.

Considering that the simulation results of the extrudate swell behavior of the PP/9.2 GP and PP/21.1GP composite do not correspond well to experimental results, respectively, here we compare the modelling extrudate swell with varying the material parameter ε since we have confirmed that ξ value should lie in the range from 0 to 1, otherwise the numerical simulation case performed by Polyflow would fail. It is seen that an increase of the ε_3 parameter from 0.65 to 1.4 does not lead to a significant change to the extrudate swell profile of PP/9.2 GP composite as a function of the flow distance, which indicates a further adjustment of the elongational parameter seems not be able to fully eliminate the discrepancy between the simulated width swell ratio B_1 and its experimental counterpart. A similar varying trend can be found in terms of the height swell ratio B_3. However, as we reported before [27], varying the parameter from 0.05 to 0.65 results in a significant decrease of the extrudate swell ratio for neat PP melt. In contrast to the large change of the elongational behavior of the polymer

melt from elongatioal-hardening to the typical elongational-thinning behavior with varying ε_3 parameter from 0.05 to 0.65 [27], the rheological properties of PP/9.2 GP composite varies slightly by changing ε_3 parameter from 0.65 to 0.05, resulting in a slight effect on the extrudate swell in return. On the other hand, for the PP/9.2 composite with already a strong strain-thinning behavior, it seems difficult for a larger elongational-thinning behavior by a further increase of the parameter ε_3.

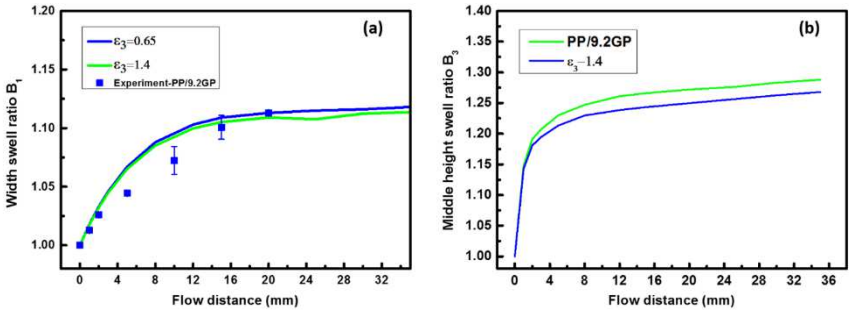


Figure 7-11. Effect of parameter on the extrudate swell B_1 and B_3 of PP/9.2 GP composite. Increasing the parameter ε_3 from 0.65 to 1.4 leads to a slight decrease of both width swell and middle height swell ratio.

Fig. 7-12 exhibits the sensitive analysis of the parameter ε on the width swell ratio B_1 and height swell ratio B_3 of PP/21.1GP composite. We increased the ε parameter in each mode from 0.9 in Table 1 to the value of 2, shown in Fig. 12. Similar changes are seen as compared to that of PP/9.2GP composite, namely a rather slight decrease of both width swell ratio B_1 and B_2 are noted, which still shows a significant difference from the experimental measurement in Fig. 7-11a.

It seems that a further change of the parameter could not cover and eliminate the discrepancy between the PTT-based predicted extrudate swelling and the experimental measurement for PP composite with high filler content. Phan-Thien pointed out that the intriduction of slippage condition at die wall reduces the amount

of the extrudate swell of the planar polymer flow [43]. On the other hand, previous reports demonstrated that the slippage behavior in capillary measurement leads to a lower real viscosity than its apparent viscosity [37, 44], which is also at least one of the reason for the failure of Cox-merz rule for polymer composites with high filler content. Therefore, the significant discrepancy between the PTT predicted extrudate swell behavior and that of PP/21.1GP composite might be attributed to its slippage behavior which is not taken into consideration for numerical simulation in this study. A further study regarding this issue needs to be carried out.

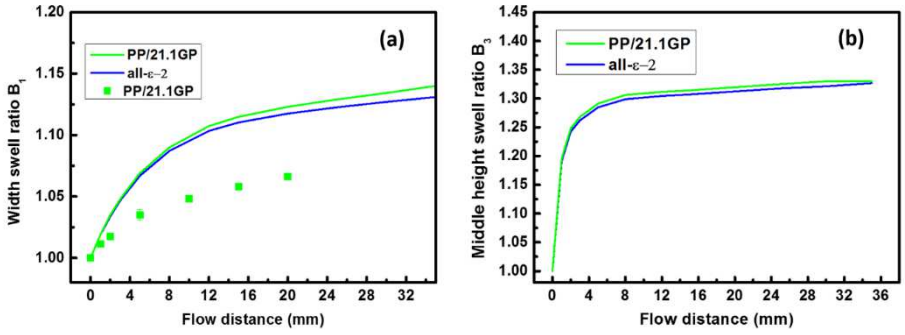


Figure 7-12. Effect of parameter ε on the extrudate swell B_1 and B_3 of PP/21.1GP composite. Increasing the parameter ε from 0.9 to 2 leads to a slight decrease of both width swell and middle height swell ratio.

7.4.4. From simulations with no slip boundary conditions to simulations doing so

As we mentioned above, the reason for PTT model failing in predicting the extrudate swell behavior of PP composites with high filler content might be attributed to the possible slippage behavior during the extrusion processing. There are many reports that pointed out that the occurrence of the slippage behavior for polymer melts tends to decrease the swell ratio through a slit die based on a 2D modelling. Fig. 7-13

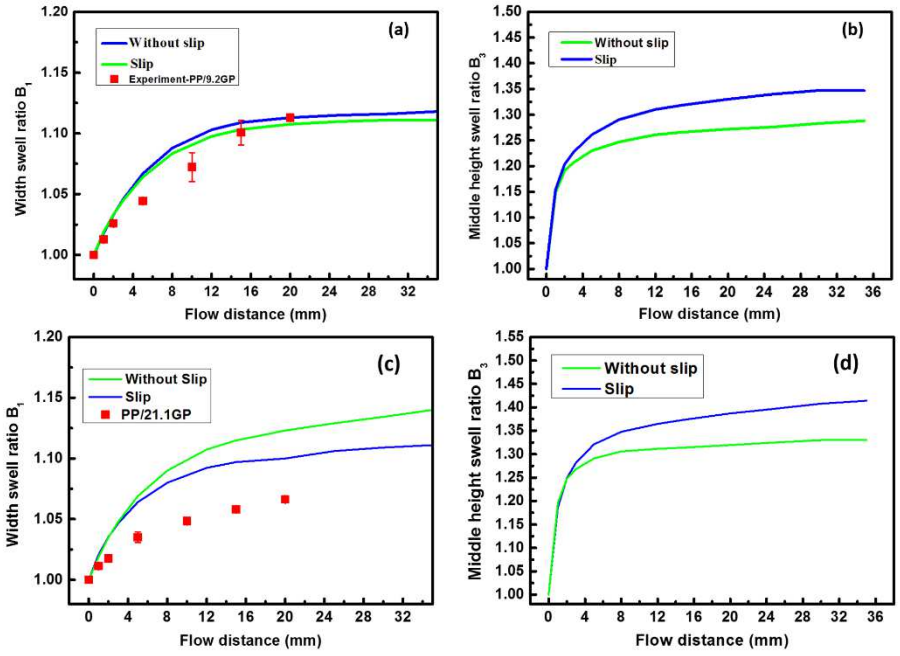


Figure 7-13. Effect of slip behavior on the extrudate swell B_1 and B_3 of PP/9.2GP (a-b) and PP/21.1GP (c-d) composite.

compares the extrudate swell behavior of PP composite with 9.2% and 21.1% graphite filler by introduction of the slippage behavior or not. It is seen that the slippage behavior decreases the extrudate swell ratio of the extrudate width as expected, which is closer to the experiment measurement results. However, the swell behavior at the middle height direction of the extrudate unexpectedly increases with introducing the slippage behavior along the die wall inside the die. It is worth mentioning that the swell behavior at the middle height direction with the realistic 3D modelling configuration corresponds to the swell behavior with the ideal 2D modelling configuration. Different from the general varying trend with 2D modelling, the swell ratio B_3 increases by an introduction of the slip behavior shown in Fig. 7-13. Since the experimental measurements of the swell ratio B3 for polymer composites are not available with the experimental setup in this study, it is an open question for the effect

of the slip behavior on the 3D extrudate swell behavior from a slit die. The unexpected increasing B3 swell ratio might be attributed to the mass conservation rule of the polymer melts when the swell behavior at the extrudate width direction decreases.

7.5. Conclusions

In this preliminary study, the rheological properties of PP/Graphite composites with various volumetric contents have been presented and discussed extensively. It is found that the original PTT model has an excellent ability to predict the linear rheological properties including the storage G' and loss G'' modulus for all PP composites. However, with increasing filler content, an overprediction of the non-linear rheological properties such as the shear viscosity η_s and the first normal stress difference N_1 by PTT mode result, although the rheological data by means of experiment and fitting with the PTT model has at least the same order of magnitude. The reason might be attributed to the deconstruction of the interaction between filler-filler and filler-matrix once there is a large strain in the non-linear viscoelastic region applied to the polymer chains. This factor seems to not be accounted for by PTT model combined with basic functions.

We have compared the evolution profiles of the predicted swelling of PP/Graphite composites in the height at the edge and middle, and the width direction of the extrudate from a slit die with the viscoelastic constitutive PTT model. It is found that the addition of filler particles is decreases the extrudate swell behavior in all dimensional directions but unexpectedly increases the extrudate swelling behavior with a further addition of filler content up to 9.2%. This is different from the experimental results, indicating the constitutive PTT model with basic functions fails in predicting the extrudate swell behavior of polymer composite with high volumetric

filler content. We attribute this to the deconstruction of the network architecture between filler and matrix as a large strain is applied, which is not taken into consideration by PTT model. The consideration of slip conditions however reveals interesting shifts in material behavior.

Furthermore, in this preliminary study, focus is on one type of the rigid filler, graphite. As a consequence, the filler characteristics such as the filler shape, filler size and the interaction between filler and matrix thus affecting the rheological properties should be taken into consideration with respect to the modified constitutive PTT model to account for the impact on extrudate swell behavior of polymer composites caused by adding fillers. This is an interesting research topic which deserves to be paid attention in future work.

REFERENCES

1. Wieme, T., et al., *The relevance of material and processing parameters on the thermal conductivity of thermoplastic composites.* Polymer Engineering & Science, 2018. **58**(4): p. 466-474.
2. Velayudhan, S., et al., *Extrusion of hydroxyapatite to clinically significant shapes.* Materials Letters, 2000. **46**(2-3): p. 142-146.
3. Miller, E. and J.P. Rothstein, *Control of the sharkskin instability in the extrusion of polymer melts using induced temperature gradients.* Rheologica acta, 2004. **44**(2): p. 160-173.
4. Ebrahimi, M., et al., *Melt fracture of linear low-density polyethylenes: Die geometry and molecular weight characteristics.* Physics of Fluids, 2018. **30**(5): p. 053103.
5. Tian, H., et al., *Study on extrudate swell of polypropylene in double-lumen micro profile extrusion.* Journal of Materials Processing Technology, 2015. **225**: p. 357-368.
6. T'Joen, C., et al., *A review on polymer heat exchangers for HVAC&R applications.* international journal of refrigeration, 2009. **32**(5): p. 763-779.
7. Chen, X., et al., *Recent research developments in polymer heat exchangers–A review.* Renewable and Sustainable Energy Reviews, 2016. **60**: p. 1367-1386.
8. Luo, W., et al., *Thermal, electrical and rheological behavior of high-density polyethylene/graphite composites.* Iranian Polymer Journal, 2015. **24**(7): p. 573-581.
9. Tu, H. and L. Ye, *Thermal conductive PS/graphite composites.* Polymers for Advanced Technologies, 2009. **20**(1): p. 21-27.
10. Muratov, D., et al., *Thermal conductivity of polypropylene filled with inorganic particles.* Journal of Alloys and Compounds, 2014. **586**: p. S451-S454.
11. Zhou, W., et al., *Study on insulating thermal conductive BN/HDPE composites.* Thermochimica Acta, 2007. **452**(1): p. 36-42.
12. Ma, A., et al., *Preparation and properties of multi-walled carbon nanotubes/carbon fiber/epoxy composites.* Polymer Composites, 2014. **35**(11): p. 2150-2153.
13. Liang, J., et al., *Melt extrudate swell behavior of multi-walled carbon nanotubes filled-polypropylene composites.* Polymer Composites, 2017 2017, 38: 2433-2439. **38**: p. 2433.
14. Liang, J.-Z., *Effects of particle size on melt viscoelastic properties during capillary extrusion of glass bead-filled LDPE composites.* Journal of Thermoplastic Composite Materials, 2006. **19**(6): p. 703-713.
15. Liang, J.-Z., J. Yang, and C.-Y. Tang, *Die-swell behavior of PP/Al (OH) 3/Mg (OH) 2 flame retardant composite melts.* Polymer testing, 2010. **29**(5): p. 624-628.
16. Sentmanat, M. and S.G. Hatzikiriakos, *Mechanism of gross melt fracture elimination in the extrusion of polyethylenes in the presence of boron nitride.* Rheologica acta, 2004. **43**(6): p. 624-633.

17. Allal, A. and B. Vergnes, *Molecular design to eliminate sharkskin defect for linear polymers.* Journal of Non-Newtonian Fluid Mechanics, 2007. **146**(1-3): p. 45-50.
18. Allal, A., et al., *Relationships between molecular structure and sharkskin defect for linear polymers.* Journal of non-newtonian fluid mechanics, 2006. **134**(1-3): p. 127-135.
19. Ariffin, A., Z. Ariff, and S. Jikan, *Evaluation on extrudate swell and melt fracture of polypropylene/kaolin composites at high shear stress.* Journal of Reinforced Plastics and Composites, 2011. **30**(7): p. 609-619.
20. Liang, J., et al., *Melt extrudate swell behavior of multi-walled carbon nanotubes filled-polypropylene composites.* Polymer Composites, 2015.
21. Liang, J.Z., et al., *Extrudate swell behavior of polypropylene composites filled with microencapsulated red phosphorus.* Journal of Applied Polymer Science, 2013. **129**(6): p. 3497-3501.
22. Dangtungee, R. and P. Supaphol, *Melt rheology and extrudate swell of titanium (IV) oxide nanoparticle-filled isotactic polypropylene: Effects of content and surface characteristics.* Polymer Testing, 2008. **27**(8): p. 951-956.
23. Aral, B.K. and D.M. Kalyon, *Viscoelastic material functions of noncolloidal suspensions with spherical particles.* Journal of Rheology, 1997. **41**(3): p. 599-620.
24. Stabik, J., *Influence of filler particle geometry on die swell.* International Polymer Processing, 2004. **19**(4): p. 350-355.
25. Tang, D., et al., *Evaluating the exit pressure method for measurements of normal stress difference at high shear rates.* Journal of Rheology, 2020. **64**(3): p. 739-750.
26. Tang, D., et al., *Isothermal flow of neat polypropylene through a slit die and its die swell: Bridging experiments and 3D numerical simulations.* Journal of Non-Newtonian Fluid Mechanics, 2019. **266**: p. 33-45.
27. Tang, D., et al., *Three-dimensional flow simulations for polymer extrudate swell out of slit dies from low to high aspect ratios.* Physics of Fluids, 2019. **31**(9): p. 093103.
28. Kiriakidis, D. and E. Mitsoulis, *Viscoelastic simulations of extrudate swell for an HDPE melt through slit and capillary dies.* Advances in Polymer Technology, 1993. **12**(2): p. 107-117.
29. Kádár, R., I.F. Naue, and M. Wilhelm, *First normal stress difference and in-situ spectral dynamics in a high sensitivity extrusion die for capillary rheometry via the 'hole effect'.* Polymer, 2016. **104**: p. 193-203.
30. Macosko, C.W. and R.G. Larson, *Rheology: principles, measurements, and applications.* 1994.
31. Meissner, J., R. Garbella, and J. Hostettler, *Measuring normal stress differences in polymer melt shear flow.* Journal of Rheology, 1989. **33**(6): p. 843-864.
32. Mitsoulis, E., et al., *Flow Behavior of a Polypropylene Melt in Capillary Dies.* International Polymer Processing, 2018. **33**(5): p. 642-651.
33. Konaganti, V., et al., *Extrudate swell of high density polyethylenes in slit (flat) dies.* International Polymer Processing, 2016. **31**(2): p. 262-272.

34. Barnes, H.A., *A review of the rheology of filled viscoelastic systems.* Rheology reviews, 2003: p. 1-36.
35. Ohl, N. and W. Gleissle, *The second normal stress difference for pure and highly filled viscoelastic fluids.* Rheologica acta, 1992. **31**(3): p. 294-305.
36. Prashantha, K., et al., *Masterbatch-based multi-walled carbon nanotube filled polypropylene nanocomposites: Assessment of rheological and mechanical properties.* Composites science and technology, 2009. **69**(11): p. 1756-1763.
37. Hristov, V., E. Takacs, and J. Vlachopoulos, *Surface tearing and wall slip phenomena in extrusion of highly filled HDPE/wood flour composites.* Polymer Engineering & Science, 2006. **46**(9): p. 1204-1214.
38. Thien, N.P. and R.I. Tanner, *A new constitutive equation derived from network theory.* Journal of Non-Newtonian Fluid Mechanics, 1977. **2**(4): p. 353-365.
39. Konaganti, V.K., et al., *Extrudate swell of a high-density polyethylene melt: II. Modeling using integral and differential constitutive equations.* Journal of Non-Newtonian Fluid Mechanics, 2015. **225**: p. 94-105.
40. Normandin, M., et al., *Three-dimensional extrudate swell experimental and numerical study of a polyethylene melt obeying a memory-integral equation.* Journal of non-newtonian fluid mechanics, 1999. **87**(1): p. 1-25.
41. Yang, C. and Z. Li, *A study of wall slip in the capillary flow of a filled rubber compound.* Polymer Testing, 2014. **37**: p. 45-50.
42. Tang, D., et al., *The impact of upstream contraction flow on three-dimensional polymer extrudate swell from slit dies.* Journal of Non-Newtonian Fluid Mechanics, 2020. 282: 104337.
43. Spanjaards, M., M. Hulsen, and P. Anderson, *Transient 3D finite element method for predicting extrudate swell of domains containing sharp edges.* Journal of Non-Newtonian Fluid Mechanics, 2019. **270**: p. 79-95.
44. Mazzanti, V., F. Mollica, and N. El Kissi, *Rheological and mechanical characterization of polypropylene-based wood plastic composites.* Polymer Composites, 2015.

Chapter 8

CONCLUSIONS AND OUTLOOK

8.1. Conclusions

A comprehensive study of the flow behavior inside and outside the slit die has been fundamentally conducted, considering polyolefin melts and going beyond the state of the art as put forward in Chapter 2. Advanced 3D numerical modelling has been performed considering the finite element method based POLYFLOW algorithm combined with 3D experimental validations. Several major conclusions could be drawn, as highlighted below.

Firstly, the isothermal flow of neat PP at 200 °C through a slit die and upon subsequent swelling has been investigated in Chapter 3 by extrusion experiments and 3D numerical simulations with the generalized Newtonian constitutive model with the Cross law viscosity function and the viscoelastic multi-mode PTT model. The pressure profiles predicted by both models inside the die agree well with experimental data obtained for all flow rates evaluated. The slightly larger exit pressure predicted by the PTT model compared to that of Cross law model causes different extrudate swell behavior, which corresponds to experimental results for extrudate swell through real-time measurements. The swell behavior in both height and width directions depends on the distance from the die exit and both swell ratios increase with the flow rate, which is in contrast to the simulation results obtained with the Cross law model. In addition, the swell ratio in the width direction increases in a much lower rate than the swell ratio in the height direction until equilibrium is achieved in both directions.

As a result, the distance from the die exit in which the final extrudate shape is obtained strongly depends on the die width.

Secondly, the impact of the die geometry including the aspect ratio namely the width/height ratio of slit dies on the 3D extrudate swell ratio has been investigated in Chapter 4. High aspect ratio leads to a low width swell ratio B_1 and edge height swell ratio B_2 and shifts the onset of the axial equilibrium swelling position to a further distance. Contract flow at the edge of the extrudate height is noted while increasing the edge height swell ratio B_2. The middle height swell ratio B_3 profiles for the 3D flow significantly deviate from that of the 2D simulation. This phenomenon of a secondary shrinkage is not eliminated even if the aspect ratio increases to the highest value of 20. The mechanism for the above phenomenon is illustrated by the flow velocity and stress fields. A significant deviation of the 3D configurations from the corresponding 2D one inside and outside the die is generally noted. Increasing the aspect ratio of the flow cells narrows the discrepancy but cannot vanish the 3D effect. For sure the deviation out of the die still cannot be neglected, even if the flow behavior in the die (y direction) seems almost the same as that of the 2D flow with an aspect ratio higher than 2. The larger axial velocity v_x for a larger aspect ratio outside the die contributes to a slower normal stress relaxation, thereby a slower swell behavior delaying the swelling equilibrium position. Furthermore, a parametric study reveals that the width swell ratio B_1 largely decreases with increasing ξ which is related to the second normal stress difference. An increasing ε controlling the elongational viscosity decreases both the width well ratio B_1 and the height swell ratio B_3. In addition, the secondary shrinkage flow becomes large with decreasing ξ but still cannot be observed in the corresponding 2D flow. This implies that the 3D effect on the

extrudate swell behavior depends not only on the geometric characteristics of the flow channel but also on the melt material parameters.

Thirdly, we evaluated the impact of upstream contract flow on polymer extrudate swell from slit dies through numerical simulations for different flow rates by means of adjusting the die length (l_2)/height ratio in Chapter 5. Decreasing die length leads to an opposite variation trend of the swell ratio in the width and edge height direction (decreases up to 30%) compared to the middle height direction (increases up to 55%). The area swell ratio remains limited with decreases below 5%, specifically for lower flow rates. This implies that an identification of possible anisotropy should in general not be based on the area swell ratio. Furthermore, a method to obtain an extrudate product with a less uneven profile is to elongate the die, especially for polymer melts that experience large extensional deformations.

The l_2 value does not significantly affect the normal stress distribution until the polymer flow reaches the die entry through the contraction flow channel. Downstream the die entry, a significantly larger magnitude of the normal stresses τ_{xx} and τ_{yy} in the flow region close to the top of the die wall is observed upon decreasing l_2, indicating larger extensional and compression forces being applied to the flowing melt. However, an opposite varying trend is noted regarding the τ_{xx} and τ_{zz} in vicinity of the side wall of the die, further highlighting the relevance of 3D simulations in which the side wall effects are fully accounted for. Outside the die exit, there is a large difference of the stress redistribution behavior caused by the variations of the die length l_2, which demonstrates the corresponding anisotropic swell behavior mentioned above. The similar final extrudate average axial velocity regardless of the l_2 value is consistent with the similar area swell ratios and implies a similar axial velocity redistribution

behavior. Additionally, the evolution of the transversal velocity v_y and lateral velocity v_z components after the die exit directly illustrate the opposite varying trend of the swell behavior in the extrudate middle height and width direction upon increasing die length.

Fourthly, the 3D modelling of the extrudate swell behavior of several polymer melts is utilized in Chapter 6 to validate the exit pressure method for measuring the normal stress difference data at high stain rate range, which is a challenging research topic in the field of rheology. For neat polymer melts at 200 ^{o}C, we have comprehensively evaluated the exit pressure method via the slit rheometer to measure N_1 values at high shear rates. In this method, the (quasi-)linear axial pressure profiles for the polymers at various wall shear rates are first extrapolated to the die exit, yielding the corresponding exit pressure values, which in turn are related to the associated shear stresses to deliver N_1 values. For these neat polymers, the empirical Cox-Merz rule is valid. The N_1 values at the shear-rate magnitude order of 10 to 100 s^{-1} as measured by the exit pressure method lie additionally in the value range calculated by the Laun rule with an exponent α of 0 and 0.7.

3D numerical simulations with respect to the extrudate swell behavior have been performed with the differential viscoelastic multi-mode PTT model. The corresponding material parameters have been obtained by tuning the rheological functions including fitting the N_1 data obtained from the empirical Laun rule that are consistent with the exit pressure method based N_1 data. There is a good agreement between the predicted extrudate swell and experimental measurements for the neat polymer melts, further confirming that the exit pressure method is appropriate to determine N_1 values. In addition, the pressure contribution from velocity

rearrangement near the die exit accounts for *ca.* 25-40% at various shear rates, which although does not dismiss the exit pressure method, since the actual simulated N_1 values with 3D modelling by PTT model are consistent with those by the exit pressure method based on the simulated pressure profiles. In addition, a negligible effect coming from viscous heating of polymer melts on the pressure field near the die exit has been demonstrated. Overall, the exit pressure method can be reliable utilized for the neat polymers studied. In addition, even though the Laun rule fails in calculating the N_1 data for PP composite, the N_1 values obtained with the exit pressure method appear to be in the extrapolation region of those obtained by the rotational rheometer, implying that the exit pressure method appears to have also potential for more complex materials.

Lastly, with the aim of investigating the extrudate swell behavior of such more complex polymer composites, the numerical simulations by PTT model are compared to experimental measurements in Chapter 7. The rheological properties of PP/Graphite composites with various volumetric contents have been compared and discussed. It is found that the original PTT model has an excellent ability to predict the linear rheological properties including the storage G' and loss G'' modulus for all PP composites. However, with the increasing of the filler content, an overprediction of the non-linear rheological properties such as the shear viscosity η_s and the first normal stress difference N_1 by PTT model results, especially as the volumetric filler content grows up to 21.1% a. A modified PPT model is proposed by means of establishing the functions of the material parameters such as η_i, ξ and ε against the volumetric content of graphite filler. Furthermore, it is found that adding filler particles is decreases the simulated extrudate swell behavior in all dimensional directions, in agreement with experiment results. However, an increase of the

extrudate swelling behavior is noticed with a further addition of filler content to 9.2%, which is opposite to the experimental results, indicating the constitutive PTT model with basic functions fails in predicting the extrudate swell behavior of polymer composite with high volumetric filler content. It is attributed to the deconstruction of the network architectures between filler and matrix as a large strain is applied, which is not fully taken into consideration by current PTT model.

Hence, die swell phenomenon has been fully captured for the neat polyolefin melts but for the related composites further refinements are still needed.

8.2. Outlook

The PhD research has focused on the comprehensive investigation of the complicated flow behaviour of various viscoelastic flows through the flow channels with different flow geometries, specially the extrudate swell, by 3Dnumerical modelling. Several research perspectives are identified which are thought to merit from future work.

For example, in this PhD research, the efforts to figure out the 3D complicated extrudate swell behaviour are involving polyolefin component, such as neat PP, LDPE and HDPE. For polymer blends and even immiscible polymer systems, for example PP/PS blends, the relevance of the thermal kinetics of molecular migrations on extrudate swell once the melts emerge the die exit caused by the phase-separating behaviour are interesting to figure out. To address this issue, the proper viscoelastic constitutive model should be firstly selected to capture the rheological behaviour in dynamic or steady mode.

In addition, with respect to some highly chain-branched or polydisperse polystyrene melts, interests lie in the investigations to see if the constitutive PTT model is able to

accurately predict the rheological properties especially the non-linear normal stress difference and elongational viscosity data, which seems to be difficult to obtain at high strain rates. In terms of these polymer systems, the molecule-based constitutive Double Extended Pom-pom (DCPP) model appears to be a substitution to allow for the prediction of the rheological properties. Consequently, this may provide insights into deviations of the simulations by PTT model from experimental measurements regarding the extrudate swelling behaviour of highly chain branched polymers stemming from inherent disadvantage of PTT model or the numerical scheme methods. Experimentally, for these polymer systems, a 3D image measurement setup should be able to accurately capture the extrudate swelling behaviour far away from the die exit due to the more complicated multiscale relaxation behaviour by avoiding the sagging or gravity effect and maintaining the isothermal temperature to avoid the impact of the crystallizations of the polymer melts on the swelling behaviour over the whole evolution.

With respect to the polymer composites, although a modified PTT model has been proposed by establishing the functions of the material parameters against the volumetric filler content, further steps should be taken to explore how to add items accounting for the deconstructions of the filler-filler and filler-matrix network into the original viscoelastic PTT model once a large strain is applied to the polymer melts. It should be mentioned that for the polymer composites with ultrahigh filler content, a yield stress phenomenon might happen, which is suggested to be also taken into consideration. The rheological properties of more kinds of fillers with various geometric characteristics should be measured and then fitted by PTT model, so that a modified PTT model is proposed to account for the filler particles with generalized filler characteristics such as filler size, aspect ratios, filler content and filler-matrix

interactions. This in other hand allows for a generalized viscoelastic model which not only be able to predict the flow behaviour of neat polymer melts but also the composites systems with various filler contents. Here also the variation of processing temperature crucial.

In addition, the slippage behaviour might happen in extrusion processing as the shear stress is beyond a critical value. Although slippage behaviour is generally thought to decrease the swelling behaviour of polymer melts, how it affects the 3D anisotropic swelling behaviour in each dimension of the extrudate from slit dies also seems interesting via a further 3D modelling study for various polymer melts.

Finally, die designs in industry are based on the understanding of the complicated extrudate swell behaviour to obtain the final desired products in various processing conditions. A reverse extrusion engineering based on the 3D numerical modelling should be the next goal to establish the proper die design regarding the flow channels.

Appendix A

Extra details on viscoelastic PTT model

A.1. Predictions of PTT model in simple shear flow

The basic constitutive equations of PTT model to compute the extra stress tensor τ_p is written like:

$$g(\boldsymbol{\tau}_p)\boldsymbol{\tau}_p + \lambda\left[(1-\tfrac{\xi}{2})\overset{\frown}{\boldsymbol{\tau}_p} + \tfrac{\xi}{2}\overset{\frown}{\boldsymbol{\tau}_p}\right] = 2\eta_p\mathbf{D} \qquad \text{(A-1)}$$

$$g(\boldsymbol{\tau}_p) = \exp\left[\frac{\varepsilon\lambda}{\eta_p}\mathrm{tr}(\boldsymbol{\tau}_p)\right] = \exp\left[\frac{\varepsilon\lambda}{\eta_p}(\tau_{xx} + \tau_{yy} + \tau_{zz})\right] \qquad \text{(A-2)}$$

in which $\mathrm{tr}(\boldsymbol{\tau_p})$ is the trace of the tensor stress $\boldsymbol{\tau}_p$. $\boldsymbol{\tau}_p$ and the deformation strain rate tensor **D** can be written like:

$$\boldsymbol{\tau}_p = \begin{bmatrix} \tau_{pxx} & \tau_{pxy} & \tau_{pxz} \\ \tau_{pyx} & \tau_{pyy} & \tau_{pyz} \\ \tau_{pzx} & \tau_{pzy} & \tau_{pzz} \end{bmatrix},\ \mathbf{D} = \begin{bmatrix} D_{xx} & D_{xy} & D_{xz} \\ D_{yx} & D_{yy} & D_{yz} \\ D_{zx} & D_{zy} & D_{zz} \end{bmatrix} \qquad \text{(A-3)}$$

In which the subscripts *x*, *y* and *z* correspond to the flow direction and the direction perpendicular to the flow direction, respectively. As **D** is defined as the half sum of the velocity gradient tensor $\nabla\boldsymbol{v}$ and its transpose $\nabla\boldsymbol{v^T}$, therefore **D** can be written as well:

$$\mathbf{D} = \frac{\mathbf{1}}{\mathbf{2}}\begin{bmatrix} \frac{\partial v_x}{\partial x} & \frac{\partial v_y}{\partial x} & \frac{\partial v_z}{\partial x} \\ \frac{\partial v_x}{\partial y} & \frac{\partial v_y}{\partial y} & \frac{\partial v_z}{\partial y} \\ \frac{\partial v_x}{\partial z} & \frac{\partial v_y}{\partial z} & \frac{\partial v_z}{\partial z} \end{bmatrix} + \frac{\mathbf{1}}{\mathbf{2}}\begin{bmatrix} \frac{\partial v_x}{\partial x} & \frac{\partial v_x}{\partial y} & \frac{\partial v_x}{\partial z} \\ \frac{\partial v_y}{\partial x} & \frac{\partial v_y}{\partial y} & \frac{\partial v_y}{\partial z} \\ \frac{\partial v_z}{\partial x} & \frac{\partial v_z}{\partial y} & \frac{\partial v_z}{\partial z} \end{bmatrix} \qquad \text{(A-4)}$$

For a simple shear flow, $\boldsymbol{\tau}_p$ and **D** can be simplified as:

$$\boldsymbol{\tau}_p = \begin{bmatrix} \tau_{pxx} & \tau_{pxy} & 0 \\ \tau_{pyx} & \tau_{pyy} & 0 \\ 0 & 0 & \tau_{pzz} \end{bmatrix} \tag{A-5}$$

$$\mathbf{D} = \begin{bmatrix} 0 & \frac{1}{2}\frac{\partial v_x}{\partial y} & 0 \\ \frac{1}{2}\frac{\partial v_x}{\partial y} & 0 & 0 \\ 0 & 0 & 0 \end{bmatrix} = \begin{bmatrix} 0 & \frac{1}{2}\dot{\gamma} & 0 \\ \frac{1}{2}\dot{\gamma} & 0 & 0 \\ 0 & 0 & 0 \end{bmatrix} \tag{A-6}$$

Back to Eq. A-1, the upper convected time derivative $\overset{\frown}{\boldsymbol{\tau}_p}$ and the lower convected time derivative $\overset{\smile}{\boldsymbol{\tau}_p}$ are defined as:

$$\overset{\frown}{\boldsymbol{\tau}_p} = \frac{\boldsymbol{D}\,\boldsymbol{\tau}_p}{\boldsymbol{Dt}} - (\,\boldsymbol{\tau}_p \cdot \nabla \boldsymbol{v} + \nabla \boldsymbol{v}^{\boldsymbol{T}} \cdot\, \boldsymbol{\tau}_p) \tag{A-7}$$

$$\overset{\smile}{\boldsymbol{\tau}_p} = \frac{\boldsymbol{D}\,\boldsymbol{\tau}_p}{\boldsymbol{Dt}} + (\,\boldsymbol{\tau}_p \cdot \nabla \boldsymbol{v} + \nabla \boldsymbol{v}^{\boldsymbol{T}} \cdot\, \boldsymbol{\tau}_p) \tag{A-8}$$

in which $\frac{\boldsymbol{D}\boldsymbol{\tau}_p}{\boldsymbol{Dt}} = 0$ for steady flow, Eq. A-5 are introduced into Eq. A-7 and Eq. A-8, then $\overset{\frown}{\boldsymbol{\tau}_p}$ and $\overset{\smile}{\boldsymbol{\tau}_p}$ are rewritten:

$$\overset{\frown}{\boldsymbol{\tau}_p} = -\left(\begin{bmatrix} \tau_{pxx} & \tau_{pxy} & 0 \\ \tau_{pyx} & \tau_{pyy} & 0 \\ 0 & 0 & \tau_{pzz} \end{bmatrix} \cdot \begin{bmatrix} 0 & 0 & 0 \\ \dot{\gamma} & 0 & 0 \\ 0 & 0 & 0 \end{bmatrix} + \begin{bmatrix} 0 & \dot{\gamma} & 0 \\ 0 & 0 & 0 \\ 0 & 0 & 0 \end{bmatrix} \cdot \begin{bmatrix} \tau_{pxx} & \tau_{pxy} & 0 \\ \tau_{pyx} & \tau_{pyy} & 0 \\ 0 & 0 & \tau_{pzz} \end{bmatrix}\right) = -\begin{bmatrix} 2\tau_{pxy} & \tau_{pyy} & 0 \\ \tau_{pyy} & 0 & 0 \\ 0 & 0 & 0 \end{bmatrix}\dot{\gamma} \tag{A-9}$$

$$\overset{\smile}{\boldsymbol{\tau}_p} = \begin{bmatrix} \tau_{pxx} & \tau_{pxy} & 0 \\ \tau_{pyx} & \tau_{pyy} & 0 \\ 0 & 0 & \tau_{pzz} \end{bmatrix} \cdot \begin{bmatrix} 0 & \dot{\gamma} & 0 \\ 0 & 0 & 0 \\ 0 & 0 & 0 \end{bmatrix} + \begin{bmatrix} 0 & 0 & 0 \\ \dot{\gamma} & 0 & 0 \\ 0 & 0 & 0 \end{bmatrix} \cdot \begin{bmatrix} \tau_{pxx} & \tau_{pxy} & 0 \\ \tau_{pyx} & \tau_{pyy} & 0 \\ 0 & 0 & \tau_{pzz} \end{bmatrix} = \begin{bmatrix} 0 & \tau_{pxx} & 0 \\ \tau_{pxx} & 2\tau_{pxy} & 0 \\ 0 & 0 & 0 \end{bmatrix}\dot{\gamma} \tag{A-10}$$

Then Eq. A-5, Eq. A-6, Eq. A-9 and Eq. A-10 are plugged into Eq. A-1, and Eq. A-1 is rewritten:

$$g(\boldsymbol{\tau}_p)\begin{bmatrix}\tau_{pxx} & \tau_{pxy} & 0\\ \tau_{pyx} & \tau_{pyy} & 0\\ 0 & 0 & \tau_{pzz}\end{bmatrix}+\lambda\begin{bmatrix}(\xi-2)\,\tau_{pxy} & \frac{(\xi-2)}{2}\,\tau_{pyy}+\frac{\xi}{2}\,\tau_{pxx} & 0\\ \frac{(\xi-2)}{2}\,\tau_{pyy}+\frac{\xi}{2}\,\tau_{pxx} & \xi\tau_{pxy} & 0\\ 0 & 0 & 0\end{bmatrix}\dot{\gamma}=$$

$$2\eta\begin{bmatrix}0 & \frac{1}{2}\dot{\gamma} & 0\\ \frac{1}{2}\dot{\gamma} & 0 & 0\\ 0 & 0 & 0\end{bmatrix} \qquad \text{(A-11)}$$

These kinematic equations lead to the following non-linear systems of equations of τ_{pxx}, τ_{pyy} and τ_{pxy}:

$$g(\boldsymbol{\tau}_p)\,\tau_{pxx}+\lambda(\xi-2)\,\tau_{pxy}\dot{\gamma}=0 \qquad \text{(A-12)}$$

$$g(\boldsymbol{\tau}_p)\,\tau_{pxy}+\lambda\left(\frac{(\xi-2)}{2}\,\tau_{pyy}+\frac{\xi}{2}\,\tau_{pxx}\right)\dot{\gamma}=\eta_p\dot{\gamma} \qquad \text{(A-13)}$$

$$g(\boldsymbol{\tau}_p)\,\tau_{pyy}+\lambda\xi\tau_{pxy}\dot{\gamma}=0 \qquad \text{(A-14)}$$

Based on the system of equations, we can therefore obtain the viscometric material functions of $\tau_{pxy}(\dot{\gamma})$, $N_1(\dot{\gamma})$ and $N_2(\dot{\gamma})$:

$$\tau_{pxy}(\dot{\gamma})=\frac{g(\boldsymbol{\tau}_p)\eta_p\dot{\gamma}}{g(\boldsymbol{\tau}_p)^2+\frac{(\lambda\dot{\gamma})^2}{2}\xi(2-\xi)} \qquad \text{(A-15)}$$

$$N_1(\dot{\gamma})=\tau_{pxx}-\tau_{pyy}=\frac{2\lambda\dot{\gamma}}{g(\boldsymbol{\tau}_p)}\,\tau_{pxy} \qquad \text{(A-16)}$$

$$N_2(\dot{\gamma})=\tau_{pyy}-\tau_{pzz}=\frac{-\lambda\xi\dot{\gamma}}{g(\boldsymbol{\tau}_p)}\,\tau_{pxy} \qquad \text{(A-17)}$$

$$\frac{N_1(\dot{\gamma})}{N_2(\dot{\gamma})}=-\frac{\xi}{2} \qquad \text{(A-18)}$$

From Eq. A-18, it shows that the magnitude value of the ratio of $N_1(\dot{\gamma})$ and $N_2(\dot{\gamma})$ is determined by the parameter ξ. It can be seen that the absolute value of $N_2(\dot{\gamma})$

increases with ξ value increasing, which increases with a more significant shear-thinning behavior.

A.2. Prediction of PTT model in shear-free or extensional flow

For a shear-free flow, the unidirectional elongational viscosity is defined:

$$\eta_e(\dot{\varepsilon}) = \frac{\tau_{pxx} - \tau_{pyy}}{\dot{\varepsilon}} \qquad \text{(A-19)}$$

In order to obtain the uniaxial extensional viscosity data, a velocity field $\boldsymbol{v} = \dot{\varepsilon}\,(x, -\frac{y}{2}, -\frac{z}{2})$ is considered, then the deformation strain rate **D** shown in Eq. A-4 can be written like:

$$\mathbf{D} = \dot{\varepsilon}\begin{bmatrix} 1 & 0 & 0 \\ 0 & -\frac{1}{2} & 0 \\ 0 & 0 & -\frac{1}{2} \end{bmatrix} \qquad \text{(A-20)}$$

Where $\mathrm{tr}(\mathbf{D}) = 0$ corresponds to the mass conservation rule. The stress tensor $\boldsymbol{\tau_p}$ in Eq. A-3 is written here like:

$$\boldsymbol{\tau}_p = \begin{bmatrix} \tau_{pxx} & 0 & 0 \\ 0 & \tau_{pyy} & 0 \\ 0 & 0 & \tau_{pzz} \end{bmatrix} \qquad \text{(A-21)}$$

According to the definition of $\overset{\frown}{\boldsymbol{\tau}}_p$ and $\overset{\frown}{\boldsymbol{\tau}}_p$ in Eq. A-7 and Eq. A-8.

$$\overset{\frown}{\boldsymbol{\tau}}_p = -\begin{bmatrix} 2\tau_{pxx} & 0 & 0 \\ 0 & -\tau_{pyy} & 0 \\ 0 & 0 & -\tau_{pzz} \end{bmatrix}\dot{\varepsilon}\,,\ \overset{\frown}{\boldsymbol{\tau}}_p = \begin{bmatrix} 2\tau_{pxx} & 0 & 0 \\ 0 & -\tau_{pyy} & 0 \\ 0 & 0 & -\tau_{pzz} \end{bmatrix}\dot{\varepsilon} \qquad \text{(A-22)}$$

Then introducing Eq. A-22 into Eq. A-1, the equation for extensional flow is:

$$\boldsymbol{g}(\boldsymbol{\tau}_p)\begin{bmatrix}\tau_{pxx} & 0 & 0\\ 0 & \tau_{pyy} & 0\\ 0 & 0 & \tau_{pzz}\end{bmatrix}+\lambda\begin{bmatrix}(2\xi-2)\,\tau_{pxx} & 0 & 0\\ 0 & (1-\xi)\,\tau_{pyy} & 0\\ 0 & 0 & 0(1-\xi)\,\tau_{pzz}\end{bmatrix}\dot{\varepsilon}\;=$$

$$2\eta\begin{bmatrix}1 & 0 & 0\\ 0 & -\frac{1}{2} & 0\\ 0 & 0 & -\frac{1}{2}\end{bmatrix}\dot{\varepsilon} \qquad \text{(A-23)}$$

Based on the system of equations, we can therefore obtain the extensional material functions:

$$g(\boldsymbol{\tau}_p)\,\tau_{pxx}\;+2\lambda(\xi-1)\dot{\varepsilon}\,\tau_{pxx}=2\,\eta_p\dot{\varepsilon} \qquad \text{(A-24)}$$

$$g(\boldsymbol{\tau}_p)\,\tau_{pyy}\;+\lambda(1-\xi)\dot{\varepsilon}\,\tau_{pyy}=-\,\eta_p\dot{\varepsilon} \qquad \text{(A-25)}$$

Combining Eq. A-24, Eq. A-25 and Eq. A-19, then we obtain:

$$\eta_e(\dot{\varepsilon})=\frac{\tau_{pxx}-\tau_{pyy}}{\dot{\varepsilon}}=3\,\eta_p\left[\frac{g(\boldsymbol{\tau}_p)}{(g(\boldsymbol{\tau}_p)-2\lambda(1-\xi)\dot{\varepsilon})(g(\boldsymbol{\tau}_p)+\lambda(1-\xi)\dot{\varepsilon})}\right] \qquad \text{(A-26)}$$

Here it can be seen that when the part in the big bracket in the right side of Eq. (A-26) equal the value of 1, the ratio of elongational viscosity to shear viscosity namely the Trouton ratio is equal to 3, which is a typical value for the Newtonian flow. It should be noted that when the parameter ξ is equal to 1, the rheological properties including η_e, η_s and N_1 are independent on the value of parameter ε.

A.3. Contributions of each mode to final rheological properties

Based on the discussion above, it shows the analytical equation systems derived from a single mode PTT model regarding the simple shear behavior and uniaxial extensional behavior. For the fit of the rheological properties by PTT model, all these

equation systems above are also should be coupled with the modulus equation shown as below:

$$G'(\omega) = \frac{\eta\lambda\omega^2}{1+(\lambda\omega)^2},\ G''(\omega) = \frac{\eta\omega}{1+(\lambda\omega)^2} \qquad \text{(A-27)}$$

Multi-mode PTT model with relaxation spectrum is utilized to capture the viscoelastic response to polymer chains with various time-scale deformation history. Consequently, it is meaningful to figure out the contribution from each mode to the total rheological properites:

$$\tau_p = \sum_i^N \tau_{pi} \qquad \text{(A-28)}$$

Here we select the material parameters of neat PP in Table 3-2. Fig. A-1 shows the rheological properties, namely storage modulus G', shear viscosity η_p, first normal stress difference N_1, and extensional viscosity η_e, predicted by 4-mode constitutive PTT model and the corresponding each mode of the multi- mode. It is seen that the reological properties G', η_{ps}, N_1 and η_{pe} at high $\dot{\gamma}$ or $\dot{\varepsilon} \geq 100\ s^{-1}$ dominantly come from the contribution of mode-4 from the multi-mode PTT model. In terms of G' and N_1 at extraly low strain rate range, around $\leq 0.1\ s^{-1}$, it is mainly composed of the contribution of mode-1. With regard to the terms η_e and η_p, by contrary, the contribution of mode-1 to the total magnititude of η_{pe} and η_{ps} no longer plays a main role, which might be because of the small value of η_p in mode-1. In addition, the

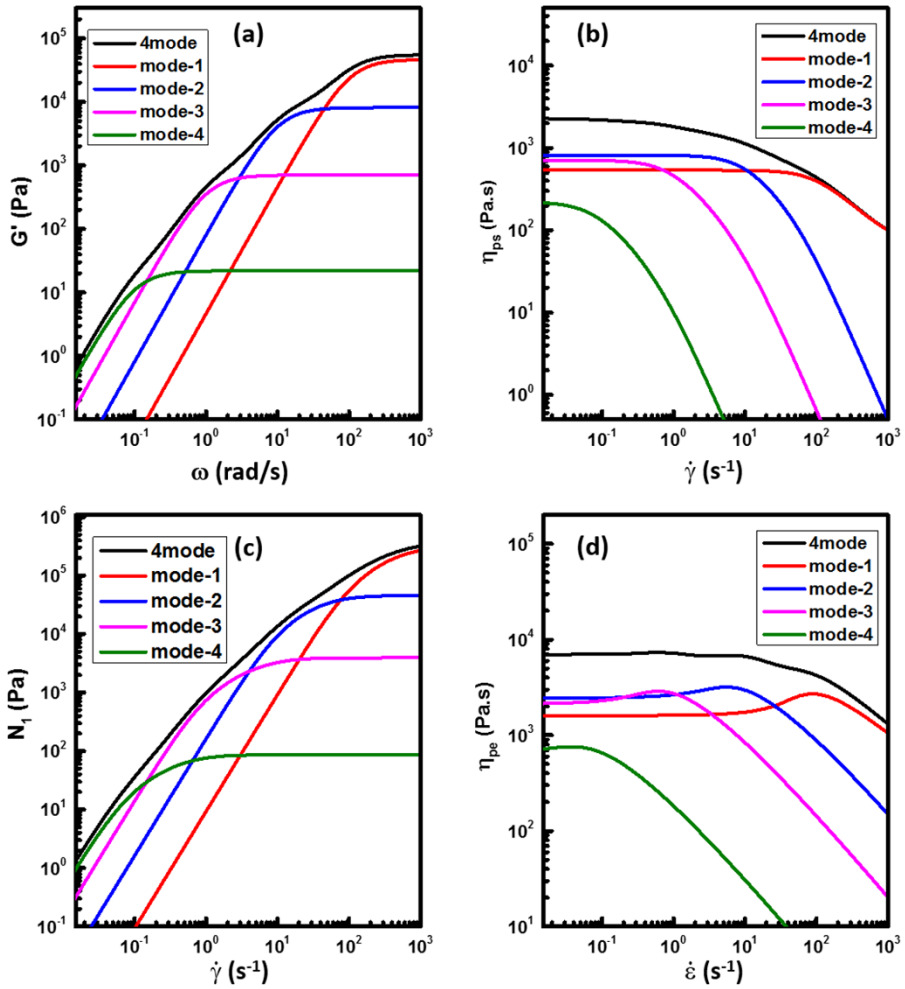


Figure A-1. Rheological properties of neat PP predicted by 4-mode PTT model (the label 4mode in legend) and its each mode (label mode-1, mode-2, mode-3 and mode-4): (a) elastic modulus G'; (b) shear viscosity η_{ps}; (c) first normal stress difference N_1; (d) elongational viscosity η_{pe}.

rheological properties predicted by mode-2 and mode-3 mainly compose the final rheological properties at middle strain rates between 10 s^{-1} and 100 s^{-1}. It should be interesting to note that the reciprocal of strain rate range mentioned above is equal to the corresponding parameter relaxation time λ_i in the ith mode of the multi-mode model. This might be the reason for the phenomenon oberseved above. Consequently,

it is easy to understand that manually tuning the rheological property at a certain strain range can be conducted by adjusting the material parameters in the corresponding mode predominantly. Therefore, next focus is on the evaluation of the sensitivity of the material parameters on the rheological properties of polymer melt.

A.4. Sensitivity of the material parameters on the rheological properties

The parameter λ_i and η_{pi} are related to the linear rheological properties of polymer melt like G', G'' and zero shear-rate viscosity η_0, which are easily obtained from the Small Amplitude Oscillatory Steady (SAOS) test in the linear viscoelastic region. Therefore, here our focus is on the effect of the nonlinear parameter ξ_i and ε_i on the nonlinear reological properties like η_{si}, N_1, N_2 and η_{ei}. On the basis of the discussion above, we figure out how each mode of the multi-mode PTT model contributes to the final or total rheological properties, hence we select the corresponding nonlinear parameters in mode 3 as an example to illustrate the effect on the rheological properties. Important to mention that the parameter ξ_i or ε_i cannot affect the storage modulus G' and loss modulus G''.

Fig. A-2 shows the sensitivity of parameter ξ_3 on the rheological properties of neat PP melt. It is seen in Fig. A-2(a) that increasing parameter ξ_3 significantly leads to an increase of the magnitude value of $|N_2|$ but a decrease for N_1 value. In addition, seen from the right axil, an obvious increasing ratio value of $|N_2|/N_1$ is noted as well with ξ_3 increasing. As presented in Fig. A-2(b), the shear viscosity obvisouly decreases in the order of the ξ_3 value from 0.05 to 0.8, while little change of the extensional viscosity is noticed in Fig. A-2(c).

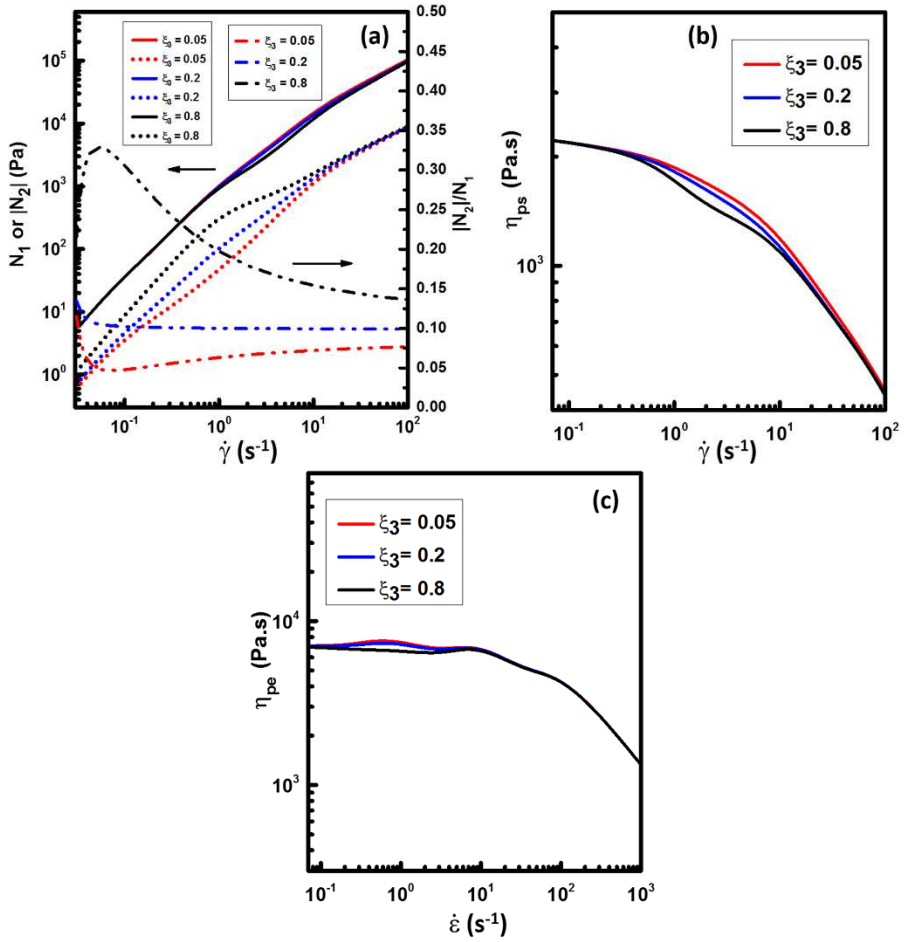


Figure A-2. The effect of parameter ξ_3 on the rheological properties of neat PP predicted by 4-mode PTT model: (a) the left axil: N_1 (solid curve) and $|N_2|$ (dot curve); right axil: the ratio value of $|N_2|/N_1$ (dashed dotted curve); (b) shear viscosity; (c) elongational viscosity η_{pe}.

Fig. A-3 exhibits the changes of the rheological properties caused by varying the parameter of ε_3 in the range of 0.05 to 0.65. Same as the paramter of ξ_3, increasing the parameter of ε_3 results in a smaller N_1 value. It should be noted that although the value of $|N_2|$ shows an increasing trend with increasing ε_3, the variation degree is

much smaller than that in the situation of increasing ξ_3 shown in Fig. A-2(a). A s a result, the ratio value of $|N_2|/N_1$ keeps unchanged due to the unchanged value of the ξ_3. Back to Eq. A-18, it might be explained by the reason that the $|N_2|/N_1$ value is only determined by the value of ξ. Shown in Fig. A-3(b), little change of the shear viscosity η_{ps} is caused by varying the parameter of ε_3. While a sharp increase of the extensional viscosity η_{pe} value correspond to the well-known strain-hardening behavior, is noticed in contrast as the ε_3 value decreases to 0.05.

Overall, based on the discussion above, it is conclued that the material parameters ξ_i and ε_i mainly control the shear behavior including the variation of N_1, N_2 and η_{ps}, and the elongational behavior like extensional viscosity η_{pe}, respectively. However, the material parameter ξ_i could as well tune the elongational visocsity, just as the material parameter ε_i can tune the shear-based rheological properties including N_1 and N_2 to a very limited extent.

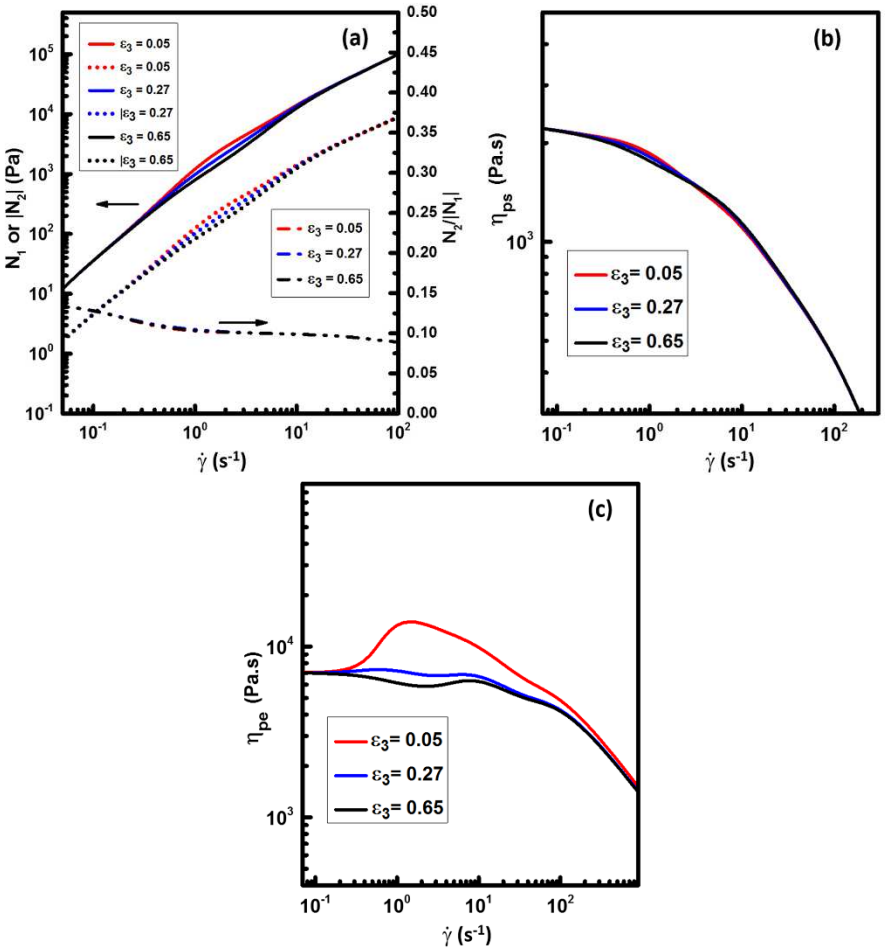


Figure A-3. The effect of parameter ξ_3 on the rheological properties of neat PP predicted by 4-mode PTT model: (a) the left axil: N_1 (solid curve) and $|N_2|$ (dot curve); right axil: the ratio value of $|N_2|/N_1$ (dashed dotted curve); (b) shear viscosity; (c) elongational viscosity η_{pe}.

Appendix B

Supplementary information for Chapter 4

B.1. Mesh patterns for 3D and 2D simulations

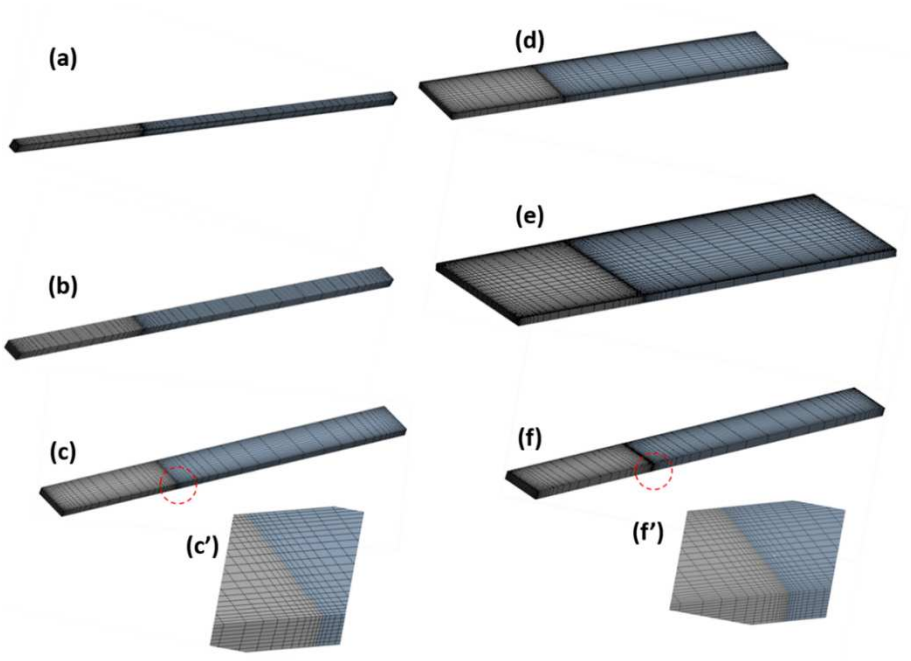


Figure B-1. Meshes for 3D geometries with various aspect ratios in Table 4-2: (a): 1:1, (b) 2:1, (c) 5:1, (d) 10:1, (e) 20:1, (f) refined mesh pattern for the geometry with aspect ratio 5:1; (c') and (f') reveal the close view of the mesh grids near the die exit.

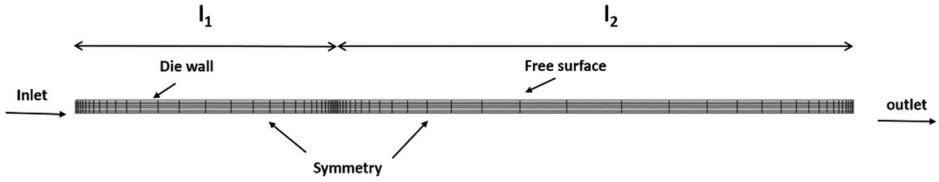


Figure B-2. Mesh for the 2D flow domain; *x-y* mesh sizes are maintained.

The mesh-independence of the simulation results for each slit die is verified at $\dot{\gamma}_a$ = 48 s^{-1}, as shown in Table B-1. It should be noted that for the highest aspect ratio of 20, the simulation for PP flow based on the refined Mesh 6 could not be fully conducted since the computational memory for the calculation is beyond that of the computer server used. However, the final area swell ratio of the simplified Newtonian flow in terms of Mesh 6 and the refined Mesh 6 are compared, with a discrepancy less than 0.6%. To reduce the computational cost, the simulation results are obtained based on the less refined mesh patterns in the sections below.

TABLE B-1. Mesh information and swell ratios with various aspect ratios at $\dot{\gamma}_a$ = 48 s^{-1}.

Aspect ratio	Mesh	Elements	Nodes	B_1	B_2	B_3	B_4
1	1	4736	6075	1.3	1.3	1.145	1.555
	Refined-1	9240	11220	1.29	1.29	1.132	1.536
1.5	2	6240	7722	1.284	1.309	1.06	1.533
	Refined-2	11250	13376	1.28	1.307	1.052	1.52
2	3	8320	10098	1.26	0.99	1.31	1.507
	Refined-3	12000	14212	1.26	0.99	1.308	1.504
5	4	10920	13068	1.22	0.86	1.31	1.478
	Refined-4	18750	21736	1.218	0.86	1.308	1.47
10	5	15600	18414	1.19	0.81	1.294	1.452
	Refined-5	22500	25916	1.188	0.798	1.292	1.446
20[a]	6	20800	24354	1.15	0.78	1.288	1.417
	Refined-6	34000	38786	---	---	---	---
2D	7	520	594	---	---	1.314	---
	Refined-7	850	946	---	---	1.31	---

B.2. Details on extrudate area swell

Figure B-3 compares the final area swell ratios B_4 of the extrudates along the flow distance. It is shown that increasing the aspect ratio significantly decreases the final B_4. For example, as the aspect ratio increases from 1 to 20, the corresponding area swell ratio falls from 1.55 to 1.417. This is mainly attributed to the abrupt decrease in the width swell ratio B_1 even though there is a very slight drop in the middle height swell ratio B_3. In terms of the low aspect ratios, the equilibrium swelling positions can be reached immediately in a very short distance, while for high aspect ratios (≥ 5) an obvious gradual swelling follows the initially sharp swelling behavior until the final equilibrium positions are reached. Therefore, increasing the aspect ratio delays the onset at which the equilibrium is achieved, in agreement with the results in Figure B-4 and B-5.

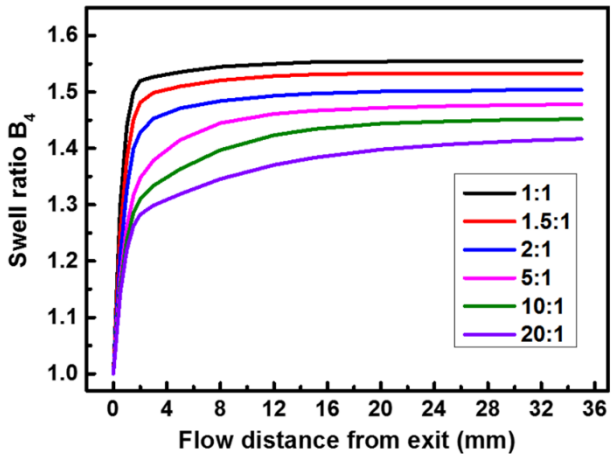


Figure B-3. Extrudate profiles of area swell ratio B_4 (Eq. 4-3) with different aspect ratio at $\dot{\gamma}_a$= 48 s^{-1} (200 ^oC; PP die extrudate).

B.3. Extra information on axial velocity component

Figure B-4 compares the axial velocity (v_x) profiles of the fully developed flows along the transversal (y variation at z=0 mm) and lateral direction (z variation at y=0 mm) with x=-10 mm before die exits with different aspect ratios for $\dot{\gamma}_a$ = 48 and 15 s^{-1}(left and right column). For the sake of comparison, the corresponding dimensions of the flow cells ($2H$ and $2W$) normalize the y and z coordinates. The v_x values are scaled by the corresponding 2D average velocity ($v_{xa\text{-}2D}$). It follows that as the aspect ratio increases, the velocity profile of the central flow (y=0 mm; z variation; right part of the subfigure) along the width direction is closer to flat compared to its analogue (z=0; y variation; left part of the subfigure), indicating that the flow behavior in the width and height direction differs gradually from each other, consistent with our previous work at an aspect ratio of 10 in Chapter 3 [1].

Regarding aspect ratio of 5, the velocity gradient keeps almost zero only when $\left|\frac{z}{2W}\right|$ value is equal to 0.2, while for higher aspect ratios of 10 and 20, a non-zero velocity gradient only begins when $\left|\frac{z}{2W}\right|$ value reaches a value around 0.3 and 0.4. This implies that in the z direction the flow can be thought as planar flow except for the flow region close to the side confining wall, again highlighting the 3D effect. Along the y direction, a significant alternation from 2D to 3D simulations is also noted due to the 3D effect, but more gradient variation is observed with the region where the impact of 3D effect on the flow field is dominant now is close to the symmetry plane. The largest deviation from the 2D simulation in Figure B-2, B-3 and B-4(a) is observed for aspect ratio of 1, in which the maximum velocity is quite smaller than that of the 2D flow. The ratio of the maximum velocity value to that of 2D flow decreases from

0.858 ($\dot{\gamma}_a$ = 15 s^{-1}) to 0.847 ($\dot{\gamma}_a$ = 48 s^{-1}) in terms of an aspect ratio of 1, which indicates that increasing the shear rate increases the 3D effect.

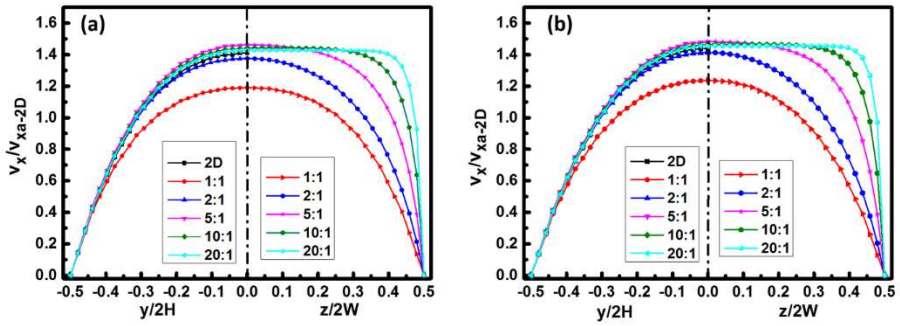


Figure B-4. A comparison of the axial velocity profile of the center flow (normalized with the average 2D value, z/y=0 mm (left/right part of the subfigure) 10 mm before the die exit (x=-10 mm) at two apparent shear rates: (a) $\dot{\gamma}_a$ = 48 s^{-1} and (b) $\dot{\gamma}_a$ = 15 s^{-1}; 200°C; PP extrudate (Table II); a stronger gradient is obtained for the *y* direction.

B.4. Extra input on stress in die

Figure B5 shows the calculated fully developed stress components at x= -10 mm (shear stresses: τ_{yx} and τ_{zx}; normal stress differences (N_{xy} (τ_{xx}-τ_{yy}) and N_{xz} (τ_{xx}-τ_{zz})) for all 3D and 2D flows at $\dot{\gamma}_a$ = 48 s^{-1}. In Fig. B-5(a), for the simplified 2D flow, the shear stress τ_{yx} (left part of subfigure) linearly grows with the die height and is almost the same as that of the one of the 3D flow with higher aspect ratios (>2). Regarding small aspect ratios, the shear stress τ_{yx} profiles show a clear discrepancy from that of the 2D flow, particularly in case the aspect ratio equals to 1. The region where the 3D effect on τ_{yx} is dominant is for $\left|\frac{y}{2H}\right|$ between 0.15 and 0.45. The maximum stress values on the "top" die wall for all simulation cases are nearly the same, confirming the reasonability of the strategy used in this study to maintain the same $\dot{\gamma}_a$ for all 3D and

2D simulations. Similar trends are found for N_{xy} profiles in Figure B-5 (again left part of subfigure). Increasing the aspect ratio narrows the N_{xy} profile difference. Due to the almost same τ_{yx} and N_{xy} value on the "top" die wall for all simulations, there is a small deviation in the final B_3 values (cf. Eq. 4-11; Table 4-3) although with different extrudate evolution profiles in Figure B-5.

The τ_{zx} and N_{xz} profiles along the width (z) direction are also presented in Figure B-5 (right parts of subfigures). Significant changes of the stress profiles (also as a function of z) come from varying the aspect ratios. For instance, for an aspect ratio of 1, the N_{xz} magnitude (Fig. B-5(b)) is up to around 70 *kPa*. As the aspect ratio increases, the stress profile is closer to be nearly flat in most of the flow region with much lower maximum N_{xz} magnitudes at the edge. Here, the relevance of accounting for z direction and the consideration of 3D model is thus again highlighted.

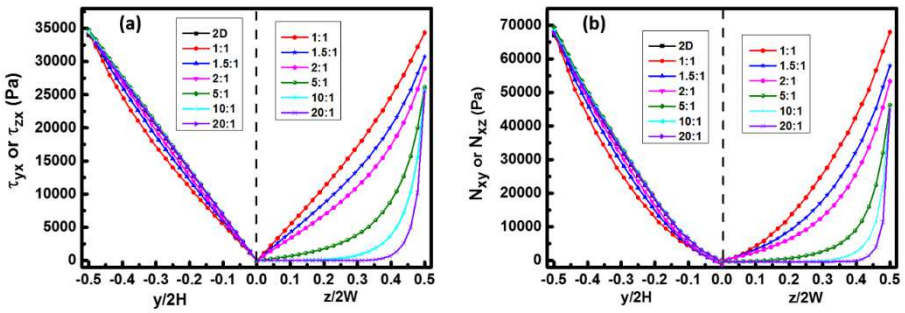


Figure B-5. A comparison of stress components for fully developed 3D flow (x= -10mm) with different aspect ratios and 2D flow (Table 5-2; PP extrudate; 200 °C): (a) shear stress components (τ_{yx} and τ_{zx}); (b) normal stress difference components ($N_{xy}(\tau_{xx}-\tau_{yy})$ and $N_{xz}(\tau_{xx}-\tau_{zz})$) at $\dot{\gamma}_a$ = 48 s^{-1}.

REFERENCES

1. Tang, D., et al., *Isothermal flow of neat polypropylene through a slit die and its die swell: Bridging experiments and 3D numerical simulations.* Journal of Non-Newtonian Fluid Mechanics, 2019. **266**: p. 33-45.

Appendix C

Supplementary information for Chapter 5

C.1. Extra input on the redistribution of stress components τ_{xx}, τ_{yy} and τ_{zz} along flow distance

Figure C-1 reveals the evolution of the normal stress component τ_{xx} along the flow direction on the flow cross section y-z planes, namely 3 mm (a, b and c) before the die exit and 2 (d, e and f), 5 (g, h and i) and 10 mm (j, k and l) after the die exit, respectively. It is seen in Fig. C-1(a) that negative τ_{xx} close to the flow region inside the die is noted, corresponding to a compression force applied to the flow layers. As the flow just leaves the die exit, a larger magnitude of the stronger τ_{xx} indicating a larger compression force is observed. This corresponds to the τ_{xx} variations in Fig. 5-5. Interesting to note that the flow region close to the side edge of the extrudate in Fig. C-1(d), Fig. C-1(g) and Fig. C-1(j) with the largest τ_{xx} value instead of the flow region close to the top die wall in Fig. C-1(a). This implies the axial velocity v_x redistribution behavior. In addition, decreasing the die length seems to increase the compression force in the flow region and the elongational force close to the die walls, shown in Fig. C-1(d)-(l). Therefore, a larger velocity redistribution is expected due to the less homogenous flow distribution shown in Fig. C-1(a) as compared to that in Fig. C-1(b) and Fig. C-1(c).

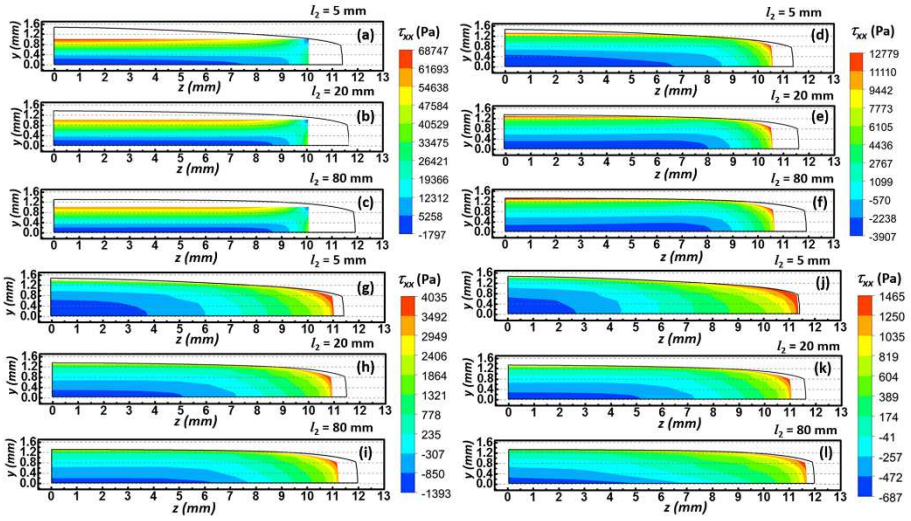


Figure C-1. The distributions of the stress component τ_{xx} in different y-z planes of the flow cross sections at different flow distances for the cases of die length of 5 mm (a, d, g and j), 20 mm (b, e, h, k) and 80 mm (c, f, i, l); Figure C-1(a)-(c) indicate the τ_{xx} distributions at a distance of 3 mm before the die exit; Figure C-1(d)-(f) indicate the τ_{xx} distributions at a distance of 2 mm after the die exit; Figure C-1(g)-(i) indicate the τ_{xx} distributions at a distance of 5 mm after the die exit; Figure C-1(j)-(l) indicate the τ_{xx} distributions at a distance of 10 mm after the die exit. Black curve in each figure represents the final extrudate profile in various cases. Flow rate of 620 mm^3/s.

Figure C-2 reveals the evolution of the normal stress component τ_{yy} on the flow cross section y-z planes. Consistent with Fig. 5-6(b), negative stress τ_{yy} corresponding to the compression force in the center flow region and the small positive stress τ_{yy} corresponding to the elongational force close to the die edge are observed. As the flow leaves the die exit, however, seen in Fig. C-2(d)-(l) that at the edge corner, the negative value of τ_{yy} is noticed for all cases, indicating a compression force applied to that region due to flow redistributions. Therefore, contraction flow (B_2 < 1) is observed in edge height direction shown in Fig. 5-3. Furthermore, the larger

magnitude value of τ_{yy} is observed with decreasing the die length to 5 mm, leading to smaller B_2 ratio with shorter die length. Larger magnitude value of τ_{yy} close to the middle top of the extrudate is noted with l_2=5 mm in Fig. C-2(j) than that with l_2=20 mm and l_2=80 mm in Fig. C-2(k) and Fig. C-2(l) at the flow distance of 10 mm after the die exit. This might result in the larger middle swell ratio B_2 for l_2=5 mm in Fig. 5-3.

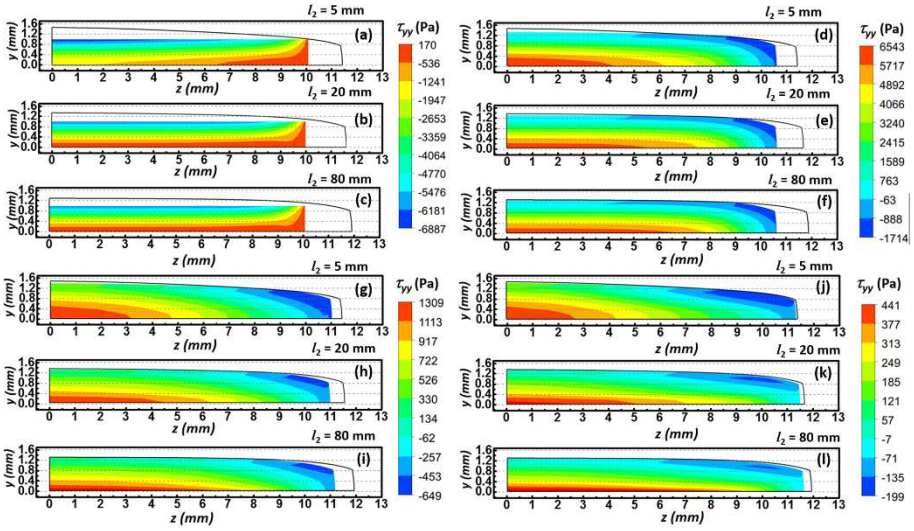


Figure C-2. The distributions of the stress component τ_{yy} in different y-z planes of the flow cross sections at different flow distances for the cases of die length of 5 mm (a, d, g and j), 20 mm (b, e, h, k) and 80 mm (c, f, i, l); Figure C-2 (a)-(c) indicate the τ_{yy} distributions at a distance of 3 mm before the die exit; Figure C-2 (d)-(f) indicate the τ_{yy} distributions at a distance of 2 mm after the die exit; Figure C-2 (g)-(i) indicate the τ_{yy} distributions at a distance of 5 mm after the die exit; Figure C-2 (j)-(l) indicate the τ_{zz} distributions at a distance of 10 mm after the die exit. Black curve in each figure represents the final extrudate profile in various cases. Flow rate of 620 mm^3/s.

Figure C-3 reveals the evolution of the normal stress component τ_{zz} on the flow cross section y-z planes. The main difference of the stress τ_{zz} distribution in Fig. C-3(a) with

respect to l_2= 5 mm stems from the much larger τ_{zz} of the center flow inside the die as compared with that in terms of l_2= 20 mm in Fig. C-3(b) and l_2= 80 mm in Fig. C-3(c). This indicates a stronger elongational force along the width direction in the former case. Fig. C-3(d)-(f) depicts the negative τ_{zz} close to the side edge of the extrudate as the flow just leaves the die exit, leading to a 'damping effect' on the width swell behavior. With a further distance after the die exit, the blue region taking up the stress contour of the extrudate cross section near the side edge of the extrudate applied with negative τ_{zz} in Fig. C-3(d)-(l) becomes larger as the die length is lowered to 5 mm. This explains the smallest width swell ratio B_3 due to the strongest 'damping effect' on the width swell behavior in Fig. 5-3 for the case of l_2= 5 mm.

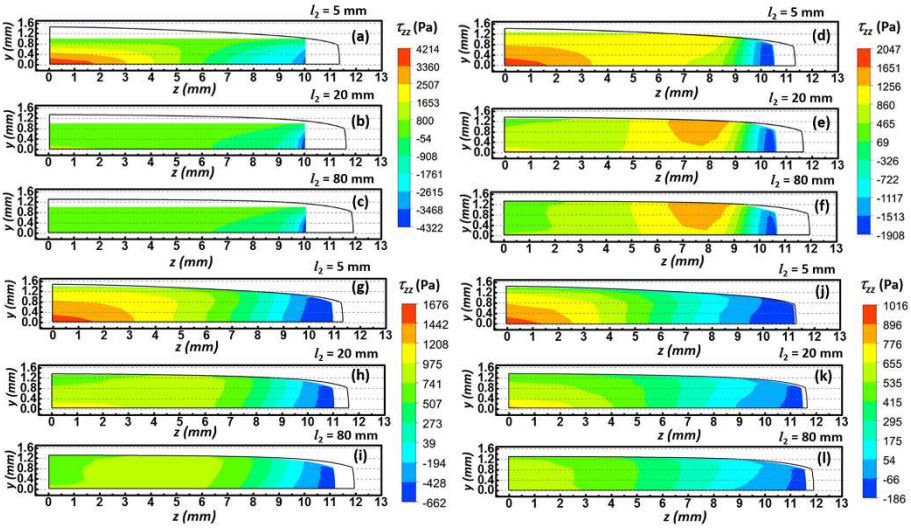


Figure C-3. The distributions of the stress component τ_{zz} in different y-z planes of the flow cross sections at different flow distances for the cases of die length of 5 mm (a, d, g and j), 20 mm (b, e, h, k) and 80 mm (c, f, i, l); Figure C-3(a)-(c) indicate the τ_{zz} distributions at a distance of 3 mm before the die exit; Figure C-3(d)-(f) indicate the τ_{zz} distributions at a distance of 2 mm after the die exit; Figure C-3(g)-(i) indicate the τ_{zz} distributions at a distance of 5 mm after the die exit; Figure C-3(j)-(l) indicate the τ_{zz} distributions at a distance of 10 mm after the die exit.

Black curve in each figure represents the final extrudate profile in various cases. Flow rate of 620 mm^3/s.

Appendix D

Supplementary information for Chapter 6

D.1. Detailed explanation for the exit pressure method through a slit die

For a detailed analysis regarding the exit pressure method, a comprehensive momentum balance theory is adapted to illustrate the flow behavior over the exit region of the slit die shown in Figure D-1. The fully developed flow is assumed at the position of $x = 0$, where a control surface is taken upstream far from the die exit with a distance of $x = S$. A second surface passed through a jet at a point sufficiently far from the exit where a uniform velocity v_j distribution is assumed [1]. Important to mention that a steady isothermal, incompressible, pressure-independent, and creeping laminar flow without surface tension and air drag effects is assumed through the slit die.

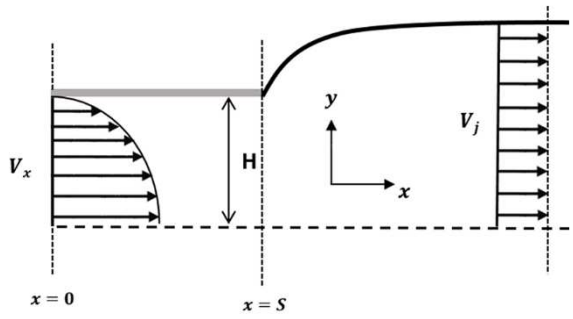


Figure D-1. Flow behavior over the slit die exit region, of which a half cross-section is considered. The macroscopic momentum balance theory is adopted to obtain the exit pressure.

The overall momentum balance theory for the steady planar flow layer at the distance of y = 0 leads to the following equation:

$$\int_0^H \rho {V_x}^2(y,0)2W dy - \rho {V_j}^2(y,0)2WH_j - \int_0^H T_{xx}(y,0)\,2W dy + \int_0^S 2(W + H)\tau_{xy}(H,x)\,dx = 0 \quad \text{(D-1)}$$

in which T_{xx} is the normal stress applied to the flow, ρ is density of the flow, τ_{xy} is the shear stress with a negative magnitude value along the exit flow region. Since W $\gg$ H (Large aspect ratio), Eq. D-1 is simplified into:

$$\int_0^H \rho {V_X}^2(y,0)2W dy - \rho {V_j}^2(y,0)2WH_j - \int_0^H T_{xx}(y,0)\,2W dy + \int_0^S 2W\tau_{xy}(H,x)\,dx = 0 \quad \text{(D-2)}$$

As for the term reactive thrust *Tr* which is equal to the momentum flux, therefore this indicates that the total reduced thrust through this flow region is defined as:

$$\nabla Tr = \int_0^H \rho {V_x}^2(y,0)2W dy - \rho {V_j}^2(y,0)2WH_j \quad \text{(D-3)}$$

∇Tr is equal to zero as ignoring the inertial effect of the polymer flow with ultralow Reynolds number (*Re*) [2], Eq. D-2 is reduced to:

$$-\int_0^H T_{xx}(y,0)\,dy + \int_0^S \tau_{xy}(H,x)\,dx = 0 \quad \text{(D-4)}$$

The viscometric normal stress difference is defined as:

$$N_1(y,0) = T_{xx}(y,0) - T_{yy}(y,0) \quad \text{(D-5)}$$

Taking Eq. D-5 into Eq. D-4, Eq. D-4 is rewritten as:

$$-\int_0^H N_1(y,0)\,dy - \int_0^H T_{yy}(y,0)dy + \int_0^S \tau_{xy}(H,x)\,dx = 0 \quad \text{(D-6)}$$

Since $\frac{\partial T_{yy}}{\partial y} = 0$ for fully developed flow, $T_{yy}(y,0)$ is equal to a constant, then

$$-\int_0^H N_1(y,0)\,dy - T_{yy}(H,0)H + \int_0^S \tau_{xy}(H,x)\,dx = 0 \qquad \text{(D-7)}$$

Rearranging Eq. D-7, it becomes

$$\int_0^H N_1(y,0)\,dy = -T_{yy}(H,0)H + \int_0^S \tau_{xy}(H,x)\,dx \qquad \text{(D-8)}$$

Assuming that the pressure of atmosphere air equals to zero, the magnitude value of the term $-T_{yy}(H,0)$ equals to the pressure $P_w(0)$ measured by the pressure transducer.

Considering the linear pressure decrease along the flow region ($\frac{\partial p}{\partial x} = \frac{\tau_w}{H}$), it is reasonable to extrapolate the pressure gradient to acquire the exit pressure, $P_e(S)$:

$$P_w(0) = \frac{\tau_w}{H} S + P_e(S) \qquad \text{(D-9)}$$

Combining Eq. D-9 with Eq. D-8, Eq. D-8 is rewritten

$$\int_0^H N_1(y,0)\,dy = \left(P_e(S) + \frac{\tau_w}{H} S\right) H + \int_0^S \tau_{xy}(H,x)\,dx \qquad \text{(D-10)}$$

Substituting the variable y in the left side of Eq. D-10 with $y = H\frac{\tau}{\tau_w}$, Eq. D-10 is written as:

$$\int_0^{\tau_w} N_1(\tau,0)\,d\tau = \tau_w P_e(S) + \frac{{\tau_w}^2}{H} S + \frac{\tau_w}{H}\int_0^S \tau_{xy}(H,x)\,dx \qquad \text{(D-11)}$$

The term τ_{xy} represents the wall shear stress in the exit region from $x = 0$ to $x = S$ and differ from the fully developed stress due to the velocity rearrangement behavior. It is rather difficult to derive a rule to express the term quantitatively, but a qualitative expression related to the effect from the length of the exit region, wall shear stress and Re number of the flow, can be deducted as:

$$\tau_{xy} = -\tau_w f(\theta, \tau_w; Re) \qquad \text{(D-12)}$$

In which, θ is defined as $\theta = \frac{x}{S} (0 \leq x \leq S)$.

Taking Eq. D-12 into Eq. D-13, then Eq. D-13 is rewritten as:

$$\int_0^{\tau_w} N_1(\tau, 0)\, d\tau = \tau_w P_e(S) + \frac{{\tau_w}^2}{H} S - \frac{{\tau_w}^2}{H} S \int_0^1 \tau_w f(\theta, \tau_w; Re)\, d\theta \quad \text{(D-13)}$$

Differentiating with respect to τ_w on both sides, the equation for N_1 calculation is finally obtained:

$$N_1 = P_e(S) + \tau_w \frac{\partial P_e}{\partial \tau_w} + \frac{\partial}{\partial \tau_w} \frac{{\tau_w}^2}{H} S \left(1 - \int_0^1 \tau_w f(\theta, \tau_w; Re)\, d\theta\right) \qquad \text{(D-14)}$$

Where the last right term indicates the flow redistribution behavior close to the die exit. Therefore, ignoring the flow redistribution behavior closed to die exit, Eq. D-14 is be reduced to:

$$N_1 = P_e(S) + \tau_w \frac{\partial P_e}{\partial \tau_w} \qquad \text{(D-15)}$$

Generally, N_1 is expressed as a function of the wall shear stress for the fully developed flow:

$$N_1 = K {\tau_w}^a \qquad \text{(D-16)}$$

This indicates that there should be a similar equation to combine the exit pressure $P_e(S)$ and the wall shear stress τ_w:

$$P_e(S) = K' {\tau_w}^b \qquad \text{(D-17)}$$

Taking Eq. D-17 into Eq. D-15, then the final simplified equation regarding the exit pressure method is:

$$N_1 = P_e(S) + P_e(S) \frac{\partial \log P_e}{\partial \log \tau_w} \qquad \text{(D-18)}$$

D.2. Extra input on discussions of Chapter 5

D.2.1. Extra input on pressure measurements for slit die

Table D-1. Measured pressures for various polymer melts (material parameters in Table 6-1; plot in Fig. 6-2) at 200 °C (P_i (i=1, 2, 3) at different die distances (20, 120, 170 mm) and the calculated (experimental) exit pressure P_{ex}. Also given is the coefficient of determination for the associated linear fit.

Material	shear rate (s^{-1})	P_1(bar)	P_2(bar)	P_3(bar)	P_{ex}(bar)	R^2 (-)
PP	34.3	43.25	30.99	5.18	0.187	0.99970
	43.9	50.28	35.61	6.09	0.216	1
	64.2	62.17	44.12	7.51	0.257	0.99998
	82.2	69.77	49.97	8.35	0.290	0.99970
	93.4	73.46	52.5	8.83	0.323	0.99980
LDPE	34.3	55.29	39.07	6.58	0.085	1
	45.8	61.74	43.6	7.35	0.094	1
	56.6	67.76	47.98	8.09	0.152	0.99999
	66.7	71.21	50.32	8.54	0.191	1
	97.3	85.88	60.98	10.30	0.279	0.99996
HDPE	18.7	98.26	70.21	11.85	0.469	0.99981
	35.0	131.60	93.78	15.92	0.638	0.99990
	51.8	157.37	112.30	19.07	0.832	0.99986
	64.1	172.68	123.34	20.94	0.941	0.99983
	76.7	185.91	132.92	22.64	1.139	0.99981
PP/G20	23.5	47.98	33.55	5.83	0.140	0.99980
	33.0	54.66	38.22	6.65	0.165	0.99981
	52.0	65.44	45.81	7.96	0.204	0.99983
	68.4	70.80	49.67	8.60	0.233	0.99990
	77.5	77.54	54.60	9.46	0.338	0.99997

D.2.2. Geometry and Mesh patterns for 3D modelling

Figure D-2 presents two types of mesh patterns with different mesh grids or densities. Denser and smaller mesh elements are utilized near the exit singularity regions in the case of refined mesh in Fig. D-3 in comparison with less refined mesh in Fig. D-3.

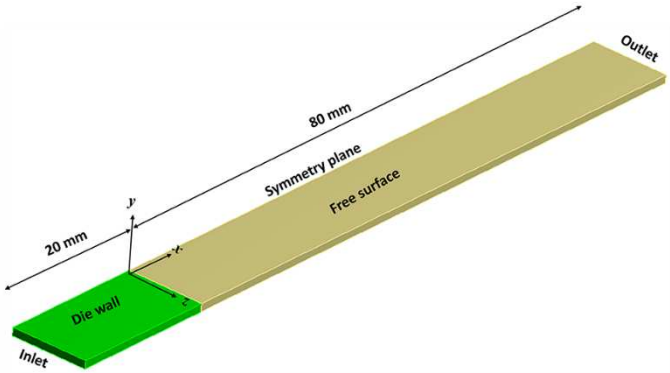


Figure D-2. 3D flow domain of a slit die profile for the isothermal (200 °C) flow simulations; one quarter of the geometry is considered.

Fig. D-4 compares the extrudate width swell ratio B_1 and edge height swell ratio B_2 for HDPE melt with varying shear rates to check the mesh sensitivity on the simulated swell behavior. It is seen that there is no change of the evolution profiles of both swell ratios with refining the mesh configuration. The largest difference for B_1 and B_2 is less than 0.3% and 0.5%, respectively. This indicates that the swell behavior is independent of the mesh pattern.

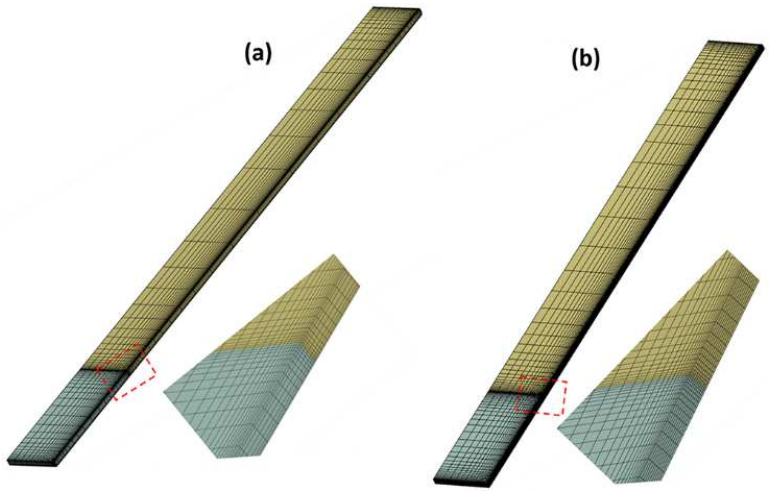


Figure D-3. Mesh arrangements for two mesh patterns.

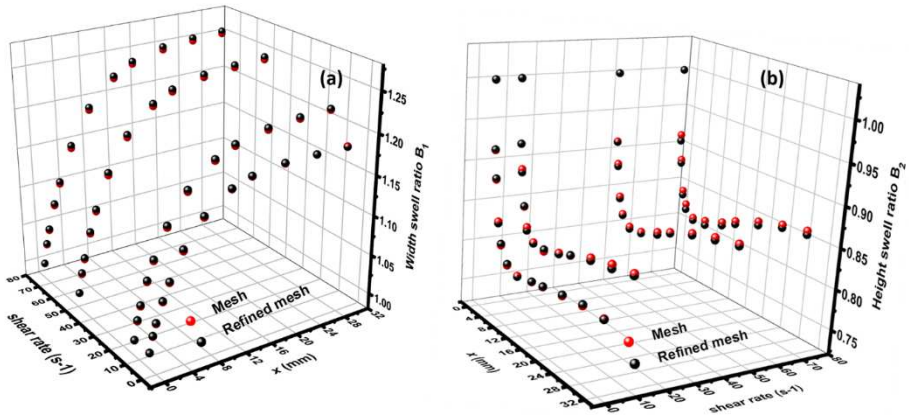


Figure D-4. A comparison of the extrudate width swell ratios B_1 and edge height swell ratio B_2 of HDPE melt as a function of wall shear rate with two mesh patterns: Mesh and Refined mesh.

D.2.3. Extra information on the rheological properties of PP composites

Figure D-5(a) shows that only if the filler amount increases to 40 m%, a yield stress phenomenon might start to occur, which cannot be observed for the PP/10GP and PP/20GP melt in this study. Importantly, if the filler amount is lowered to 10 m%, the Cox-Merz rule is valid again, as shown in Fig. D-5(b).

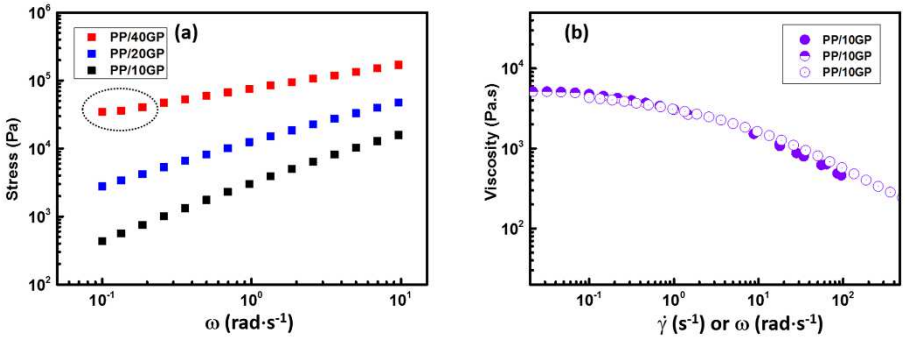


Figure D-5. (a) Stress as function of the angular frequency for PP composites with mass amount of 10%, 20%, 40% graphite; (b) Various types of viscosity for PP composite with 10% graphite filler: complex viscosity from rotational rheometer: filled symbols; shear viscosity also from rotational rheometer: open symbols; shear viscosity from inline slit die method: half-filled symbols.

D.2.4. Extra details on the PTT model at 200 °C

D.2.4.1. Isothermal fit at 200 °C

Figure D-6 exhibits the fit of the rheological properties of HDPE and LDPE melt, as recorded in the present work (focus on *G*', *G*", complex viscosity, shear viscosities and extensional viscosity), using the PTT model at 200 °C. Good fittings for both HDPE and LDPE melts indicate the reasonability of the material parameters in Table 6-2. It should be noted that the parameter ε is obtained according to the general trend for the extensional behavior like no strain-hardening for polymers with linear molecular structures like PP and HDPE, and strain-hardening behavior at the smaller strain rate range for polymer with chain-branched structures like LDPE [3-6]. For completeness, parameters for PP melt at 200 °C can be found Table 3-2 in Chapter 3 [7].

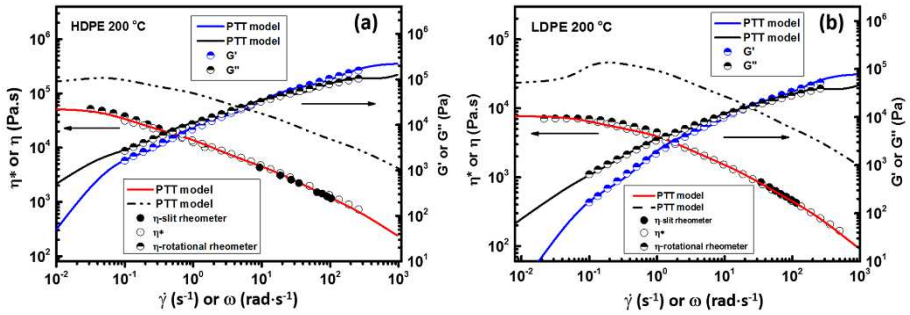


Figure D-6. The viscosity values (left axis) obtained from various measurement ways; the storage and loss modulus, G' and G'' from the rotational rheometer (right axis): symbols represent the experimental data and the curves show the fittings by PTT model (dash curve represents the fitted extensional viscosity data): (a) HDPE and (b) LDPE at 200 °C. Parameters in Table 6-2 in the main text.

D.2.5. Extra details on the impact of the flow redistributions

For the three neat polymer melts (200 °C), Fig. D-7 (left axis) compares at three shear rates the simulated so-called P_{ex} values obtained by extrapolation of red lines in Fig. D-7 (shaded colored bars) with the simulated $P_{ex,r}$ values based on the purple curves in Fig. D-7 (evaluation at -0.15 mm; full colored bars; explanation see main text). It is found that for all melts the flow disturbance in vicinity of the die exit leads to a significantly higher-pressure value. In addition, the relative contribution to the die exit stemming from the velocity redistribution R_v, defined as $(P_{ex,r} - P_{ex})/P_{ex,r}$, $ca.$ 25-40%, is as shown in Fig. D-8 (right axis; black/grey bars). For example, for HDPE flow at a shear rate of 51.8 s^{-1}, $P_{ex,r}$ and P_{ex} are 1.8 and 1.28 bar, and therefore R_v is around 30%.

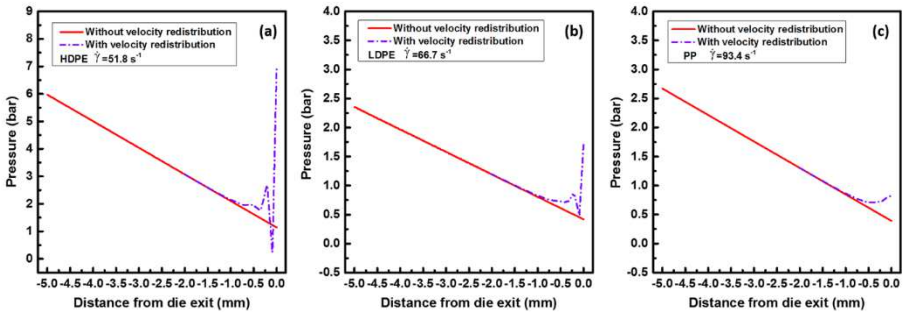


Figure D-7. The pressure profiles along the die wall direction to the die exit while considering the flow velocity rearrangements (purple dashed dotted curve; full 3D model) and without doing so (red curve; linear extrapolation) for (a) HDPE, (b) LDPE, and (c) PP melt as approaching the die exit at 200 °C. For the purple dashed dotted curves, based on the results in Fig. 6-8 in the main text, a position of -0.15 mm is used as marker to minimize the impact of a possible artificial error, i.e. the 3D simulated exit pressure $P_{ex,r}$ is determined there.

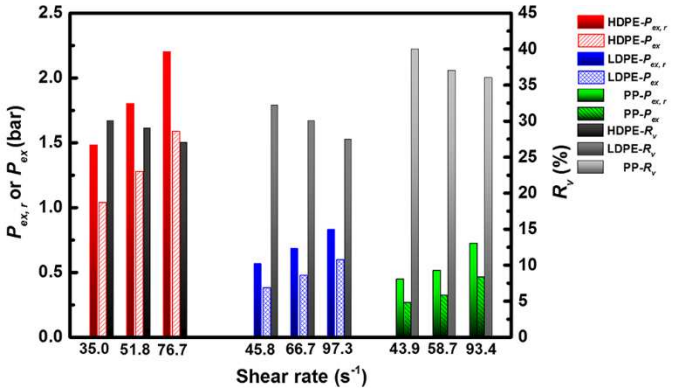


Figure D-8. Left axis: a comparison of the simulated exit pressure while considering the velocity redistribution near the die exit (so-called $P_{ex,r}$; *cf.* purple curves in Fig. D-7) and without doing so (so-called P_{ex} values; *cf.* red extrapolation lines in Fig. D-7) for HDPE (red), LDPE (blue), and PP (green) melt at 200 °C and different shear rates; Right axis (grey scale): the relative contribution to the exit pressure coming from the velocity rearrangement (R_v being $(P_{ex,r} - P_{ex})/P_{ex,r}$). There are significant deviations, but for a reliable N_1 determination (*cf.* the application of the conventional Eq. 6-4) this deviation can be ignored, as shown in Fig. 6-9 in the main text.

D.2.6. Non-isothermal modelling with PTT model

Figure D-9 presents the non-isothermal viscosities and G'/" data for the three polymer melts, HDPE, LDPE and PP at the temperature of 180, 200 and 230 °C. Referring to Eq. 6-15 in the main text 200 °C is selected as the reference temperature and the corresponding viscosity functions at 180 and 230 °C are obtained through a non-isothermal fit of the experiment data. Good agreement is shown in Figure D-9 and the corresponding material parameters are shown in Table 6-3.

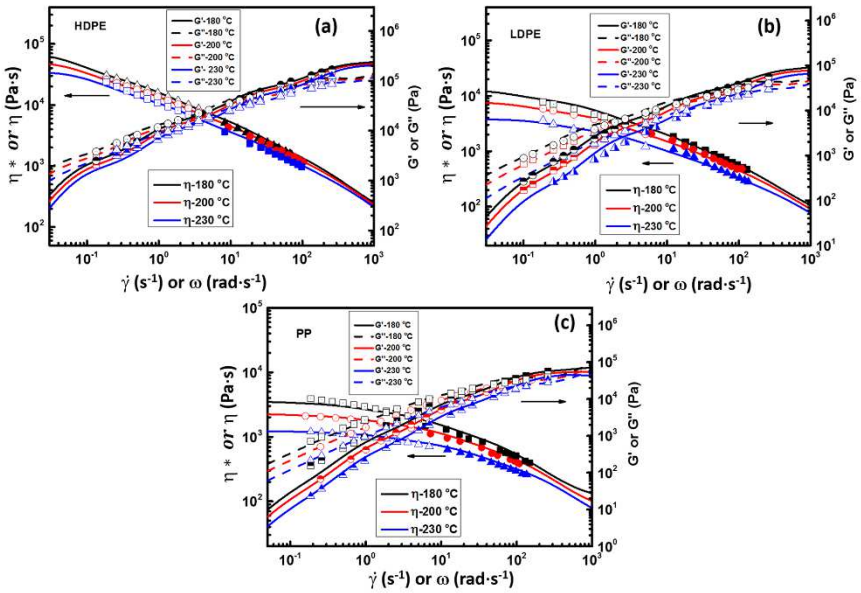


Figure D-9. The viscosity values (left axis) obtained at three different temperatures (180, 200 and 230 °C): open symbols: viscosity at low shear rate (Cox-Merz rule); filled symbols: viscosity at high shear rate from slit rheometer; The storage G' and loss G'' modulus (right axis) obtained at different temperatures: half-filled symbols: G'; open symbols: G''. All the curves show the fit by the PTT model: (a) HDPE, (b) LDPE and (c) PP.

Table D-2. Extra material parameters of the neat polymer melts at the corresponding highest shear rate (cf. Eq. 6-15 and Eq. 6-16).

	HDPE	LDPE	PP	Reference
k ($W\,m^{-1}\cdot K^{-1}$)	0.44	0.3	0.11	[8]
E ($kJ\,mol^{-1}$)	27.3	46.6	40.5	This work
U $(m \cdot s^{-1})$	0.024	0.026	0.03	This work
T_r (K)	473	473	473	This work

In Table D-2, in comparison with HDPE, LDPE has a larger activation energy *E* due to the presence of chain branching [9]. To reduce the computational cost, 2D modeling is utilized now to assess the non-isothermal flow behavior caused by the viscous heating effect.

Fig. D-10(a)-(c) reveal the temperature distribution in the region close to die exit at the corresponding maximum wall shear rate studied for each neat polymer melt, at which the temperature gradient caused by the viscous heating effect is generally acknowledged to be the largest [10]. It is found that the maximum temperature increase occurs on the symmetry flow plane close to the die exit, which is similar to the previous results [10, 11]. The temperature variations at various shear rates can be found in Fig. D-10(d). The corresponding maximum temperature increases are 1.2 ^{o}C for HDPE, 0.7 ^{o}C for LDPE and 0.6 ^{o}C for PP melt, considering an ideal start temperature profile with respect to the set temperature of 200 °C. This indicates that the temperature increases (at least in the region very close to the die exit) are less than 2 ^{o}C so that they can be neglected. This indicates that the viscous heating effect vanishes so that the N_1 measurements by the means of the exit pressure method are free from this effect, at least considering the experimental ranges investigated in this work.

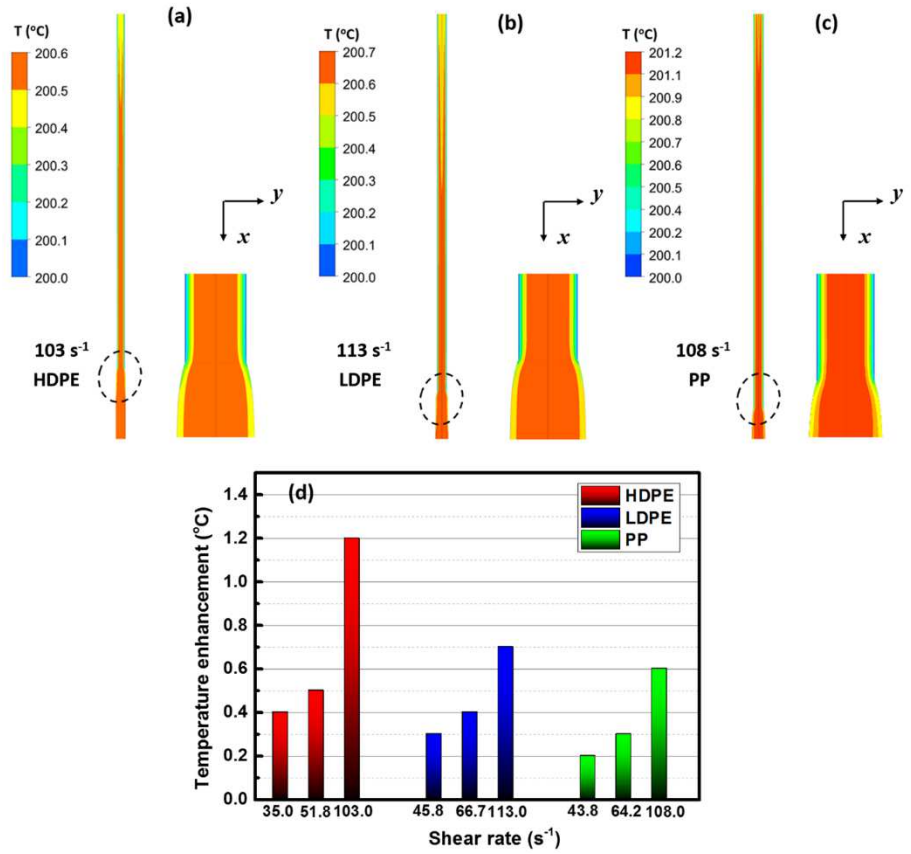


Figure D-10. The simulated simplified 2D temperature distribution of the three neat polymer melts (reference PTT model parameters in Table 6-2 and Table D-3) at the largest wall shear rates with 200 °C applied at the inlet and die wall; also a zero heat flux *q* is set for simplicity on the free surface and die outlet as we are only focusing in the present work on the region very close to the die exit; (a) PP at wall shear rate of 108 s^{-1}; (b) LDPE at wall shear rate of 113 s^{-1}; (c) HDPE at wall shear rate of 103 s^{-1}; (d) the maximal temperature increase at different wall shear rates due to the heating effect; all simulations with an ideal set extrusion temperature of 200 °C. The results indicate that the viscous heating effect can be neglected for the determination of the exit pressure.

REFERENCES

1. Boger, D.V. and M.M. Denn, *Capillary and slit methods of normal stress measurements.* Journal of Non-Newtonian Fluid Mechanics, 1980. **6**(3-4): p. 163-185.
2. Han, C.D., *On Silt-and Capillary-Die Rheometry*. Transactions of the Society of Rheology, 1974. **18**(1): p. 163-190.
3. Guillet, J., et al., *Comparison between experimental data and numerical models*, in *Rheology Series*. 1996, Elsevier. p. 285-336.
4. Kiriakidis, D. and E. Mitsoulis, *Viscoelastic simulations of extrudate swell for an HDPE melt through slit and capillary dies.* Advances in Polymer Technology, 1993. **12**(2): p. 107-117.
5. Ansari, M., E. Mitsoulis, and S.G. Hatzikiriakos, *Capillary extrusion and swell of a HDPE melt exhibiting slip.* Advances in Polymer Technology, 2013. **32**(S1).
6. Aloku, G.O. and X.-F. Yuan, *Numerical simulation of polymer foaming process in extrusion flow.* Chemical Engineering Science, 2010. **65**(12): p. 3749-3761.
7. Tang, D., et al., *Three-dimensional flow simulations for polymer extrudate swell out of slit dies from low to high aspect ratios.* Physics of Fluids, 2019. **31**(9): p. 093103.
8. Han, Z. and A. Fina, *Thermal conductivity of carbon nanotubes and their polymer nanocomposites: A review.* Progress in polymer science, 2011. **36**(7): p. 914-944.
9. Resch, J.A., *Elastic and viscous properties of polyolefin melts with different molecular structures investigated in shear and elongation.* 2010.
10. Ansari, M., S.G. Hatzikiriakos, and E. Mitsoulis, *Slip effects in HDPE flows.* Journal of Non-Newtonian Fluid Mechanics, 2012. **167**: p. 18-29.
11. Chan, T., B. Pan, and H. Yuan, *An experimental study of exit pressures for polymer melts.* Rheologica Acta, 1990. **29**(1): p. 60-70.